ECO-ENVIRONMENTAL VULNERABILITY ASSESSMENT IN CHANDEL DISTRICT, MANIPUR, USING GEOSPATIAL TECHNIQUES

THESIS SUBMITTED IN PARTIAL FULFILLMENT OF THE REQUIREMENTS

FOR THE DEGREE OF DOCTOR OF PHILOSOPHY

BY
MIDLERTHANGLIAN LEIVON
PHD/GEO/00283

DEPARTMENT OF GEOGRAPHY
SCHOOL OF SCIENCES
NAGALAND UNIVERSITY LUMAMI 798627
NAGALAND
OCTOBER 2025

ECO-ENVIRONMENTAL VULNERABILITY ASSESSMENT IN CHANDEL DISTRICT, MANIPUR, USING GEOSPATIAL TECHNIQUES

THESIS SUBMITTED IN PARTIAL FULFILLMENT OF THE REQUIREMENTS

FOR THE DEGREE OF DOCTOR OF PHILOSOPHY

IN

GEOGRAPHY

BY
MIDLERTHANGLIAN LEIVON
PHD/GEO/00283
Dated: 21/08/2019

Under the Supervision of
Dr. Kedovikho Yhoshü

DEPARTMENT OF GEOGRAPHY
SCHOOL OF SCIENCES
NAGALAND UNIVERSITY LUMAMI
NAGALAND
OCTOBER 2025

NAGALAND UNIVERSITY

Dr. Kedovikho Yhoshü
Assistant Professor
Department of Geography
Nagaland University Lumami-798627

Mobile: 8731896565
Email:kedovikho@nagalanduniversity.ac.in

CERTIFICATE

The thesis presented by Mr. Midlerthanglian Leivon Ph.D. Research Scholar of the Department of Geography, Nagaland University bearing Registration No. Ph.D./GEO/00283, dated 21st August 2019, embodies the results of investigations carried out by him under my supervision and guidance.

I certify that this work has not been presented for any degree elsewhere and that the candidate has fulfilled all conditions laid down by the University.

(Dr. Kedovikho Yhoshü)

(Supervisor)

PLAGIARISM SELF DECLARATION UNDERTAKING

Name of Research Scholar	Midlerthanglian Leivon
Ph.D. Registration Number	PHD/GEO/00283 of 21st August, 2019
Title of Ph.D. thesis	Eco-Environmental Vulnerability Assessment in Chandel District, Manipur, Using Geospatial Techniques.
Name & Institutional Address of the Supervisor	Dr. Kedovikho Yhoshü Assistant Professor Department of Geography Nagaland University
Name of the Department & School	Department of Geography/ School of Sciences
Date of submission	10/10/2025
Date of plagiarism check	9/10/2025
Percentage of similarity detected	9%

I hereby declare / certify that the Ph.D. thesis submitted by me is complete in all respects, as per the guidelines of the Nagaland University for this purpose. I also certify that the thesis (soft copy) has been checked for plagiarism using DrillBit plagiarism detection software. It is also certified that the contents of the electronic version of the thesis are the same as the final hard copy of the thesis. A copy of the report generated by the DrillBit plagiarism detection software is also enclosed.

Date:9/10/2025

Place: Lumami (Name & Signature of the Scholar)

Name & Signature of the Supervisor with seal.

List of Figures

List of Tables

CONTENTS

Chapter 1

Introduction.

1.1 Introduction

Landscape ecology and conservation biology has made it clear that habitat loss and fragmentation are the primary threats to biodiversity and ecosystem function (Wilcox and Murphy, 1985; Forman 1995; Wilcove *et al.*, 1998). Landscapes become less capable of supporting wildlife, filtering water, abating floods, cleaning air, and providing a variety of other benefits characteristic of functional ecosystems, as it is converted for other uses (Daily 1997; Pimentel *et al*., 2000). Identification of critical areas that is critical ecosystems for protecting various ecosystem functions is essential for conserving natural resources and minimizing the degradation of ecological integrity caused by habitat fragmentation and other impacts (Noss and Harris, 1986; Noss and Cooperrider, 1994).

Land use and land cover change is gaining recognition as a key driver of environmental change (Meyer and Turner, 1991). Many of these changes will have an immediate and strong effect on soil and water quality, ecosystem processes, function, and global climatic systems as a whole (Chen *et al*., 2001; Turner, 1994). With the awareness of the importance of land-use in global change, the study of regional or global land use and land cover change has become the focus of much scientific endeavour internationally (Turner *et al.,* 1993). A better understanding of the relationship between land use and land cover changes, the factors driving these changes will help generate future projection, thus enabling for a better management and maintenance of the ecosystem balance.

Environmental vulnerability assessment is an important tool to aid in knowing how natural and anthropogenic stresses are affecting the local environment. Environmental vulnerability assessment is used for comprehensive evaluation of the critical ecosystem affected by natural condition as well as those influenced by human activities (Fan *et al.*, 2009). Moreover, it is an important method to determine the potential causes of environmental vulnerability, for formulation of proper conservation and restoration measures for sustaining the ecosystem as well as generation of future forecast of threats to environment for reduction of risk.

A state may be defined as environmentally vulnerable if its ecosystem, species and process are susceptible to damaging anthropogenic and natural pressures and these pressures are high (Kaly *et al.*, 1999). The issue of environmental vulnerability to external and internal stress factor has been subject of active research and several methods have been reported to analyse vulnerability. Some study used mathematical modelling (Wilson *et al.*, 2005), and others used Analytical Hierarchal Process (Wang *et al*., 2008), Fuzzy Evaluation Method (Enea and Salemi, 2001), Artificial Neural Network (Dzeroski *et al*., 2001), comprehensive evaluation method (Goda and Mastuoka, 1986), grey evaluation method (Hao and Zhou, 2002), spatial multicriteria evaluation (SMCE) is also used for environmental vulnerability assessment (Enete *et al*., 2010). A method of geospatial modelling used by Roy and Srivastava (2012) to identify the hotspots of land use and land cover change for environmental vulnerability assessment has been found to be good, which involves the use of different landscape-based indices, terrain features and anthropogenic influences for assessment of environmental vulnerability. In the last two decades, advances in Geographic Information Systems (GIS) technology have led to significant improvements in the amount and quality of spatial data, analysis tools, and applications. These trends have allowed researchers and other organizations to develop spatial data and analytical tools relevant to identifying critical ecosystems.

1.2 Background of the Study

Chandel lies in the south-eastern part of Manipur, bordering Myanmar, characterized by hills channelling network of rivers and dense forests covers. The district's rich biodiversity is part of the Indo-Burma hotspot; hence its ecosystems is not only valuable but also extremely prone to disturbance. This region has a subtropical to temperate climate receiving heavy rainfall during monsoon season. The mountainous topography in addition to heavy rainfall makes it prone to landslides.

Anthropogenic activities also add to the degradation of this region. the widespread practice of Jhum Cultivation or Shifting Cultivation on hill slopes causes significant

deforestation and soil erosion. Timber harvesting, cutting down trees for firewood and agricultural land also massively lead to deforestation. This causes disruption in water cycle and subsequently soil degradation. The ever-growing population pressure puts an increasing stress on natural resources, causing habitat loss and encroachment.

Thus, the need to assess the Eco-environmental Vulnerability in Chandel is crucial for effective adaptation and sustainable resource management. A systematic study to identify the vulnerable areas is needed so that governing agencies can intervene with a tailored policy to rejuvenate and develop sustainably.

1.3 Concept of Eco-Environmental Vulnerability.

Eco-environmental vulnerability refers to the degree to which an ecosystem is susceptible to damage or disturbance from both natural and human-induced stressors, and its ability to recover (Hou *et al.,* 2022). Ecosystem is also affected by internal materials, so there are differences in regional ecological vulnerability characteristics (Turner *et al*. 2003)**.** Which means that it is a dynamic concept that involves the interplay of three key factors; exposure, sensitivity and adaptive capacity. The Key components often include Exposure, sensitivity and Adaptive capacity. While exposure here comprises of both human activity and natural and climatic disturbances. Sensitivity refers to the level of responds to the stressors and adaptive capacity is the ability of the ecosystem to adjust, cope, recover and adapt. Thus, Eco-environmental vulnerability encompasses both ecological and environmental interaction. Ecological vulnerability assessment (EVA) is a necessary means to assess the differences of fragile state and spatial distribution pattern of regional habitats, which is of practical significance for maintaining the sustainable development of ecosystems (Li *et al.* 2009).

1.4 Need and Significance of the study.

Developmental activities and increase of population have resulted in the exploitation of the environment surrounding the study area for resources. This have led to the

Environmental and ecological stress through not only climate change but anthropogenic activities as well; clearance of forest cover for cultivation and settlement built-up, as a result of these activities the ecosystem is disturbed and pose a threat of being unable to recover from the damage caused. Thus, the ecosystem in the study area has become vulnerable and it has become crucial to scientifically identify the areas critical-ecosystem and vulnerable Eco-environmental regions in the study area for restoration, conservation, proper management and protection of the ecosystem of the study area.

This study aims at identifying the areas of critical ecosystem and analyse the eco-environmental vulnerability of the study area by means of exploring different remotely sensed data, GIS applications, methodology, analytical tools and techniques.

1.5 Objectives of the study

The following objectives were executed for the study;

1) To derive the Spatio-temporal variation in land use land cover distribution of the study area.
2) To highlight the disturbance determinants for Eco-environmental vulnerability study.
3) To identify the regions under critical Eco-environment in the study area.
4) To assess and integrate algorithms and geospatial technology for deciphering eco-environmental vulnerability.

1.6 Research Methodology

This research aims to assess the Eco-environmental vulnerability of the study area by means of deploying Remote Sensing and GIS technologies. Land use land cover maps across various time period namely 1994, 2003, 2014 and 2021, have been generated from satellite images. Ground truth survey were conducted on the land use classification through field survey as well and google earth.

The land use land cover change dynamics will be generated from these different timed LULC. The Spatio-temporal change of the land use land cover map is used as input

along with ancillary data to support the generation of vulnerable eco-environment region of the study area. The change patterns across multiple spatial and temporal landscape will assist the identification of areas with high concentration of change causing activities and determine whether these activities are of natural or anthropogenic origin.

Thematic maps such as Aspect, Slope, Elevation, etc were generated from SRTM DEM (Shuttle Radar Topography Mission Digital Elevation Model). Vegetative Indices such as Normalised Difference Vegetation Index, Land Surface Temperature, Normalised Difference Soil index, Normalised Difference Moisture index, Normalised Difference Built-up index, etc were derived from Landsat Images. These generated data are then used as input for the assessment of the ecological status of the study area.

The output layer as a resultant from integrating the above change factors shows the Ecological vulnerability status of the study area. The areas of critical ecosystem in the study area are then identified from the ecological vulnerability status by means of zoning the level of vulnerability and thus the areas with the highest degree of vulnerability can be termed as Critical area which is the Critical Ecosystem of the study area, and accordingly measures to protect, conserve and restore are suggested for these areas.

The flow-chart depicted in figure 1.6, represents the working Methodology step on which the entire research has been carried out. Pre-processing & Data Tabulation includes the various steps and procedures involved in pre-processing of satellite images like Conversion of Digital Numbers values into Reflectance values, Atmospheric correction, sharpening of images by incorporating Panchromatic band where applicable, etc. Ground truth and field Surveys includes site visits, capturing Images of landscapes for ground verification and Field survey for monitoring air quality as well.

Input Data generation and derivation includes the generation of various thematic maps layers and vegetation indices. These generated maps are then used as input or determinant to decipher the Eco-Environmental vulnerability Assessment.

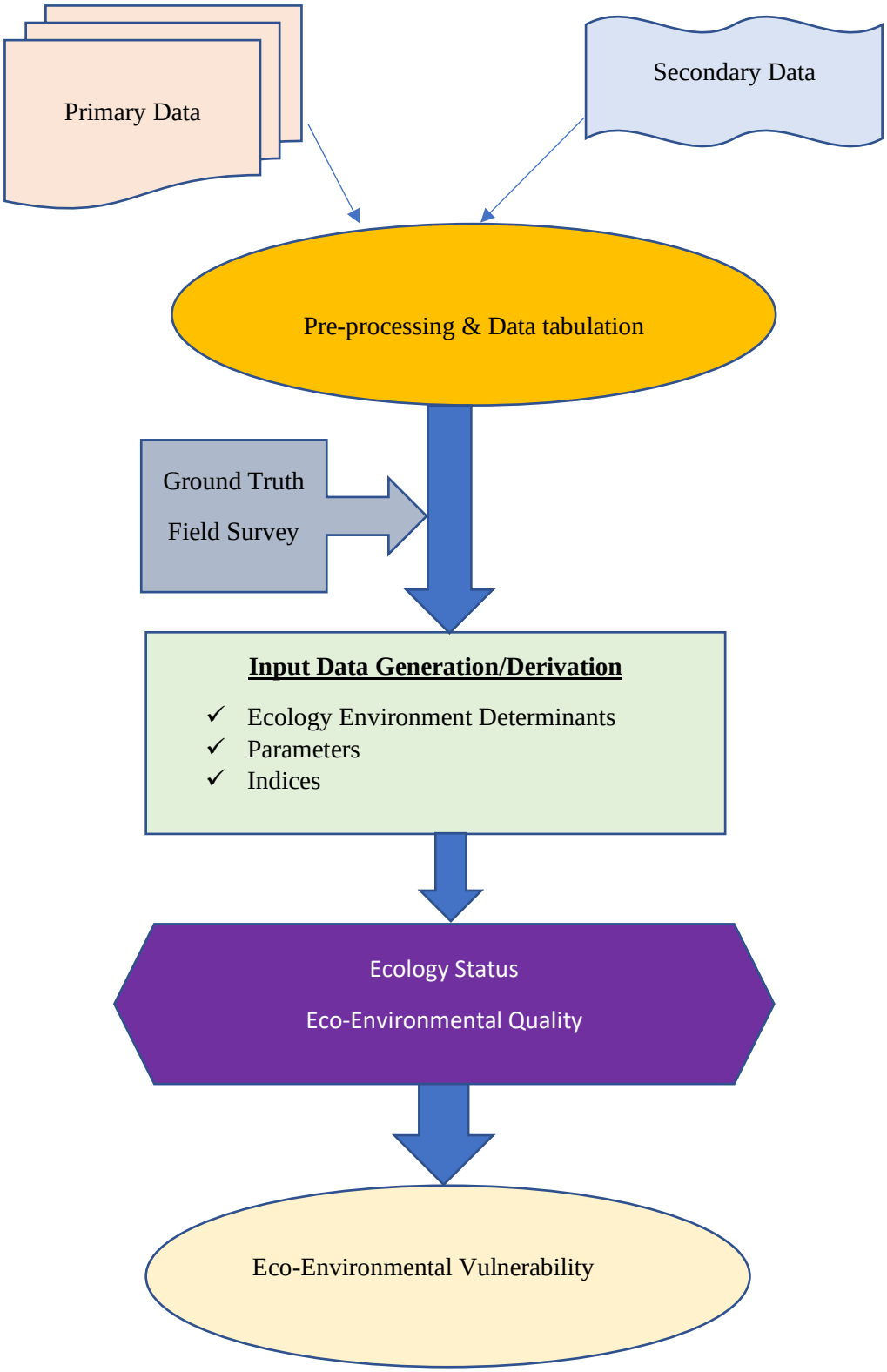

Figure 1.6 Flow Chart of Research Methodology

1.6.1 Landsat TM

The TM sensor is an opto-mechanical or whisk-broom scanner that captures imagery in seven distinct spectral bands. It has a swath width of 185 km and a temporal resolution of 16 days, meaning it can revisit the same area of Earth every 16 days. The TM sensor's design allows for higher resolution and improved separation of different features on the Earth's surface compared to its predecessor. TM data are sensed in seven spectral bands simultaneously. Band 6 senses thermal (heat) infrared radiation. Landsat can only acquire night scenes in band 6. A TM scene has an Instantaneous Field of View (IFOV) of 30m x 30m in bands 1-5 and 7 while band 6 has an IFOV of 120m x 120m on the ground.

Table1.6.1 Landsat 5 TM Technical Specifications.

Band	Name	Wavelength (μm)	Resolution (m)
1	Blue	0.45 - 0.52	30
2	Green	0.52 - 0.60	30
3	Red	0.63 - 0.69	30
4	NIR	0.76 - 0.90	30
5	SWIR 1	1.55 - 1.75	30
6	Thermal IR	10.40 - 12.50	120
7	SWIR 2	2.08 - 2.35	30

Source: USGS (United States Geological Survey)

1.6.2 Landsat & ETM+

The Enhanced Thematic Mapper Plus (ETM+) is a multispectral scanning radiometer and the primary instrument on the Landsat 7 satellite, launched on April 15, 1999. It was designed to build upon the capabilities of the Thematic Mapper (TM) instruments on previous Landsat satellites (Landsat 4 and 5), providing improved spatial and spectral resolution. The ETM+ is a sun-synchronous orbiting at an altitude of 705 Km and captures imagery in eight spectral bands, with a 183 km wide swath and a 16-day repeat cycle. The ETM+ has a spatial resolution of 30 meters for its six visible, near-infrared (NIR), and shortwave infrared (SWIR) bands (Bands 1-5 and 7). It also has a

15-meter resolution panchromatic band (Band 8) and an improved 60-meter resolution thermal infrared band (Band 6).

Table 1.6.2 Landsat 7 ETM+ Technical Specifications.

Band	Name	Wavelength (µm)	Resolution (m)
1	Blue	0.45 - 0.52	30
2	Green	0.52 - 0.60	30
3	Red	0.63 - 0.69	30
4	NIR	0.76 - 0.90	30
5	SWIR 1	1.55 - 1.75	30
6	Thermal IR	10.40 - 12.50	60
7	SWIR 2	2.08 - 2.35	30
8	Panchromatic	0.52-0.90	15

Source: USGS (United States Geological Survey)

1.6.3 Landsat 8 OLI

The Operational Land Imager (OLI) is one of two instruments on the Landsat 8 satellite, a joint mission between NASA and the U.S. Geological Survey (USGS). Launched in 2013, Landsat 8's OLI and its companion instrument, the Thermal Infrared Sensor (TIRS), were designed to continue the decades-long record of global land observations. The OLI instrument collects data in the visible, near-infrared (NIR), and shortwave infrared (SWIR) portions of the electromagnetic spectrum.

The OLI is an advanced "push-broom" sensor, which uses a long array of detectors to image the entire swath of the Earth's surface at once, unlike older Landsat sensors that used a scanning mirror. This design has no moving parts, which improves its reliability and provides a better signal-to-noise ratio. It captures data with a 12-bit radiometric precision, which is a significant improvement over the 8-bit data from previous Landsat satellites.

Table 1.6.3 Landsat 8 OLI Technical Specifications.

Band	Name	Wavelength (μm)	Resolution (m)
1	Coastal Aerosol	0.43-0.45	30
2	Blue	0.45 - 0.51	30
3	Green	0.53 - 0.59	30
4	Red	0.64 - 0.67	30
5	NIR	0.85 - 0.88	30
6	SWIR 1	1.57 - 1.65	30
7	SWIR 2	2.11 – 2.29	30
8	Panchromatic	0.50-0.68	15
9	Cirrus	1.36-1.38	30
10	TIRS 1	10.6-11.19	100
11	TIRS 2	11.5-12.51	100

Source: USGS (United States Geological Survey)

1.6.4 Shuttle Radar Topography Mission (SRTM)

The Shuttle Radar Topography Mission (SRTM) was an 11-day mission flown aboard the Space Shuttle Endeavour in February 2000. It was a joint project between NASA, the National Geospatial-Intelligence Agency (NGA), and the German and Italian space agencies. The primary goal of SRTM was to obtain high-resolution digital elevation data on a near-global scale, creating one of the most comprehensive topographic databases of Earth. The SRTM data is distributed as Digital Elevation Models (DEMs) in a gridded format, with elevation values for each cell with a resolution of 90 metres.

1.6.5 TROPOMI

TROPOMI is an imaging spectrometer that measures solar radiation scattered by the Earth's atmosphere and surface. It operates in multiple spectral bands, including the ultraviolet (UV), visible (VIS), near-infrared (NIR), and shortwave infrared (SWIR). This broad spectral range allows it to detect and quantify various trace gases and aerosols that impact air quality and climate. The Tropospheric Monitoring Instrument

(TROPOMI) on the Sentinel-5 Precursor (Sentinel-5P) satellite is a state-of-the-art push-broom spectrometer. It's the sole payload on the Sentinel-5P mission, which is the first Copernicus mission dedicated to monitoring our atmosphere. Launched in 2017, the satellite's primary objective is to provide high-resolution, global data on atmospheric composition for air quality forecasts and climate research. It has as wide swath of 2600 km approximately and spatial resolution of 3.5 km x 5.5 km.

TROPOMI provides global coverage with an unprecedented spatial resolution. It measures the concentrations of a multitude of key atmospheric constituents, including:

- Nitrogen Dioxide (NO_2): A key air pollutant from combustion processes.
- Ozone (O_3): Both stratospheric ozone, which protects life from UV radiation, and tropospheric ozone, a harmful pollutant and greenhouse gas.
- Carbon Monoxide (CO): An important trace gas produced by combustion and biomass burning.
- Methane (CH_4): A major Greenhouse gas.
- Sulphur Dioxide (SO_2): A pollutant emitted from industrial processes and volcanic activity.
- Formaldehyde (HCHO): A product of the oxidation of volatile organic compounds (VOCs).
- Aerosols: Tiny particles in the atmosphere that affect air quality and climate.

1.6.6 District Boundary

The district Boundary in the form of shapefile were acquired from Manipur Remote Sensing Application Centre (MARSAC), an autonomous government institution under the department of Science and Technology, Government of Manipur.

1.6.7 Software and Hardware

GIS software such as ArcMap, QGIS, Google Earth Engine, Google Earth, etc, has been used for processing and analysing data. Microsoft Word, Excel, google Docs, Sheets, etc, were used for tabulation and word processing. For field survey and ground truthing, instruments like GPS camera, Handheld and portable Air quality Monitor, etc, were used.

1.7 Review of Literature

Rawat *et al.,* (2015) illustrated the Spatio-temporal dynamics of land use/cover of Hawalbagh block of district Almora, Uttarakhand, India. Landsat satellite imageries of two different time periods, i.e., Landsat Thematic Mapper (TM) of 1990 and 2010 were acquired by Global Land Cover Facility Site (GLCF) and earth explorer site and quantify the changes in the Hawalbagh block from 1990 to 2010 over a period of 20 years. Supervised classification methodology has been employed using maximum likelihood technique in ERDAS 9.3 Software. The images of the study area were categorized into five different classes namely vegetation, agriculture, barren, built-up and water body. The results indicate that during the last two decades, vegetation and built-up land have been increased by 3.51% (9.39 km2) and 3.55% (9.48 km2) while agriculture, barren land and water body have decreased by 1.52% (4.06 km2), 5.46% (14.59 km2) and 0.08% (0.22 km2), respectively.

Mathan *et al.,* (2019) analyzed the spatial and temporal changes of the urban and peri-urban landscape of the Chennai Metropolitan Area (CMA), Tamil Nadu, India, using satellite images. Imageries from Landsat 5 (TM) and Landsat 8 (OLI/TIRS) for the years 1988, 1997, 2006, and 2017. Ensembles of remote sensing spectral indices (NDVI, MNDWI, NDBI, and NDBI) were calculated for the land-use/land-cover classification. The confusion matrix was used for assessing the accuracy for the year 2017. The overall accuracy of the LULC classification obtained was 91.76% with the kappa coefficient of 0.84. The results show that during the period of February 1988 to February 2017, the agriculture/fallow land, barren/semi barren, vegetation, and water bodies/wetlands have decreased by 53.62%, 1.45%, 58.99%, and 30.59%, respectively. This decrease has contributed to an increase of 173.83% in built-up area. About 26,881 ha of agriculture/fallow land, 10,482 ha of vegetation land, and 2454 ha of water bodies/wetlands were converted to built-up and other land-use over the period.

Krishna *et al.,* (2001) used the geometrically corrected satellite digital data from IRS 1C LISS III of March 1999. Supervised maximum classification likelihood algorithm was adopted for land cover mapping. Nineteen classes, based on spectral reflectance's,

were delineated. The areas of dominant cropping pattern were digitized using the base digital data, ground truth and landforms (plain, upland, tobacco growing and forest). The two maps were overlaid and reclassified as per the cover classes. The crop calendar of the area was linked with the land cover map to estimate the month wise crop canopy cover percentage.

Kamal *et al.*, (2012) performed quantitative analysis of land use and land cover change in one of the non-glacial-fed watersheds of Kumaun Lesser Himalaya, India, viz., the Gagas watershed. The Survey of India topographic sheet of the year 1965 and LISS III satellite data for the year 2008 have been utilized to quantify the change from 1965 to 2008, i.e., over a period of 43 years. Supervised classification methodology has been employed using maximum likelihood technique in ERDAS 9.3 and mapped using ARC GIS to categorize the images into three classes, viz., forest, agriculture and barren land. The results indicate that during the last four decades, due to afforestation, the forest cover in the Gagas watershed has been increased by about 8.5% (or 43.62 km2) and the agricultural and barren land have decrease by 0.14 (6.69 km2) and by 7.2% (36.93 km2), respectively.

Mishra *et al.*, (2019) monitored the changes in LULC patterns of Rani Khola watershed of Sikkim Himalaya for the periods 1988–1996, 1996–2008 and 2008–2017. Images from Landsat-5 Thematic Mapper (TM) and Sentinel 2A (Multispectral Instrument) MSI data were used to extract land cover maps. Supervised classification using Maximum Likelihood Classifier (MLC) was applied to prepare LULC maps of the watershed. Results shows, dense forest, built-up area and water bodies have increased by 16.40% (41.76 km2), 2.13% (5.41 km2) and 0.11% (0.28 km2) while open forest, agriculture and barren land have decreased by 13.98% (35.59 km2), 2.83% (7.22 km2) and 1.82% (0.4.64 km2) respectively.

Adhikary *et al*., (2019) used historical topographic sheets, IRS P6 LISS-III, and LANDSAT TM images of the Eastern Ghats Highlands of east India to perform supervised classification. The supervised classification results were further improved by employing image enhancement and visual interpretation. Ratio Vegetation Index

with fuzzy-based possibilistic c-means classification approach has improved the classification accuracy of the shifting cultivated area. Post-classification comparisons of the classified images indicated that the major change consisted of barren land and forestland changing into agricultural land and scrubland. Between 1931 and 2008, forest cover was decreased from 52.7% to 29.6% of total area. There was an increase in the scrub area from 874 (10.4%) to 1269 km2 (15.2%), and agricultural land from 978 (11.7%) to 2864 km2 (34.2%) during the same period. The rate of deforestation was found to be 0.65 km2 per year for reserve forest and 24.50 km2 per year for mixed forest. The shifting cultivated area in the district was 308.7 km2 during 2004, and that has been reduced since then and now is stabilized to 186.4 km2 area. Among this 186.4 km2 area, nearly half is covered by abandoned shifting cultivation. The decadal rate of decrease of shifting cultivated area is 0.15% per year.

Huda *et al*., (2019) analysed the land use/land cover changes using satellite imagery in GIS environment of South Garo Hill District of Meghalaya. It was noticed that the agricultural land increases 6.24% in 2009 to 7.41% in 2013. On the other hand, shifting cultivation area increased 0.07% per year during the study period. The forests cover area whether it is dense or open, both categories decreased during this period. Whereas degraded forest increased due decreasing rate of dense and open forest. The increasing rate of shifting cultivation, encroachment in forest land, illegal timber businesses, traditional agricultural practices, lack of knowledge are the main causes of decreasing forest cover in the South Garo hill district of Meghalaya.

John *et al.,* (2020) assessed the Land Use/Land Cover (LULC) classification and Land Surface Temperature (LST) in Wayanad district during the years 2004 and 2018. The LULC classification of Wayanad district was identified using IRS P6 (Linear Imaging Self Scanner) LISS- III, and LST using thermal band of (Enhanced Thematic Mapper Plus) ETM+ imageries. Maximum likelihood classification (MLC) technique was opted to categorize six land-use features: water body, paddy field, forest, dense, agricultural crops and built-up. From 2004 to 2018, impacts of changes in features are correlated with the raised LST. Overall vegetation cover shows an increasing pattern

during the study period. The water bodies in Wayanad district improved from 4.30 to 32.68 sq.km due to construction of two dams: Banasurasagar and Karappuzha. However, agricultural crops and paddy field area have decreased by 4.7% in last 14 years. Decreasing rate of agricultural crops can be directly linked to population growth, thereby developing various built-up zones for basic needs. Forest and dense vegetated cover area are increased nearly 2.3 and 3.0%, respectively, during the study period, while bamboo degradation has also been witnessed from 2008 to 2013. The built-up class shows growth from 1.48 to 5.69% of total land area during 2004 and 2018. LULC have noticeable influences on LST with a negative correlation between vegetation cover and LST with a decrease of 1.75 C.

Venkatesh *et al*., (2020) performed the extraction of variables using Landsat 8 OLI, Sentinel-2B, ALOS PALSAR DEM and IMD rain gauge data respectively. The generated parameters affecting the environment are weighed and ranked through the Analytical Hierarchical Process (AHP) with Geospatial technology for eco-environment vulnerability assessment. Then vulnerability level is categorised into five classes like very high, high, moderate, low and very low with an area of 10%, 12%, 37%, 23%, and 18% respectively. The very high and high classes are distributed in low lying plain regions, where there is high anthropogenic activities, urbanisation and industrialisation, a moderate vulnerable class is more in plateau region due to deforestation and over exploitation. However, very low and low classes are sparsely distributed in higher altitude. The integration of Geospatial technology with AHP makes a powerful tool to assess the eco-environment vulnerability and therefore, three focus regions are demarcated to devote a massive concern on protection and management in the essence of sustainable development.

Li *et al.,* (2006) analysed the eco-environmental vulnerability, remote sensing (RS) and geographical information system (GIS) technologies are adopted, and an environmental numerical model is developed using spatial principal component analysis (SPCA) method. The model contains nine factors including elevation, slope, accumulated temperature, drought index, land use, vegetation, soil, water-soil erosion,

and population density. Using the model, the integrated eco-environmental vulnerability index (EVI) of study area in 1972, 1986, and 2000 are computed. According to the numerical results, the vulnerability is classified into five levels: potential, slight, light, medial, and heavy level by means of the cluster principle. The eco-environmental vulnerability distribution and its dynamic change in the last 30 years from 1972 to 2000 are analysed and discussed. The results show that the eco-environmental vulnerability in study area is at medial level, and presents apparent vertical-belt distribution, and that driving force of dynamic change are mainly caused by human social economic activities and the contribution of late national eco-environmental protection policies, such as Natural Forest Protection and Grain for Green. According to these results, the study area is regionalized into three sub-regions, which may serve as a base for decision-making for eco-environmental recovering and rebuilding. The results of this study indicate that the method that integrates RS, GIS, and the SPCA to evaluate eco-environment vulnerability in mountainous region, cannot only distinctly represent the input subject spatial distribution of mountain vertical-belt feature, but also respect the river-valley as a whole system.

Boori *et al.,* (2011) identified, assessed and classified the vulnerability and environmental change in the Apodi valley region using a combined approach of landscape pattern and ecosystem sensitivity. Models were developed using the following five thematic layers: Geology, geomorphology, soil, vegetation and land use/cover, by means of a geographical information system (GIS)-based on hydro-geophysical parameters. In spite of the data problems and shortcomings, using ESRI's ArcGIS 9.3 program, the vulnerability score, to classify, weight and combine a number of 15 separate land cover classes to create a single indicator provides a reliable measure of differences (6 classes) among regions and communities that are exposed to similar ranges of hazards. Indeed, the ongoing and active development of vulnerability concepts and methods have already produced some tools to help overcome common issues, such as acting in a context of high uncertainties, taking into account the dynamics and spatial scale of asocial-ecological system, or gathering viewpoints from different sciences to combine human and impact-based approaches. Based on this assessment, this paper proposes concrete perspectives and possibilities

to benefit from existing commonalities in the construction and application of assessment tools.

Ifeanyi *et al.,* (2010) evaluated the environmental vulnerability of Efon-Alaye located in Ekiti State, Nigeria, which is a typical mountainous region with steep slope and an upland ecosystem. An Integrated Remote Sensing and Geographical Information System approach was used to analyse the environmental vulnerability of the region. Satellite data of the study area for two periods 1986 and 2002 were used for the analysis. Spatial multi-criteria evaluation operation was used to generate the vulnerability map of the study area. Indicators used were land-use, vegetation map (NDVI) and slope map generated from digital elevation model. The vulnerability distribution was classified into five levels: potential, slight, moderate, high and extreme. The results show that the environmental vulnerability in the study is at potential level and the driving force of this change is attributed mainly to the cultural activities of the inhabitants of the study area. The result of this study has also shown that using Integrating remote sensing, geographical information system and spatial multi-criteria evaluation model to evaluate environmental vulnerability in mountainous regions will assist decision makers in environmental management.

Zhang *et al.,* (2017) analysed the ecological vulnerability in Fuzhou district in China and its causes, systematic assessment and zoning of ecosystem vulnerability were proposed. Using the remote sensing and geographic information system technologies, ecological vulnerability was spatially, explicitly, and comprehensively assessed. Results showed that the most vulnerable areas of Fuzhou district include Pingtan Comprehensive Experimental Area, Fuqing City, Fuzhou City and Changle City. Counties of Yongtai, Minhou and Minqing feature good vegetation coverages and low ecological vulnerability. In Fuzhou City, three zones, namely, Taijiang, Gulou and Cangshan Zones, feature high or extremely high percentage vulnerability. The other two zones comprise better ecosystems. Analysis of correlation coefficients between vulnerability value and various indices showed distinct factors of ecological vulnerability for each region. The main factors affecting the ecosystems in Fuqing, Jin'an Zone, and Changle City include climate, vegetation and soil, respectively, whereas the factors that simultaneously affect the ecosystem in Cangshan Zone consist

of soil, land use, topography and vegetation. The key challenge in improving ecological vulnerability of these areas is optimization and coordination of land use/coverage under natural conditions.

Jabbar *et al.,* (2015) developed a methodology to evaluate natural and social pressure, environment sensitivity, and ecological stability in a GIS-based approach for the Basrah Province, Iraq. The information used in this study was obtained from two different sources: (i) a soil survey with more than 500 soil samples positioned by GPS to quantitatively assessment land map quality with the method of integrated environmental vulnerability index (EVI) within the study area, and (ii) the environmental information implemented in the Geo-scientific map of the Basrah Province digitized on an Arc/Info GIS with remote sensed imagery (Landsat TM 1990 and ETM 2003). From the characteristics and the causes of ecological vulnerability, we established multi-objective ecological vulnerability evaluation index system framework, and a Pressure-State-Respond model is built to evaluate the environmental vulnerability. The results showed that more than 56.3% of the area has reached high vulnerability level, and nearly 1/5 of the area is at a moderate level. The integration of different factors contributing to environmental vulnerability may lead to plan a successful combating.

SB *et al.,* (2017) identified the natural and environmental vulnerability distribution in Astrakhan, Russia. His study identifies, assess, and classify natural and environmental vulnerability using landscape pattern from multidisciplinary approach, based on remote sensing and Geographical Information System (GIS) techniques. A model was developed by following thematic layers: land use/cover, vegetation, geology, geomorphology, and soil in ArcGIS 10.3 software. According to numerical results vulnerability classified into five levels: low, reasonable, moderate, high and extreme vulnerability by mean of cluster principal. Results are shows that in natural vulnerability maximum area covered by moderate (54.62%) and environmental vulnerability concentrated by moderate (54.00%) vulnerability. So, study area has at medial level vulnerability. In the study area encroachment, population growth, industrialization and governmental polices for environmental protection are main cause for vulnerability.

He *et al.,* (2018) attempt to provide a prototype framework that can assess ecological vulnerability and evaluate potential impacts of natural, social, economic, environmental pollution, and human health elements on ecological vulnerability with integrating spatial analysis of Geographic Information System (GIS) method and multi-criteria decision analysis (MCDA). A general ecological vulnerability index was constructed to describe the vulnerability status in an ecological hot- spot of China. The assessment results of this study confirm the poor ecological vulnerability in China that only 1.32% of the China's population lives in not vulnerable ecosystem. A very high percentage (98.68%) of Chinese with 1.34 billion people lives in vulnerable and highly vulnerable area. This situation is mainly caused by increasing population pressure, exhausted nature resources, extensive economic growth, severe environmental pollution, insufficient environmental protection investment, and accelerating population aging. The spatial comparison indicates that spatial disparity existed in China with the central and north western provinces showing higher ecological vulnerability than the north-eastern and southern provinces.

Mukesh *et al.,* (2017) identified the natural and environmental vulnerability distribution in Astrakhan, Russia. His paper identifies, assess, and classify natural and environmental vulnerability using landscape pattern from multidisciplinary approach, based on remote sensing and Geographical Information System (GIS) techniques. A model was developed by following thematic layers: land use/cover, vegetation, geology, geomorphology, and soil in ArcGIS 10.3 software. According to numerical results vulnerability classified into five levels: low, reasonable, moderate, high and extreme vulnerability by mean of cluster principal. Results are shows that in natural vulnerability maximum area covered by moderate (54.62%) and environmental vulnerability concentrated by moderate (54.00%) vulnerability. So, study area has at medial level vulnerability. In the study area encroachment, population growth, industrialization and governmental polices for environmental protection are main cause for vulnerability. This study is helpful for decision making for eco-environmental recovering and rebuilding as well as predicting the future development.

Wanyama *et al.,* (2021) characterized ecological and environmental (eco-environmental) vulnerability for the MEE using freely available Earth observation, topographic, and socioeconomic data. Spatial principal component analysis (SPCA) was used to compute a new eco-environmental vulnerability index (EEVI) by integrating natural, environmental, and socioeconomic conditions. The final EEVI was then categorized into five classes (potential, slight, light, moderate, and severe). Temporal principal component analysis (TPCA) was also conducted to identify persistent changes in multi-year variables spanning the period 2001– 2018.

Further, the precipitation concentration index (PCI) was assessed to evaluate changes in the Spatio-temporal distribution of precipitation in the MEE. The study found that EEVI indicates the most aggregate vulnerability on the Ugandan side, especially in savanna regions. Majority of the MEE was moderately vulnerable, and savannas and grasslands constituted the largest proportion of the severe vulnerability class. There was also a marked increase in vulnerability with decrease in elevation. Eco-environmental vulnerability was strongly associated with multi-year variables based on precipitation, temperature, and population density. The study also found that precipitation concentration is amplifying especially in the wet season, thus threatening agriculture and community livelihoods.

Jing *et al,* (2019) in their study discusses how remote sensing technology can objectively and quantitatively evaluate spatial-temporal change of ecological environmental quality by examining the ecological environment quality within the Ebinur Lake Wetland National Nature Reserve, located in an arid region of China changed over time. The study used satellite remote sensing images from three year i.e., 2007, 2013, and 2016 to extract four indicators that effect the environment i.e., how green the area is, which reflects vegetation health; the wetness of the area, corresponding to surface water availability; How hot the area is, measured as land surface temperature; and the dryness of it, representing soil and bare land conditions and applied a multi-indicator approach to evaluate ecosystem health. The principal component analysis (PCA) used the evaluating ecological environment quality of the

Ebinur Lake Wetland National Nature Reserve to explore the characteristics of spatial differentiation for ecological quality in environment as indicated in the remote sensing ecological index (RSEI). The findings reveal an overall improvement in the ecological environment quality from 2007 to 2016, highlighting significant positive trend in vegetation cover and increased wetness within the reserve. Wetness emerged as one of the largest contributors to ecological recovery, which shows the importance of water resources in sustaining wetland ecosystems in arid climates. The findings shows that different areas within the study region are experiencing varying degrees of environmental changes, with some southern areas experiencing degradation due to natural factors such as wind-driven sand erosion, and anthropogenic factors including agricultural expansion. This dual pressure on the ecosystem demonstrates the complexity of managing conservation areas facing both natural factors and human activities. Furthermore, spatial autocorrelation analyses conducted in the study indicated that ecological quality before 2016 exhibited clustered patterns, suggesting regions of consistently high or low environmental health. However, these patterns became more fragmented and dispersed by 2016, potentially reflecting more localized and complex ecological dynamics at play. This was further supported by the Moran's I values, which first showed an increasing trend between 2007 and 2013, indicating stronger spatial clustering of ecological quality during this period. However, by 2016, Moran's I declined, reflecting a weakening of spatial autocorrelation and a shift towards a more fragmented and dispersed ecological pattern. The High-High (HH) clusters of ecological quality reached statistical significance at the 0.05 level in 2007, strengthening to the 0.01 level in both 2013 and 2016, highlighting persistent but increasingly localized ecological hotspots. Based on these results, the authors highlight the critical role of preserving water bodies and wetland habitats as foundational for maintaining overall ecosystem health.

Maity *et.al.*, (2021), states how the global ecosystem has been significantly disrupted on various spatiotemporal scales over the last three decades due to human activities. However Geospatial technology can quickly, effectively, and quantitatively to evaluate the spatiotemporal change of eco-environmental quality (EEQ). In their paper the author studies how the environment around Kolkata, one of India's largest urban

areas, has changed over the last 30 years. The researchers used satellite images from 1990, 2000, 2010, and 2020 to assess environmental quality by looking at four key elements: how green the land is, how much moisture is present, how dry the land and built-up areas are, and how hot the land surface gets. The principal component analysis (PCA) and spatial autocorrelation analysis can relate all indicators with each other's and RSEI. A Spatial autocorrelation analysis (Moran's I) value was used to detect environmental clustering, supporting targeted spatial interventions. What they found shows a worrying trend. Over these three decades, more of the city moved into poor ecological health categories. The areas rated as having bad or very bad ecological conditions grew sharply, primarily due to urban sprawl which reduced green spaces and wetlands, increased built-up areas, and raised surface temperatures. On the flip side, regions near water bodies and places with more vegetation tended to have better ecological scores. Using spatial analysis, the study also found clusters of poor and good areas that shifted over time, reflecting the impact of rapid urban growth. The authors emphasize that the fast expansion of Kolkata's urban footprint has seriously impacted local ecology, raising temperatures, shrinking habitats, and threatening biodiversity. They stress the need to protect wetlands and preserve green spaces as key strategies for improving the city's environmental health. The study shows how combining satellite data with spatial statistics can provide detailed insights useful for planning sustainable urban development in fast-growing cities like Kolkata.

Lan *et al.,* (2023) shows an insightful examination of ecological vulnerability in Zhongxian County, situated within the natural landscape of Chongqing's Three Gorges Reservoir region. The authors adapted the Remote Sensing Ecological Index (RSEI) into an Ecological Vulnerability Body Index, covering 2002, 2009, and 2016. They blend four indices; The ecological vulnerability evaluation index was established through Normalized Difference Vegetation Index (NDVI) for vegetation vitality, Wetness (WET) for surface moisture, Normalized Difference Build-up and Soil Index (NDBSI) for built-up and bare soil metric and Land Surface Temperature (LST) indicators. The study used Principal Component Analysis (PCA) assign their true weights. The research underscores the dynamic interplay between human activity and ecological stability in this particular locale. Over the fourteen-year span, the

landscape’s most vulnerable pockets steadily shrank, while zones classified as having minimal or light vulnerability expanded. The Ecological Vulnerability Body Index (EVBI) mirrored this shift, falling from its 2002 peak to much lower values by 2016, a clear signal of genuine ecological recovery on the ground. When these changes were mapped, it became apparent that flat, developed areas, especially those hugging rivers or dense settlements, continued to register higher vulnerability scores. In contrast, rugged hillsides and less accessible tracts held up far better, weathering environmental pressures with surprising resilience. The study has been divided into two phases, from 2002 until about 2009, improvements were barely perceptible, just a nudge away from higher vulnerability toward slightly safer ground. Then, after 2009, the landscape seemed to catch its breath: gains accelerated noticeably, a shift that coincides with the rollout of local restoration projects and stricter conservation rules. The findings indicated that farmers noted healthier soils and downstream communities celebrated fuller streams, which matched the satellite readings almost perfectly. The study is a blend of high-resolution satellite data with sound statistical methods. For regions under pressure from rapid development, this approach offers both a detailed map of where the risks lie and a hopeful reminder that even modest conservation efforts can pay off.

Kang Hou *et al*., (2022), "A new perspective on ecological vulnerability and its transformation mechanisms," shifts the focus of ecological vulnerability research from static assessments to a dynamic analysis of how and why vulnerability changes over time. Traditional studies often concentrated on creating assessment models and analysing influencing factors. However, this new perspective emphasizes the need to understand the process of vulnerability transformation itself. The core idea is that ecological vulnerability isn't a fixed state but a dynamic process. The authors argue that it is crucial to understand how a region's ecological vulnerability evolves from one level to another over time. This includes identifying factors that drive a system toward a more vulnerable state or, conversely, toward greater stability. The paper focuses on the mechanisms that regulate this transformation. It goes beyond simply identifying pressures (like pollution or climate change) and sensitivities (like a lack of biodiversity). Instead, it seeks to identify the regulating factors that cause a system to

shift between different levels of vulnerability. This involves a quantitative analysis to understand the cause-and-effect relationships. The authors propose that vulnerability transformation in a heterogeneous region is a complex process regulated by multiple factors. These factors can be natural, like climate variables, or human-induced, like land use change or policy interventions. The research aims to pinpoint which of these factors are most significant in driving the transformation process. This new perspective has significant practical implications.

Xu *et al.,* 2024 in the paper "Ecological vulnerability assessment and spatial-temporal variations analysis in typical ecologically vulnerable areas of China," presents a comprehensive framework for evaluating ecological vulnerability and analysing how it changes over time and space. The study aims to address the limitations of previous assessment methods by introducing a more robust indicator system. The researchers developed an indicator system based on a "natural cause-result performance" model. This system integrates various data sources, including remote sensing, meteorological, and socio-economic data, to create a generalized Ecological Vulnerability Index (EVI). They then used GIS-based spatial analysis to assess and map the vulnerability of five typical ecologically fragile regions in China. The methodology is designed to be quantitative and objective, allowing for refined assessments at the pixel scale. The study's findings reveal a generally high level of ecological vulnerability in the regions studied, with significant spatial and temporal variations: The average EVI values for some areas, such as Zhangbei County, were consistently among the highest, indicating a high degree of vulnerability. In contrast, other regions like Taihe County and the Sanjiangyuan region showed lower EVI values at different times. The paper also highlights that vulnerability is not uniform and varies significantly across different land-cover types. For example, bare land was found to be the most vulnerable, while forests were the least vulnerable. The researchers found that, despite fluctuations, the average EVI values remained relatively stable from 2005 to 2020. This stability suggests that environmental protection measures and projects implemented by the Chinese government have had a positive effect in curbing the deterioration of the ecological environment in these areas. In conclusion, the paper provides a valuable and replicable framework for ecological vulnerability assessment that can be used to

inform and guide effective ecological conservation and environmental management policies.

1.9 Organisation of the thesis

The thesis is divided into six chapters. Which is then followed by the Bibliography and Field Photographs.

Chapter 1. Introduction

Chapter 2. Geographic profile of the study area.

Chapter 3. Spatio-temporal variation in Land Use Land Cover distribution of the study area.

Chapter 4. Eco-environmental vulnerability and Disturbance Determinants

Chapter 5. Identification and assessment of vulnerability of Eco-Environment in study area.

Chapter 6. Summary and conclusion.

Reference.

Field Photographs.

.

Chapter 2. Geographic profile of the study area.

2.1. Location and extent

The study area is Chandel district which lies the south-eastern part of the North-eastern state of Manipur. It lies at 24º40′ North Latitude and 93º50′ East Longitude approximately. The total geographical area of district is 2100 km^2. The district is bounded on the south and east by Myanmar (Burma), west by Thoubal and Churachandpur districts.

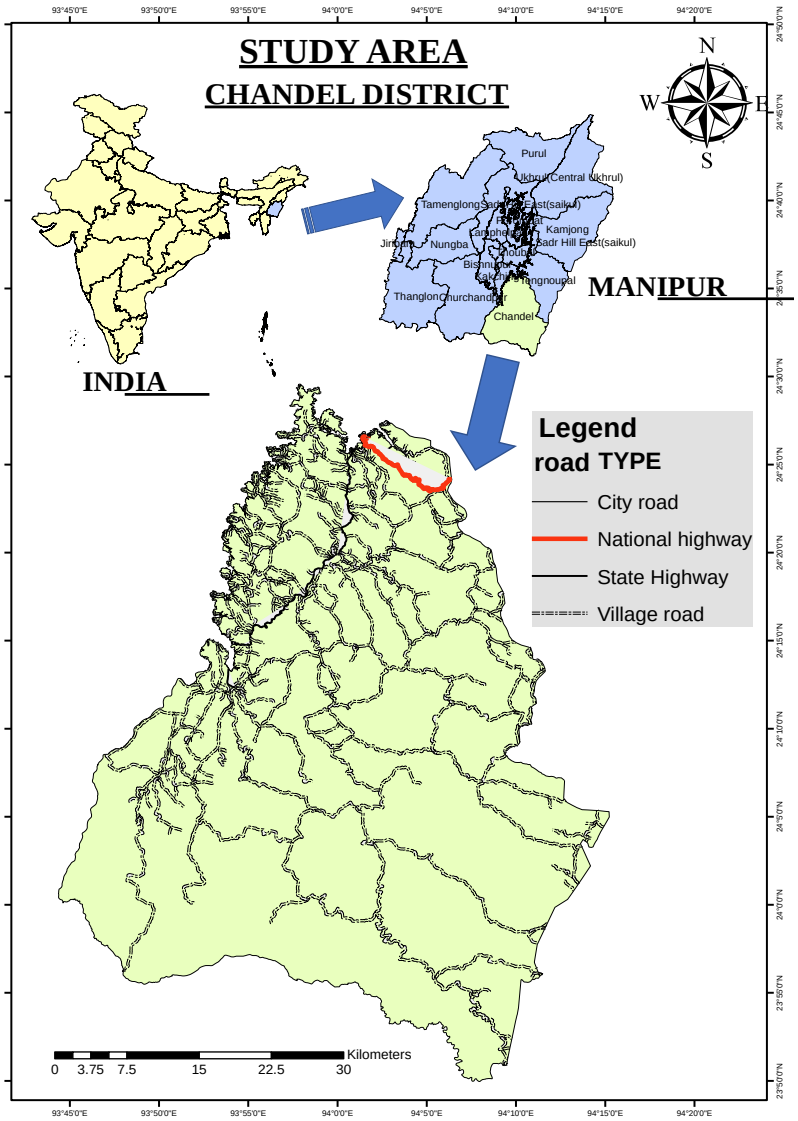

Figure 2.1. Location Map of Study Area

2.2 Topographical profile

Chandel District is part of the Indo-Myanmar Ranges which are an extension of the Tertiary Himalayan System. It is topographically composed of rough, hilly terrain that slopes east and west. A large range that stretches from the north through the centre of the district Nangte Vum, which rises 2,373 meters to the south, separates the two river systems; one runs eastward and empties into Myanmar's Yu River, while the other flows westward and empties into the Manipur River. The Chandel district is separated into three hilly areas namely, The Western Hilly Region, the Eastern Hilly Region, and the Southern Hilly Region.

The western hilly region consists of three subdivisions covering more than half each of the Tengnoupal and Machi sub-divisions and major part of Chandel sub/division. There are 4 small hill ranges stretching east-west. The important peaks of this region are Eawoiching (1,933m), Sita Chingjao (1,597 m), Anal Khullen (1,580 m), Mittong Khullen (1,578 m), Tollen (1,543 m), Charanging (1,536 m), Anal Khullen (1,447 m), Khudei Khuno (1,316m) etc.

The eastern hilly region occupies the north eastern corner of the district and consists of small portions each of three sub-divisions. The major peaks of this region are Khangbung (1,562 m), Larong Khunou (1,241 m), Dolaibung (1,196 m), Narum (1,097 m), Sibong (839 m), Jitahang ching (745m), etc.

The southern hilly region occupies the entire Chakpikarong sub-division and very small portions each of Chandel and Tengnoupal sub-divisions. In this region, some small springs (maximum height upto 150 ft) occur in the south-eastern corner, Nungle Vum (2,373 m), Holbol Ching (2,085 m), Lungpon Ching (1,763 m), Klaichin Bung (1,707 m), Sheikui (1,593 m), Kholen Khailet (1,561 m), Aibol Joupi (1,401m), etc. are the main peaks of the region.

2.2.1 Slope

Slope is defined as the measure of steepness or incline of a surface. Slope is a critical topographic parameter that profoundly influences ecological and environmental processes. As a fundamental component of the landscape, it governs the flow of water and materials, shapes soil development, and creates diverse habitats for plant and animal life (Zhang *et al.*, 2018). The study area has the slope degrees ranging from 0 º-66 º. The slope ranges have been divided into five classes; (0º-11º) very gentle slope, (11º-19º) Gentle slope, (19º-26º) Moderate slope, (16º-33º) Steep slope, and (33º-66º) Very steep slope.

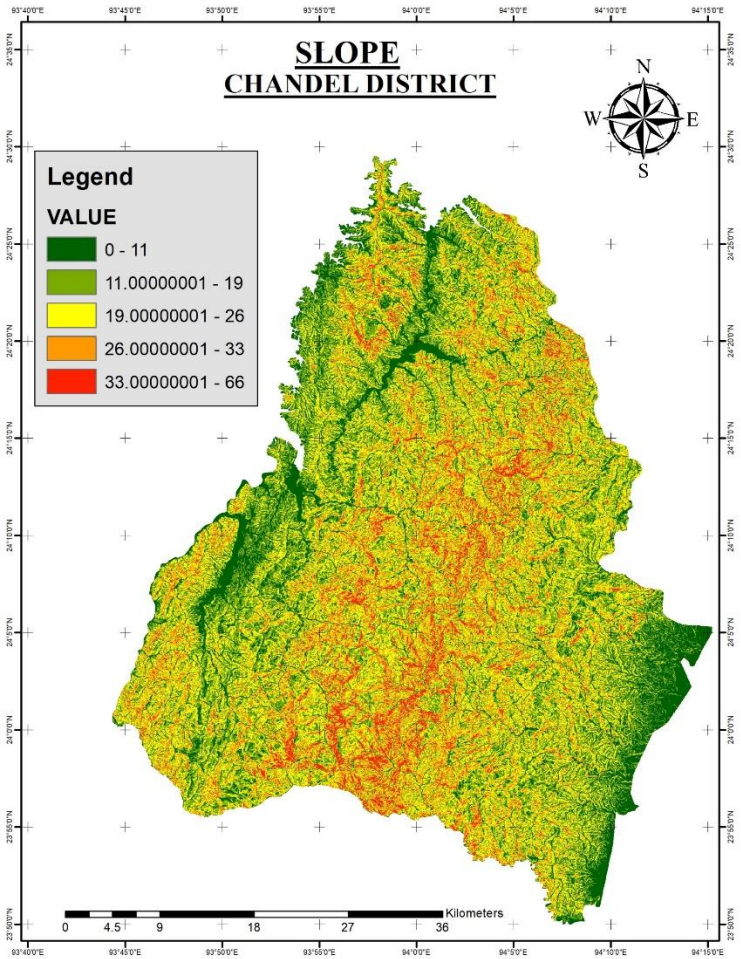

Figure 2.2.1 Slope Distribution of Chandel

2.2.2 Aspect

Aspect is defined as the directional orientation of a slope on a surface. It indicates the direction the surface is facing. Aspect is a major determinant of local microclimate. In the Northern Hemisphere, south-facing slopes receive more direct sunlight, making them warmer and drier, which can lead to sparser vegetation and different plant species. Conversely, north-facing slopes are shadier and moister, often supporting denser, more diverse plant communities (Singh et al., 2020). The study area aspects have been classified as Flat (-1), North (0°–22.5°), Northeast (22.5°–67.5°), East (67.5°–112.5°), Southeast (112.5°–157.5°), South (157.5°–202.5°), Southwest (202.5°–247.5°), West (247.5°–292.5°) and Northwest (292.5°–337.5°).

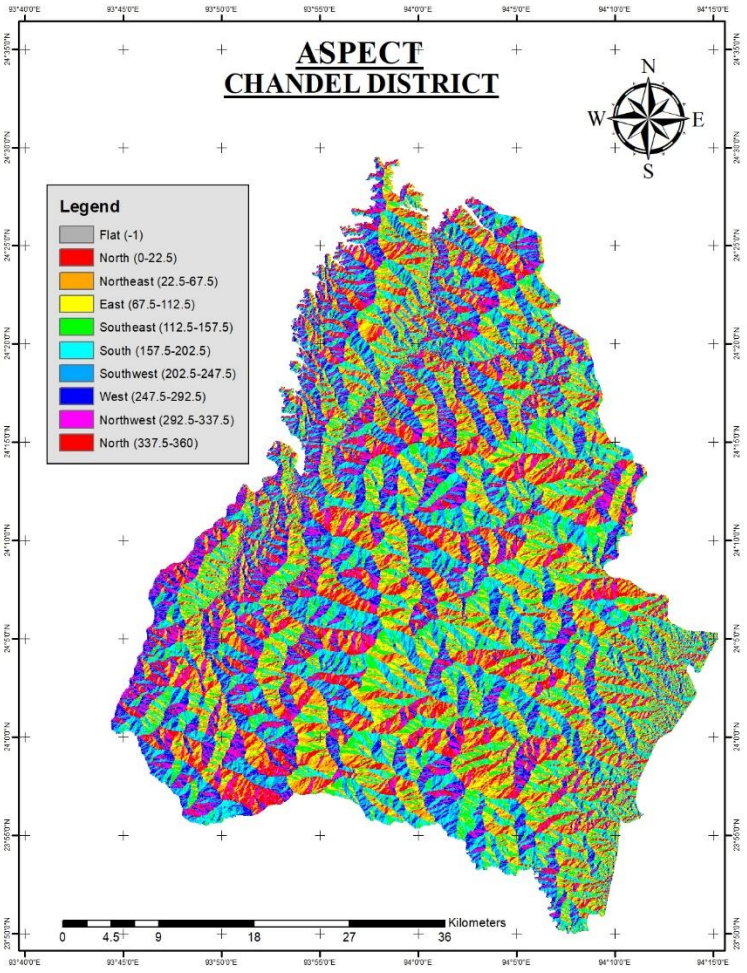

Figure 2.2.2. Aspect Distribution of Chandel

2.2.3 Elevation

Elevation has a profound influence on both ecological and environmental systems, acting as a powerful determinant of climate, biodiversity, and soil characteristics. As altitude increases, a series of interrelated changes create distinct environmental zones, leading to a phenomenon known as altitudinal zonation (Prager *et al.,* 2021). Climatic factors like temperature, precipitation and solar Radiation and air pressure are influenced by elevation. This changes in climatic factor directly influence and shape ecological factors like vegetation zone and species distribution. The study area has the minimum elevation of 379m above sea level while the maximum elevation is at 1822m above sea level.

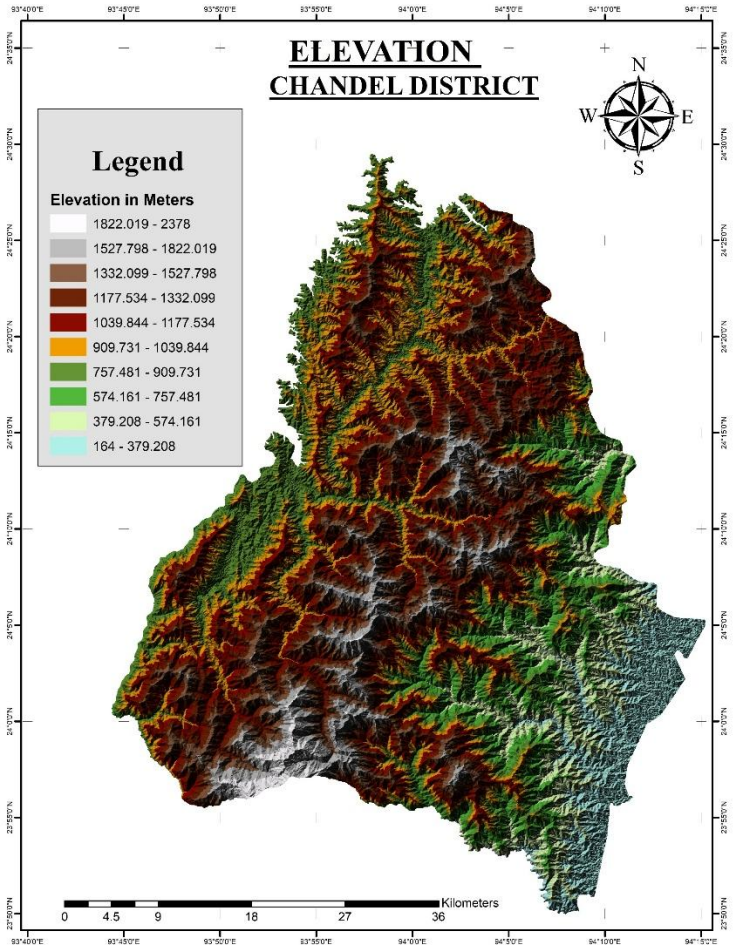

Figure 2.2.4. Elevation (metres above sea level)

2.3. Climate and Weather Patterns

The climate of Chandel district of Manipur is sub-tropical to temperate, with distinct seasons and regional variations in rainfall and temperature. The South-West Tropical Monsoon has the biggest impact on the climate. Some of the major Seasonal Features are; Summer (March through May/June): The summer months are hot, with highs of up to 35°C; Monsoon season has intense rainfall that occurs during the monsoon season, which runs from June to September and Winter (October to February) is lengthy with frigid winters, with some regions experiencing temperatures as low as 0°C. The coldest month of the year is usually January.

Table 2.3 Monthly Average Temperature in 2022 of Chandel District

Month	Max (°C)	Min (°C)
January	28.18	9.06
February	32.25	8.76
March	38.65	12.78
April	39.99	13.26
May	36.94	15.18
June	35.49	17.88
July	37.15	18.25
August	38.02	18.1
September	36.38	18.13
October	35.05	17.82
November	32.24	14.1
December	31.11	12.22

Source: Annual report 2022-23, Manipur's Directorate of Environment & Climate Change

Although there are local variations in the distribution of rainfall due to its hilly topography, which ranges from roughly 790 meters to over 3,000 meters above sea level, the overall climate is defined by high rainfall concentrated in a few months of the year. Rainfall is largely governed by south-west monsoon winds. The seasonal distribution of rainfall in Chandel is highly uneven. July and August are usually the wettest months, and the monsoon season (June–September) receives between 75 and 80 percent of the total each year. The winter months (December–February) are typically dry with little precipitation, while, the pre-monsoon months (March–May) provide some rainfall that encourages early cropping.

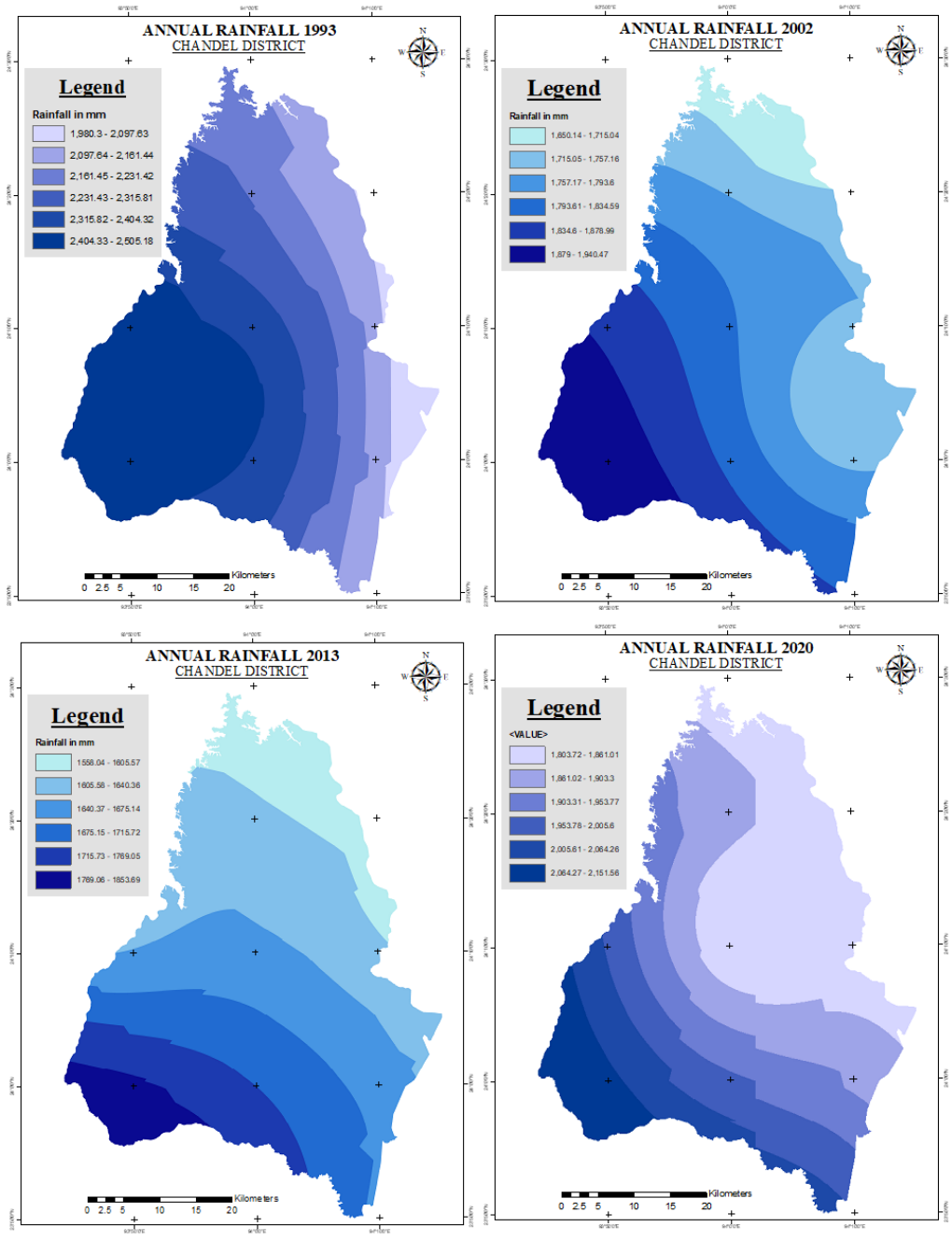

Figure 2.2.5. Annual Rainfall in the year 1993, 2002, 2013 and 2020

The rainfall regime in Chandel plays a decisive role in shaping the district's agriculture and environment. The abundant monsoon rains sustain rainfed rice cultivation and shifting (jhum) farming practices, while variability in annual rainfall often leads to challenges such as soil erosion, floods in valley areas, and landslides on steep hill

slopes. Hence, rainfall is both a vital natural resource and a source of environmental risk in the district.

2.4. Biodiversity and Wildlife

Chandel being part of the Indo-Burma Biodiversity Hotspot, it hosts a diverse array of flora and wildlife, including numerous rare and endangered species. The rugged landscape and varying elevations provide a mosaic of forest kinds, offering numerous habitats for fauna.

Chandel's wildlife is particularly significant for its population of rare and elusive animals. Key species found in the district include:

- Primates: The only ape found in India, the Hoolock Gibbon, is native to Chandel's forests. Other primates include the Slow Loris, Stump-tailed Macaque, and Pig-tailed Macaque.
- Carnivores: Rare nocturnal carnivores like the Clouded Leopard and the Golden Cat have been sighted. The forests also harbour the Himalayan Black Bear and the elusive Malayan Sun Bear.
- Other Mammals: Herds of Bison and Sambar are present, and Thai Pangolins are also sighted in the Indo-Myanmar border areas. Elephants also make seasonal migrations into the region.
- Birds: The district is home to various bird species, including the Pheasant, Burmese Peafowl, and Jungle Fowl.

A significant part of the district's biodiversity is protected mainly due to the existence of Yangoupokpi-Lokchao Wildlife Sanctuary, a protected area on the Indo-Myanmar border. This sanctuary provides a critical habitat for a variety of mammals, birds, reptiles, and fish species.

2.4.1 Flora

The forests of Chandel are rich in a variety of plant life, including numerous medicinal and ornamental plants. The dominant tree species in the region's moist deciduous and teak-gurjan forests include:

- *Dipterocarpus turbinatus* (Gurjan)
- *Tectona grandis* (Teak)
- *Melanorrhoea usitata* (Burmese Lacquer)
- *Terminalia chebula* (Black Myrobalan)
- *Emblica officinalis* (Indian Gooseberry)
- *Cedrella toona* (Indian Cedar)
- *Quercus spp* (Oak)
- *Bauhinia*
- *Dillenia*

2.4.2 Fauna

The district's fauna is notable for its rare and endangered species. Key wildlife found in the region includes:

- Primates: The only ape found in India, the Hoolock Gibbon, is native to this area. Other rare primates include the Slow Loris, Stump-tailed Macaque, and Pig-tailed Macaque.
- Bears: The forests are home to the Himalayan Black Bear and the rare and elusive Malayan Sun Bear.
- Other Mammals: Herds of Bison and Sambar are seen in the New Samtal area. Other animals include the Thai Pangolin, Clouded leopard, Golden Cat, and migratory elephants that move seasonally in the border areas.
- Birds: The Yangoupokpi-Lokchao Wildlife Sanctuary is recognized as an Important Bird Area (IBA) where the endangered Green Peafowl can still be sighted. Other birds include the Burmese peafowl, pheasants, and jungle fowls.

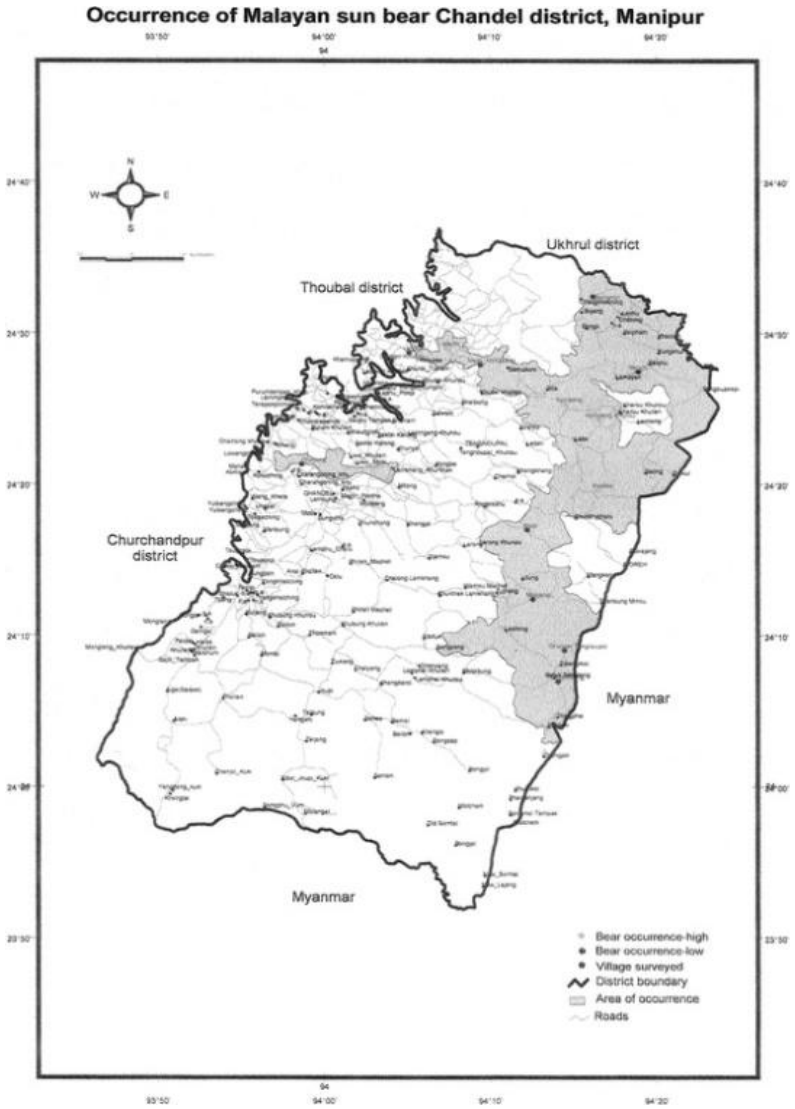

Figure 2.4.2. Occurrence of Mayalan Sun bear around the study area.
Source: Chauhan, N. P. S., *et al.* (2006) "Status and distribution of sun bears in Manipur, India."

2.5. Geological Profile

The soil and geological profile of Chandel district in Manipur are influenced by its position within the intricate geomorphology of the Indo-Myanmar Ranges. The region's dynamic tectonic environment and undulating topography produce distinct soil types and a geological framework abundant in diverse mineral deposits. Geologically, Chandel is part of the Indo-Burma Accretionary Complex, an active tectonic zone formed by the subduction of the Indian Plate beneath the Burma Plate.

The district's geology is dominated by a sequence of sedimentary rocks from the Cretaceous and Tertiary periods.

Ultisols, Inceptisols, and Alfisols are the three main soil orders that primarily comprise the generally acidic soils found in the Chandel district. The soil texture of Chandel is predominantly coarse, varying from fine loamy to sandy. Although acidic, the soils frequently possess high levels of organic carbon and nitrogen, particularly in forested regions. Nevertheless, they may lack important micronutrients like as zinc and exhibit low to moderate levels of accessible phosphorus due to their acidic characteristics.

The geological survey of India has undertaken systematic survey in the two sub-divisions in the district. Viz, Chandel and Chakpikarong and discovered valuable minerals deposits like limestone, copper, lignite, nickel, cobalt, asbestoses, clay, etc. In the district, limestone is available between 32/4 and 32/6 milestone on Imphal Moreh road in the Tengnoupal sub-division. A small quantity of copper is also available at Ningthi and Kwatha area of Tengnoupal sub-division and little quantity of Chromites is also available near the Nepali Basti of Chandel sub-division covering an area of about 38 sq. km. and having the maximum thickness of 0.3 metre.

2.6. Drainage System

Chandel district is drained by the two river systems: TheManipur river and its tributaries like Chakpikarong river, Kaha Lok river and Sekmai drains the western portions. while number of small rivers falling into the Yu river of Myanmar (Burma) (a tributary of Chindwin river) like Taret river, Lokchao river, Thuidam river, Tiwan Lam river, Tuisa Dung river, etc. drain the eastern portions of the district.

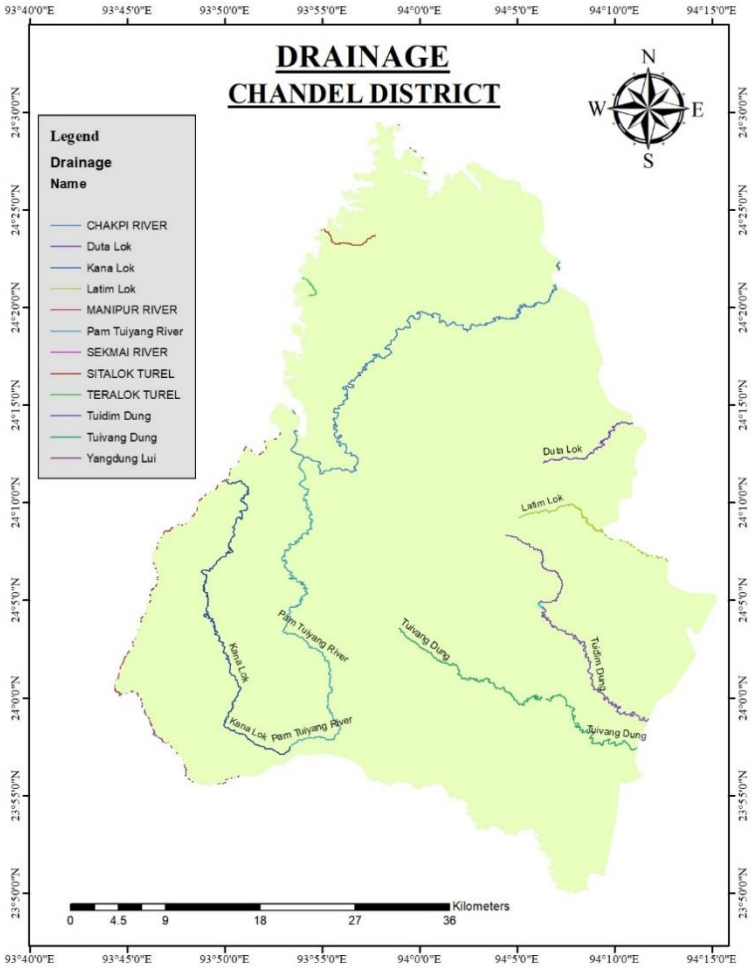

Figure 2.6 Drainage system (source MARSAC)

2.6.1 Distance to River

Distance to river refers to the shortest measurable distance between a spatial location (point, cell, or feature) and the nearest river or stream. Land-use planning, hydrology, and environmental sciences all make extensive use of this spatial metric. For example, when assessing flood risk, the distance to a river aids in locating infrastructure or settlements that are more vulnerable to flooding. In ecology, it is used to study species distribution and habitat suitability, since proximity to rivers often influences biodiversity, vegetation growth, and soil fertility (Ward *et al.*, 2002).

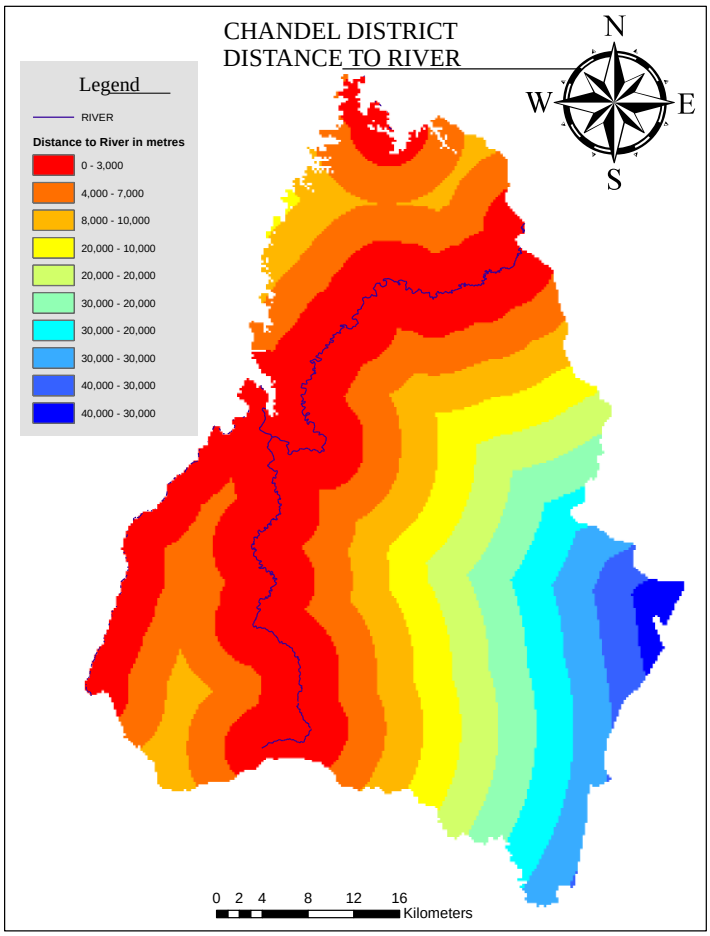

Figure 2.6.2 Distance to River.

2.7 Road Network

Road Network being the most important element of infrastructures, connects the district's isolated villages to towns and then to the rest of the state and country. The district's hilly terrain and heavier rainfall pose serious challenges to the network. The study area's road system comprises of village roads, state and National highways. The headquarter town is about 64km from the capital Imphal. Major roads include the National highway NH-102C which connects Chandel to Pallel.

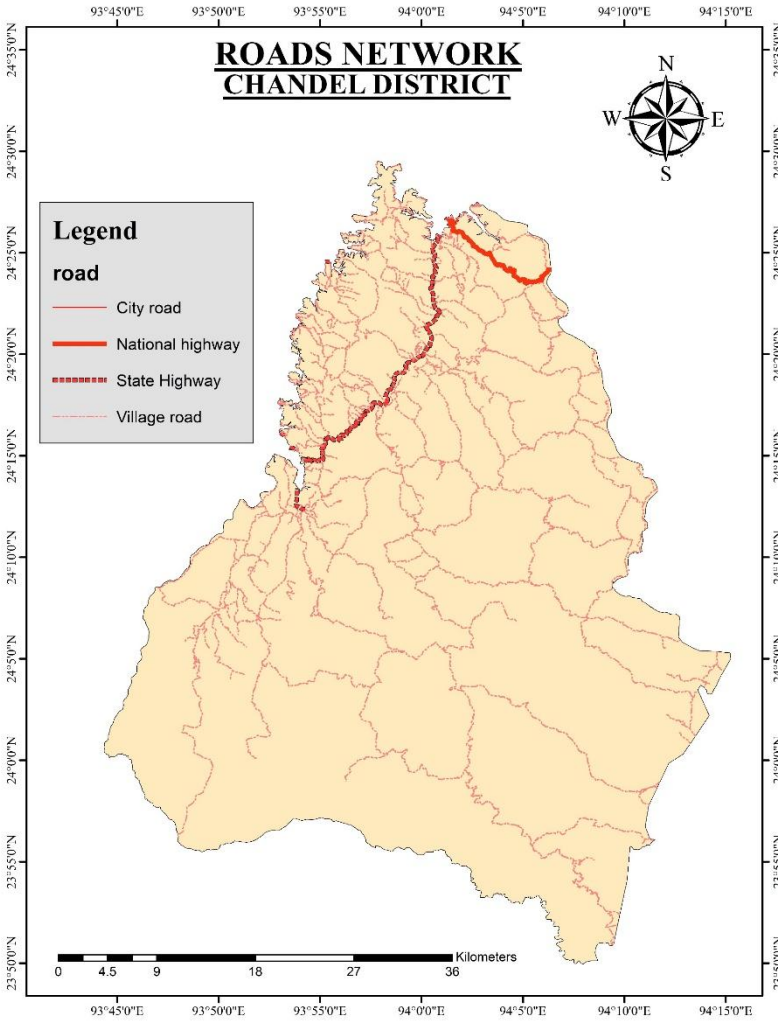

Figure 2.7 Road Network (source: MARSAC)

2.7.1 Distance to Road

The distance to road is an important indicator in various fields of spatial analysis. It aids in assessing accessibility and locating places where transportation infrastructure is lacking in urban and regional planning (Kumar *et al.*, 2019). In environmental and ecological studies, distance to road is widely used to assess human disturbance, habitat fragmentation, and land degradation risks (Forman & Alexander, 1998; Laurance *et al.*, 2009). For example, areas located farther from roads tend to have higher ecological integrity, while those close to roads are more prone to anthropogenic pressures.

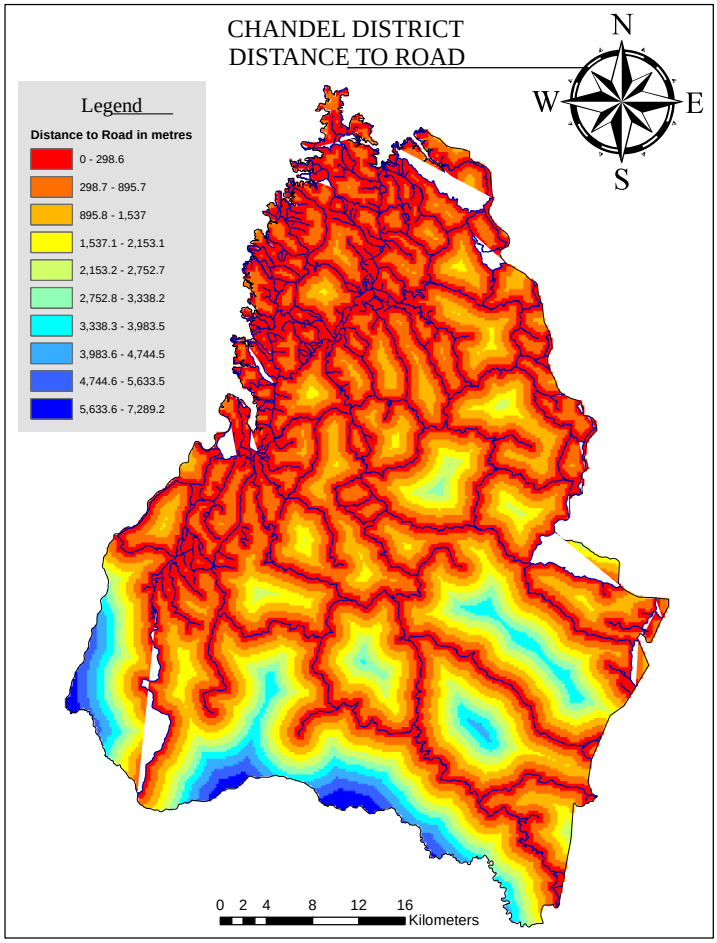

Figure 2.7.1 Distance to Road

2.8 Population and Settlement

Chandel is one of the hill districts of Manipur, located in the south-eastern part of the state, sharing an international boundary with Myanmar and serves as a home to a predominantly tribal population with rich cultural diversity. The district is known for its picturesque landscapes, as well as its mosaic of ethnic communities. According to the 2011 Census of India, Chandel district had a total population of 144,182, showing a 21.85% growth compared to the 2001 census. Out of the total, 74,579 were males and 69,603 were females, giving the district a sex ratio of 933 females per 1000 males, which is slightly below the state average. With a population density of only 44 persons per sq. km, Chandel is one of the least densely populated districts of Manipur. The

sparse population reflects both its hilly terrain and limited infrastructure development. Chandel is primarily a rural district, with 127,335 persons (88.32%) residing in villages and only 16,847 persons (11.68%) living in urban areas. This highlights the agrarian nature of the economy and the limited degree of urbanisation.

Agriculture is the main occupation of the people in Chandel. Rice is the main crop grown. Both jhum and terrace cultivation is done in the hill slopes of the district. Though it is not an entirely rural economy, urbanization has been a very slow process.

Table 2.8 Decadal growth of population in Chandel District

Census Year	Persons	Absolute Growth	Percentage	Males	Females
1951	24049	na	na	11566	12483
1961	27679	3630	15.09	13784	13895
1971	38723	11044	39.9	19605	19118
1981	56444	17721	45.76	29174	27270
1991	71014	14570	25.81	37118	33896
2001	118327	47313	66.62	59741	58586
2011	144182	25855	21.85	74579	69603

Source: compiled by Scholar according to Census of India.

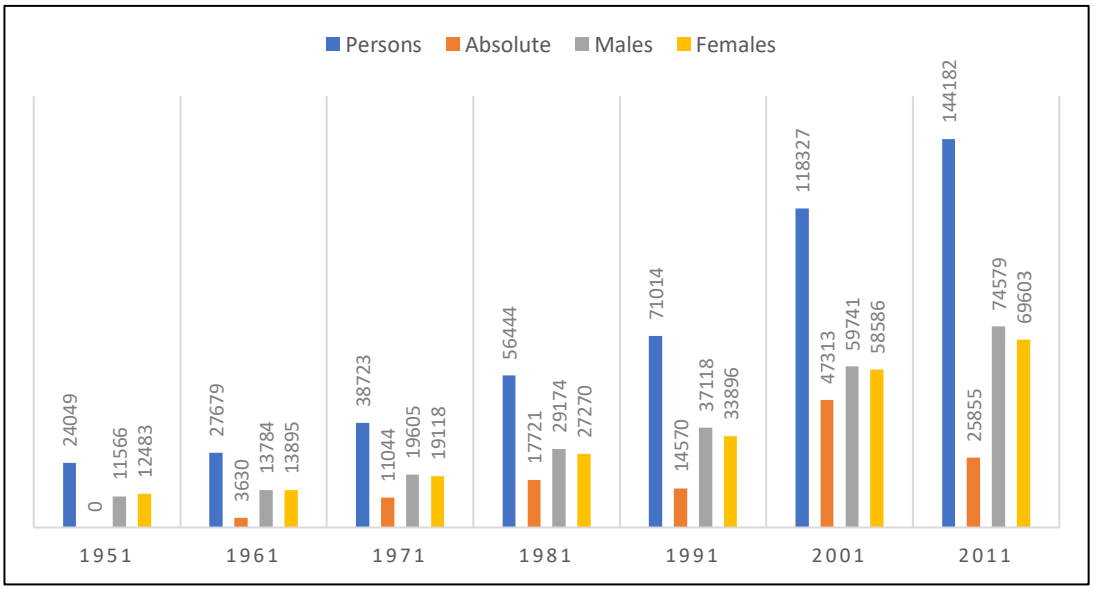

Figure 2.8. Decadal growth of population

Table 2.9 Forest Cover distribution of Chandel

Year	Dense forest	Moderately Dense Forest	Open forest	Total	% of Geographical Area
1999	756	0	1998	2754	83.12707516
2001	812	0	1906	2718	82.04044673
2003	0	768	1935	2703	81.58768488
2005	0	734	1955	2689	81.16510715
2007	0	734	2065	2799	84.4853607
2011	0	744	2085	2829	85.39088439
2013	0	734	2055	2789	84.18351947
2015	0	710	2097	2807	84.72683369
2017	11	970	1926	2907	87.745246
2019	10.76	950.42	1902.17	2863.35	86.42770903

Source: compiled by Sholar from Indian State of Forest report

2.9 Forest Status

Chandel district comes under Tengnoupal Forest Division of the state. It has about 81 percent forest cover of the total geographical area. The dense forest on Myanmar border has valuable teak tree in abundance. Forest provides firewood, charcoal, wood and many other forest resources. As per the state Forest Report of 1991 and 2001, 756 sq.km areas were under dense forest in 1991, which had increased to 812 sq. km in 2001; open forest area in 1991 was 1998 sq.km and in 2001 it was 1906 sq. km., area of scrubs increased in 2001 from 20 sq. km in 1991 to 49 sq.km in 2001. Nevertheless, total forest area in the district has gone down in recent years due to excessive practice of shifting cultivation. Chandel is one of the districts severely affected by the practice of shifting or Jhum cultivation with a reducing Jhum cycle. Forest is one of the most important constituents of the resource base of the district. But from 1997-98, revenue generated by forest has gone down. This may be due to Supreme Court's ban on the fell of timber. Chandel has the highest timber production among the districts. It has also large area of forest under bamboo covering 478.38 hectares.

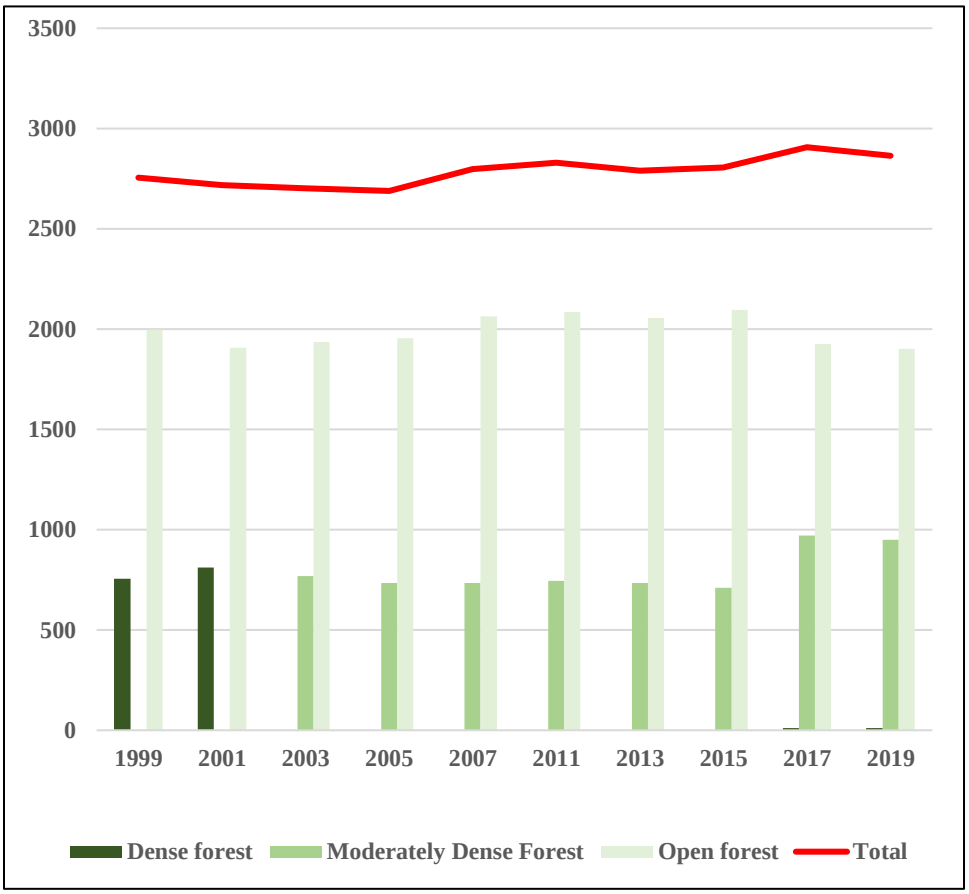

Figure 2.9 Graph Showing the Temporal variation in Forest Cover

Chapter 3

Spatio-temporal variation in Land Use Land Cover distribution of the study area.

3.1 Introduction

Land Use and Land Cover are two distinct yet closely related concepts that are used often in Environmental studies (Han 2015). Land Cover refers to the biophysical aspects of the earth's surface, such as the distribution of plant, water, soil, and other physical elements of the land. While the term "land use" describe how humans have utilised land and its ecosystem, most often with a focus on the usefulness of land for economic activity. Mapping LULC changes at regional scales serve a wide variety of purposes, including mitigating and controlling the effects of various calamities like landslides, climate change, urban floods, etc.., (Reis 2008). Globally, there is rapid convergence of distinct land uses and land cover types (Lambin, Geist, and Lepers 2003). Population growth and human activity in a region are the main drivers of changes in land cover (Achmad *et al.* 2015), agriculture requirements (Cammerer, Thieken, and Verburg 2013; Li, Zhou,and Ouyang 2013; Daleetal. 1997), various causes, including economic and urbanization development (Rimal *et al.* 2019; Khanetal. 2014), natural disasters (Dubovyk, Sliuzas, and Flacke 2011), as well as others (Mustafa *et al.* 2018). Knowledge on land use or land cover aids in a better understanding of characteristics of land use, such as cropping patterns, fallow lands, forests, grazing areas, wastelands, and surface water bodies, which are essential for development planning. The availability of land-use land-cover change information facilitates better environmental planning and management decision-making (Prenzel 2004; Fan,Weng, and Wang 2007).

The importance of Land use and Land cover (LULC) dynamics in general and forest cover dynamics in particular is duly recognized by the International Geosphere Biosphere Programme (IGBP), the United Nations Framework Convention on Climate Change (UNFCC), the United Nations Collaborative Programme on Reducing Emissions from Deforestation and Forest Degradation in Developing Countries (UN-REDD Programme) and many other national and international organizations. Remote sensing data has emerged as a significant application for mapping change in LULC, with numerous applications (Lo and Choi 2004). Remote sensing monitoring and

assessment of LULC changes entails the use of multiple multi-date images that can often detect various environmental conditions and human actions involved in those changes (Singh 1989; Duraisamy *et al.* 2018).

3.2. Materials and Methodology

For this study, a set of cloud free Landsat series satellite imageries LEVEL 1 was used for the classification of Land Use Land Cover of the study area for the period of year 1994, 2003, 2014 and 2021. Landsat-5 Thematic Mapper (TM) acquired on 21st February 1994, Landsat 7 ETM+ Level 1 for 2003 and Landsat 8 operational Land Imager (OLI) for 2014 and 2021 has been used for LULC classification. These data which are used in this study are downloaded from the United States Geological Survey (USGS EARTH EXPLORER) website. For this study, QGIS (Quantum GIS 3.16 Hannover) and ArcGis 10.5 are used for processing and analysing the above images. Table 1 depicts the detailed description of the datasets.

Table 3.2. Satellite images descriptions

Satellite images	Date of acquisition	Path/Row	Source
Landsat 5 TM Level 1	21st February 1994	135/43	USGS (https://earthexplorer.usgs.gov)
Landsat 7 ETM+ Level 1	10th March 2003	135/43	
Landsat 8 OLI level 1	16th March 2014	135/43	
Landsat 8 OLI Level 1	30th January 2021	135/43	

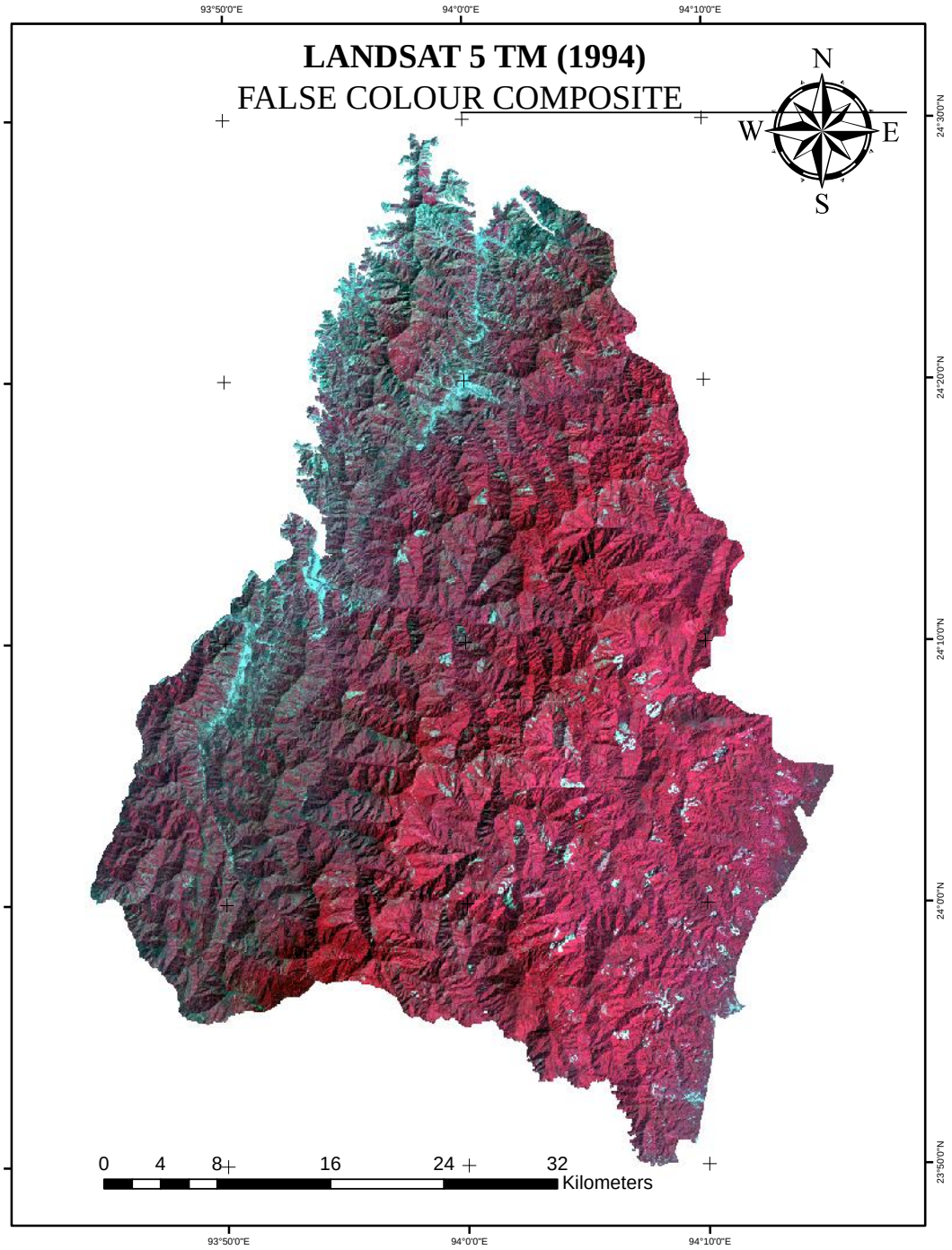

Figure 3.2 (a) 1994 False colour composite (Landsat 5)

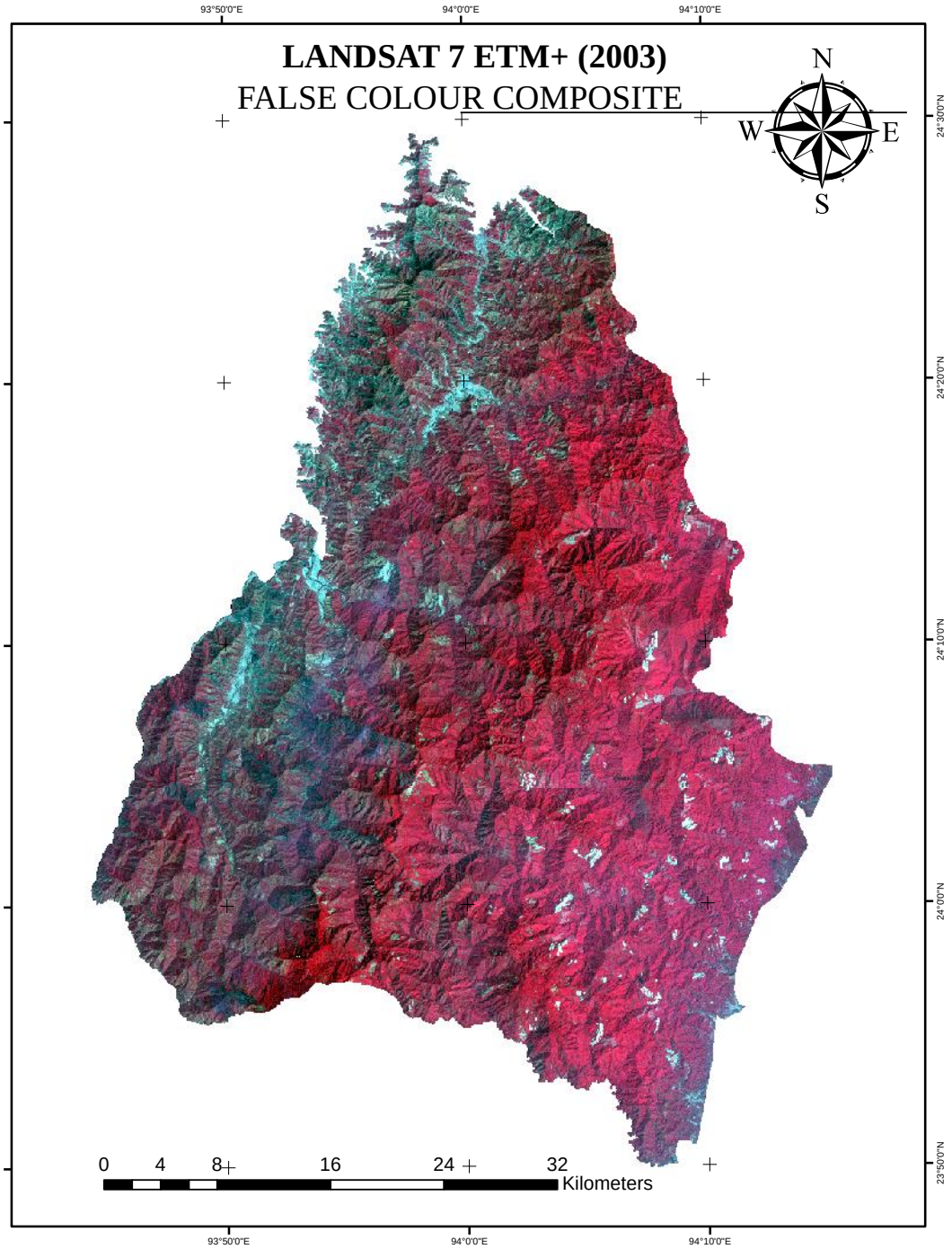

Figure 3.2 (b) 2003 False colour composite (Landsat 7)

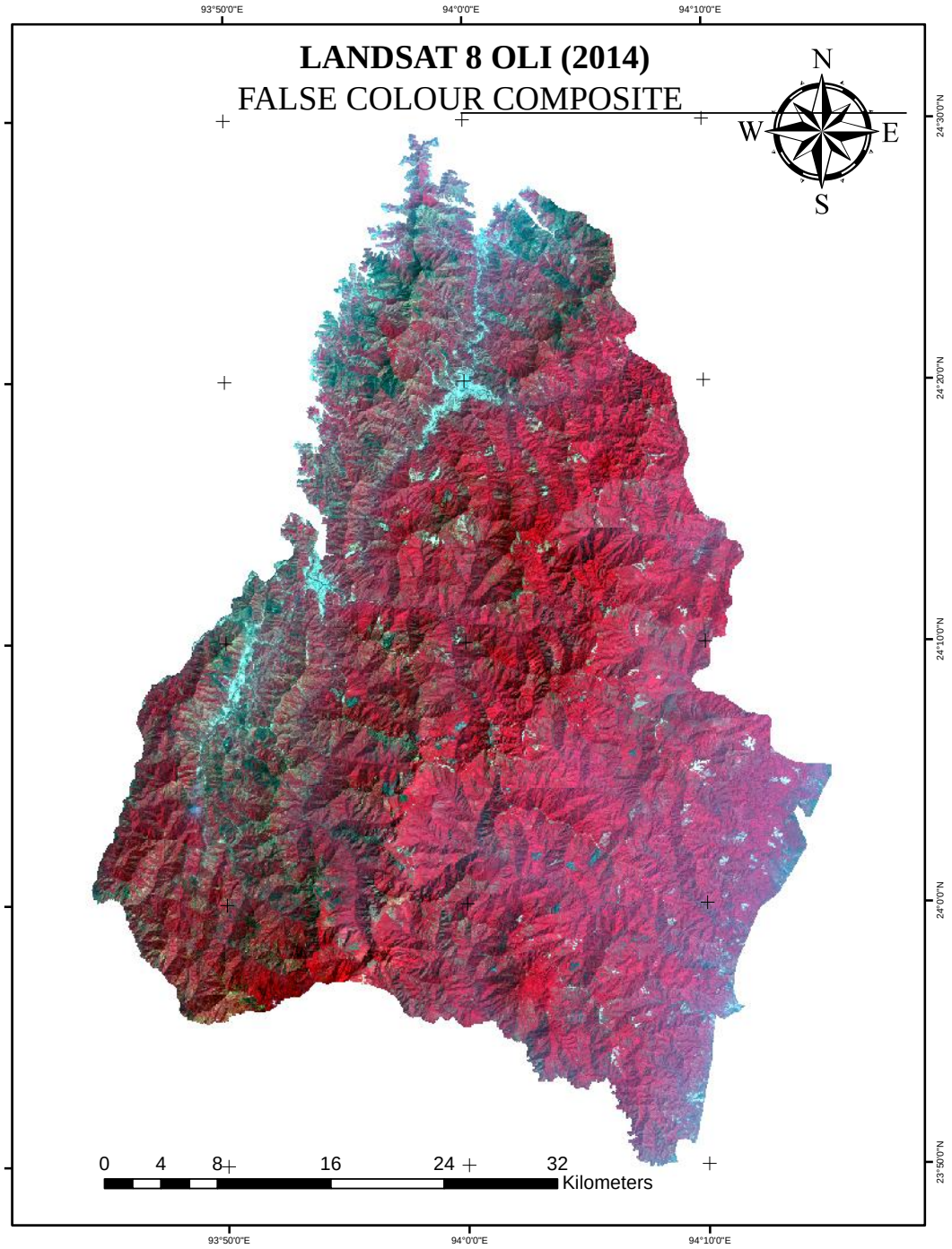

Figure 3.2 (c) 2014 False colour composite (Landsat 8)

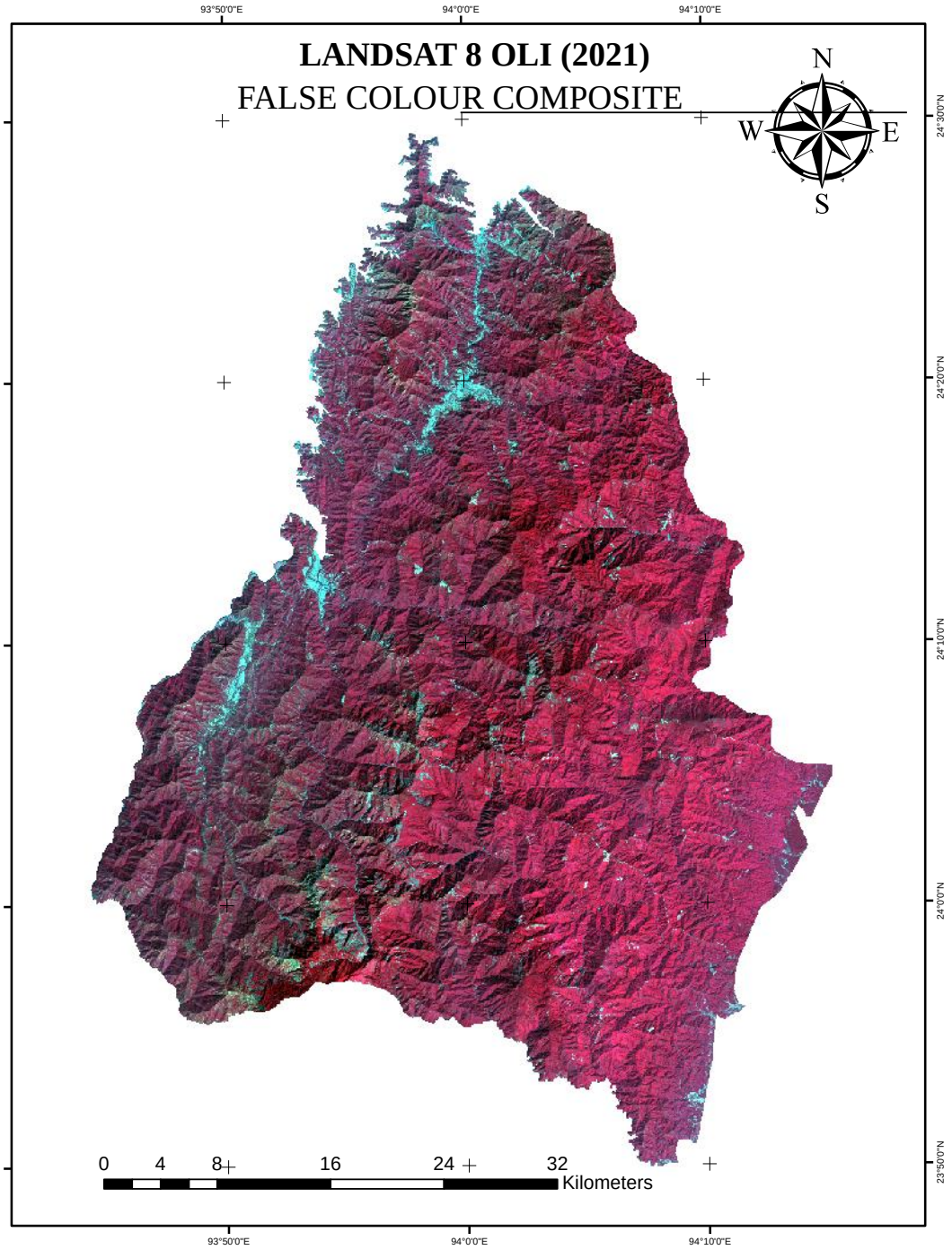

Figure 3.2 (d) 2021 False colour composite (Landsat 5)

3.2.1 Image Pre-processing

Below, Figure 3.2.1 illustrates the working Methodology Flow chart of LULC

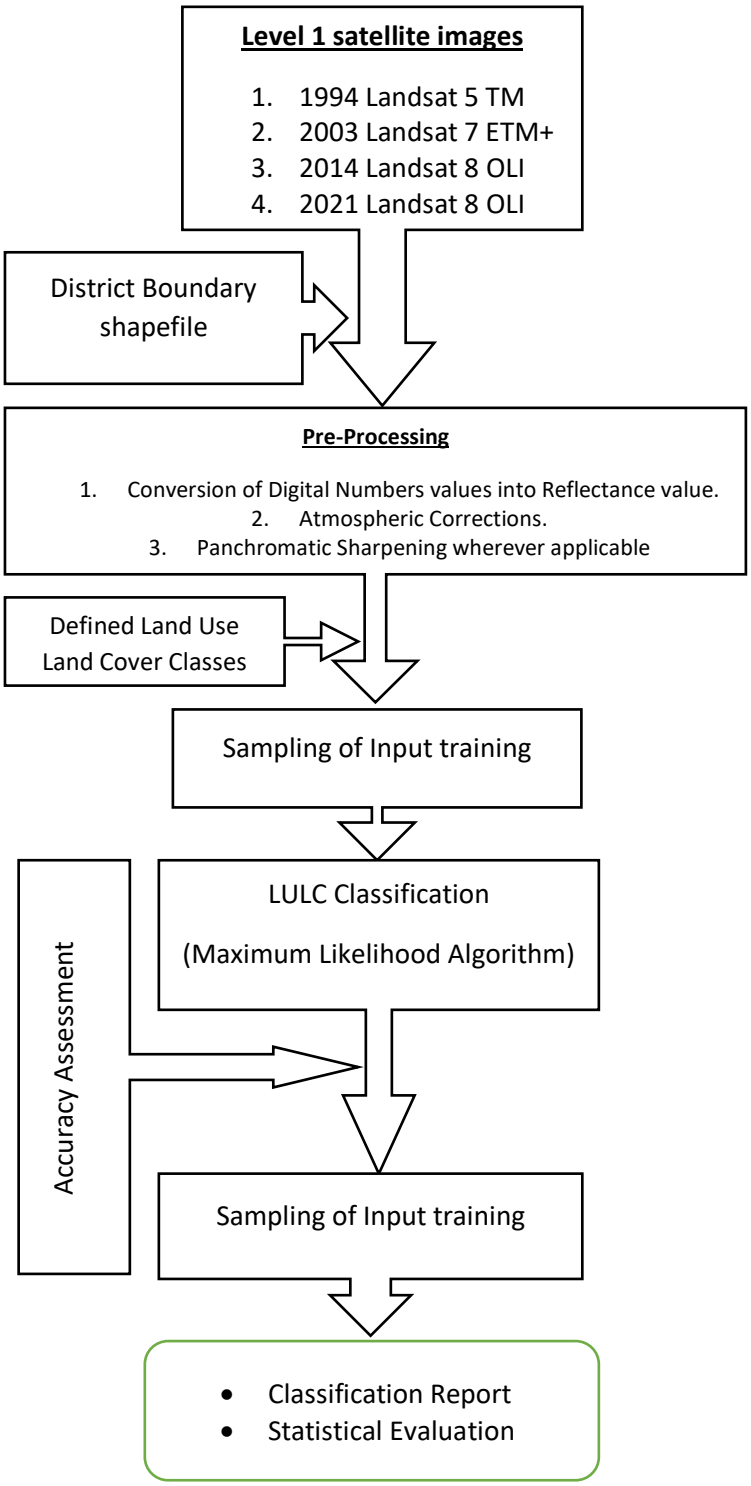

Figure 3.2.1 Flow Chart of the Working Methodology for LULC

3.2.1.1 Conversion to TOA Radiance

Landsat level 1 data was converted to TOA spectral radiance with the help of the Radiance Rescaling factors given in the MTL file that comes with the Level 1 downloaded Data:

$$L_\lambda = M_L Q_{cal} + A_L$$

Where:

L_λ = TOA Spectral radiance

M_L = Band-specific multiplicative rescaling factor from the metadata (RADIANCE_MULT_BAND_x, where x is the band number)

Q_{cal} = Quantized and calibrated standard product pixel values (DN)

A_L = Band-specific additive rescaling factor from the metadata (RADIANCE_ADD_BAND_x, where x is the band number)

3.2.1.2 Conversion to TOA Reflectance

Reflective band DN's was coverted to TOA Reflectance using the rescaling co-efficients bundled in the MLT file. The equation for conversion was:

$$\rho_\lambda{}' = M_\rho Q_{cal} + A_\rho$$

Where:

$\rho_\lambda{}'$ = TOA planetary reflectance, without correction for solar angle. Note that $\rho\lambda'$ does not contain a correction for the sun angle.

M_ρ = Band-specific multiplicative rescaling factor from the metadata (REFLECTANCE_MULT_BAND_x, where x is the band number)

Q_{cal} = Quantized and calibrated standard product pixel values (DN)

A_ρ = Band-specific additive rescaling factor from the metadata (REFLECTANCE_ADD_BAND_x, where x is the band number)

TOA reflectance with a correction for the sun angle is then:

$$\rho_\lambda = \frac{\rho_\lambda{}'}{cos(\theta_{SZ})} = \frac{\rho_\lambda{}'}{sin(\theta_{SE})}$$

Where:

ρ_λ = TOA planetary reflectance

θ_{SE} = local sun elevation angle. The scene centre sun elevation angle in degrees is provided in the metadata (SUN_ELEVATION).

θ_{SZ} =Local solar zenith angle; $\theta_{sz} = 90^o - \theta_{SE}$

3.2.1.3 Conversion to Top of Atmosphere Brightness Temperature

Thermal band data was converted from spectral radiance to top of atmosphere brightness temperature using the thermal constants in the MTL file. The conversion equation was

$$\mathbf{T}=\frac{K_2}{ln\left(\frac{K_1}{L_\lambda}+1\right)}$$

Where:

T = Top of atmosphere brightness temperature.

L_λ = TOA Spectral radiance

K_1 = Band-specific thermal conversion constant from the metadata (K_1_CONSTANT_BAND_x, where x is the thermal band number)

K_2 = Band-specific thermal conversion constant from the metadata (K_2_CONSTANT_BAND_x, where x is the thermal band number)

3.2.2 Training Set

Training sets play a crucial role in LULC classification, especially for supervised classification workflows. A training set is a collection of geographically referenced areas (usually polygons or points) on a satellite image where the true LULC class is known. These labelled samples are used to "teach" the classification algorithm the spectral signature—the reflectance values across different bands—that uniquely identifies each LULC class (Talukdar *et al.,* 2020; Wulder *et al.,* 2018). The trained algorithm then uses this information to classify the rest of the unknown pixels in the image.

The following procedures were used to create training sets in QGIS by using the Semi-Automatic Classification Plugin (SCP) to perform supervised classification.

i. Initialling Setup (Using SCP Plugin): The Semi-Automatic Classification Plugin (SCP) was installed and active in QGIS.
ii. Defining Band Set: the satellite image bands (e.g., Landsat) was loaded and a Band set was defined in the SCP Dock, specifying the band numbers and their corresponding wavelengths.
iii. Creation of Training Input File: In the SCP Dock, a new training input file was created.
iv. Defining Classes: In the SCP Dock's Training Input section, the Macro-classes (MC) and Classes (C) were defined, a unique ID (MC ID and C ID) and name were assigned to each LULC category (e.g., MC ID 1 = Water, C ID 1 = Lake).
v. Digitizing ROIs: Using the SCP toolbar tools (usually a polygon or rectangle tool) to draw polygons directly on the satellite image, making sure each polygon covered an area that is clearly and exclusively of a single LULC class.
vi. Saving ROIs: After drawing, the polygon was saved as an ROI to the Training Input file, assigning it to the appropriate Class ID and Macro-class ID.

3.2.3 Land Use Land Cover Classification

For Classification of the study area, 5 LULC classes was Categorized:

1. Vegetation cover
2. Built-up
3. Agricultural Land
4. Bare soil and
5. Water Bodies.

After training samples were collected for individual classes using visual interpretation. The collected pixel samples were then assigned to derived LULC via the recorded spectral signature of each sample pixel. Upon satisfactory classification output, classification Report was then generated. Dense forest cover and regenerated forest has been categorised under vegetation cover. Areas under shifting cultivation as well

as permanent areas of cultivation are also categorised under agricultural land whereas built-up comprises of settlements, roads, etc., those areas which has been previously under shifting cultivation and has now been abandoned and left fallow was categorised under bare soil. Areas with exposed soil without vegetation was also categorised under bare soil as well.

3.2.3.1 Maximum Likelihood

One of the most well-known and frequently used methods for classifying Land Use Land Cover (LULC) using remote sensing and GIS platforms is the maximum likelihood algorithm, also known as Maximum Likelihood Classification (MLC). Its popularity stems from its solid statistical underpinnings and ease of interpretation, which make it a crucial technique for supervised classification tasks in resource management, urban planning, and environmental studies.

The foundation of Maximum Likelihood Classification lies in the concepts of statistics and probability theory. It was predicated on the idea that each land cover class's pixel values have a normal (Gaussian) distribution. The algorithm estimates the mean vector and covariance matrix for each land cover class, characterizing its statistical characteristics, using training data, which are representative samples from each class. Using the computed statistics and the observed spectral values, MLC determines the probability (likelihood) that each pixel in the remote sensing image belongs to each land cover class. The class with the highest probability was assigned to each pixel.

Supervised classification was performed on the images using Maximum Likelihood on the images to generate the Land Use Land Cover of the study area.

3.2.3.2 Accuracy Assessment

Accuracy assessment was performed for all the classified images through stratified random sampling of the reference pixels. Table 3.2.3.2 (a), (b), (c) and (d) represents the results of the accuracy assessment of the classified maps of year 1994, 2003,2014 and 2021 respectively. Overall accuracy is the indication of the degree of accuracy of the land use land cover classification as a whole. User’s accuracy and producer’s

Table 3.2.3.2 (a) Error Matrix LULC 1994

Classes	Vegetation Cover	Built up	Agricultural Land	Bare Soil	Water Bodies	Area Sq. Metres
Vegetation Cover	0.8254	0	0	0	0	1683609300
Built up	0	0.0007	0	0	0.0001	1587600
Agricultural Land	0.0039	0.0037	0.0546	0.0023	0	131432400
Bare soil	0.0154	0	0.0173	0.0765	0	222760800
Water Bodies	0	0	0	0.0001	0.0001	441900
Total	0.8446	0.0043	0.0719	0.0789	0.0002	2039832000
Area	1722876117	8858424	146684867	161012147	400445	2039832000
SE	0.0005	0.0002	0.0006	0.0006	0	
SE area	1057743	425770	1206819	1314629	46802	
95% CI area	2073176	834510	2365366	2576672	91732	
PA [%]	97.72	15.08	75.92	96.98	68.60	
UA [%]	100	84.16	84.73	70.10	62.16	
Kappa hat	1	0.84	0.84	0.68	0.62	
Overall accuracy [%] = 95.72						
Kappa hat classification = 0.85						

accuracy is indication of the degree of accuracy of each individual class. Kappa Coefficient indicates the degree of agreement in the classified data. Overall accuracy stands at 95%,83%, 94% and 98% for LULC of 1994, 2003, 2014 and 2021 respectively. Whereas, the Kappa coefficient, at 0.8, 0.6, 0.8 and 0.9 for 1994, 2003, 2014 and 2021 LULC indicates a relatively good agreement for the study area was determined.

Table 3.2.3.2 (b) Error Matrix for LULC 2003

Classes	Vegetation Cover	Built Up	Agricultural Land	Bare Soil	Water Bodies	Area Sq. Metres
Vegetation Cover	0.6445	0	0	0.1563	0	1633469400
Built up	0	0.0013	0	0	0	2795175
Agricultural Land	0.0005	0	0.0575	0.0046	0	127647900
Bare Soil	0	0	0.002	0.133	0	275365350
Water Bodies	0	0	0	0.0001	0.0001	487125
Total	0.6451	0.0013	0.0596	0.294	0.0001	2039764950
Area	1315810020	2653174	121526862	599631399	143494	2039764950
SE	0.0012	0	0.0002	0.0012	0	
SE area	2473188	18333	492950	2514666	19627	
95% CI area	4847448	35932	966183	4928746	38469	
PA [%]	99.91	100.00	96.55	45.23	100.00	
UA [%]	80.48	94.92	91.92	98.49	29.46	
Kappa hat	0.45	0.95	0.91	0.98	0.29	
Overall accuracy [%] = 83.63						
Kappa hat classification = 0.62						

Table 3.2.3.2 (c) Error Matrix for LULC 2014

Classes	Vegetation Cover	Built Up	Agricultural Land	Bare Soil	Water Bodies	Area Sq. Metres
Vegetation Cover	0.8251	0	0	0.0279	0	1739919150
Built Up	0	0.0034	0	0.0001	0.0001	7378200
Agricultural Land	0.0006	0.0104	0.0356	0.0092	0	113831100
Bare Soil	0.002	0	0.0001	0.0854	0	178268850
Water Bodies	0	0	0	0	0.0002	386100
Total	0.8278	0.0137	0.0357	0.1225	0.0003	2039783400
Area	1688463075	28043246	72803319	249961979	511781	2039783400
SE	0.0003	0.0002	0.0002	0.0003	0	
SE area	599304	335585	414176	673592	17253	
95% CI area	1174637	657747	811785	1320241	33816	
PA [%]	99.68	24.59	99.73	69.65	71.09	
UA [%]	96.73	93.45	63.78	97.66	94.23	
Kappa hat	0.81	0.93	0.62	0.97	0.94	
Overall accuracy [%] = 94.96						
Kappa hat classification = 0.82						

Table 3.2.3.2 (d) Error Matrix for LULC 2014

Classes	Vegetation Cover	Built Up	Agricultural Land	Bare Soil	Water Bodies	Area Sq. Metres
Vegetation Cover	0.8803	0	0	0	0	1795560975
Built Up	0.0002	0.0041	0.0003	0	0	9369450
Agricultural Land	0.0001	0	0.0378	0.0074	0	92541150
Bare Soil	0	0	0.0058	0.0631	0	140590125
Water Bodies	0	0	0	0.0001	0.0008	1721700
Total	0.8806	0.0042	0.0439	0.0706	0.0008	2039783400
Area	1796139782	8494416	89546609	144072192	1530400	2039783400
SE	0.0001	0.0001	0.0005	0.0005	0	
SE area	160446	191933	979270	964584	52308	
95% CI area	314474	376189	1919369	1890586	102524	
PA [%]	99.97	99.37	86.21	89.40	100.00	
UA [%]	100.00	90.09	83.42	91.62	88.89	
Kappa hat	1.00	0.90	0.83	0.91	0.89	
Overall accuracy [%] = 98.61						
Kappa hat classification = 0.93						

3.3 Spatial Distribution of Land Use Land Cover

3.3.1 LULC 1994

The LULC for 1994 shown in Table 3.3.1, reveals a landscape overwhelmingly dominated by natural cover, with minimal development and small areas dedicated to agriculture. The total surveyed area is 2039.83 Km^2. Vegetation cover is the most significant land use, accounting for 82.54% of the total area, which translates to 1683.61 Km^2. This indicates that the vast majority of the region was covered by natural or semi-natural vegetation. Bare Soil was the second-largest class, covering 10.92% (222.76 Km^2. This indicates that the study areas were prone to erosion, naturally barren land, or land temporarily cleared for future use. Agricultural Land accounts for the third-largest class at 6.44% (131.43 Km^2). This suggests that agriculture plays a relatively minor role in the total land use. Built up area was extremely small, constituting only 0.08% (1.59 Km^2). This suggests a very low level of urbanization or human settlement density in the study area. Water bodies were the least represented class, covering a negligible 0.02% (0.44 Km^2).

Table 3.3.1. Land Use Land Cover 1994

Class	Class Name	Percentage %	Sq. Km
1	Vegetation cover	82.54	1683.61
2	Built up	0.08	1.59
3	Agricultural Land	6.44	131.43
4	Bare Soil	10.92	222.76
5	Water bodies	0.02	0.44

The 1994 LULC profile suggests that the study area was dominated in its pristine state with a total built-up area of approximately 2 square kilometres. The minimal presence of Built up and the relatively low Agricultural Land suggest that human-induced changes (anthropogenic pressure) on the environment was minor at this time. The vast Vegetation cover indicates the area likely had a high ecological value, providing significant ecosystem services (e.g., carbon sequestration, habitat). In essence, the 1994 environment was characterized by natural dominance and very

low human footprint. The LULC classification of 1994 was highly skewed, with Vegetation Cover being the overwhelmingly dominant class.

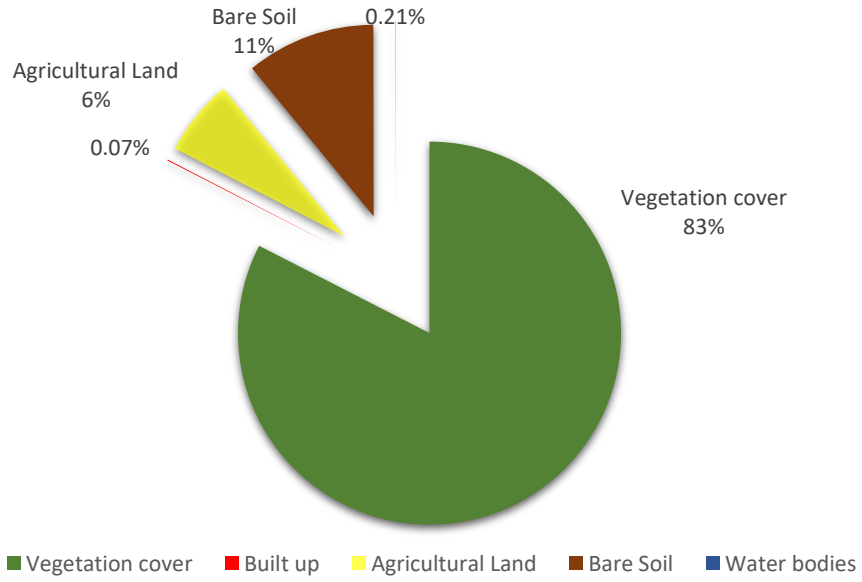

Figure 3.3.1 (a). Pie-chart showing Distribution of LULC 1994

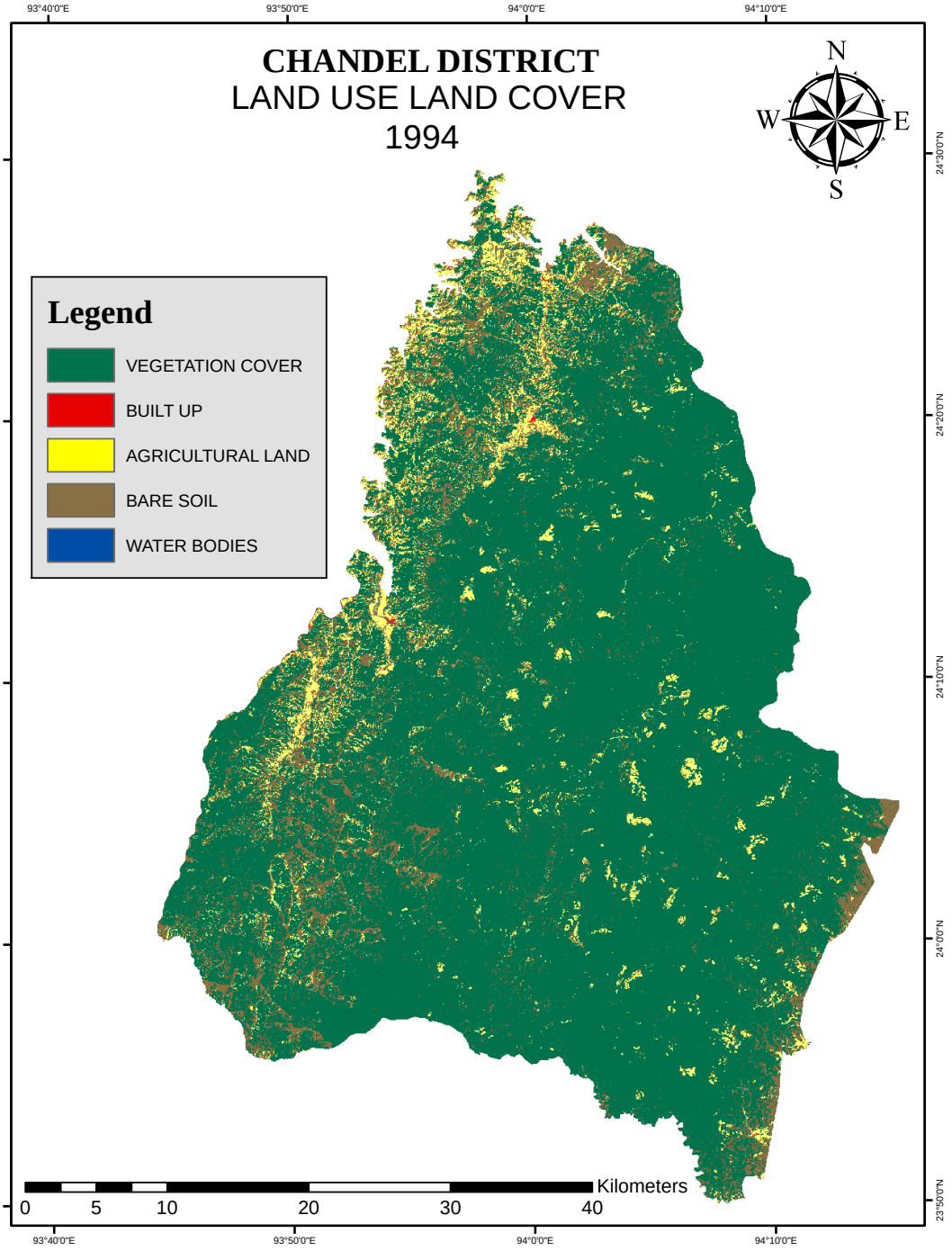

Figure 3.3.1 (b) Land Use Land Cover Map 1994

3.3.2 LULC 2003

Table 3.3.1 shows that natural cover remains dominant, but there are initial signs of land conversion, particularly a rise in bare soil and built-up area in the year 2003.

Table 3.3.2 Land Use Land Cover 2003

Class	Class Name	Percentage %	Sq. Km
1	Vegetation cover	80.08	1633.47
2	Built up	0.14	2.80
3	Agricultural Land	6.26	127.65
4	Bare Soil	13.50	275.37
5	Water bodies	0.02	0.49

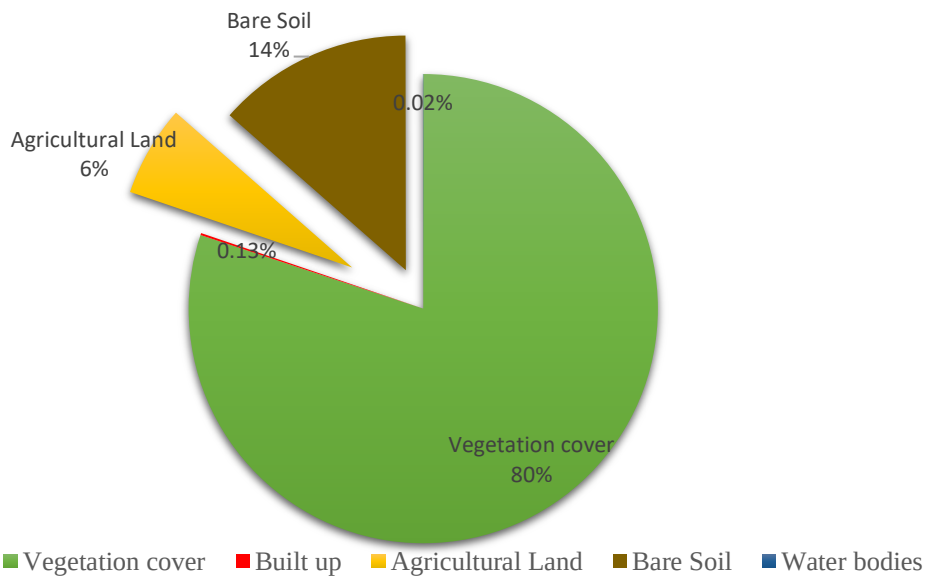

Figure 3.3.2 (a) Pie-Chart showing distribution of LULC 2003

Vegetation cover remains the single largest category, covering 80.08% of the area. While still dominant, it has slightly decreased compared to the year 1994. This indicates a highly forested or naturally green landscape.

Bare Soil was the second-largest category at 13.50%. This is a significant finding, as it indicates a large portion of the land is exposed. This suggests intensified land clearing, erosion, or preparation for future development or agriculture. This large presence also suggests areas of exposed ground, which could be naturally occurring (e.g., rocky outcrops) or a result of land degradation/temporary clearing. Agricultural Land accounts for 6.26%. This figure is quite stable or only marginally reduced, suggesting agriculture continues at a similar scale. Built up area, though still very small in absolute terms, has nearly doubled its percentage from a previous likely low value of 0.08% in 1994. This minimal but noticeable increase signals the beginning of modest urbanization or infrastructure development.

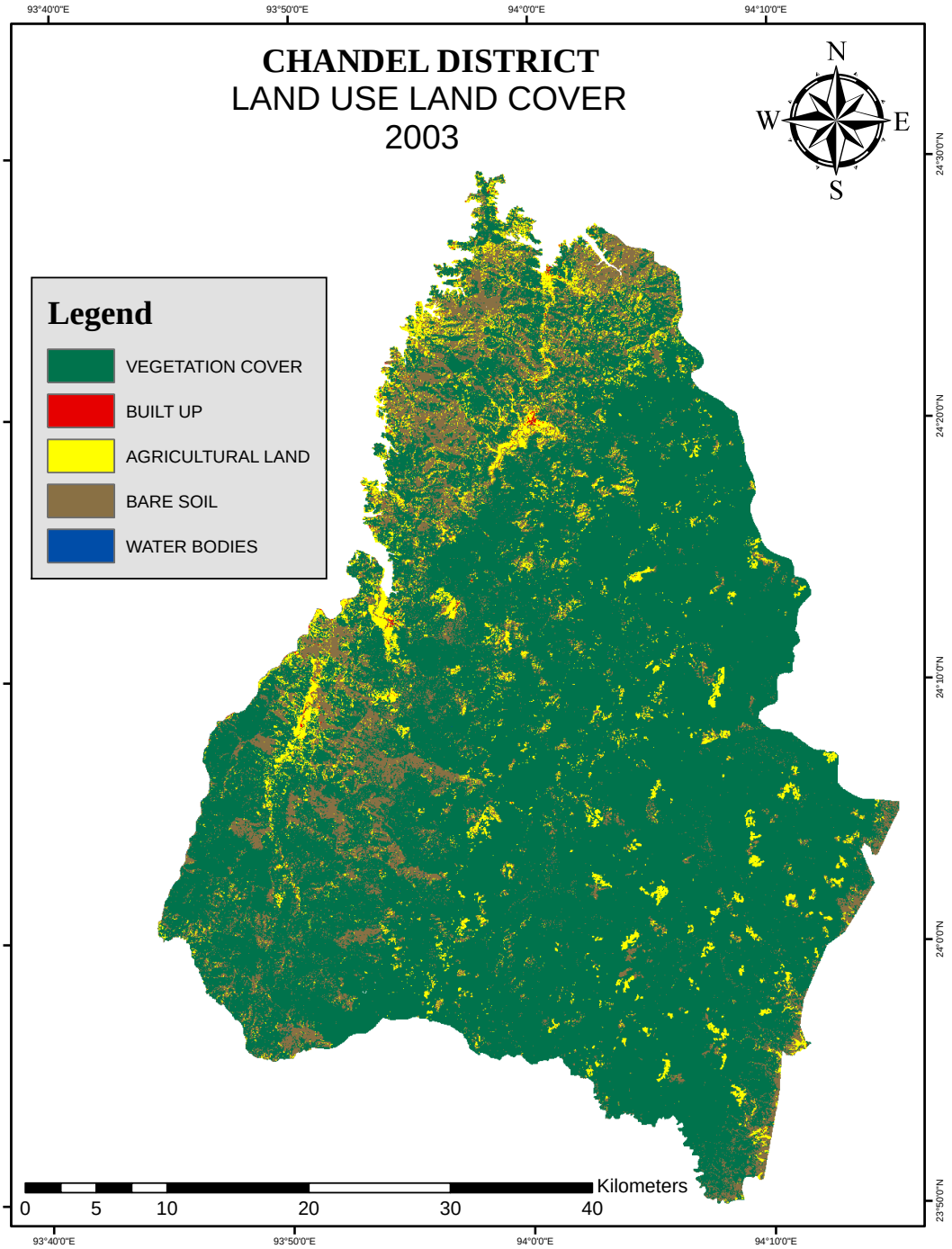

Figure 3.3.2 (b). Land Use Land Cover Map 2003

3.3.3 LULC 2014

Table 3.3.3 shows a increase in Vegetation cover and a significant increase in Built up area, alongside a reduction in both Bare Soil and Agricultural Land in the year 2014 in comparison to 2003.

Table 3.3.3 Land Use Land Cover 2014

Class	Class Name	Percentage %	Sq. Km
1	Vegetation cover	85.30	1739.92
2	Built up	0.36	7.38
3	Agricultural Land	5.58	113.83
4	Bare Soil	8.74	178.27
5	Water bodies	0.02	0.39

The vast majority of the land covered by Vegetation cover, accounting for 85% (1739.92 Sq. Km) of the total area. This indicates that in the year 2014 the study area was predominantly natural or managed green space, such as forest, grasslands, or dense shrubland. The second and third largest categories are Bare Soil at 8.74% (178.27 Sq. Km) and Agricultural Land at 5.58% (113.83 Sq. Km). Together, these three classes (Vegetation, Bare Soil, and Agriculture) make up over 99.6 of the entire land areas. The two categories associated with human settlement and water resources occupy a minimal portion. Built up area is only 0.36% (7.38 Sq. Km). Water bodies are 0.02% (0.39 Sq. Km), representing the smallest class.

The LULC classification also shows a significant disparity in the distribution of land cover, as illustrated in the pie chart figure 3.3.3. The comparison can be quantified by ratios: Vegetation vs. Human Development: Vegetation cover 85.30% is approximately 237 times larger than the Built-up area 0.36%, highlighting a very low level of urbanisation or concentrated development. Vegetation vs. Bare Soil: Vegetation cover is almost 10 times the size of the Bare Soil area 8.74%, suggesting that while natural cover is dominant, a notable amount of land was un-vegetated (which are the result of due to arid conditions, or recent deforestation/clearing).

Agriculture vs. Built up: Agricultural Land 5.58% is about 15.5 times larger than the Built-up area, indicating that agriculture, despite being a minor component overall, is a far more significant land use than urbanisation.

In summary, the land use was defined by a heavy focus on natural green cover, with Bare Soil and Agriculture forming the main secondary uses, while Built up and Water bodies are low in terms of area.

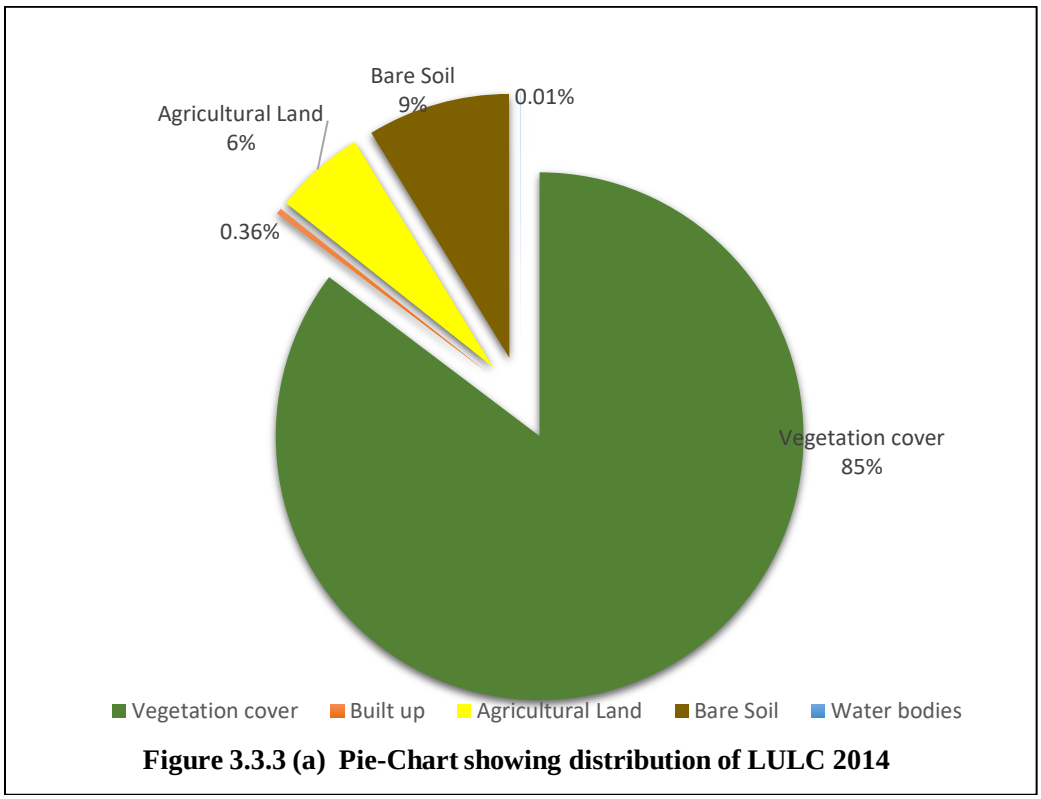

Figure 3.3.3 (a) Pie-Chart showing distribution of LULC 2014

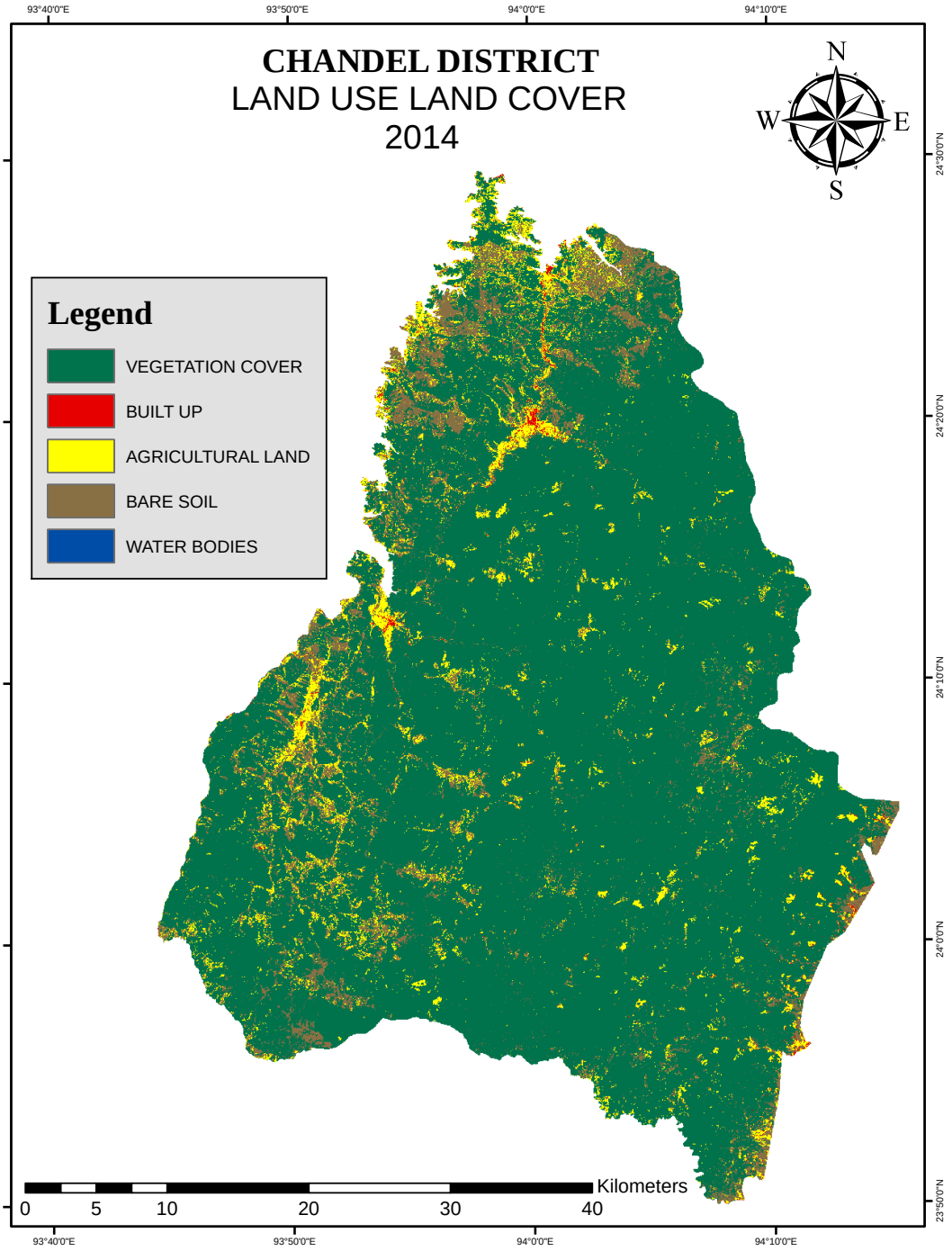

Figure 3.3.3 (b) Land Use Land Cover Map 2014

3.3.4 LULC 2021

Based on the Land Use Land Cover for 2021 in table 3.3.4, the area was dominated by natural cover, with lesser development and water bodies.

Table 3.3.4. Land Use Land Cover 2021

Class	Class Name	Percentage %	Sq. Km
1	Vegetation cover	88.03	1795.56
2	Built up	0.46	9.37
3	Agricultural Land	4.54	92.54
4	Bare Soil	6.89	140.59
5	Water bodies	0.08	1.72

The most significant land cover class was Vegetation cover, which accounts for the vast majority of the area at about 88.03% that translate to a total area of 1795.56 Km^2 .

This indicates the region is predominantly forested or covered by other forms of natural vegetation. The remaining land uses are substantially smaller, totalling at just under 12%: Bare Soil was the second largest class, comprising 6.89% (140.59 Km^2). This represents naturally bare land or areas subject to erosion, or recent clearance. Agricultural Land accounts for 4.54% (92.54 Km^2). This suggests a relatively minor role for formal agriculture in the overall land use.

Built up areas, representing urbanization and infrastructure, are extremely low at only 0.46% (9.37 Km^2). The least common land cover was Water bodies covering about 0.08% (1.72 Km^2). This suggests that the study has very few large lakes, rivers, or reservoirs, or that the area covered by water features is spatially limited for the satellite image to highlight.

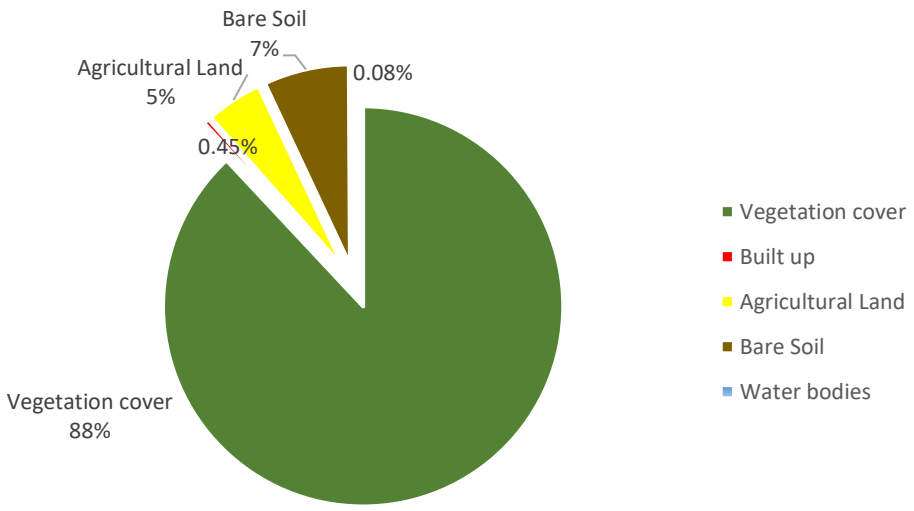

Figure 3.3.4 (a) Pie-Chart showing distribution of LULC 2021

The LULC of 2021, as shown in the figure above, thus, paints a picture of a largely natural, undeveloped area. The heavy concentration in Vegetation cover (88.03\%) combined with the very small proportion of Built-up areas (0.46\%) suggests the region is ecologically significant and has not undergone extensive urbanization or industrial development. The remaining land is primarily divided between bare and agricultural uses.

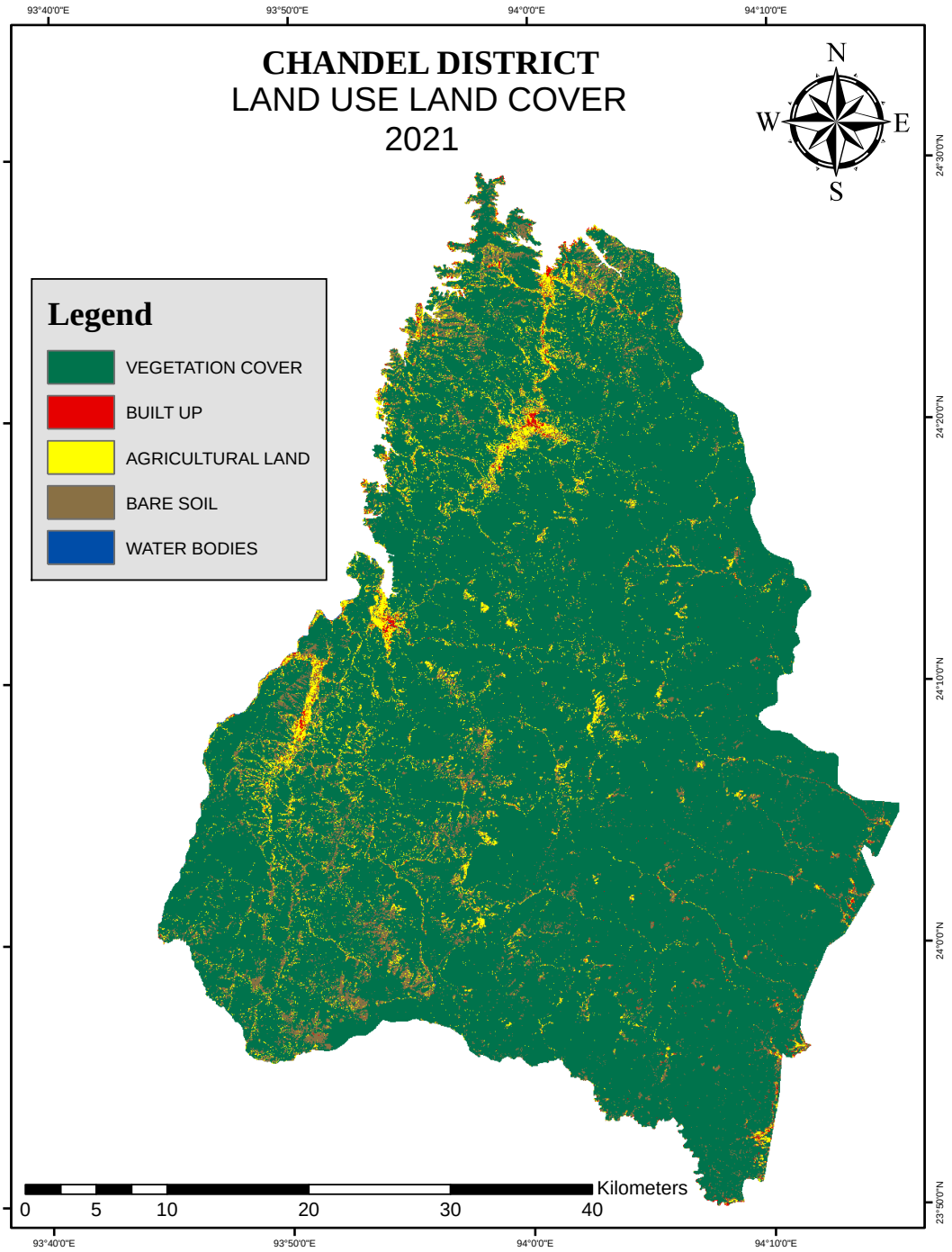

Figure 3.3.4 (b) Land Use Land Cover Map 2021

3.4 Temporal Changes

3.4.1 Temporal Change (1994-2003)

The Land Use Land Cover (LULC) change table below shows the changes from 1994 to 2003, reveals significant transformations in the study area.

Table 3.4.1 (a) Temporal comparison of LULC 1994 and 2003

Class Name	Area in 1994 Km^2	1994 (%)	Area in 2003 Km^2	2003 (%)
Vegetation cover	1683.61	**82.54**	1633.47	**80.08**
Built up	1.59	0.08	2.80	0.14
Agricultural Land	131.43	6.44	127.65	6.26
Bare Soil	222.76	10.92	275.37	**13.50**
Water bodies	0.44	0.02	0.49	0.02

- ✓ **Vegetation cover (-2.98%):** This class suffered the largest absolute loss, decreasing by 50.14 km^2(from 1683.61 Km^2 in 1994 to 1633.47 Km^2 in 2003). This loss almost equal to the gain in bare soil, suggesting a direct conversion of vegetation into bare ground.
- ✓ **Built up (+76.10%):** This class experienced the most dramatic percentage increase, growing from 1.59 Km^2 to 2.80 Km^2. This showed a strong indicator of **rapid urbanization** and development, even if the absolute area remains small.
- ✓ **Bare Soil (+23.62%):** The area of bare soil saw the largest absolute increase, gaining 52.61 Km^2. This significant rise suggests a major cause for concern, as it often results from the removal of vegetation and agricultural land due to deforestation, poor land management.
- ✓
- ✓ **Agricultural Land (-2.88%):** A decrease of 3.78 Km^2 (from 131.43 Km^2 to 127.65 Km^2 indicates a loss of arable land, which may be converted to bare soil or, in smaller part, to built-up areas.

Table 3.4.1 (b) Class growth from 1994 to 2003

Class Name	Area Change (Sq. Km)	Percentage Change (%)
Vegetation cover	-50.14	**-2.98%**
Built up	+1.21	**+76.10%**
Agricultural Land	-3.78	-2.88%
Bare Soil	+52.61	**+23.62%**
Water bodies	+0.05	+11.36%

The period between 1994 and 2003 was characterized by a net degradation of natural and managed land cover. The primary LULC transition observed is the conversion of Vegetation cover into Bare Soil, evidenced by the corresponding loss and gain in these two classes (approx. 50 Km^2 loss vs. 53 Km^2 gain).

Simultaneously, the area shows the early stages of a rapid development cycle, as demonstrated by the over 76% increase in Built-up land. The decline in Agricultural Land further highlights the pressure of development and resource exploitation on the region's productive landscapes. The visual representation of the area changes reinforces this finding as shown in figure 3.4.1.

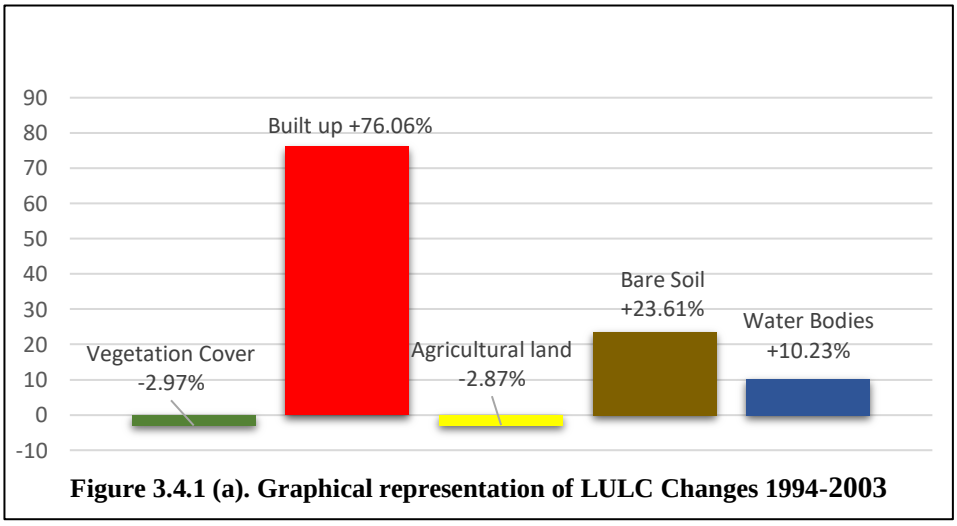

Figure 3.4.1 (a). Graphical representation of LULC Changes 1994-2003

3.4.2. Temporal Change (2003-2014)

The Land Use Land Cover classification changes from 2003 to 2014 shows a period of significant re-vegetation alongside continued urbanization.

Table 3.4.2 (a) Temporal comparison of LULC 2003 and 2021

Class Name	Area in 2003 Km^2	2003 (%)	Area in 2014 Km^2	2014 (%)
Vegetation cover	1633.47	80.08	1739.92	85.30
Built up	2.80	0.14	7.38	0.36
Agricultural Land	127.65	6.26	113.83	5.58
Bare Soil	275.37	13.50	178.27	8.74
Water bodies	0.49	0.02	0.39	0.02

The temporal changes are marked by two key trends: a major increase in vegetative cover and a dramatic expansion of built-up areas, largely at the expense of bare soil and agricultural land.

The following table summarizes the changes in area:

- ✓ **Vegetation cover (+6.52%):** In contrast to the preceding period (1994-2003), vegetation cover showed an absolute gain of 106.45 km^2. This suggests successful land recovery, re-afforestation, or natural succession, likely converting much of the previous bare soil back into vegetation.

- ✓ **Built up (+163.57%):** This class experienced the most explosive percentage growth, more than **doubling its area** from 2.80 $km^2$to 7.38 km^2. This is a clear signal of intense urbanization and development.

- ✓ **Bare Soil (-35.26%):** This class saw the largest absolute decrease, losing 97.10 km^2 (from 275.37 km^2 to 178.27 km^2). This loss closely mirrors the gain in vegetation cover, indicating that the recovery of the vegetative class was primarily due to the conversion of bare land.
- ✓ **Agricultural Land (-10.83%):** A notable loss of 13.82 km^2 (from 127.65 km^2 to 113.83 km^2) suggests a continuous decline in farmed area. This loss is attributed to conversion to built-up areas.

- ✓ **Water bodies (-20.41%):** While the absolute change is small (-0.10 km^2), the high percentage loss indicates a significant reduction in the minor water bodies

in the area, likely due to drying, drainage, or encroachment.

Table 3.4.2. (b) Class growth from 2003 to 2014

Class Name	Area Change (Sq. Km)	Percentage Change (%)
Vegetation cover	+106.45	**+6.52%**
Built up	+4.58	**+163.57%**
Agricultural Land	-13.82	-10.83%
Bare Soil	-97.10	**-35.26%**
Water bodies	-0.10	-20.41%

The 2003–2014 period reflects a dynamic landscape where the major trend of land recovery (Bare Soil to Vegetation cover) coexisted with a strong signal of urban sprawl (dramatic increase in Built up area). The primary land cover change was the re-establishment of vegetation on previously barren land, which is a positive environmental shift. However, this is offset by the exponential growth of built-up area and the continual loss of agricultural land, suggesting ongoing human pressure and development in the study area.

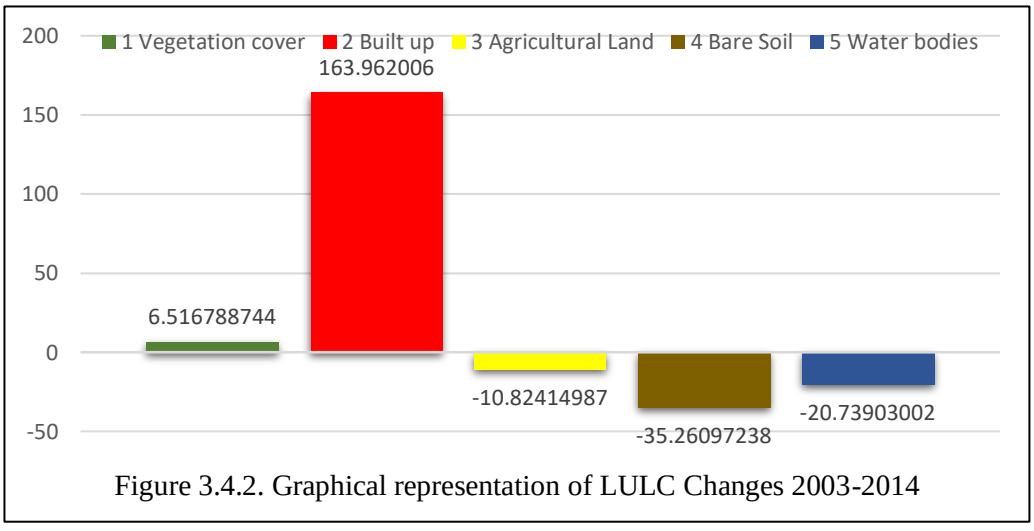

Figure 3.4.2. Graphical representation of LULC Changes 2003-2014

3.4.3 Temporal Change (2014-2021)

The Land Use Land Cover Change in table 3.4.3 (a) from 2014 to 2021 continues to show the concurrent trends of vegetation cover gain and built-up expansion, with a notable emphasis on wetland recovery/expansion.

Table 3.4.3 (a) Temporal comparison of LULC 2014 and 2021

Class Name	Area in 2014 Km^2	2014 (%)	Area in 2021 Km^2	2021 (%)
Vegetation cover	1739.92	**85.30**	1795.56	**88.03**
Built up	7.38	0.36	9.37	0.46
Agricultural Land	113.83	5.58	92.54	4.54
Bare Soil	178.27	8.74	140.59	6.89
Water bodies	0.39	0.02	1.72	**0.08**

The period saw continued gain in vegetation cover class and built-up area, with a particularly dramatic increase in water bodies, all primarily at the expense of agricultural land and bare soil.

The following summarizes the changes in area:

- ✓ **Vegetation cover (+3.20%):** Following the trend from the previous period, vegetation continues to gain ground, adding another 55 Km^2 in the year 2021 when compared to 2014.
- ✓ **Built up (+26.96%):** Although the percentage growth was lower than the previous period's rate (2003-2014 at +163.57%), the built-up area continued its expansion.
- ✓ **Bare Soil (-21.14%):** Bare soil decreased significantly by **37.68** Km^2. This land was likely the primary source for the continued gains in vegetation cover.
- ✓ **Agricultural Land (-18.70%):** This class suffered the largest absolute loss, **losing 21.29** Km^2 and decreasing its total area by almost one-fifth. This decline indicates sustained pressure on farming activities, likely due to conversion to built-up areas or abandonment and subsequent conversion to bare soil or vegetation.
- ✓ **Water bodies (+341.03%):** This class experienced the highest percentage growth, increasing from 0.39 Km^2 to 1.72 Km^2. While the absolute area remains small, this growth suggests the re-emergence, conservation, or expansion of ponds/reservoirs/wetlands, possibly due to policy or high rainfall.

Table 3.4.3 (b) Class growth from 2014 to 2021

Class Name	Area Change (Sq. Km)	Percentage Change (%)
Vegetation cover	+55.64	+3.20%
Built up	+1.99	+26.96%
Agricultural Land	-21.29	**-18.70%**
Bare Soil	-37.68	-21.14%
Water bodies	+1.33	**+341.03%**

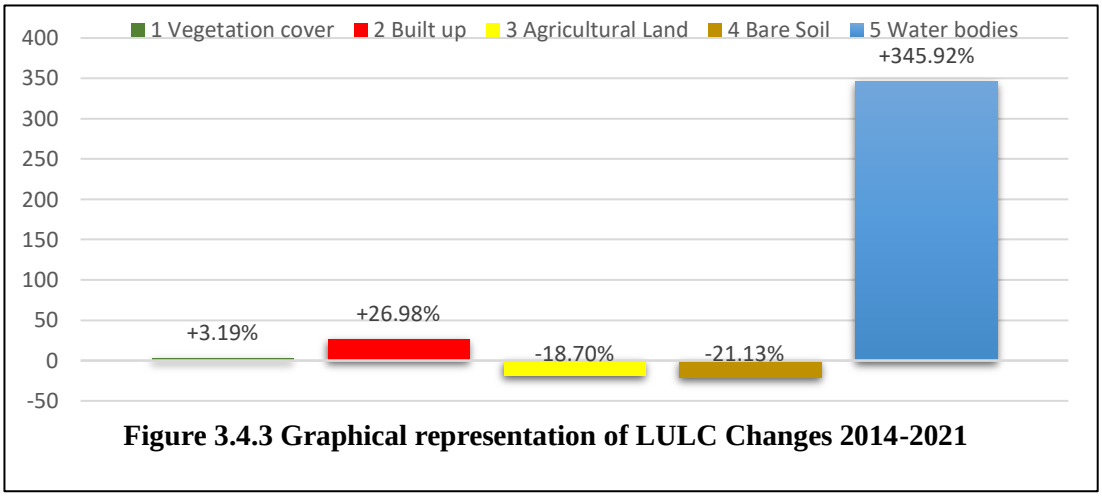

Figure 3.4.3 Graphical representation of LULC Changes 2014-2021

The 2014–2021 period highlights a landscape transitioning with the reduction of Bare Soil and the significant increase in Vegetation cover and Water bodies are strong evidence. There is substantial loss of Agricultural Land and the continued, albeit slower, expansion of the Built-up area underscore ongoing challenges related to food security and urban sprawl. The overall land use pattern changes of 2014 to 2021 as shown in Figure 3.4.3, shows a consolidation of the area's main features: more vegetation, less barren and agricultural land, and more human settlement/infrastructure.

Vegetation cover has grown by approximately 111sq.km from 1683 sq.km accounting about 82% of the total geographic area in the year 1994 to about 1795 sq.km, 88% of the total geographic area in the year 2021. The increment can be attributed to the regeneration of previously cleared forest which has now been covered with vegetation

after having it left barren for the period of time. The decreasing trend of shifting cultivation practices in the district has also reduced the clearing of vegetative cover thus directly increasing the area under vegetative cover in the total geographic area of the district.

3.5 Land use Land cover Class Transition.

3.5.1 Class Transition (1994-2003)

Table 3.5.1 shows the land use/land cover class transitions between 1994 and 2003. The most significant change was the decrease in vegetation cover and a corresponding increase in bare soil.

The net changes for each land use class:

- Vegetation Cover experienced a significant decrease, with a net loss of approximately 58.34 km^2.
- Bare Soil showed the largest increase, with a net gain of around 59.59 km^2.
- Agricultural-Land had a net loss of approximately 2.18 km^2.
- Built-up increased by about 1.42 km^2.
- Water Bodies showed a very slight net loss of 0.01 km^2.

The most prominent conversions between land use classes were:

- Vegetation Cover to Bare Soil: with an area of 153.08 km^2.
- A significant amount of Bare Soil was converted to Vegetation Cover, with an area of 104.17 km^2.
- A notable area of 67.05 km^2 transitioned from Vegetation Cover to Agricultural Land.
- There was also a substantial conversion of Agricultural Land to Vegetation Cover, with an area of 57.83 km^2.
- The transition from Agricultural Land to Bare Soil was also significant, with an area of 35.37 km^2.

In summary, the period between 1994 and 2003 was characterized by a notable loss of vegetation, primarily converting to bare soil. While there was some regeneration of vegetation from bare soil and agricultural land, it was not enough to offset the overall

loss. Urbanization, represented by the increase in built-up land, was also a contributing factor to the changing landscape, although to a lesser extent than the changes between vegetation and bare soil.

Table.3.5.1 Land use/land cover Class Transition 1994-2003 (km^2)

Class Change	1994-2003
AGRICULTURAL LAND-AGRICULTURAL LAND	33.56
BARE SOIL-AGRICULTURAL LAND	24.23
BUILT UP-AGRICULTURAL LAND	0.67
VEGETATION COVER-AGRICULTURAL LAND	67.05
WATER BODIES-AGRICULTURAL LAND	0.04
AGRICULTURAL LAND-BARE SOIL	35.37
BARE SOIL-BARE SOIL	80.13
BUILT UP-BARE SOIL	0.28
VEGETATION COVER-BARE SOIL	153.08
WATER BODIES-BARE SOIL	0.24
AGRICULTURAL LAND-BUILT-UP	0.97
BARE SOIL-BUILT-UP	0.78
BUILT UP-BUILT-UP	0.30
VEGETATION COVER-BUILT-UP	0.45
WATER BODIES-BUILT-UP	0.01
AGRICULTURAL LAND-VEGETATION COVER	57.83
BARE SOIL-VEGETATION COVER	104.17
BUILT UP-VEGETATION COVER	0.14
VEGETATION COVER-VEGETATION COVER	1478.73
WATER BODIES-VEGETATION COVER	0.10
AGRICULTURAL LAND-WATER BODIES	0.00
BARE SOIL-WATER BODIES	0.20
BUILT UP-WATER BODIES	0.00
VEGETATION COVER-WATER BODIES	0.18
WATER BODIES-WATER BODIES	0.01

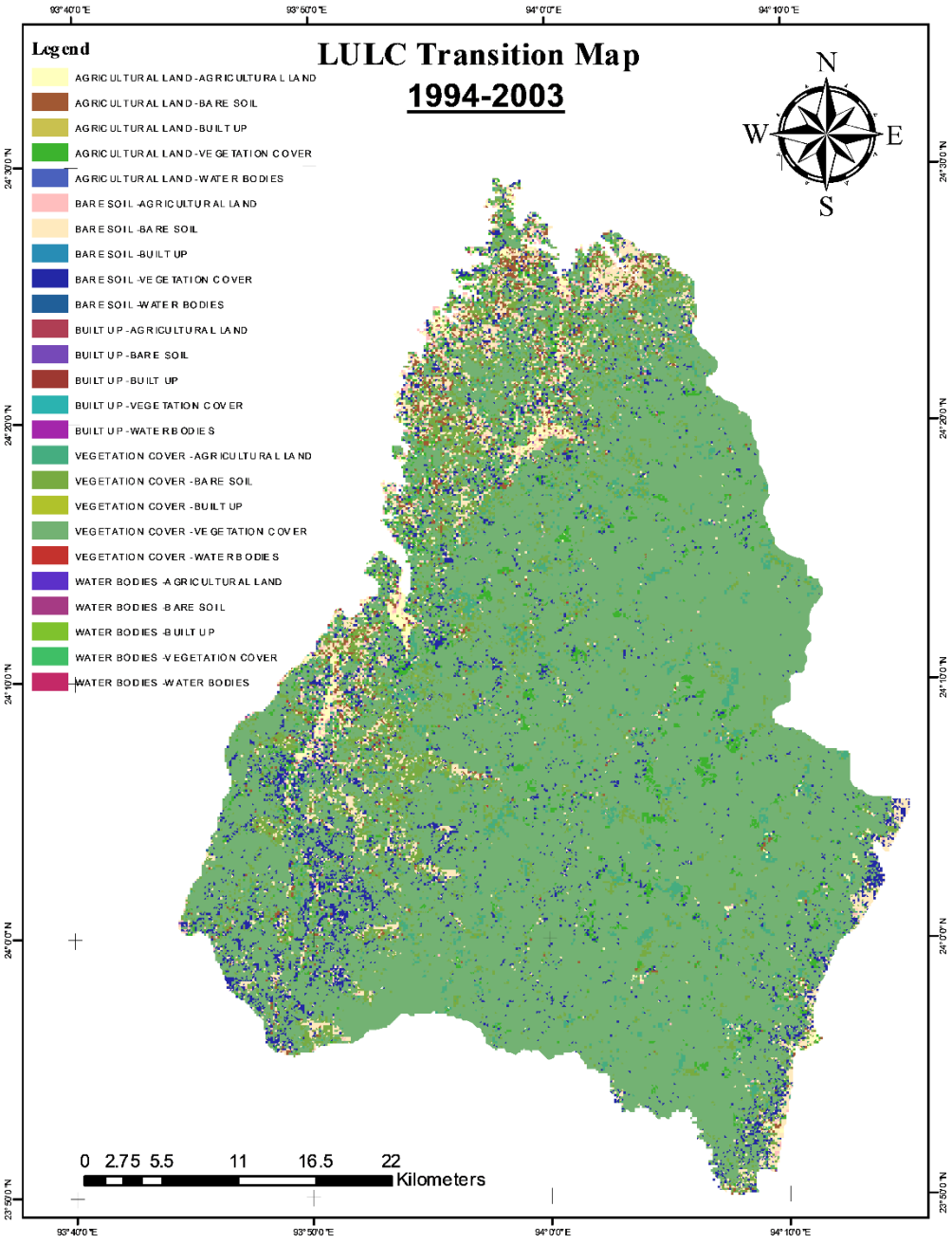

Figure 3.5.1. Land Use Land Cover Class Transition Map 1994-2003

3.5.2 Class Transition (2003-2014)

Table 3.5.2 shows land use/land cover class transitions for the period of 2003-2014, The most notable trend is the significant increase in vegetation cover at the expense of bare soil and agricultural land.

The prominent changes are as follows

- Vegetation Cover experienced a substantial increase, with a net gain of approximately 104.45 km^2.
- Bare Soil on the other hand showed the most significant decrease, with a net loss of around 94.35 km^2.
- Agricultural Land had a considerable net loss of approximately 14.48 km^2.
- Built-up land increased by about 4.41 km^2.
- Water Bodies: Showed a negligible net loss of 0.03 km^2.

The most prominent conversions between land use classes during this period were:

- Bare Soil to Vegetation Cover, with an area of 161.38 km^2.
- A significant area of 73.45 km^2 was converted from Vegetation Cover to Bare Soil.
- A substantial portion of Agricultural Land (67.05 km^2) was converted to Vegetation Cover.
- There was a notable area of 49.08 km^2 which transitioned from Vegetation Cover to Agricultural Land.
- The transition from Bare Soil to Agricultural Land was also significant, with an area of 29.16 km^2.

In summary, the period between 2003 and 2014, there is major interchange between vegetation Cover and Bare Soil. While Bare soil conversion to vegetation cover is at a higher rate with 161.38 km^2 in comparison to vegetation cover transitioning to bare soil at 73.45 km^2. Built up had a net gain of 4.41 km^2. Agricultural experienced net loss with 14.48 km^2. We see the largest loss of 94.35km^2 in Bare soil.

Table 3.5.2 Land use/land cover Class Transition 2003-2014 (km^2)	
Class Change	**2003-2014**
AGRICULTURAL LAND-AGRICULTURAL LAND	32.14
BARE SOIL-AGRICULTURAL LAND	29.16
BUILT UP-AGRICULTURAL LAND	0.86
VEGETATION COVER-AGRICULTURAL LAND	49.08
WATER BODIES-AGRICULTURAL LAND	0.09
AGRICULTURAL LAND-BARE SOIL	24.35
BARE SOIL-BARE SOIL	76.63
BUILT UP-BARE SOIL	0.41
VEGETATION COVER-BARE SOIL	73.45
WATER BODIES-BARE SOIL	0.10
AGRICULTURAL LAND-BUILT-UP	2.25
BARE SOIL-BUILT-UP	1.91
BUILT UP-BUILT-UP	0.76
VEGETATION COVER-BUILT-UP	2.01
WATER BODIES-BUILT-UP	0.00
AGRICULTURAL LAND-VEGETATION COVER	67.05
BARE SOIL-VEGETATION COVER	161.38
BUILT UP-VEGETATION COVER	0.49
VEGETATION COVER-VEGETATION COVER	1516.64
WATER BODIES-VEGETATION COVER	0.16
AGRICULTURAL LAND-WATER BODIES	0.02
BARE SOIL-WATER BODIES	0.21
BUILT UP-WATER BODIES	0.00
VEGETATION COVER-WATER BODIES	0.09
WATER BODIES-WATER BODIES	0.05

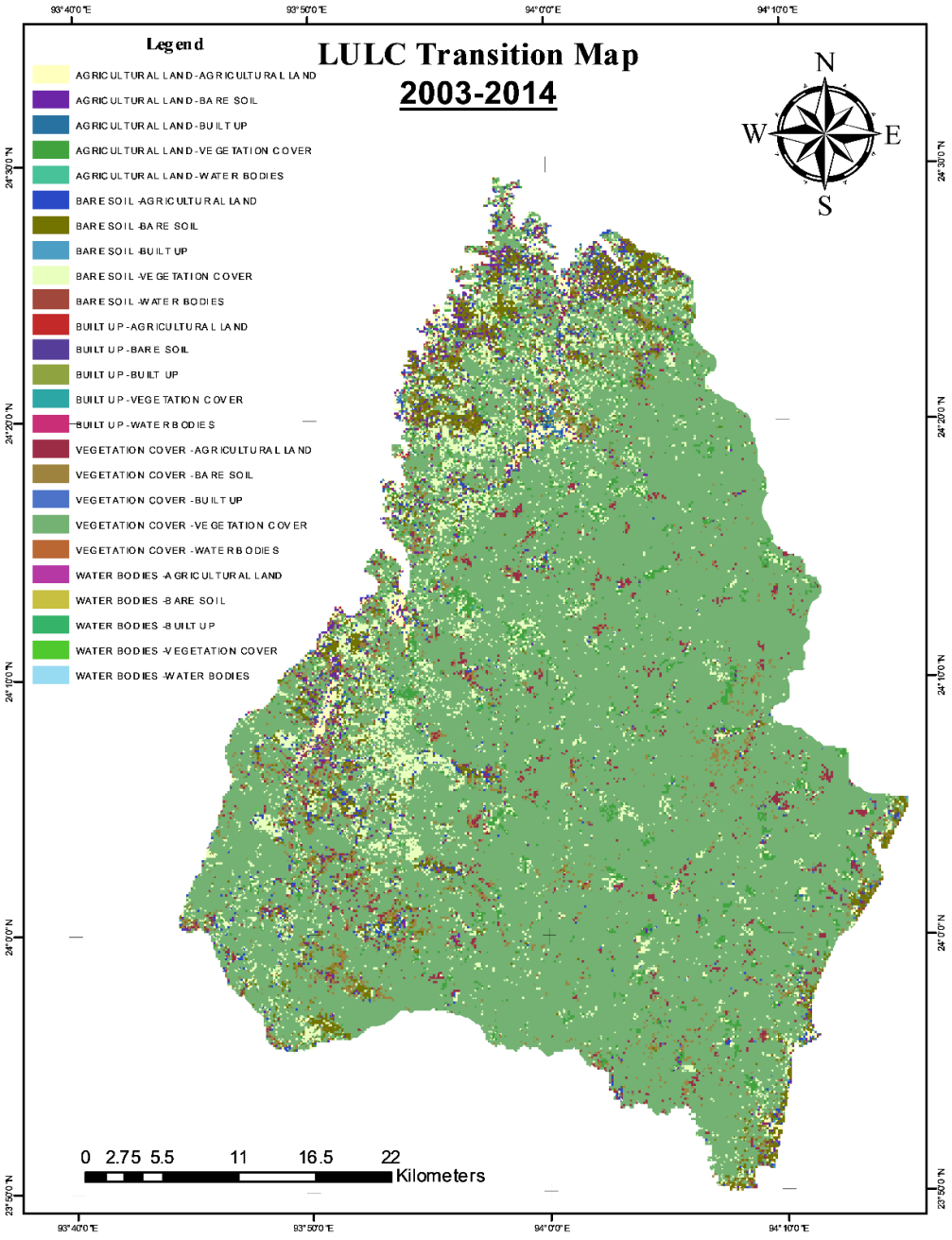

Figure 3.5.2. Land Use Land Cover Class Transition Map 2003-2014

3.5.3 Class Transition (2014-2021)

Table 3.5.3 shows the land use changes for the 2014-2021 period. The trend of increasing vegetation cover at the expense of bare soil and agricultural land continued between 2014 and 2021. Vegetation Cover continued to increase, with a net gain of approximately 57.37 km^2. Whereas, Bare Soil showed a significant decrease, with a net loss of around 37.61 km^2. Agricultural Land also experienced a substantial net loss of approximately 23.00 km^2. Whereas Built-up Land continues its increasing trend by about 2.00 km^2. Water Bodies showed a slight net increase of 1.24 km^2.

The most prominent conversions between land use classes during this period were:

- Bare Soil to Vegetation Cover, with an area of 111.82 km^2.
- A significant area of 67.33 km^2 under Vegetation Cover was converted to Bare Soil.
- A substantial portion of Agricultural Land was converted to Vegetation Cover, with an area of 57.67 km^2.
- There was a notable transition from Vegetation Cover to Agricultural Land, with an area of 44.02 km^2.
- The transition from Agricultural Land to Bare Soil was also significant, with an area of 26.59 km^2.

The analysis indicates that the period 2014–2021 was dominated by a "greening" process: Vegetation Cover was the primary net beneficiary (57.37 km^2), gaining the most area, largely from the conversion of Bare Soil and Agricultural Land. Bare soil experienced the largest net loss (37.61 km^2), as a significant portion was converted into Vegetation Cover. Agricultural land also saw a substantial net reduction, losing to both Vegetation Cover (indicating abandonment or change in land use policy) and Bare Soil (indicating degradation). Whereas Built-up area is expanding, but its net gain is minimal (2.00 units) compared to the changes in the natural and agricultural classes.

Table 3.5.3 Land use/land cover Class Transition 2014-2021 (km^2)	
Class Change	**2014-2021**
AGRICULTURAL LAND-AGRICULTURAL LAND	23.18
BARE SOIL-AGRICULTURAL LAND	19.47
BUILT UP-AGRICULTURAL LAND	1.62
VEGETATION COVER-AGRICULTURAL LAND	44.02
WATER BODIES-AGRICULTURAL LAND	0.02
AGRICULTURAL LAND-BARE SOIL	26.59
BARE SOIL-BARE SOIL	41.86
BUILT UP-BARE SOIL	1.53
VEGETATION COVER-BARE SOIL	67.33
WATER BODIES-BARE SOIL	0.03
AGRICULTURAL LAND-BUILT-UP	3.57
BARE SOIL-BUILT-UP	1.40
BUILT UP-BUILT-UP	2.01
VEGETATION COVER-BUILT-UP	1.94
WATER BODIES-BUILT-UP	0.01
AGRICULTURAL LAND-VEGETATION COVER	57.67
BARE SOIL-VEGETATION COVER	111.82
BUILT UP-VEGETATION COVER	1.67
VEGETATION COVER-VEGETATION COVER	1631.85
WATER BODIES-VEGETATION COVER	0.11
AGRICULTURAL LAND-WATER BODIES	0.30
BARE SOIL-WATER BODIES	0.40
BUILT UP-WATER BODIES	0.10
VEGETATION COVER-WATER BODIES	0.61
WATER BODIES-WATER BODIES	0.19

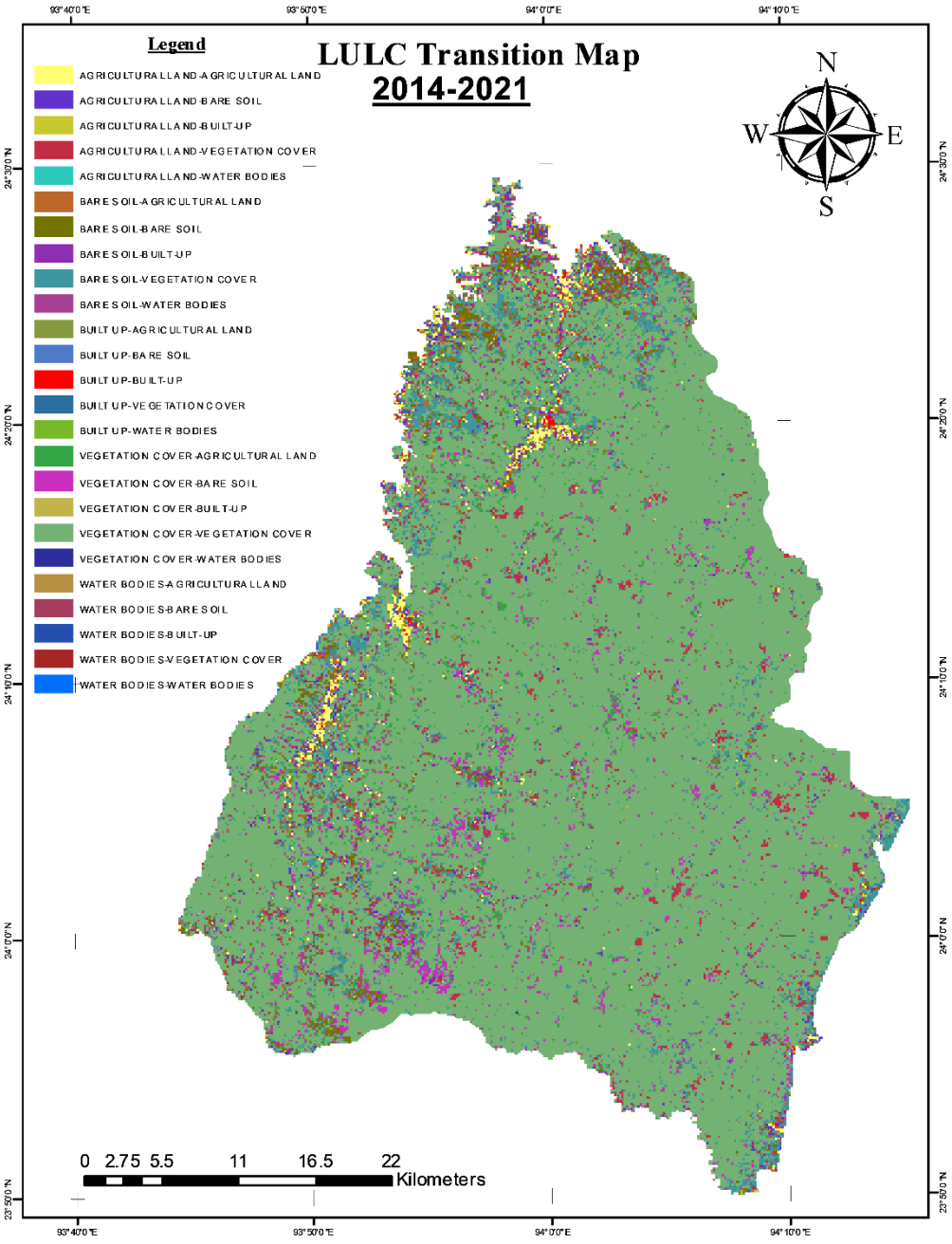

Figure 3.5.3. Land Use Land Cover Class Transition Map 2014-2021

3.6 Implications of LULC Change on Ecosystem and Environment

The LULC analysis reveals two dominant, opposing, and persistent trends across the 27-year period: a significant acceleration of urbanization and a highly dynamic, large-scale interchange between vegetative and bare land, coupled with declining stability in agricultural. The loss of vegetative cover decreased by nearly half from the first period (220.76 km^2) to the second (124.63 km^2) and continued a slight decline in the final period (113.90 km^2). The results also shows that there is a decrease in the area under vegetation initially from the year 1994 to 2003, but we observe an increasing trend for 2003 to 2014 and 2021. This positive growth in the area coverage of vegetation cover is the result of previously barre soil areas converted into scrub forest or the regeneration of vegetation coverage. There is also a steady decline of Jhum Cultivation practices in the district which are usually the main driver of forest clearing.

We can observe a positive growth in the vegetation cover class. However, the quality of the vegetation can further be assessed. The types of vegetation cover could be Dense forest, scrub forest, grassland etc. by further analysis of the type of vegetation cover can give a better comprehensive understanding of the vegetative qualities of the areas under Vegetation cover.

3.6.1 The Urbanization Trend (BUILT UP)

The rate of urbanization accelerated dramatically between the first and second periods, with the net gain increasing by over 3.5 times (1.42 Km^2 to 5.17 Km^2). While the third period saw a slight decrease from the peak, the growth in Built-up area remained substantial at 4.01 Km^2, confirming a sustained, high rate of development in the study area. This net gain in the Built-up area clearly shows an accelerating and permanent trend. The stability of the built-up class (area retained) also saw the highest relative increase, growing from 0.30 km^2 to 2.01 km^2, underscoring the irreversible nature of development.

3.6.2 Ecosystem Dynamics

The dynamic exchange between Bare soil and Vegetation cover is a persistent and dominant feature across all three periods. This suggests significant areas are undergoing cycles of deforestation/degradation, which is attributed to the clearing of forest cover for Jhum cultivation (vegetation cover to bare soil), followed by natural succession or active re-vegetation (Bare soil to Vegetation cover). While the total Vegetation cover loss slowed down, the most significant shift over the entire period is the marked acceleration of urbanization and a destabilization of Bare soil and Agricultural land to feed both new vegetative growth and urban expansion.

3.6.3 Vulnerability of Agricultural and Bare Lands

The Agricultural land and Bare soil classes show the greatest long-term vulnerability. Stability in both classes decreased significantly, especially in the final period (Bare soil stability dropped from 80.13 km^2 to 41.86 km^2), confirming these areas serve as the primary source for conversion to other classes, including Vegetation cover and Built-up. Agricultural Pressure: The sustained transition of Vegetation cover to Agricultural land and Vice vera (both around 50-70 km^2) highlights persistent pressure on farming lands, which are both reclaimed from and lost to natural cover.

In conclusion, the study area is characterized by an established and growing urban core fed primarily by the conversion of dynamic lands, while the vast majority of the landscape is dominated by a major, albeit contained, ecological flux between vegetative and bare status.

Chapter 4.
Eco-environmental vulnerability and Disturbance Determinants.

4.1 Introduction

Eco-Environmental Vulnerability (EEV) is a critical concept in environmental science and sustainability, reflecting the degree to which an eco-environmental system—encompassing both natural ecosystems and their interplay with human societies—is susceptible to harm from environmental stressors and the capacity of that system to cope and recover. Understanding and managing Eco-environmental Vulnerability is paramount for regional ecological security and sustainable development (Cao *et al*., 2022). Eco-environmental Vulnerability is fundamentally a function of three interconnected components, as widely adopted in vulnerability assessments (Turner *et al.*, 2003; IPCC, 2023):

1. Exposure: The degree to which a system is subjected to a specific environmental stressor (e.g., climate change, pollution, or resource depletion). For instance, Forest areas have high exposure resource exploitation.
2. Sensitivity: The degree to which an eco-environmental system is affected by an external stressor. This is determined by the inherent characteristics of the system. For example, a monoculture-based agricultural region is highly sensitive to drought or a single crop disease, compared to a diverse ecosystem.
3. Adaptive Capacity: The ability of a system to adjust to change, moderate potential damage, take advantage of opportunities, or cope with consequences. High biodiversity, strong institutional support, and diverse economic structures generally contribute to higher adaptive capacity (Adger *et al*., 2003).

4.2 Ecological Disturbance Determinants

An ecological disturbance is any relatively discrete event in time that disrupts ecosystem, community, or population structure and changes resources, substrate availability, or the physical environment (White & Pickett, 1985). Disturbance is a fundamental ecological concept, shaping succession, diversity, and patch dynamics.

Major Drivers of Eco-Environmental Vulnerability The factors driving EEV are numerous and often act synergistically, categorized into natural and anthropogenic forces (Wang *et al.,* 2008).

1. Natural Drivers
    a. Hydro-Meteorological Extremes: Increased frequency and intensity of events like droughts, floods, heatwaves, and tropical cyclones due to climate change.
    b. Topographical and Geological Factors: Steep slopes, high altitudes, or low-lying coastal plains inherently affect a region's susceptibility to hazards like landslides, erosion, or inundation.
    c. Climate Variability: Long-term shifts in temperature and precipitation patterns that stress ecosystems beyond their natural tolerance limits.
2. Anthropogenic Drivers
    a. Intense Human Activity and Land-Use Change: Urbanization, industrial expansion, and large-scale agricultural practices often lead to habitat fragmentation, ecosystem degradation, and loss of biodiversity (Bai *et al.*, 2016).
    b. Pollution and Resource Over-exploitation: The discharge of industrial and agricultural pollutants degrades water and soil quality, while the over-extraction of water and timber depletes natural capital, reducing system resilience.

3. Socio-Economic Factors: Poverty, inequality, weak governance, and limited access to information or technology can severely restrict the adaptive capacity of human communities, intensifying overall Eco-environmental Vulnerability (Kelly & Adger, 2000).

4.2.1 Assessment Methodologies

Assessing Eco-environmental Vulnerability is crucial for identifying high-risk areas, prioritizing interventions, and informing policy. Methodologies generally combine quantitative and qualitative approaches, often utilizing Geographic Information Systems (GIS) and remote sensing (RS) data for spatial analysis (Kamran & Yamamoto, 2023).

4.2.1.1 Indicator-Based Composite Index Method

This is the most common approach, involving the following steps: Indicator System Construction: Selecting a set of indicators that represent Exposure, Sensitivity, and Adaptive Capacity (e.g., Normalized Difference Vegetation Index (NDVI), land surface temperature, population density, Gross Domestic Product (GDP)).

1. Weighting Methods

   Assigning relative importance to each indicator using techniques like the Analytic Hierarchy Process (AHP) (a subjective weighting method) or the Entropy Weight Method (EWM) (an objective weighting method) (Zhang *et al*., 2018).
2. Vulnerability Index Calculation

   Aggregating the weighted indicators into a single composite EEV index to classify regions into vulnerability levels (e.g., extremely fragile, moderately vulnerable).

4.2.1.2 Conceptual Models

1. Pressure-State-Response (PSR) Model:
   While a general framework for environmental reporting, it can be adapted to assess vulnerability by linking Pressures (drivers like pollution), the resulting State (vulnerability level), and Response (adaptation/mitigation strategies).
2. Sensitivity-Recovery-Pressure (SRP) Model
   Explicitly focuses on the ecosystem's internal structure and function (Sensitivity), the ability to restore itself (Recovery), and the external impact (Pressure) (Li *et al*., 2009).
3. Advanced Statistical Techniques
   Methods like Principal Component Analysis (PCA), Fuzzy Comprehensive Evaluation, and Geographical Detector Models are employed to simplify complex datasets, handle uncertainty, and analyse the spatiotemporal variations and driving forces of Eco-environmental Vulnerability (Huang *et al.*, 2003; Park *et al*., 2019).

4.2.1.3 Mitigation and Adaptation Strategies

Addressing Eco-Environmental Vulnerability requires integrated strategies that reduce stressors (mitigation) and enhance the system's ability to cope with unavoidable changes (adaptation) (Fussel & Klein, 2002).

- **Mitigation Strategies (Reducing Exposure and Pressure) Greenhouse Gas (GHG) Reduction**: Transitioning to renewable energy sources and increasing energy efficiency to combat the root cause of climate-driven vulnerability (IPCC, 2023).
- **Pollution Control:** Implementing strict environmental regulations, promoting cleaner production technologies, and managing waste to reduce environmental stress.

- **Sustainable Resource Management:** Adopting sustainable forestry, fisheries, and agricultural practices to prevent over-exploitation and habitat degradation.
- **Adaptation Strategies (Reducing Sensitivity and Increasing Adaptive Capacity) Ecosystem-based Adaptation (EbA):** Utilizing biodiversity and ecosystem services to help communities adapt. Examples include restoring wetlands to buffer coastal areas against storm surges and planting trees for urban cooling and water management (WRI, 2024).
- **Infrastructure Resilience:** Building stronger, climate-resilient physical infrastructure (e.g., elevated roads, improved drainage systems).
- **Policy and Planning:** Integrating vulnerability assessments into land-use planning and establishing early warning systems for natural hazards.
- **Socio-economic Capacity Building:** Investing in education, healthcare, social safety nets, and local governance to strengthen the adaptive capacity of vulnerable populations (Adger *et al.*, 2003).

Eco-Environmental Vulnerability represents a core challenge for achieving global sustainability. It is a complex, dynamic state arising from the interaction of exposure to stressors, inherent system sensitivity, and the capacity to adapt. Effective management necessitates a holistic approach that leverages rigorous, spatial-temporal assessment methods to identify priority areas and implements integrated mitigation and adaptation strategies that enhance ecological resilience and human well-being.

4.3 Normalised Difference Vegetation Index (NDVI)

Normalised Difference Vegetation Index (NDVI) is a Standardized Metric for Quantifying Vegetation Health. The Normalised Difference Vegetation Index stands as the most widely adopted and enduring spectral index in the field of remote sensing for monitoring and quantifying the density, health, and changes in vegetation cover. Its utility stems from exploiting the unique interaction of healthy vegetation with specific wavelengths of light, providing a standardized, dimensionless indicator of photosynthetic activity (NASA Earth Observatory, 2000).

4.3.1 Conceptual and Mathematical Foundation

I. A. The Principle of Spectral Reflectance: NDVI is based on the distinct spectral signature of healthy, photosynthesizing plants: Red Light (RED): The chlorophyll in healthy leaves strongly absorbs light in the visible red region of the electromagnetic spectrum (0.63 to 0.68 m) for use in photosynthesis. Consequently, healthy vegetation exhibits low reflectance in this band. Near-Infrared Light (NIR): The internal cellular structure of healthy leaves strongly reflects light in the near-infrared. This is a defence mechanism to prevent overheating. Consequently, healthy vegetation exhibits high reflectance in this band.

NDVI is calculated as a ratio that normalizes the difference between NIR and RED reflectance values, minimizing the influence of atmospheric conditions, sun angle, and topography (Huete *et al.,* 1994):

$$\boldsymbol{NDVI = \frac{NIR - RED}{NIR + RED}}$$

Where, NIR is the reflectance measured in the Near-Infrared band. RED is the reflectance measured in the Red (visible) band. The normalization ensures that NDVI values always range from -1.0 to +1.0.

4.3.2 Applications of NDVI

The simplicity and effectiveness of NDVI have made it an invaluable tool across numerous disciplines (Pettorelli *et al*., 2005):

- Agriculture and Precision Farming: Crop Health Monitoring: Identifying areas of stress (e.g., nutrient deficiency, disease, or pests) often weeks before they are visible to the human eye.
- Yield Prediction and Biomass Estimation: Quantifying the amount of green biomass and potential harvest yields.
- Variable Rate Application: Creating field maps to guide the precise, variable application of fertilizers, pesticides, and irrigation.
- Ecology and Forestry: Drought Monitoring: Tracking anomalies in vegetation vigor as an indicator of drought onset and severity.
- Land Cover Classification: Mapping vegetation type, density, and boundary changes over time.
- Phenology Studies: Monitoring the seasonal cycles of vegetation (e.g., onset and end of the growing season) for climate change impact research.
- Disaster Management: Quickly mapping the extent and severity of burned areas where vegetation has been destroyed (NDVI approaches zero).
- Flood Impact: Identifying flood-damaged areas by sharp drops in NDVI post-event.

4.3.3 Limitations and Alternatives

Despite its widespread use, NDVI has several acknowledged limitations that have spurred the development of alternative vegetation indices:

- Saturation in Dense Vegetation: In areas of very dense, multi-layered canopy (e.g., mature forests), the RED signal is completely absorbed, and the NDVI value tends to plateau near its maximum (approaching +1.0). This limits its ability to differentiate between variations in biomass above a certain threshold (Mutanga and Skidmore, 2004).
- Soil Background Influence: In areas with sparse vegetation, the reflectance signal is significantly influenced by the brightness and colour of the exposed soil.
- Atmospheric Noise: Clouds, haze, and water vapor can scatter and absorb light, altering the measured reflectance values and introducing noise into the NDVI product.

The Normalised Difference Vegetation Index is a simple yet powerful quantitative tool that has revolutionized the fields of ecology, agriculture, and land management. By mathematically exploiting the differential absorption and reflection of light by chlorophyll and leaf structure, it provides a consistent, global measure of vegetation health. While limitations exist, the NDVI remains the benchmark for monitoring Earth's biological productivity and its evolution in response to climatic and anthropogenic pressures.

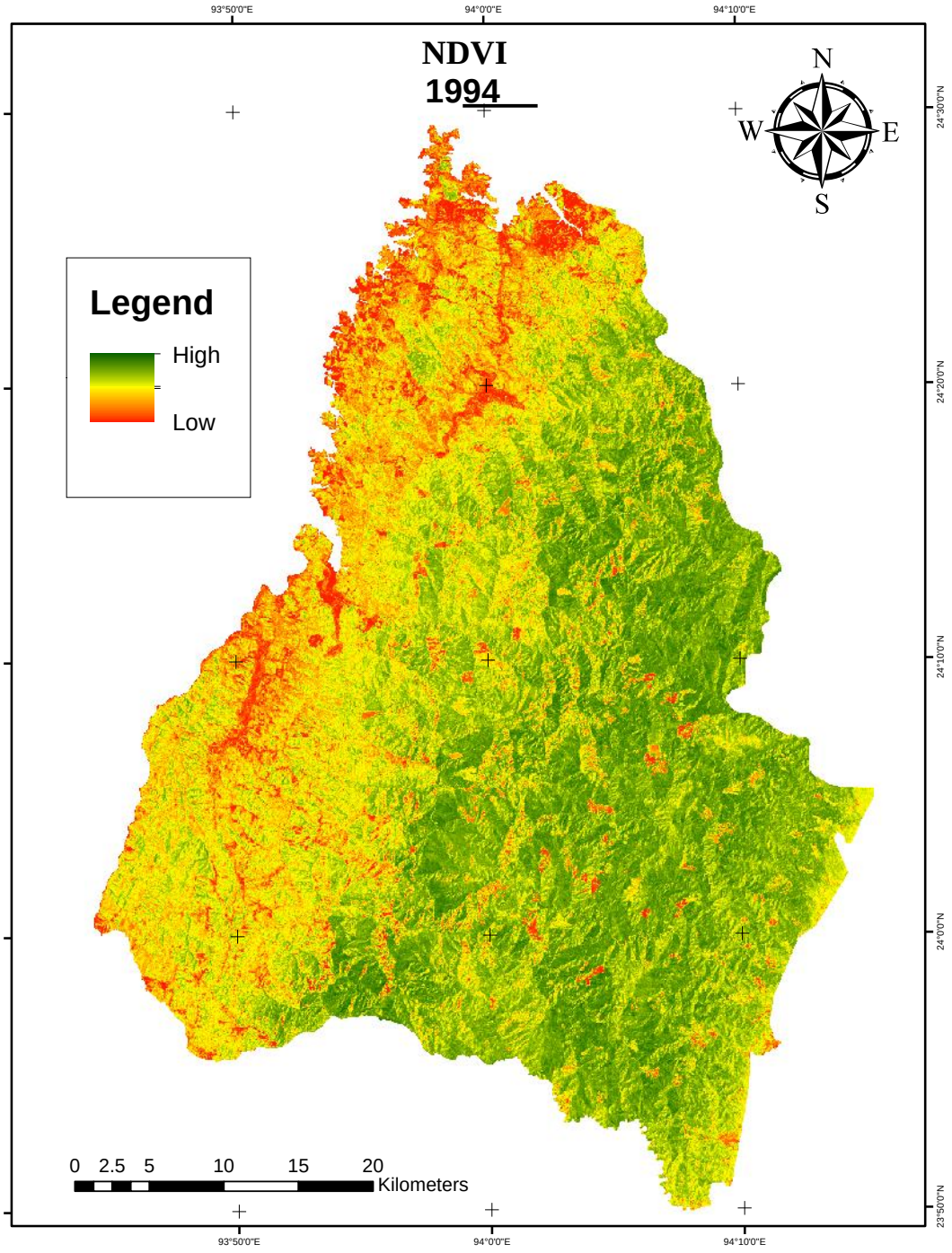

Figure 4.3 (a) NDVI Map 1994

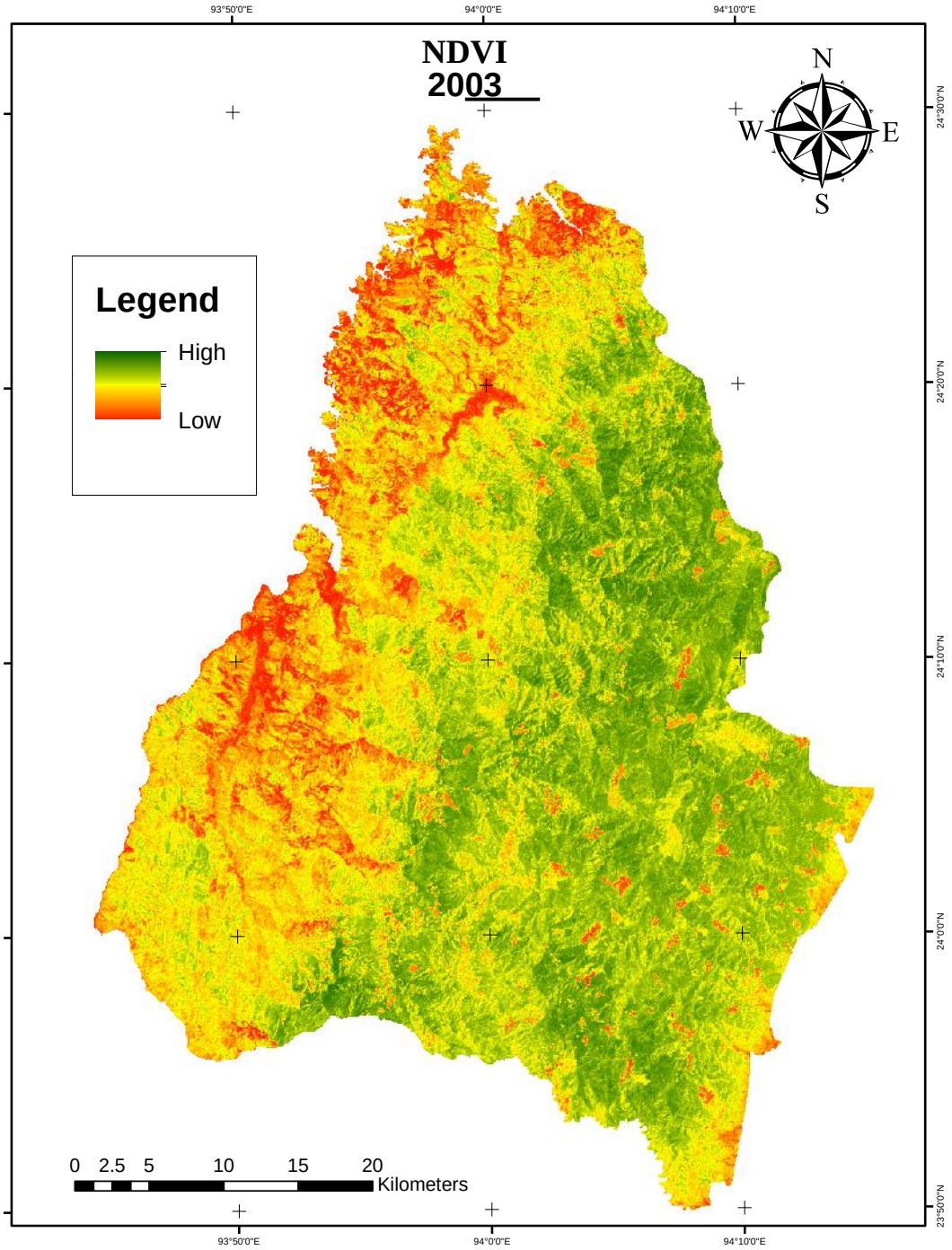

Figure 4.3 (b) NDVI Map 2003

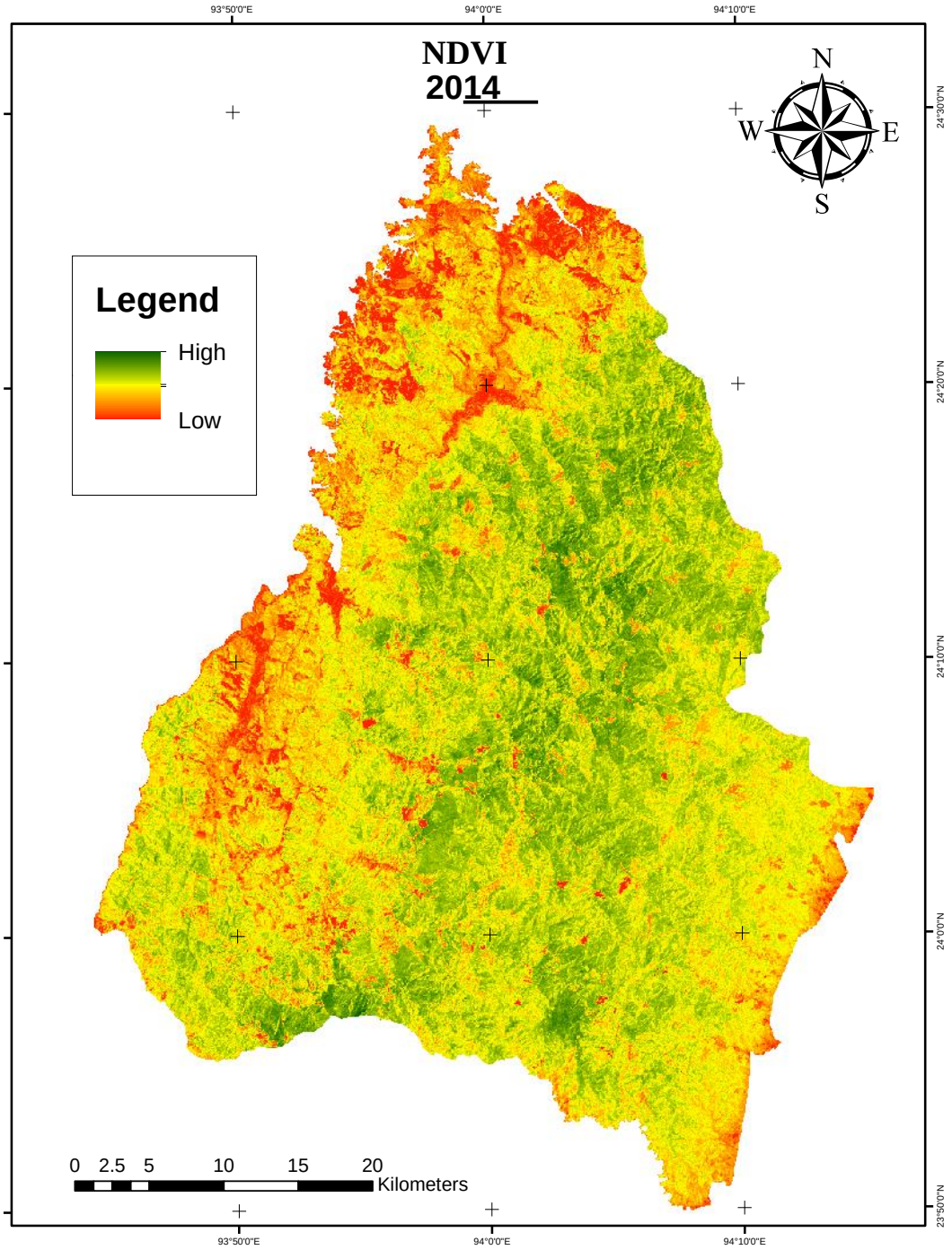

Figure 4.3 (c) NDVI Map 2014

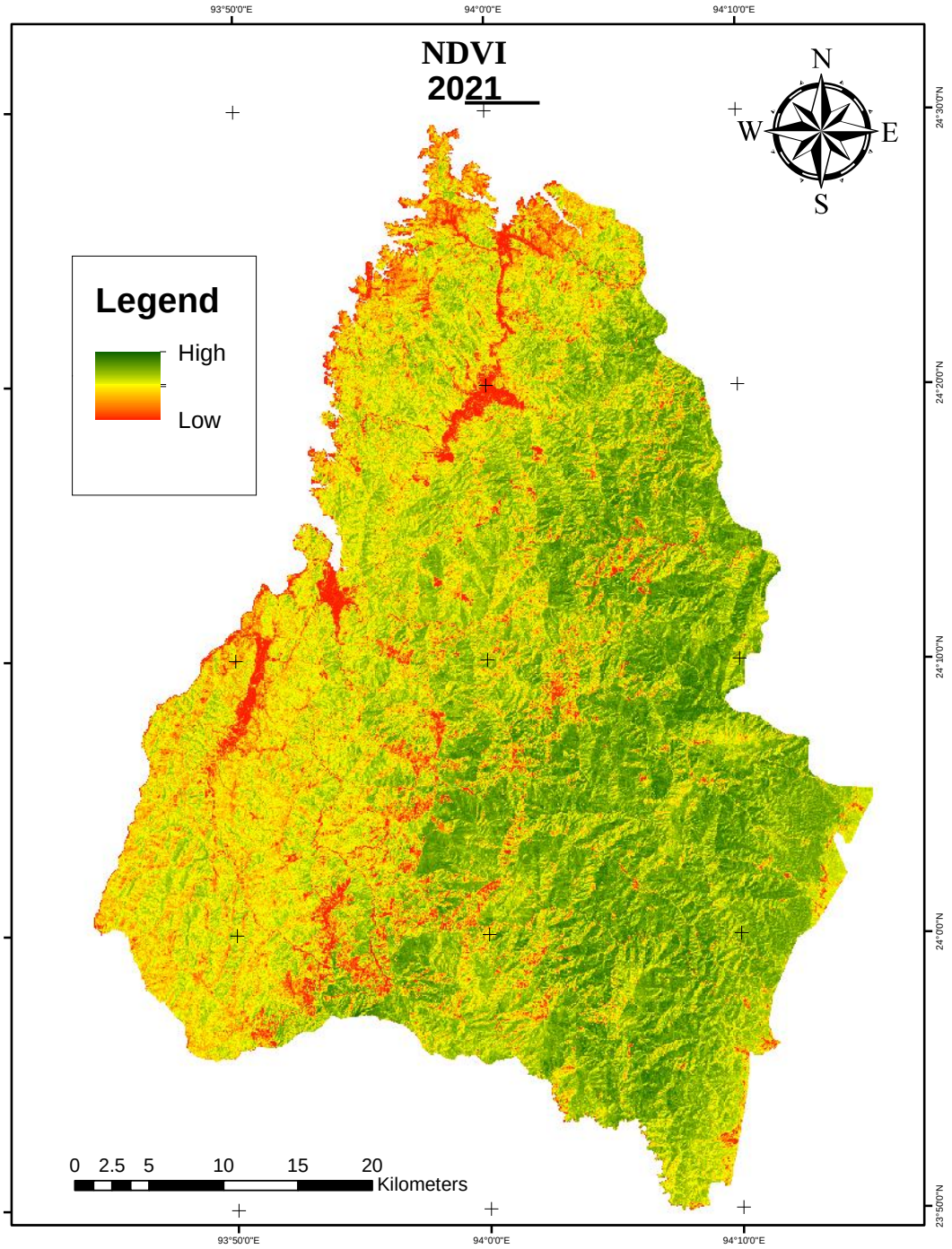

Figure 4.3 (d) NDVI Map 2021

4.3.4 Vegetation Quality

The study area moved from an already strong vegetation state (nearly 70% Dense in 1994) to one where nearly 89% of the area is classified as Dense Vegetation in 2021, primarily at the expense of the Moderate Vegetation class. Period-by-Period Analysis

Table 4.3.4 Vegetation quality NDVI

Classes	1994		2003		2014		2021	
	Area Km2	%	Area Km2	%	Area Km2	%	Area Km2	%
Non-Vegetated	0.0918	0	0.0144	0	0.0612	0	0.1422	0.01
Bare Soil	1.3239	0.06	1.3122	0.06	2.8656	0.14	0.3141	0.02
Sparse vegetation	93.7737	4.6	164.8989	8.08	119.3958	5.85	20.8638	1.02
Moderate Vegetation	526.9563	25.83	758.709	37.19	954.6417	46.8	211.5603	10.37
Dense Vegetation	1417.723	69.5	1114.934	54.66	962.9046	47.2	1806.989	88.58

- 1994 to 2014: two decades between 1994 and 2014 show a deterioration in vegetation quality, with a downward shift in the distribution: Dense Vegetation experienced continuous loss: 1994 (1417.72 km^2) ^{to} 2003 (1114.93 km^2) 2003 (1114.93km^2) to 2014 (962.90 km^2). The total area lost from this class was over 450 km2 by 2014. Moderate Vegetation and Sparse Vegetation significantly increased, absorbing the lost area. Moderate Vegetation grew from 25.83% in 1994 to a peak of 46.80% in 2014. Sparse Vegetation also peaked in 2003 at 8.08% before decreasing. The Bare Soil class peaked in 2014 (0.14%), indicating maximum exposure or degradation during that year. This phase suggests deforestation, degradation, or other environmental pressures that reduced large areas of high-quality vegetation to moderate status.

- 2014 to 2021: The final seven-year period saw an unprecedented and widespread reversal of the previous trend, resulting in a dramatic ecological improvement: Dense Vegetation soared from 962.90 km^2 (47.2% in 2014) to 1806.99 km^2 (88.58% in 2021). This represents a gain of over 844 km^2. This massive gain was fuelled by areas transitioning out of lower classes: Moderate Vegetation saw its area drop by over 743 km^2. Sparse Vegetation area dropped by nearly 99 km^2. The area under Bare Soil and Sparse Vegetation was reduced to their lowest or near-lowest recorded levels, indicating minimal degradation and high overall vegetation cover.

The study area experienced two distinct phases: Degradation (1994–2014): A long-term decline where nearly half of the dense vegetation cover was degraded into moderate or sparse classes. During the period of 2014–2021, a rapid and intense reversal, where the area of dense vegetation rebounded, making the district's overall vegetation quality in 2021 significantly better than it was even in 1994. The shift is so pronounced that by 2021, the entire district is overwhelmingly dominated by Dense Vegetation.

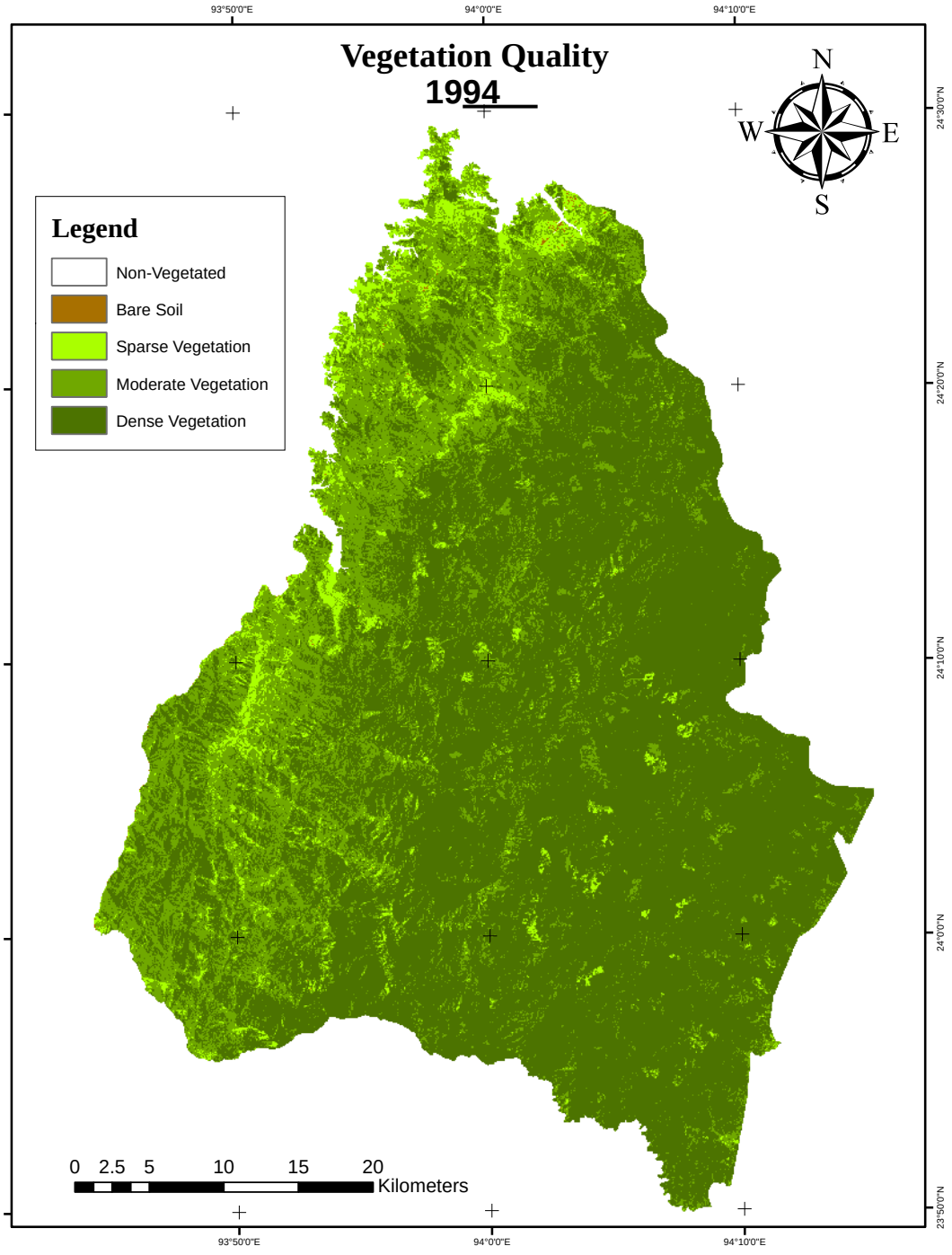

Figure 4.3.4 (a) NDVI Map 1994

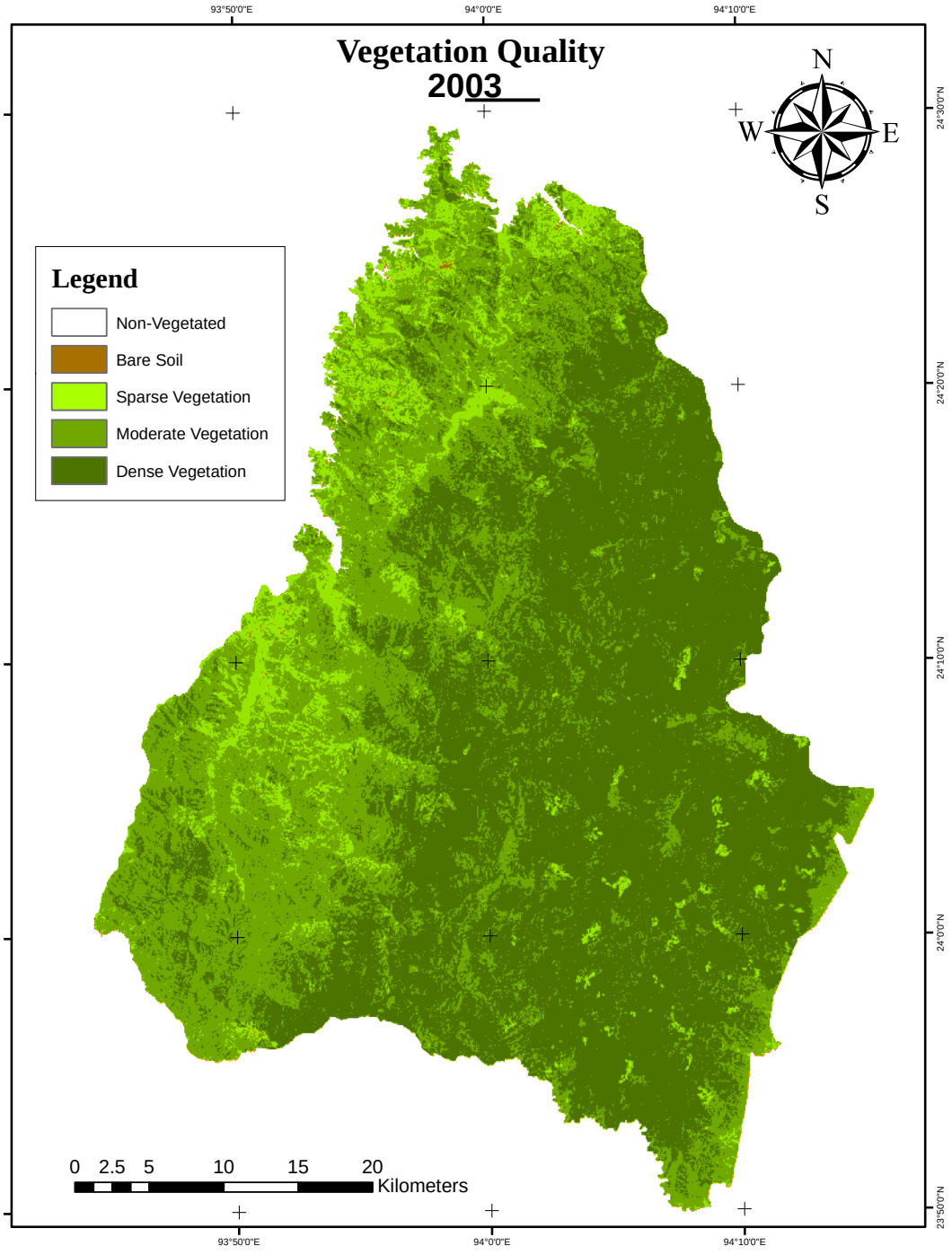

Figure 4.3.4 (b) NDVI Map 2003

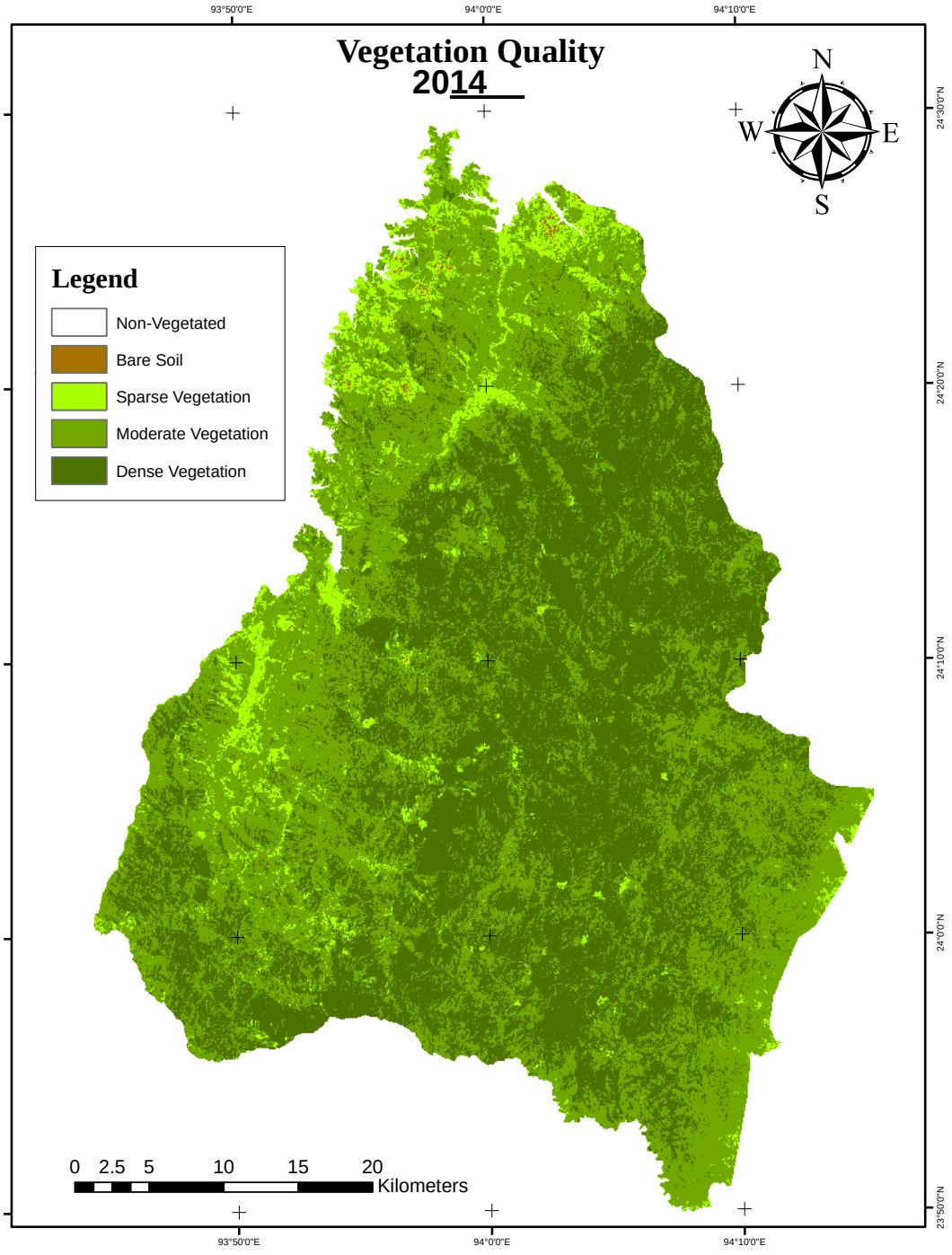

Figure 4.3.4 (c) NDVI Map 2014

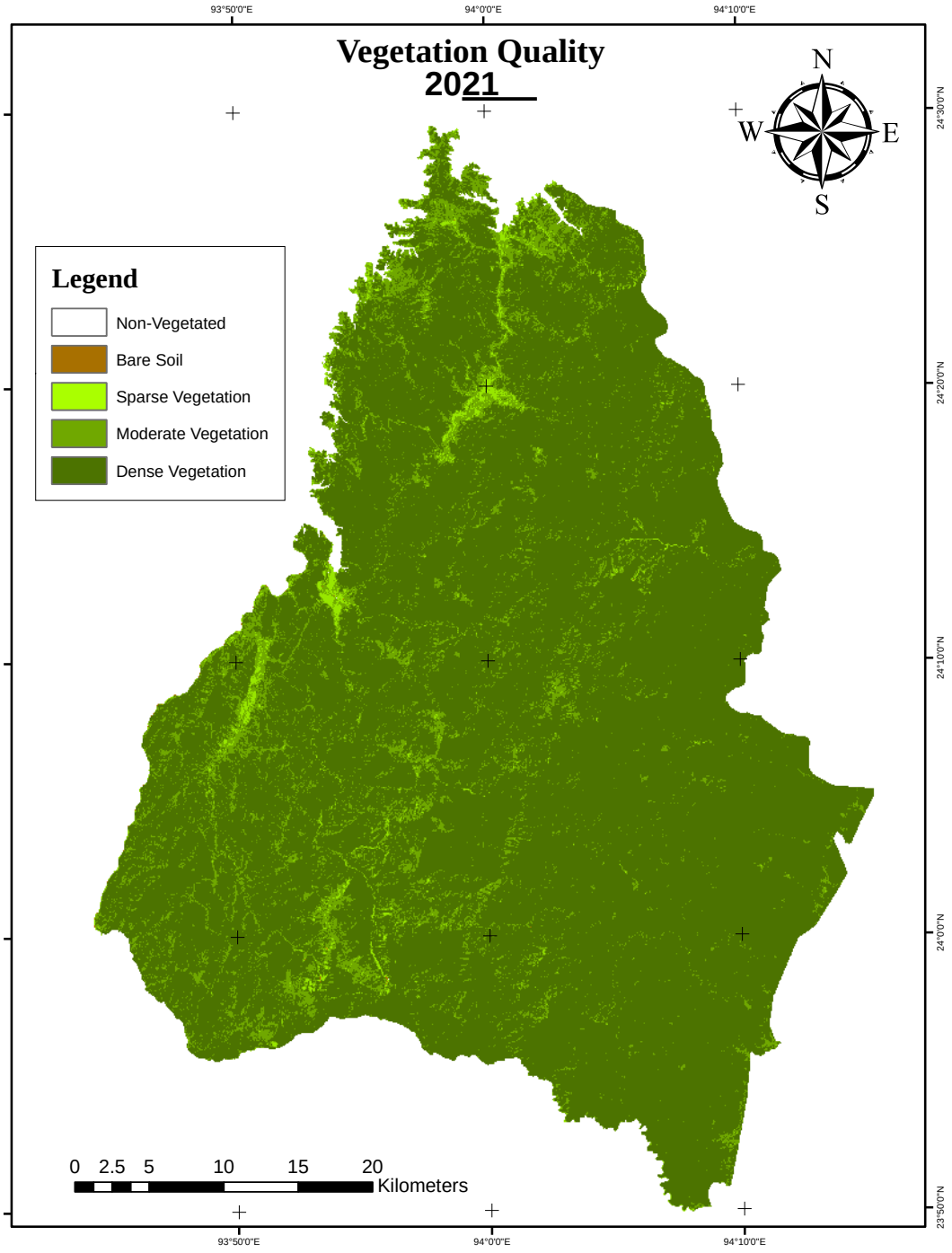

Figure 4.3.4 (d) NDVI Map 2021

4.4 Land Surface Temperature

Land Surface Temperature (LST) is a key part of climate and biology that affects organisms and ecosystems on all levels, from local to global. NASA and other international groups have called this one of the most important Earth System Data Records (King *et al*., 1999). Land Surface Temperature refers to the temperature of the Earth's surface as measured by remote sensing techniques, primarily satellites equipped with thermal infrared sensors. Unlike air temperature, LST captures how hot the land "feels" to touch, representing an immediate indicator of thermal energy interactions between the land and the atmosphere. LST data are fundamental for global energy balance studies, climate change modelling, and ecological assessments.

The common method of obtaining LST from Landsat datasets includes the conversion of digital numbers (DNs) of the thermal band, which is band 6 in Landsat TM and band 10 and band 11 in Landsat OLI, into at-satellite spectral radiance values (L_λ) as follows:

$$L = gian \times DN + bias$$

$$T = K_2 / \ln(K_1/L + 1)$$

$$LST = T / [1 + (\lambda T/\rho) \ln \varepsilon]$$

Where L is the radiance value of Landsat 5 TM infrared band and Landsat 8 OLI thermal band 10, and DN is the pixel value of the band, gain is the gain value, bias is the offset value of the thermal infrared band. T is the temperature, and K1 and K2 are the calibration parameter. K_1=607.76 W/ (m^2.sr.µm) and k_2=1,260.56 K in Landsat 5 TM and K_1=774.89 W/ (m^2.sr.µm) and K_2=1,31.108 K in Landsat 8 OLI, λ is the wavelength of the thermal band, ρ= 1.438 × 10^{-2} m K, and ε is the surface specific emissivity.

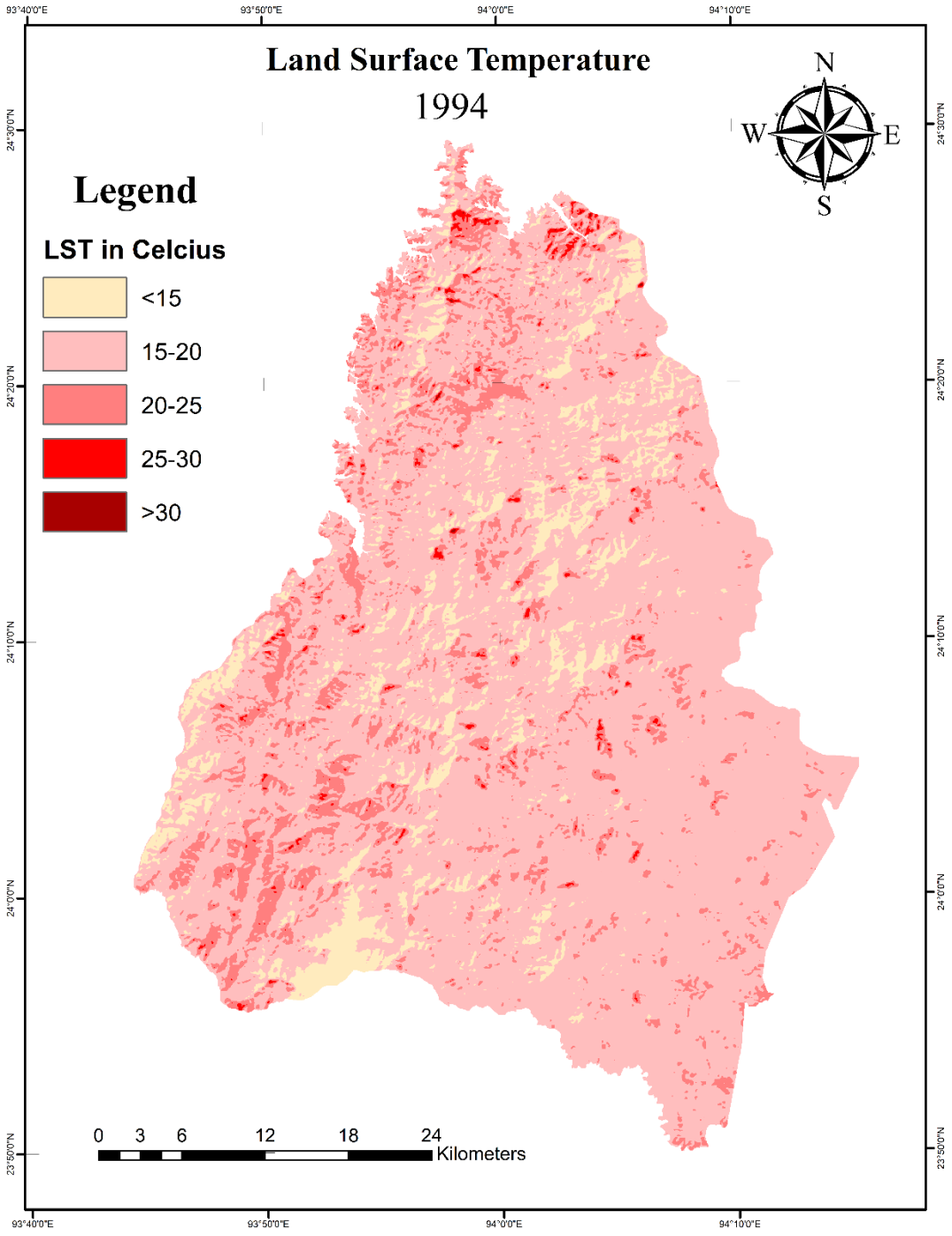

Figure 4.4 (a) Land Surface Temperature Map of 1994

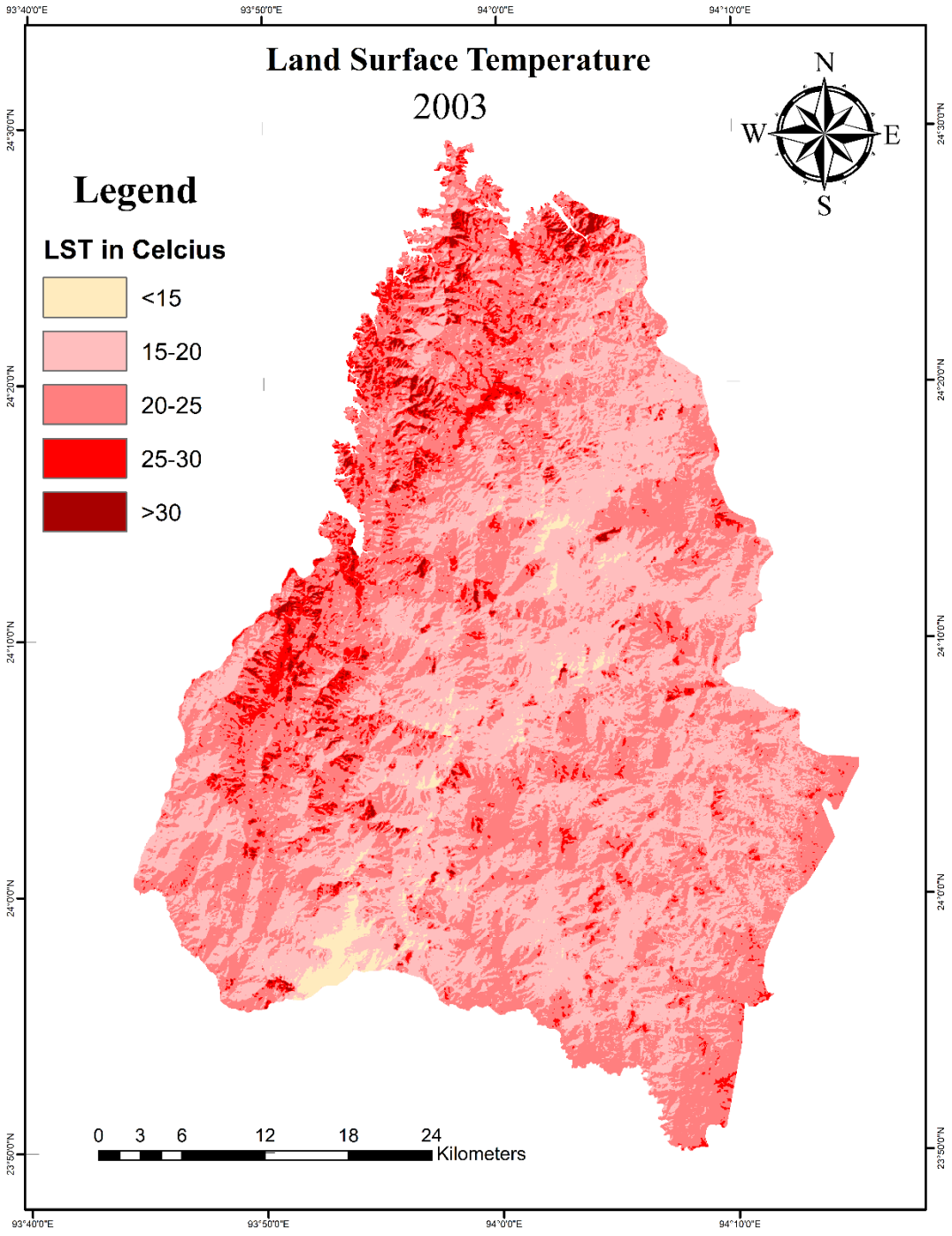

Figure 4.4 (b) Land Surface Temperature Map of 2003

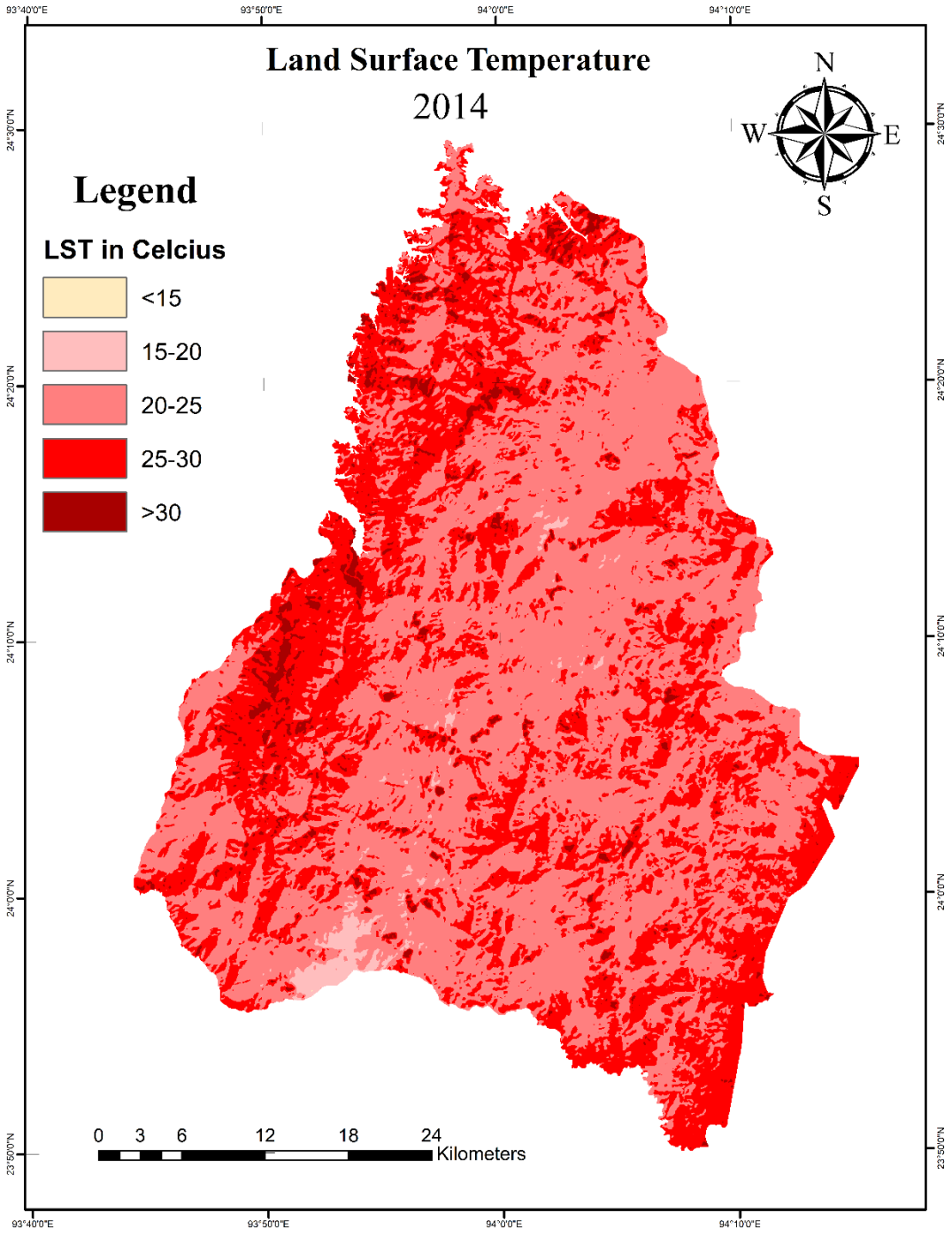

Figure 4.4 (c) Land Surface Temperature of Map 2014

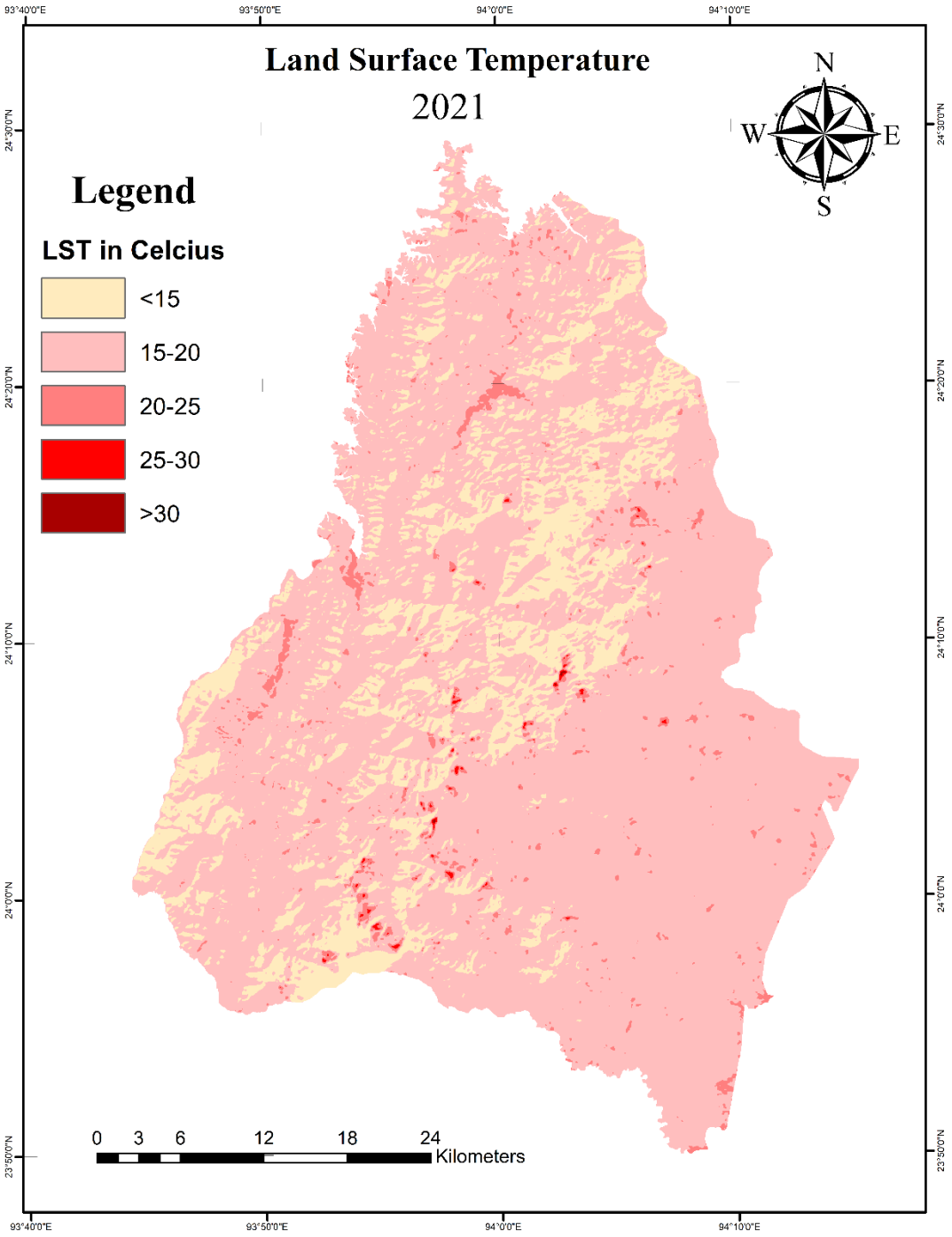

Figure 4.4 (d) Land Surface Temperature of Map 2021

Table 4.4 Land Surface Temperature Classification

Temperature	Class	1994		2003		2014		2021	
		Area Km2	%	Area Km2	%	Area Km2	%	Area Km2	%
<15	Very Low	175.5549	8.606185	30.7413	1.50703	0.0108	0.000529	352.0953	17.26076
15-20	Low	1616.325	79.23672	875.799	42.93427	22.1211	1.084442	1636.385	80.22043
20-25	Medium	235.8603	11.56252	960.8157	47.10204	1187.297	58.20483	49.0617	2.40515
25-30	High	11.8467	0.580758	148.0446	7.257586	776.9385	38.08783	2.1672	0.106243
>30	Very High	0.2817	0.01381	24.4305	1.197656	53.5014	2.622798	0.1224	0.006

Table 4.4 Land Surface Temperature (LST) Classification (1994–2021), shows the temporal evolution of land surface temperature patterns and class distribution.

In 1994, the study area exhibited predominantly low land surface temperatures, characterized by Low-temperature dominance (15–20°C) covering 79.24% of the total area. Only 0.6% of the total area was under high temperatures. This indicates stable and vegetated land surfaces with strong moisture retention and dense vegetation cover.

By the year 2003 there was a clear warming trend across the region. Low temperature areas dropped to 42.93%, a drastic decline of over 36%. Medium (20–25°C) and High (25–30°C) temperature zones expanded sharply to 47.1% and 7.26%, respectively. Very High (>30°C) temperatures also appeared significantly accounting about 1.2%of the total area. This marks the onset of thermal intensification, likely linked to land use change, vegetation loss, and increased surface exposure due to deforestation and urban growth.

In comparison the year 2014 represents the hottest phase of the study period. During this period Medium (20–25°C) and High (25–30°C) zones dominated, accounting for a combined 96.3% of total area. Very High (>30°C) temperature areas reached 2.62%, while Low (<20°C) areas almost disappeared (1.08% total). Severe thermal escalation occurred, indicating strong urban heat island effects, bare soil exposure, and loss of

vegetative cooling. This phase reflects maximum land surface degradation and ecological stress due to human activities and climate warming.

By 2021, there was a notable cooling and stabilization trend. 2021 was characterized by Low temperature (15–20°C) zones covering about 80.22% of the area whereas Very Low (<15°C) temperatures also rose to 17.26%, showing restoration of cooler microclimates. Meanwhile, Medium to Very High temperature zones drastically declined, together forming less than 3% of total area. This Indicates a major thermal reversal, possibly due to vegetation regeneration, reforestation programs, climate variability, or reduction in human-induced land stress.

4.5 Air Quality

Air pollution is a growing concern worldwide, affecting human health and ecosystems. Air pollution has become one of the most pressing environmental issues globally, posing serious risks to human health, ecosystems, and the climate. Both natural (such as wildfires and volcanic activity) and man-made (such as industrial processes, car emissions, and agriculture) sources can produce hazardous air pollutants substances that are released into the atmosphere such as Particulate matter (PM), nitrogen oxides (NO_x), sulphur dioxide (SO_2), carbon monoxide (CO), ozone (O_3), and volatile organic compounds (VOCs) (World Health Organization, 2021). To effectively manage and mitigate air pollution, air pollutants monitoring plays a crucial role. This process involves the systematic measurement and analysis of pollutant concentrations in the air to assess air quality levels, identify pollution sources, and ensure compliance with environmental standards and regulations (United States Environmental Protection Agency, 2023). Monitoring data also supports scientific research, public health studies, and the development of air quality management policies (European Environment Agency, 2022).

Numerous methods are used in modern air quality monitoring, ranging from satellite remote sensing and inexpensive pocket monitors to ground-based stations that use

sensors and analysers. These tools give governments, researchers, and the general public access to real-time data so they may comprehend pollution trends and take prompt action to save the environment and human health. (Kumar *et al*., 2015). Remote sensing technologies, such as TROPOMI, offer high-resolution data for monitoring atmospheric pollutants. This study focuses on Chandel District, examining pollution levels and identifying sources contributing to air quality degradation and aims to analyse the monthly spatial and temporal variation in the air quality of Chandel District over the study period of year 2019, 2021 and 2024 using TROPOMI on board Sentinel 5P.

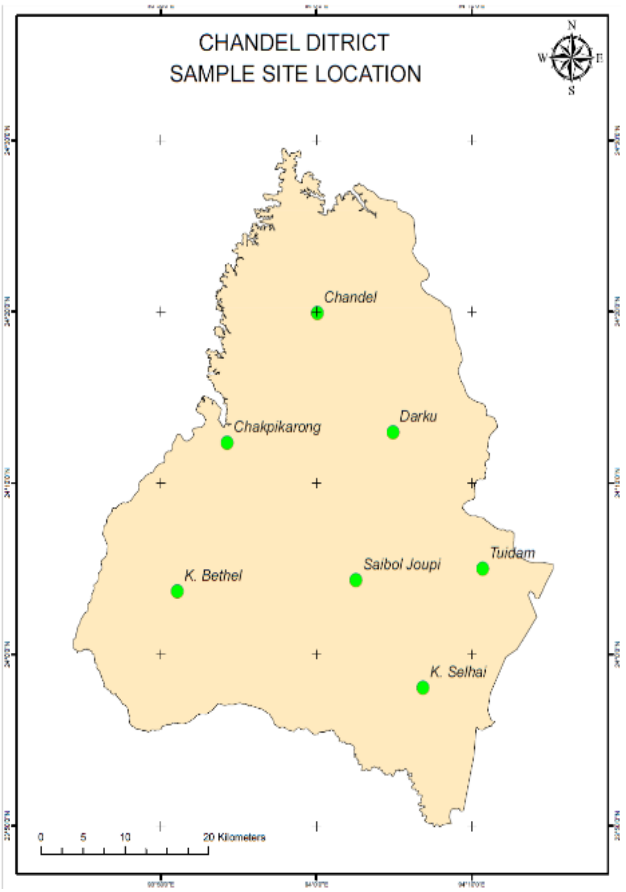

Figure 4.5 Study sample Sites

4.5.1 Air Pollutants

Air pollutants are compounds that negatively impact human health, the climate, and the environment. CO, HCHO, NO2 and O3 are a few prevalent air contaminants. (Okoduwa *et al.* 2023). Environmental pollution is a major risk factor for a number of diseases, including cancer, endocrine disorders, respiratory disorders, coronary artery diseases, and nervous system disorders. (Shehata *et al.* 2023).

All elements of the environment, including soil, groundwater, and air, can suffer greatly from air pollution. It also presents a significant risk to living things. In keeping with this, we are primarily interested in these pollutants since they are linked to more serious and widespread issues with human health and the environment. The greenhouse effect, acid rain, global warming, and climate change all have significant ecological effects on air pollution. (Meo *et al.* 2019; Zhang *et al.* 2020)

4.5.1.1 Carbon Monoxide (CO)

CO is a tasteless, odourless and colourless gas. Vehicle emissions, industrial operations, home heating, smoking, and other activities are the main sources of carbon monoxide. CO causes short-term symptoms like unconsciousness, headaches, and difficulty breathing, as well as long-term effects including heart disease, brain damage, and neurological damage by decreasing the blood's capacity to carry oxygen when it combines with haemoglobin.

Carbon monoxide also impacts the greenhouse gases that are closely linked to climate change and global warming. As a result, there will be rise in the temperatures of the soil and water leading to severe weather conditions. Additionally, it also plays an important role in creating ground-level ozone layer, which has an impact on the ecosystem.

Table 4.5.1.1 (a) Monthly CO Concentration in mol/m^2 (2019)

Name	Jan	Feb	Mar	Apr	May	Jun	Jul	Aug	Sep	Oct	Nov	Dec
Chandel	0.0310	0.0343	0.0418	0.0417	0.0388	0.0360	0.0303	0.0303	0.0327	0.0333	0.0300	0.0317
Chakpikarong	0.0313	0.0363	0.0435	0.0460	0.0395	0.0367	0.0310	0.0298	0.0320	0.0335	0.0313	0.0340
Darku	0.0313	0.0353	0.0398	0.0430	0.0390	0.0370	0.0290	0.0293	0.0323	0.0328	0.0303	0.0323
K. Bethel	0.0307	0.0333	0.0433	0.0433	0.0373	0.0357	0.0290	0.0288	0.0330	0.0333	0.0300	0.0307
Saibol Joupi	0.0313	0.0350	0.0455	0.0443	0.0403	0.0370	0.0293	0.0308	0.0333	0.0345	0.0313	0.0333
Tuidam	0.0337	0.0400	0.0520	0.0477	0.0440	0.0417	0.0323	0.0315	0.0343	0.0360	0.0353	0.0367
K. Selhai	0.0333	0.0390	0.0465	0.0513	0.0445	0.0397	0.0320	0.0308	0.0347	0.0355	0.0343	0.0343

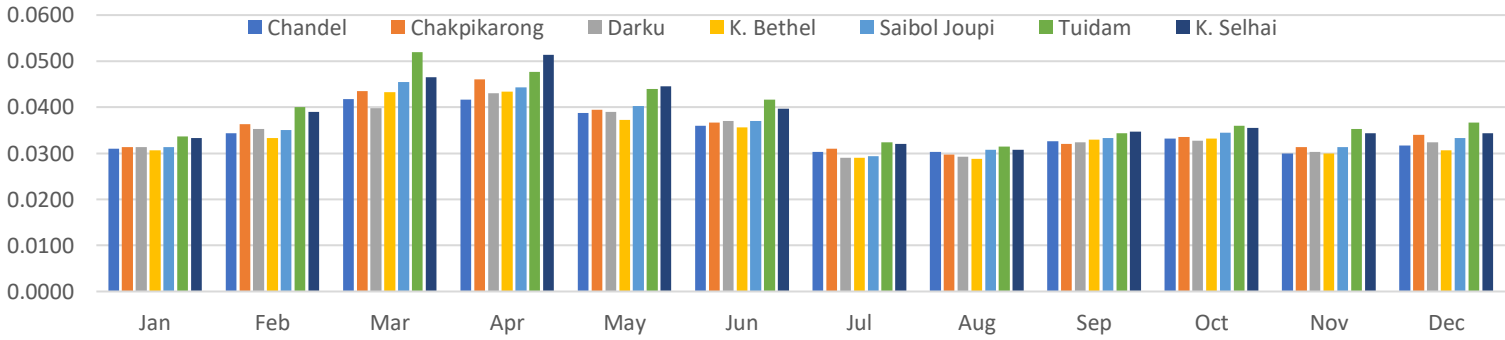

Figure 4.5.1.1 (a) Bar Graph depicting CO concentration 2019

Table 4.5.1.1 (b) Monthly CO Concentration in mol/m^2 (2021)

Name	Jan	Feb	Mar	Apr	May	Jun	Jul	Aug	Sep	Oct	Nov	Dec
Chandel	0.0355	0.0377	0.0483	0.0460	0.0388	0.0323	0.0280	0.0317	0.0277	0.0300	0.0303	0.0298
Chakpikarong	0.0373	0.0383	0.0570	0.0477	0.0388	0.0323	0.0290	0.0307	0.0297	0.0313	0.0313	0.0305
Darku	0.0353	0.0380	0.0517	0.0450	0.0400	0.0320	0.0273	0.0310	0.0280	0.0303	0.0303	0.0295
K. Bethel	0.0343	0.0357	0.0593	0.0440	0.0380	0.0333	0.0273	0.0290	0.0273	0.0295	0.0297	0.0280
Saibol Joupi	0.0375	0.0367	0.0600	0.0537	0.0400	0.0323	0.0285	0.0320	0.0283	0.0300	0.0313	0.0308
Tuidam	0.0395	0.0427	0.0660	0.0563	0.0465	0.0370	0.0303	0.0347	0.0293	0.0323	0.0330	0.0330
K. Selhai	0.0380	0.0430	0.0673	0.0580	0.0410	0.0343	0.0295	0.0337	0.0283	0.0323	0.0327	0.0325

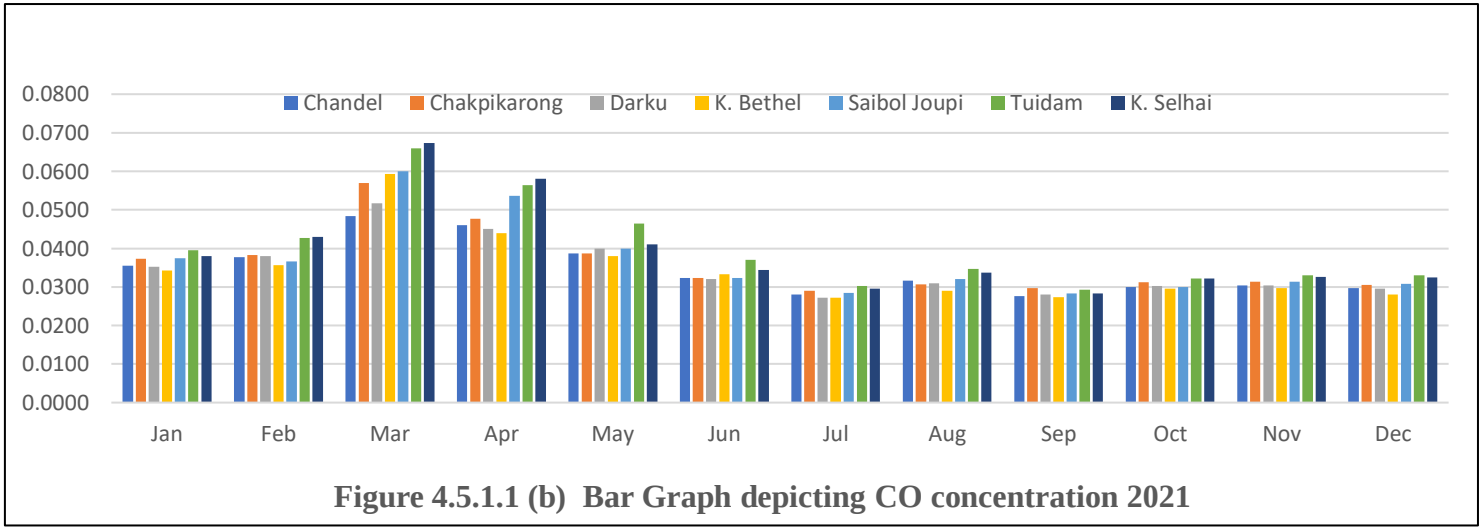

Figure 4.5.1.1 (b) Bar Graph depicting CO concentration 2021

Table 4.5.1.1 (c) Monthly CO Concentration in mol/m^2 (2024)

Name	Jan	Feb	Mar	Apr	May	Jun	Jul	Aug	Sep	Oct	Nov	Dec
Chandel	0.033	0.0353	0.041	0.042	0.0412	0.041	0.0296	0.029	0.0323	0.0315	0.0323	0.033
Chakpikarong	0.0345	0.036	0.04	0.04	0.0405	0.039	0.0295	0.028	0.0325	0.0325	0.0325	0.036
Darku	0.0313	0.0325	0.0335	0.0365	0.0427	0.04	0.036	0.0282	0.0275	0.0317	0.032	0.032
K. Bethel	0.0316	0.0325	0.033	0.039	0.0405	0.0405	0.0385	0.0277	0.0265	0.033	0.031	0.032
Saibol Joupi	0.0343	0.035	0.0362	0.036	0.0447	0.0415	0.037	0.0287	0.03	0.0332	0.033	0.0335
Tuidam	0.0366	0.038	0.0397	0.0425	0.049	0.044	0.043	0.031	0.031	0.0342	0.034	0.0355
K. Selhai	0.038	0.0395	0.0392	0.039	0.053	0.0465	0.04	0.03125	0.03	0.0332	0.034	0.0355

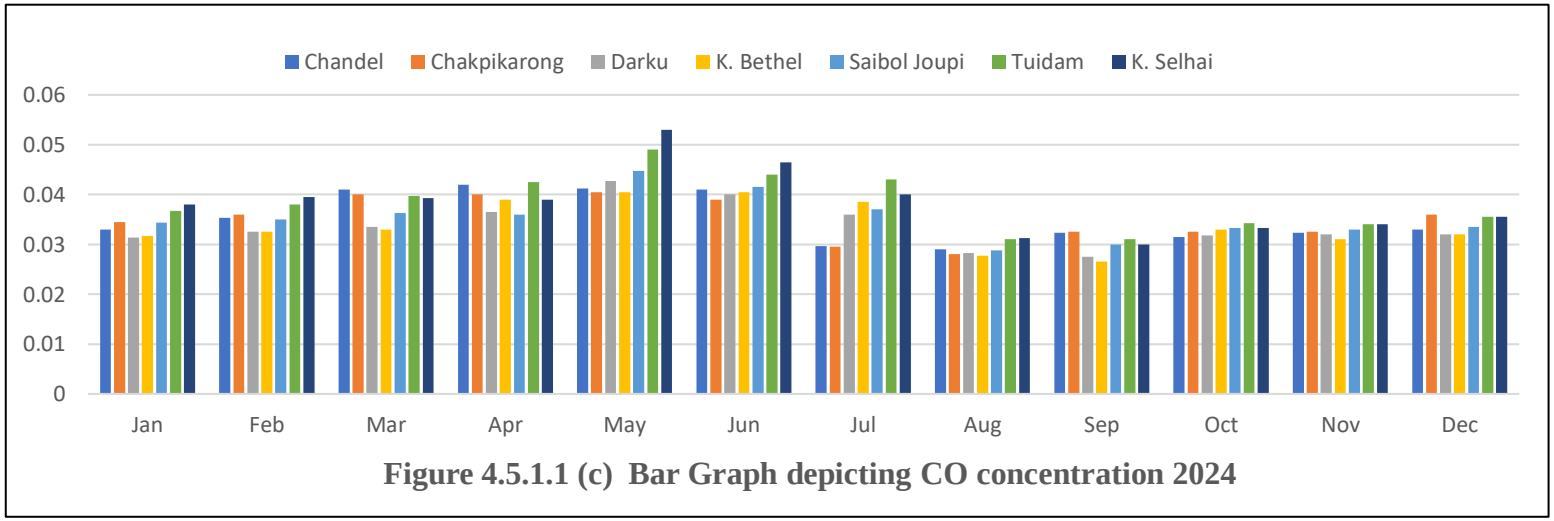

Figure 4.5.1.1 (c) Bar Graph depicting CO concentration 2024

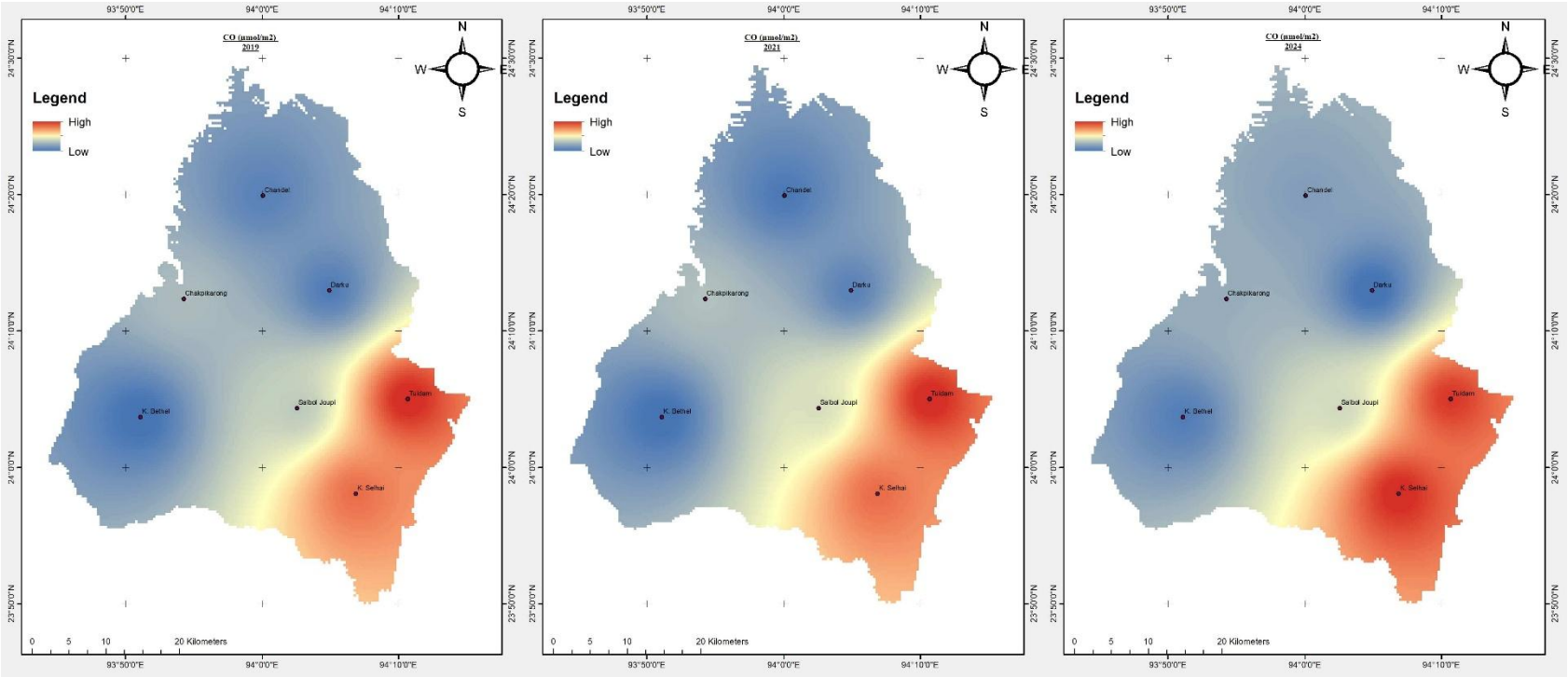

Figure 4.5.1.1 (d) Yearly Spatial Distribution of CO concentration Map

Table 4.5.1.1 (d) Yearly CO Concentration in mol/m^2

Name	2019	2021	2024
Chandel	0.0345	0.0344	0.0352
Chakpikarong	0.0355	0.0358	0.0354
Darku	0.0344	0.0346	0.0344
K. Bethel	0.0342	0.0342	0.0346
Saibol Joupi	0.0357	0.0363	0.0361
Tuidam	0.0390	0.0396	0.0386
K. Selhai	0.0381	0.0387	0.0388
Average	0.0359	0.0362	0.0361

CO concentration in mol/m2: The monthly variation in the concentration of CO for the year 2019 and 2021 as seen in table 4.5.1.1(d)**,** shows the highest recorded monthly mean concentration in the month of March-April with in most of the sample sites collectively as shown in fig. 4.5.1.1. Tuidam and K. Selhai recorded the highest level of CO concentration during the month of March and April in both 2019 and 2021. The highest reading of 0.0520 mol/m^2 and 0.0465 mol/m^2 was recorded at Tuidam and K. Selhai, respectively, during March 2019. In 2021, an even higher reading of 0.0660 mol/m^2 and 0.0673 mol/m^2 were recorded in March. Whereas in 2024, Tuidam recorded 0.03975 mol/m^2 and K. Selhai with 0.03925 mol/m^2.

Table 4.5.1.1 (a), (b), (c) and (d) Shows that Tuidam's mean CO concentration was 0.0390 mol/m^2, 0.0396 mol/m^2 and 0.0386 mol/m^2 in 2019, 20021 and 2024 respectively. The average CO concentration was calculated for each year and a reading of 0.0359 mol/m^2, 0.0362 mol/m^2 and 0.0361 mol/m^2 in 2019, 2021 and 2024 was recorded, respectively. Fig 4.5.1.1 (d). Shows the location-wise visual representation of spatial distribution of the average CO concentration. Throughout the study years, the region Tuidam and K. Selhai is shown to have higher level of CO concentration.

4.5.1.2 Formaldehyde (HCHO)

HCHO, an Organic Volatile Compound (VOC), is a colourless with a pungent smell. HCHO is released into the atmosphere through High-temperature burning, fossil fuel burning, industrial activity, etc. Additionally, building supplies like paints, plywood, adhesives, and other items also exerts HCHO indoors. The symptoms of HCHO poisoning include headache pain, dizziness, breathing issues, skin issues, and irritation of the ENT (ear, nose, and throat). With increased exposure, it can possibly result in cancer.

HCHO concentration in μmol/m^2: The concentration trend of HCHO also peaks during the month of March and April throughout for the duration of the study period as shown in Table 4.5.1.2 (a), (b) and (c). In 2019, K. Selhai recorded the highest monthly mean level of HCHO concentration with 303.80 μmol/m^2, 323.33 μmol/m^2 and 313.33 μmol/m^2 in the month of March, April and May, respectively. Similar results can be seen in 2021 with Tuidam and K. Selhai recording 338.787 μmol/m^2 and 343.50 μmol/m^2 respectively in the month of March. Whereas in 2024, Tuidam shows the highest level of monthly mean Concentration of 294.89 μmol/m^2 and 297.37 μmol/m^2 in March and April respectively.

Table 4.5.1.2 (a) Monthly HCHO Concentration in µmol/m^2 (2019)

Name	Jan	Feb	Mar	Apr	May	Jun	Jul	Aug	Sep	Oct	Nov	Dec
Chandel	123.821	161.826	114.7447	209.595	109.1713	179.1343	146.1067	120.8393	122.869	79.04233	87.509	31.93767
Chakpikarong	120.858	110.8018	139.6377	185.2868	173.659	165.701	176.066	98.64533	282.7908	59.43	101.7658	43.61867
Darku	116.9873	172.142	143.6367	182.1455	101.4827	137.08	93.03667	7.4	75.36125	64.93633	66.215	95.993
K. Bethel	62.408	122.721	180.542	123.85	136.9823	67.63525	42.38533	132.6607	70.067	56.99633	108.55	110.846
Saibol Joupi	118.2223	228.4927	263.457	187.3168	253.4093	123.112	140.5643	20.912	35.63633	128.947	168.2813	149.648
Tuidam	69.8395	157.6193	168.0413	249.9093	280.443	100.5568	71.5165	53.52125	168.181	73.75233	117.6528	58.149
K. Selhai	112.9723	188.6293	303.8073	323.785	313.3337	90.74	169.253	66.27767	63.52	-20.954	171.1225	116.2313

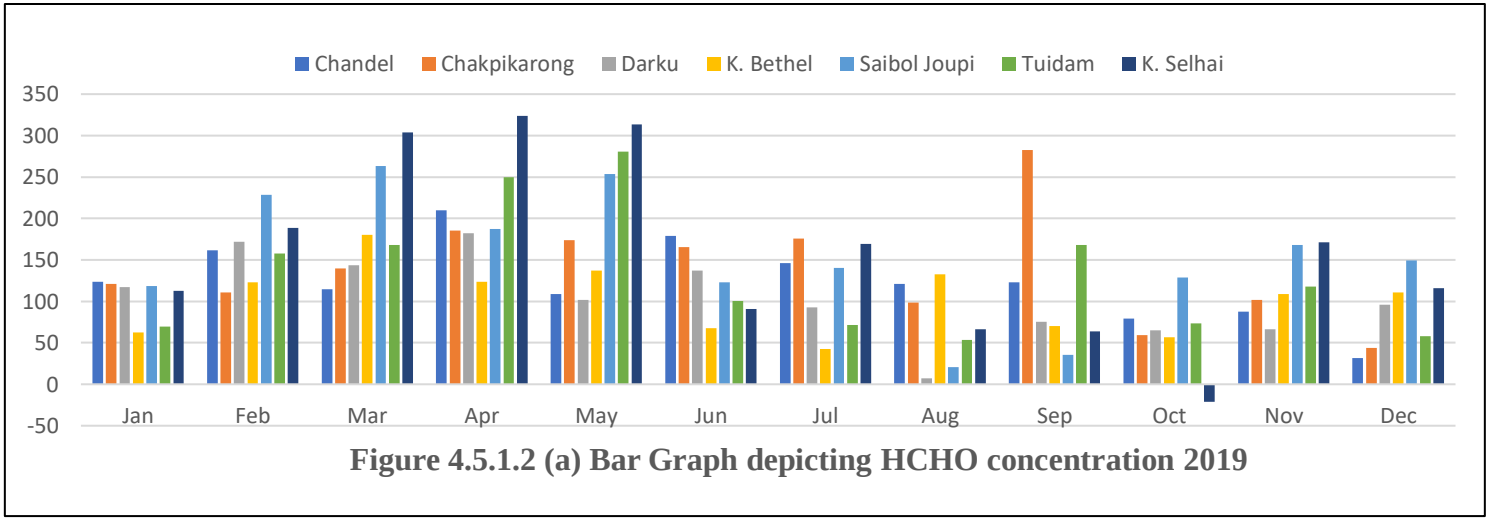

Figure 4.5.1.2 (a) Bar Graph depicting HCHO concentration 2019

Table 4.5.1.2 (b). Monthly HCHO Concentration in µmol/m^2 (2021)

Name	Jan	Feb	Mar	Apr	May	Jun	Jul	Aug	Sep	Oct	Nov	Dec
Chandel	93.298	95.56	224.0535	214.6587	92.39633	117.4933	90.9525	119.6583	74.93367	114.956	80.0855	142.7093
Chakpikarong	64.46033	99.02167	306.3795	160.2873	110.0547	91.7595	168.937	78.339	109.8303	87.25033	69.8645	74.975
Darku	112.4847	134.6663	260.5608	249.2743	128.2207	49.0385	197.593	160.6605	121.578	138.152	97.18125	49.98033
K. Bethel	87.608	148.295	324.82	201.717	158.2883	111.1033	200.1677	99.40325	88.544	94.35367	100.0548	22.613
Saibol Joupi	113.5037	138.1043	289.4398	284.493	247.286	61.464	144.254	97.6535	57.1335	180.6645	76.448	161.6857
Tuidam	97.94333	125.2327	338.787	274.4743	75.611	117.3683	184.94	88.9975	152.704	101.824	86.953	179.5513
K. Selhai	87.93067	109	343.5015	276.2297	184.857	150.739	133.26	-20.6157	75.7695	70.07867	152.0378	106.938

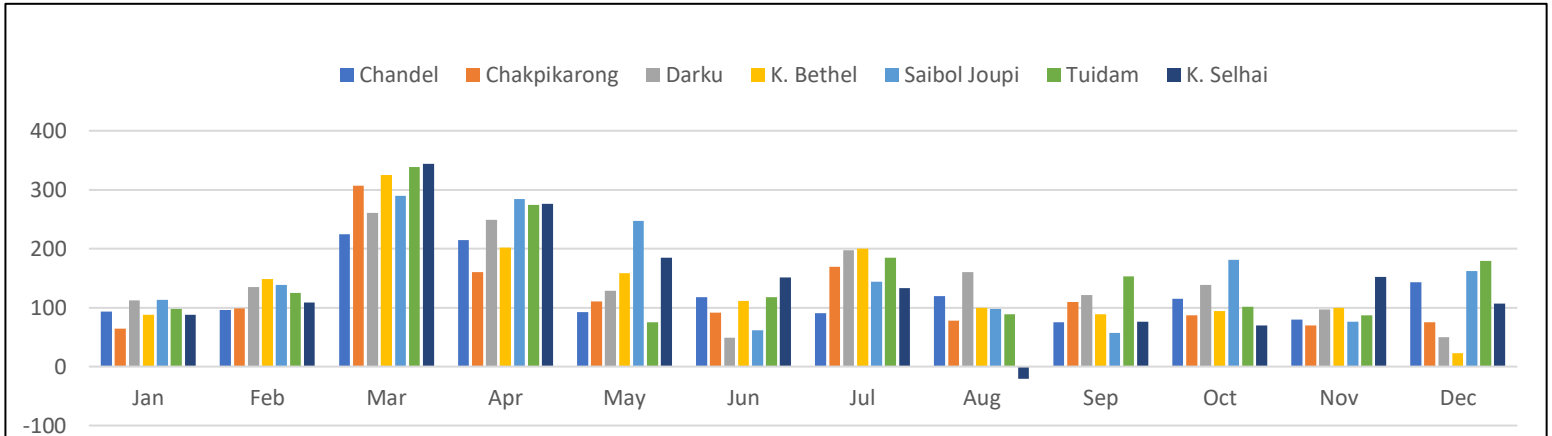

Figure 4.5.1.2 (b) Bar Graph depicting HCHO concentration 2021

Table 4.5.1.2 (c) Monthly HCHO Concentration in µmol/m^2 (2024)

Name	Jan	Feb	Mar	Apr	May	Jun	Jul	Aug	Sep	Oct	Nov	Dec
Chandel	42.49675	156.945	193.0223	176.2195	25.41367	137.3467	49.5285	187.5603	86.45667	97.64933	79.14575	147.9727
Chakpikarong	82.85975	125.9133	215.795	218.0845	253.213	111.546	66.904	118.273	74.569	131.4367	158.4018	117.523
Darku	48.763	76.42867	136.5463	181.0518	212.9913	151.301	95.4395	39.578	91.2915	145.677	70.4065	127.631
K. Bethel	104.4218	95.85633	101.7723	194.1243	190.0043	169.462	98.53267	153.605	111.401	73.33033	91.88	129.6953
Saibol Joupi	105.8198	132.606	254.7853	222.208	129.3193	-3.34533	28.33413	91.69304	123.3725	82.37033	73.3405	100.3837
Tuidam	99.545	165.364	294.8903	297.376	245.066	174.4523	62.135	229.714	149.9903	157.3443	108.2608	78.14267
K. Selhai	106.9473	117.171	227.259	268.7985	252.4283	161.24	48.23933	139.311	147.477	186.8207	103.6858	165.524

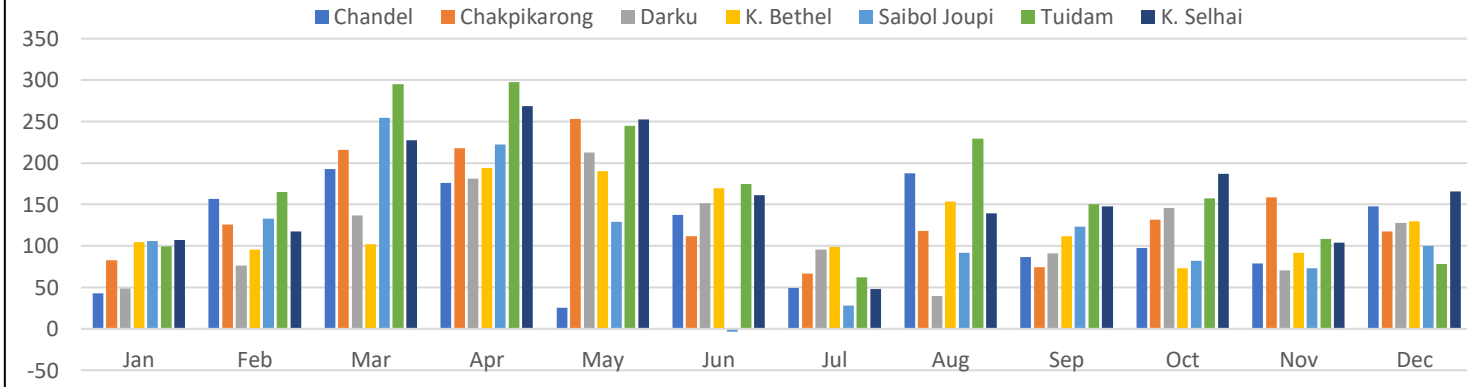

Figure 4.5.1.2 (c) Bar Graph depicting HCHO concentration 2024

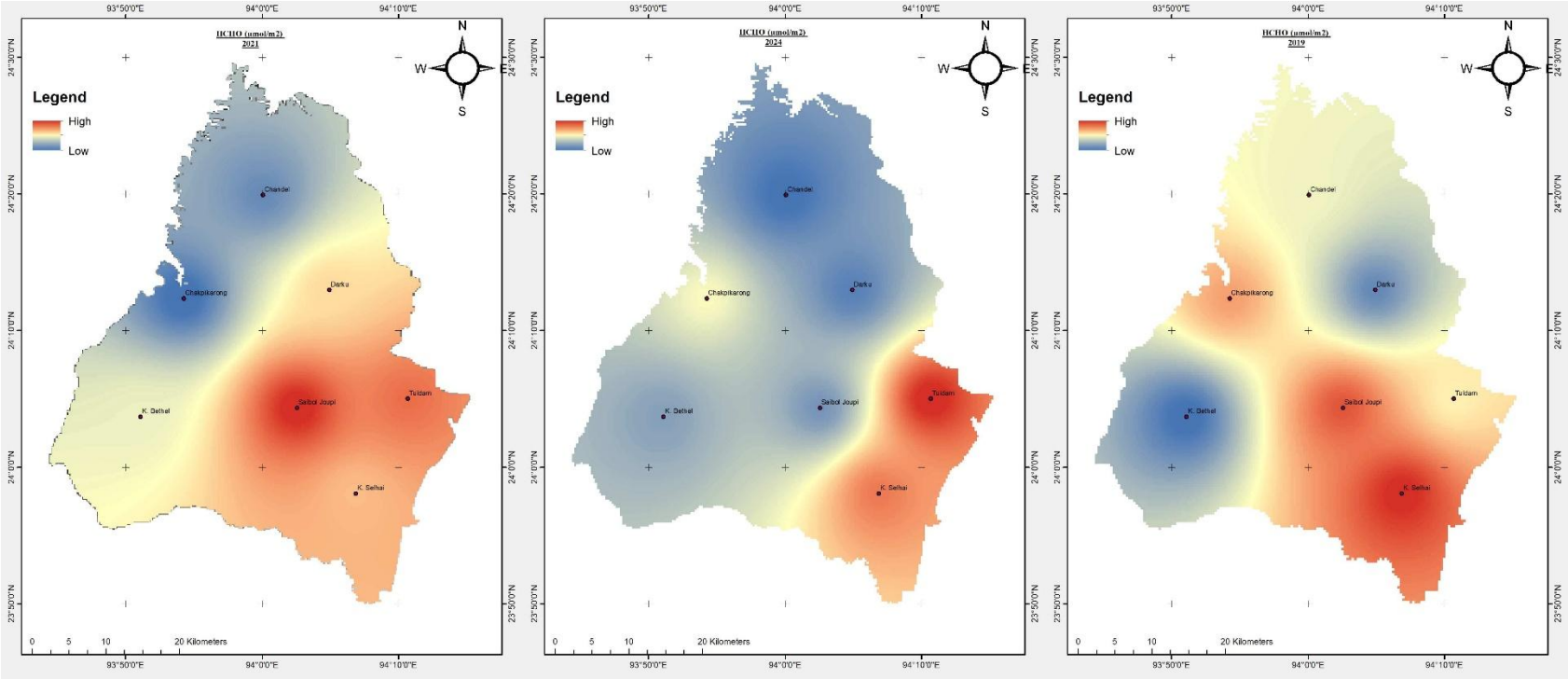

Figure 4.5.1.2 (d) Yearly Spatial Distribution of HCHO concentration Map

Table 4.5.1.2 (d). Yearly HCHO Concentration in µmol/m^2

Name	2019	2021	2024
Chandel	126.4077	123.9129	115.4633
Chakpikarong	141.1266	118.8254	142.3493
Darku	106.0253	144.4256	118.7816
K. Bethel	100.2344	138.6571	125.8035
Saibol Joupi	151.2732	163.0639	123.1565
Tuidam	130.6877	155.3406	172.3728
K. Selhai	157.226	147.2007	160.5719
Average	130.4258	141.6323	136.9284

In the context of yearly Mean concentration, Table 4.5.1.2 (d) shows that the Average yearly HCHO concentration was highest during 2021 with 141.63 µmol/m^2. While the average concentration level of year 2019 and 2024 stands at 130.42 µmol/m^2 and 136.92 µmol/m^2, respectively. Fig. 4.5.1.2 (d). gives the visual representation of the yealy mean concentration level, with the highest concentration seen at Saibol Joupi with 151.27 µmol/m^2 and 163.06 µmol/m^2 for the year 2019 and 2021. Whereas Tuidam shows highest level of concentration with 172.37 µmol/m^2 in 2024.

4.5.1.3 Nitrogen Dioxide (NO2)

NO_2 is reddish-brown, pungent smelly gas. Main source is vehicular emission. It is one of the reactive greenhouse gases that causes acid rain. It is highly acidic by nature. Because it enters the lung deeply, it irritates the respiratory system and can cause respiratory disorders, Asthma, coughing, wheezing, dyspnea, bronchospasm, and even pulmonary edema when inhaled in high concentrations. It also contributes to the formation of the ground-level ozone layer (Virghileanu *et al*. 2020).

Table 4.5.1.3 (a). Yearly NO2 Concentration in µmol/m^2

Name	2019	2021	2024
Chandel	16.4574	16.2508	12.5251
Chakpikarong	18.1888	17.2065	15.7021
Darku	15.4011	16.9384	15.0451
K. Bethel	19.1009	21.4286	16.9141
Saibol Joupi	16.4478	17.2824	13.9956
Tuidam	14.6185	17.9219	15.4334
K. Selhai	17.9608	18.5983	16.3158
Average	16.8822	17.9467	15.1330

Nitrogen Dioxide concentration in µmol/m^2: The monthly variation in the concentration level of NO_2 is shown in table 4.5.1.3 (b), (c), (d). Following the trend as above, the highest concentration was exerted during the month of March for all the study years. In 2019, we see Chakpikarong with the highest mean concentration level of 46.61 µmol/m^2, followed bu K. Bethel with 44.93 µmol/m^2. In 2021, K. Bethel recorded the highest mean concentration of 88.91 µmol/m^2 in the month of March. Whereas in 2024, we see a comparatively lower mean concentration of 36.94 µmol/m^2 recorded at K. Selhai. Table 13. Shows the average concentration of HCHO. We see an increase mean concentration from 2019 to 2021 by 6.3%, from 16.88 µmol/m^2 in 2019 to 17.94 µmol/m^2 in 2021, then decreased by 15% in 2024.

Table 4.5.1.3 (b) Monthly NO2 Concentration in µmol/m^2 (2019)

Name	Jan	Feb	Mar	Apr	May	Jun	Jul	Aug	Sep	Oct	Nov	Dec
Chandel	10.3230	11.4320	32.2423	21.1220	17.8228	20.4083	20.4083	11.7253	15.4570	12.9685	9.9190	12.6480
Chakpikarong	9.7280	13.3997	46.6195	25.7957	15.1320	19.1377	16.8245	14.3293	12.2927	13.7453	13.6183	11.4977
Darku	7.0403	11.3893	28.1670	19.6657	14.4440	16.3400	1.0010	7.2830	18.8860	16.4837	14.0813	13.9537
K. Bethel	9.5323	14.1460	44.9325	26.9887	18.8633	17.8940	14.5055	12.7337	15.8535	16.3183	11.8897	14.0053
Saibol Joupi	10.2513	13.5203	35.7065	21.7013	22.5090	12.9790	5.2890	8.5785	6.9480	6.0388	5.1295	7.3927
Tuidam	6.8800	15.1430	35.0260	18.9167	21.6618	12.7575	13.2063	5.5893	10.3193	12.4178	9.6447	7.8320
K. Selhai	6.6817	11.7320	40.0778	27.6497	26.9685	14.7413	17.2435	7.0527	9.7145	15.1223	13.3223	11.8607

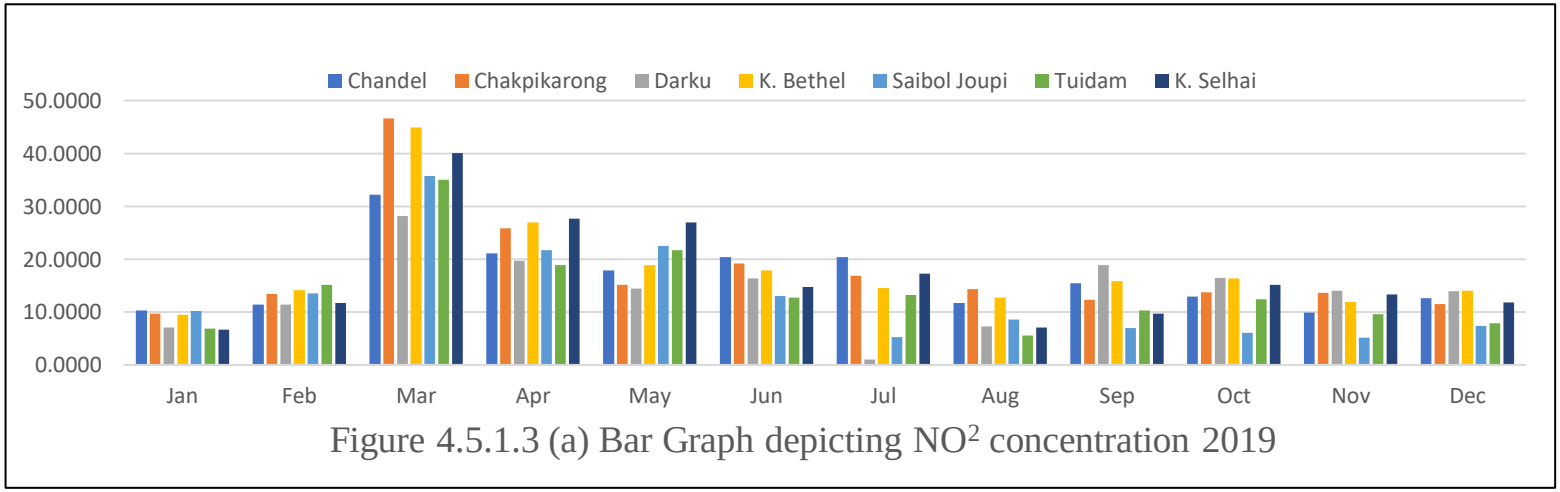

Figure 4.5.1.3 (a) Bar Graph depicting NO^2 concentration 2019

Table 4.5.1.3 (c). Monthly NO2 Concentration in µmol/m^2 (2021)

Name	Jan	Feb	Mar	Apr	May	Jun	Jul	Aug	Sep	Oct	Nov	Dec
Chandel	12.0367	14.6340	51.1733	22.0800	18.0660	12.4730	20.9378	7.8880	14.1037	14.7318	3.5757	4.7593
Chakpikarong	9.5500	13.3028	66.9627	24.0960	17.8437	7.2225	12.5838	15.0800	14.0617	15.1940	6.9603	6.0925
Darku	12.9200	12.6200	44.2347	25.4863	16.5935	14.0930	15.6200	13.5975	12.3220	14.0970	5.6570	6.5715
K. Bethel	11.4037	18.7080	88.9130	26.2243	29.1150	14.6790	16.9615	9.1340	16.3957	12.3505	9.7570	7.2885
Saibol Joupi	9.3267	10.7610	62.4033	26.9237	25.8683	16.2730	4.6360	5.9345	9.2025	6.2395	4.4000	4.1293
Tuidam	11.8200	14.4368	68.9780	32.1360	19.0670	10.4750	10.4750	11.6375	14.5005	12.5935	1.5670	4.1263
K. Selhai	11.0697	11.8640	66.4763	30.5340	21.0065	18.7360	17.7233	7.3030	12.6605	12.4268	7.2420	4.7798

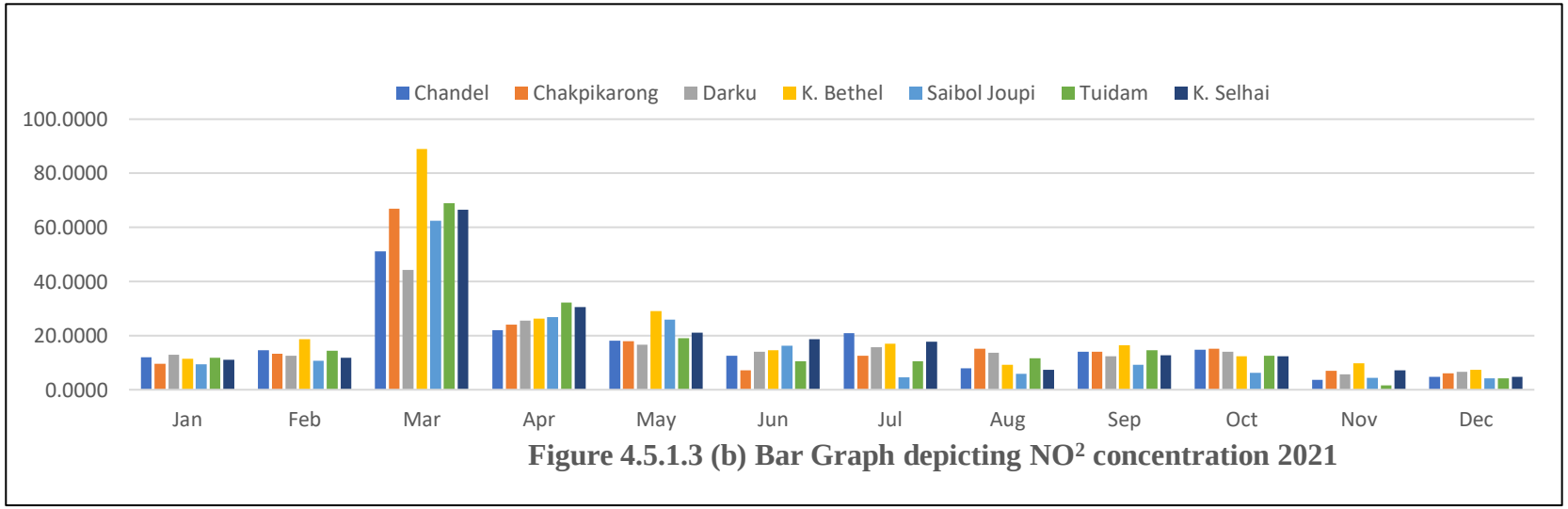

Figure 4.5.1.3 (b) Bar Graph depicting NO^2 concentration 2021

Table 4.5.1.3(d) Monthly NO2 Concentration in µmol/m^2 (2024)

Name	Jan	Feb	Mar	Apr	May	Jun	Jul	Aug	Sep	Oct	Nov	Dec
Chandel	7.5943	13.2803	20.2285	14.2427	12.9988	14.0430	10.7905	13.3610	11.5887	13.1600	9.3980	7.3753
Chakpikarong	7.3413	14.9107	25.8175	12.5283	16.9825	18.1957	12.8690	11.6910	17.9180	17.9150	14.1523	9.7420
Darku	9.2573	13.8710	18.9348	14.6283	15.7490	18.8145	13.4658	8.1170	15.8037	18.1117	25.3360	9.0750
K. Bethel	8.3283	9.7117	28.9605	23.8463	18.2193	16.4410	9.9530	23.4315	16.2330	13.3260	14.8757	12.5663
Saibol Joupi	3.1803	7.0423	25.0598	24.2450	15.1520	9.6460	11.7290	13.8120	12.3267	14.7710	18.6410	6.7210
Tuidam	7.5590	11.4327	27.8733	20.3200	16.9520	19.8510	20.2818	20.7125	15.0140	17.0570	7.4193	5.6283
K. Selhai	7.4947	9.8017	36.9428	26.6573	15.5680	30.9610	-1.5010	17.7670	14.9963	6.3067	12.3697	10.1683

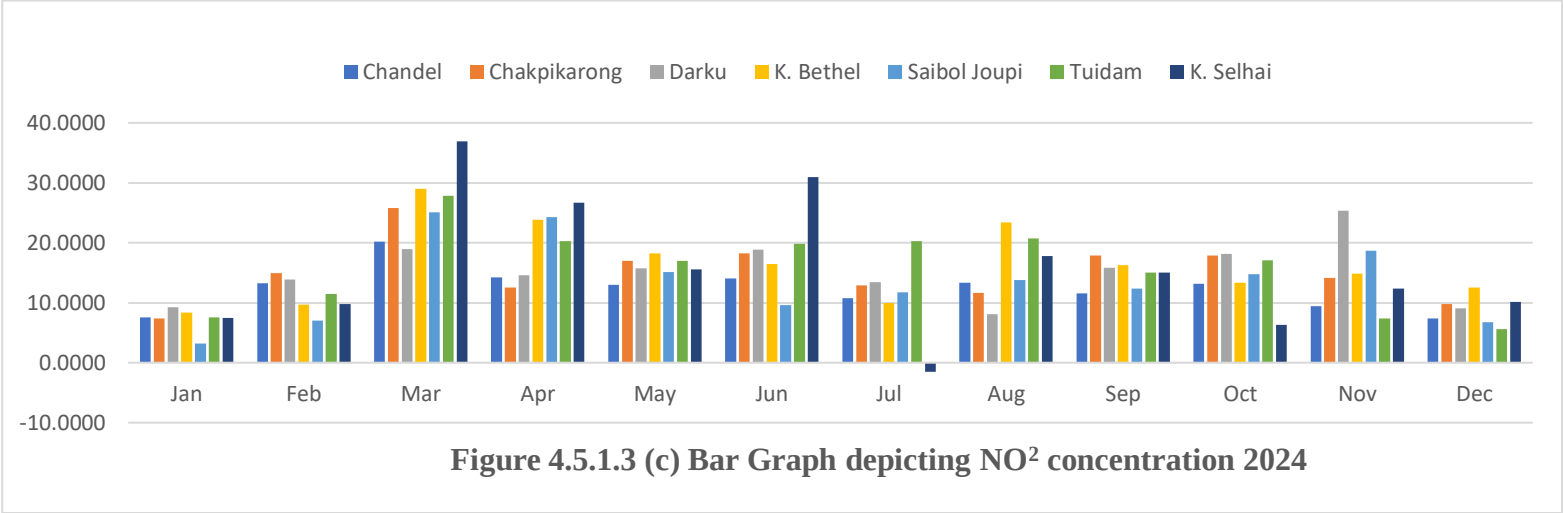

Figure 4.5.1.3 (c) Bar Graph depicting NO^2 concentration 2024

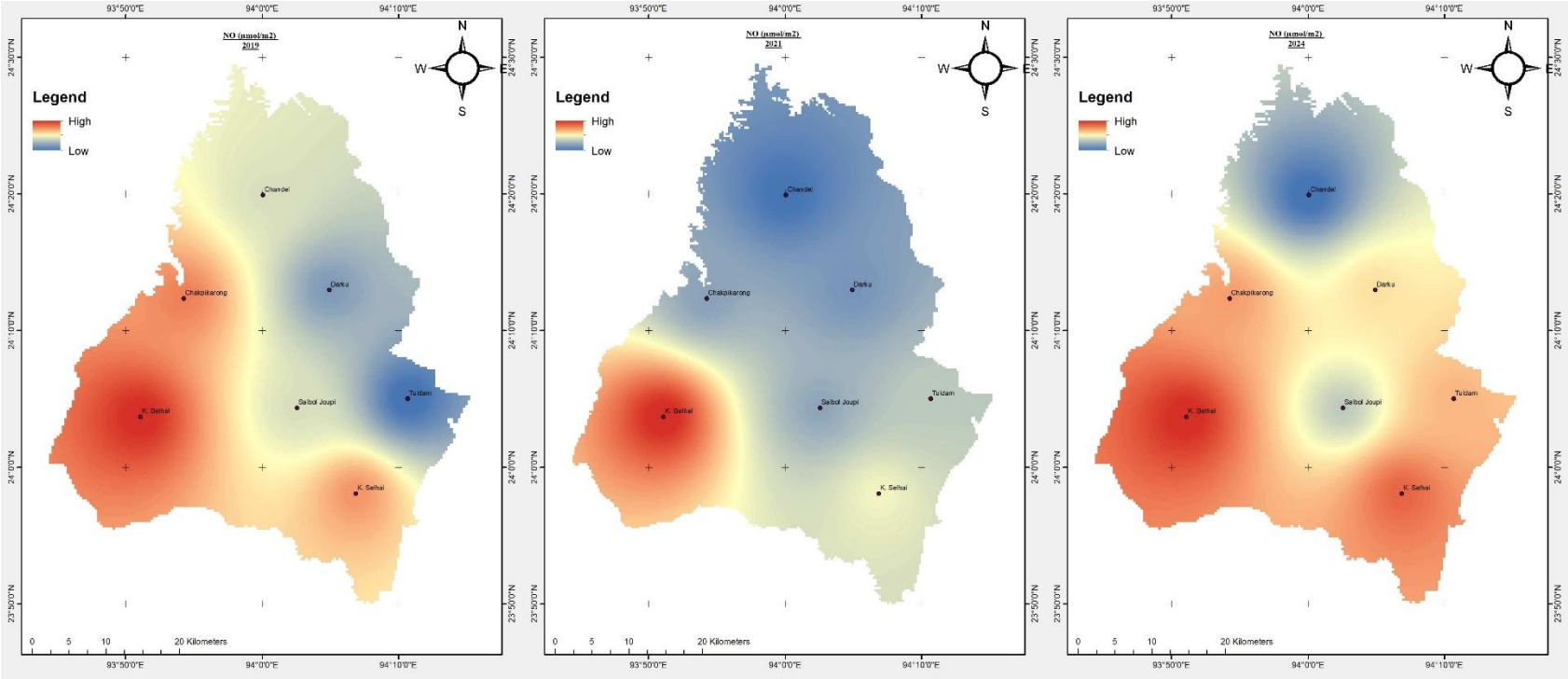

Figure 4.5.1.3 (d) Yearly Spatial Distribution of NO^2 concentration Map

4.5.1.4 Ozone (O_3)

Ozone is a gas that contains three oxygen atoms. Both the troposphere and the stratosphere contain it. It filters out the sun's UV rays in the stratosphere, protecting the Earth, but it is extremely dangerous in the troposphere. It is created by the high-temperature reaction of VOC and nitrogen oxides (NO). Asthma, respiratory issues, and lung disorders are the results of O3. Additionally, it harms crops and has a negative impact on the ecosystem. (Bugdayci *et al.* 2023; Domingo *et al*. 2020).

Table 4.5.1.4. (a) Yearly O3 Concentration in mol/m^2

Name	**2019**	**2021**	**2024**
Chandel	0.1175	0.1209	0.1232
Chakpikarong	0.1176	0.1212	0.1232
Darku	0.1177	0.1204	0.1232
K. Bethel	0.1176	0.1206	0.1225
Saibol Joupi	0.1177	0.1199	0.1228
Tuidam	0.1175	0.1207	0.1229
K. Selhai	0.1177	0.1158	0.1230
Average	0.1176	0.1199	0.1230

Table 4.5.1.4. (b). Monthly O3 Concentration in mol/m^2 (2019)

Name	Jan	Feb	Mar	Apr	May	Jun	Jul	Aug	Sep	Oct	Nov	Dec
Chandel	0.1033	0.1070	0.1148	0.1247	0.1223	0.1260	0.1230	0.1225	0.1190	0.1190	0.1117	0.1137
Chakpikarong	0.1037	0.1073	0.1143	0.1250	0.1228	0.1260	0.1227	0.1228	0.1197	0.1195	0.1107	0.1137
Darku	0.1033	0.1073	0.1150	0.1250	0.1220	0.1257	0.1227	0.1238	0.1200	0.1190	0.1113	0.1147
K. Bethel	0.1030	0.1077	0.1133	0.1250	0.1225	0.1247	0.1233	0.1238	0.1207	0.1198	0.1110	0.1137
Saibol Joupi	0.1037	0.1080	0.1145	0.1250	0.1220	0.1250	0.1227	0.1230	0.1193	0.1203	0.1123	0.1137
Tuidam	0.1043	0.1073	0.1148	0.1250	0.1218	0.1250	0.1217	0.1218	0.1197	0.1198	0.1123	0.1133
K. Selhai	0.1033	0.1073	0.1148	0.1253	0.1218	0.1263	0.1223	0.1238	0.1190	0.1190	0.1137	0.1143

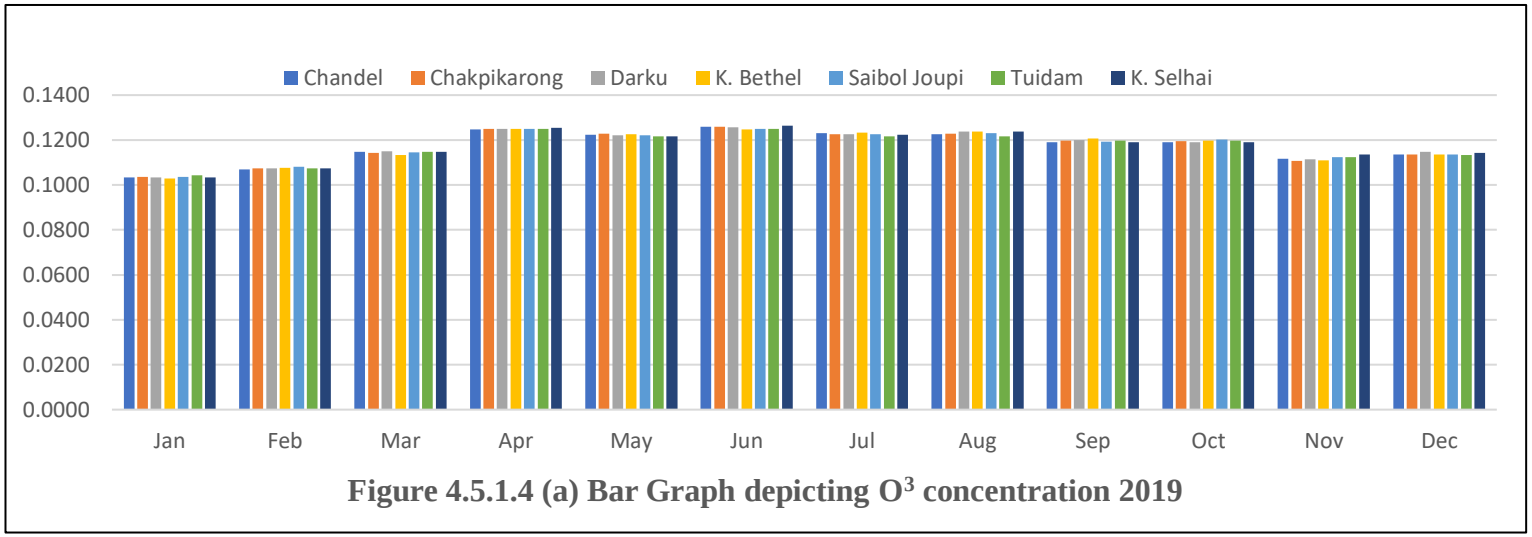

Figure 4.5.1.4 (a) Bar Graph depicting O^3 concentration 2019

Table 4.5.1.4. (c). Monthly O3 Concentration in mol/m^2 (2021)

Name	Jan	Feb	Mar	Apr	May	Jun	Jul	Aug	Sep	Oct	Nov	Dec
Chandel	0.1103	0.1247	0.1197	0.1253	0.1278	0.1230	0.1245	0.1240	0.1227	0.1200	0.1160	0.1160
Chakpikarong	0.1108	0.1240	0.1197	0.1247	0.1283	0.1260	0.1233	0.1250	0.1227	0.1200	0.1173	0.1163
Darku	0.1110	0.1240	0.1190	0.1250	0.1288	0.1225	0.1240	0.1210	0.1225	0.1197	0.1167	0.1153
K. Bethel	0.1108	0.1237	0.1193	0.1253	0.1283	0.1250	0.1235	0.1215	0.1223	0.1195	0.1167	0.1150
Saibol Joupi	0.1103	0.1237	0.1183	0.1247	0.1278	0.1220	0.1240	0.1210	0.1215	0.1193	0.1170	0.1153
Tuidam	0.1110	0.1247	0.1193	0.1247	0.1280	0.1247	0.1240	0.1220	0.1230	0.1198	0.1160	0.1160
K. Selhai	0.1115	0.1247	0.1190	0.1253	0.1288	0.1250	0.1240	0.1260	0.1230	0.1200	0.1170	0.1158

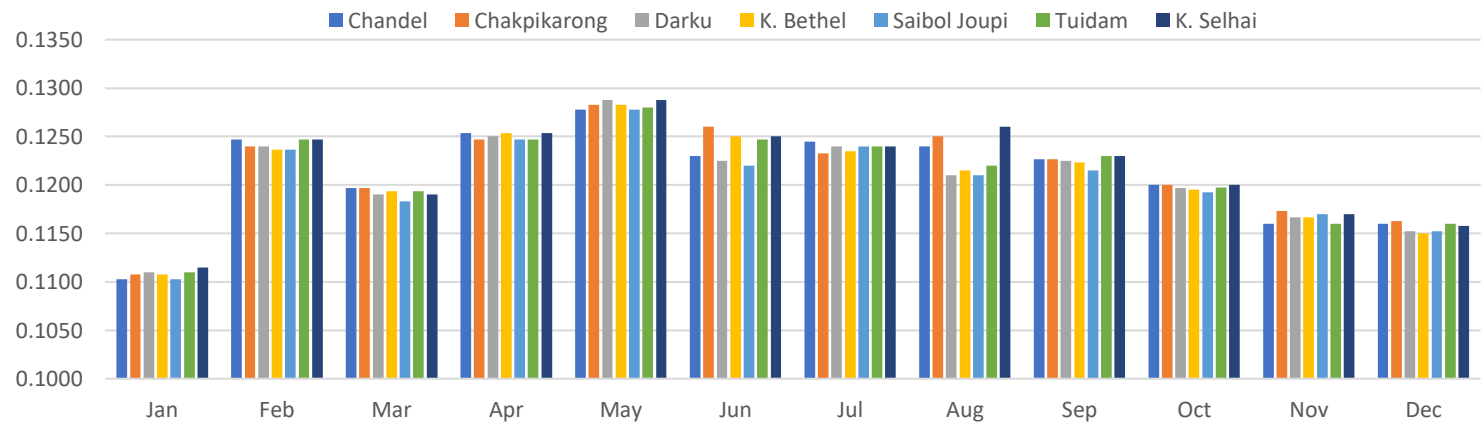

Figure 4.5.1.4 (b) Bar Graph depicting O^3 concentration 2021

Table 4.5.1.4. (d). Monthly O3 Concentration in mol/m^2 (2024)

Name	Jan	Feb	Mar	Apr	May	Jun	Jul	Aug	Sep	Oct	Nov	Dec
Chandel	0.1220	0.1210	0.1233	0.1313	0.1330	0.1280	0.1235	0.1243	0.1230	0.1197	0.1130	0.1147
Chakpikarong	0.1217	0.1200	0.1228	0.1310	0.1333	0.1287	0.1230	0.1237	0.1237	0.1203	0.1130	0.1137
Darku	0.1217	0.1193	0.1245	0.1303	0.1325	0.1303	0.1264	0.1225	0.1227	0.1203	0.1130	0.1140
K. Bethel	0.1213	0.1197	0.1210	0.1307	0.1318	0.1265	0.1245	0.1245	0.1230	0.1200	0.1130	0.1137
Saibol Joupi	0.1210	0.1197	0.1235	0.1303	0.1323	0.1305	0.1268	0.1230	0.1227	0.1200	0.1123	0.1153
Tuidam	0.1217	0.1187	0.1235	0.1300	0.1325	0.1300	0.1230	0.1240	0.1223	0.1207	0.1133	0.1140
K. Selhai	0.1213	0.1187	0.1243	0.1293	0.1328	0.1290	0.1223	0.1253	0.1230	0.1210	0.1133	0.1143

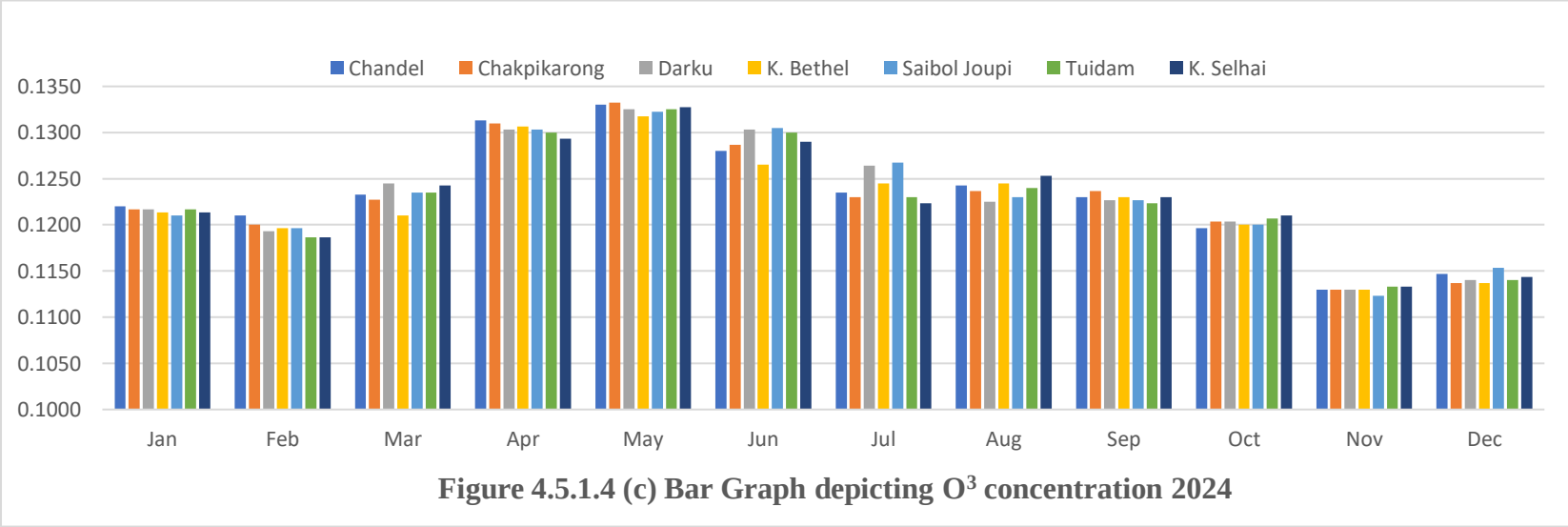

Figure 4.5.1.4 (c) Bar Graph depicting O^3 concentration 2024

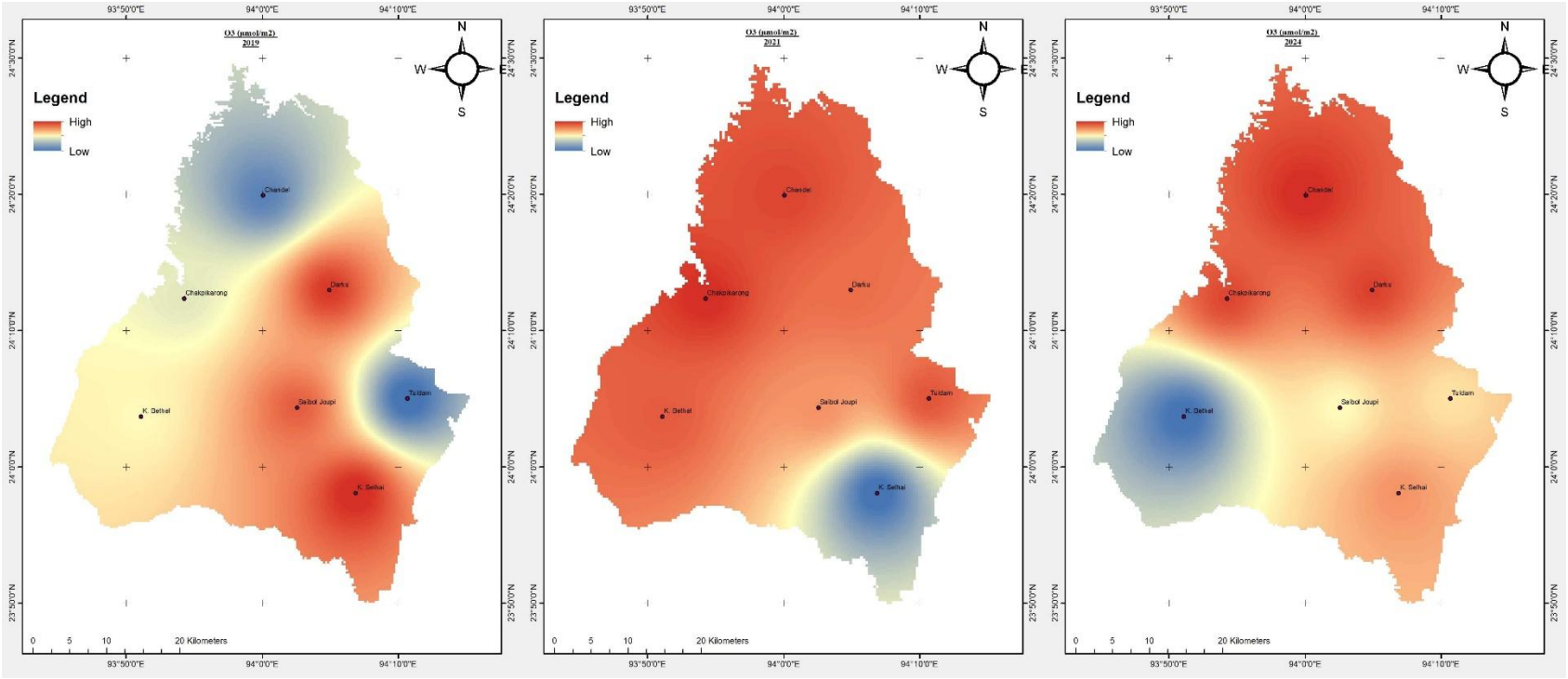

Figure 4.5.1.4 (d) Yearly Spatial Distribution of O^3 concentration Map

Ozone concentration in mol/m^2

The monthly mean O_3 concentration are shown in Fig 9. We can observe that there is no drastic variation in the concentration level from one sample site to another. Table 14. Shows that the mean monthly concentration in the year 2019 ranges between 0.1030 mol/m^2 to 0.1263 mol/m^2. We also observe minor to no variation in concentration level across the sample sites, especially in 2019. In the year 2021, the monthly mean concentration of O_3 was highest in the month of May with approximately 0.12 mol/m^2 at all the sample sites. Similarly, the month of May recorded the highest mean concentration of O_3 in the year 2014, with around 0.13 mol/m^2 at all the sample sites. In the context of yearly average, we observed that 2019 recorded 0.1176 mol/m^2, 2021 with 0.1199 mol/m^2 and 0.1230 mol/m^2 in 2024. We can see an increasing trend in the average concentration.

4.6 Air Quality Status

Analysing the monthly variation in the mean Concentration for CO, HCHO and NO_2 for all the study period years, it is seen that the level of concentration follows a similar pattern, where the peak level in concentration is exerted during the month of March. This phenomenon is attributed to dry weather and the agricultural practice of Shifting cultivation, which is a common agricultural practice in addition to permanent cultivation. The burning of fallen vegetation exerts pollutants gases into the atmosphere. While we observe lower level of overall pollutants Concentration in the month of July-September, which is the result of rainfall and wind dispersion.

Chandel town is the Head-quarter of Chandel District and Chakpikarong is sub-division, and the rest of the sample sites are situated at location largely comprising of vegetative covers. However, upon analysing the monthly mean concentration we see that in the year 2019, CO concentration at Tuidam (0.0520 mol/m^2), K. Selhai (0.0465 mol/m^2) and Saibol Joupi (0.0455 mol/m^2) were higher than Chandel (0.0418 mol/m^2) and Chakpikarong (0.0435 mol/m^2). We see the same trend in the year 2021, where K. Selhai with highest concentration of 0.673 mol/m^2, followed by Tuidam with 0.0660 mol/m^2 and Saibol Joupi with 0.0600 mol/m^2. Which are relatively higher than

its urban counterparts namely Chakpikarong with 0.0570 mol/m^2 and Chandel (0.0483 mol/m^2) with the least level of concentration during the month of March. Even in the case of yearly Co average concentration, we see in the year 2019, Saibol Joupi (0.0357 mol/m^2, Tuidam (0.0390 mol/m^2) and K. Selhai (0.0381 mol/m^2) recorded higher CO concentration than Chandel (0.0345 mol/m^2) and Chakpikarong (0.0355 mol/m^2).

We see a similar pattern in the Concentration level for 2021 and 2024 as well. In 2021, chandel and chakpikarong recorded 0.0344 mol/m^2 and 0.0358 mol/m^2 respectively, which were relative lower than Saibol Joupi with 0.0363 mol/m^2, Tuidam with 0.0396 mol/m^2 and K. Selhai with0.0387 mol/m^2. Similarly, in 2024, Chandel had 0.0353 mol/m^2 and Chakpikarong recorded 0.0354, while K. Selhai had the highest level of mean concentration with 0.0388, followed by Tuidam and Saibol Joupi with 0.086 mol/m^2 and 0.0361 mol/m^2 respectively. Analysing the monthly mean concentration variation for both HCHO and NO_2 across the study years, we see variation across the sample sites, similar to that of CO concentration. We see highest recorded concentration of NO2 in the month of March for all the three study years. We can also observe the urban centre namely Chandel and Chakpikarong recorded lesser level of concentration in the peak month of March for the year 2024, when compared to K. Bethel, Tuidam and K. Selhai. In the context of HCHO concentration as well, the peak months of March and April, both Tuidam and K. Selhai had the highest level of concentration.

Ozone seasonal variation across all location showed the higher level of concentration are recorded in the month of April-June. This peak level of concentration can be attributed to higher level of solar or sunlight associated with the early to mid-summer, as sunlight is the key ingredient for the formation of O_3 in the lower. On the other hand, lower O_3 concentration level is recorded in the winter season. Cooler temperature along with lesser radiance sunlight means lesser production of VOCs and sunlight for the formation of ozone. Since Ozone pollutant is not exerted from a source point, but rather a result of reaction of NO_2 in the presence of sunlight. The result is minute variation in the concentration level across sample site.

Chapter 5.

Identification and assessment of vulnerability of Eco-Environment in study area.

5.1 Introduction

Anthropogenic activities of the growing population in addition to climate changes leading to natural disasters, constantly affected adversely our fragile ecology and environment. The irrational utilization of resources leads to the destruction of the ecological balance (Yan and Zhao, 2009). The quality status of ecological environment is necessary for the well-being of not only humans and our survival, but also for other organisms. As a result, there is loss of habitats, degradation of ecosystem functions, and global climate changes (Foley *et al*. 2005; Zhang *et al.* 2016). Hence, there is much need to monitor our ecosystem for protection as well as sustainable development.

The concept of sustainable land management calls for integrated technology, policies and activities aimed at integrating socio-economic principles with environmental concerns, so as to simultaneously enhance productivity, attain security, prevent further degradation of natural resources and gain viable economical returns acceptable to the society (Rajendra *et al.,* 1999). With the advancement and innovation in remote sensing technology, the indexes and methods of ecological environmental quality assessment and change detection at large scale is enhanced (Kerr and Ostrovsky 2003; Foody, 2007; Huang *et al.* 2012; Zhang *et al.,* 2017).

5.2 Remote Sensing-based Ecological Index (RSEI)

The remote sensing based environmental index (RSEI) is a recently formulated index that is capable of differentiating the ecological status of a region across time through remotely sensed datasets like Landsat etc. RSEI is favourable to quantitatively evaluate the variation of ecological environment quality for region (Xu and Tang, 2013; Lin and Pan, 2014). RSEI has been a proven method deployed to monitor and assess the ecological quality of a region. First introduced by Hu and Xu (2018) to evaluate the ecological quality of Fuzhou city, China. Many studies have used RSEI

to assess the quality of ecosystems like forests (Xu *et al*., 2019), cities (Hu & Xu, 2018; Zhai et al., 2019), wetlands Jing *et al*., (2020).

5.2.1 RSEI Indicators

This study takes four crucial indicators for RSEI, which are related closely to Human survival among many natural factors reflecting ecological quality. They can be directly perceived by people and are often used to evaluate the eco-environmental quality (Gupta et al., 2012). The four indices calculated using related thematic remote sensing indexes:

$$RSEI = f\ (NDVI, WET, LST, NDSI)$$

Where, RSEI is Remote Sensing Ecological, NDVI is Normalized difference vegetation index, WET (wetness), LST (Land Surface Temperature) and NDSI is Normalized Difference Soil Index.

5.2.2 Normalised Difference Vegetation Index

NDVI represents Greenness, which reflects the measurement of the biomass, leaf area index, vegetation coverage, vegetation health (*Rouse et al., 1973)*. NDVI is expressed as:

$$NDVI = (NIR-R)/(NIR+R)$$

Where, NIR and R represents Near Infrared Band and Red Band, respectively.

5.2.3 WET

The Tasseled Cap Transformation (TCT) of brightness, greenness and wetness has been extensively used in monitoring Land cover as well as ecological studies (Zawadzki et al., 2016). TCT also represent soil moisture which is crucial to study soil and plants moisture (*Kauth and Thomas 1976; Huang et al. 2002*).

WET for Landsat5 TM can be expressed as follows (*Crist, 1985; Baig et al., 2014*)

$$WET_{TM} = 0.0315\,\rho_{Blue} + 0.2021\,\rho_{green} + 0.3102\,\rho_{Red} + 0.1594\,\rho_{NIR} - 0.6806\,\rho_{SWIR1} - 0.6109\,\rho_{SWIR2}$$

Where ρ_{Blue}, ρ_{green}, ρ_{Red}, ρ_{NIR}, ρ_{SWIR1} and ρ_{SWIR2} are the corresponding bands of Blue, Green, Red, Near Infrared, Short-Wave Infrared 1 and Short-Wave Infrared 2 of TM, respectively.

The Wetness (WET) component of Landsat8 OLI can be expressed as follows (*Baig et al., 2014*)

$$WET_{OLI} = = 0.1511\,\rho_{Blue} + 0.1972\,\rho_{green} + 0.3283\,\rho_{Red} + 0.3407\,\rho_{NIR} - 0.77117\,\rho_{SWIR1} - 0.4559\,\rho_{SWIR2}$$

Where ρ_{Blue}, ρ_{green}, ρ_{Red}, ρ_{NIR}, ρ_{SWIR1} and ρ_{SWIR2} are the corresponding bands of Blue, Green, Red, Near Infrared, Short-Wave Infrared 1 and Short-Wave Infrared 2 of OLI, respectively.

5.2.4 Normalised Difference Soil Index

Normalized difference soil index (NDSI) denates the dry index proxy (Xu et al., 2017; Li et al., 2020a) which is the average of the sum of Soil index andf Index Based Built-up Index:

$$NDSI = (SI+IBI)/2$$

$$SI = [(\rho_{SWIR1+}\,\rho_{Red}) - (\rho_{Blue+}\,\rho_{NIR})]/[(\rho_{SWIR1-}\,\rho_{Red})+(\rho_{Blue+}\,\rho_{NIR})]$$

$$IBI= \{2\,\rho_{SWIR1}/(\rho_{SWIR1}+\rho_{NIR})-[\rho_{NIR}/(\rho_{NIR}+\rho_{Red})+\rho_{Green}/(\rho_{Green}+\rho_{SWIR1})]\}/\{2\,\rho_{SWIR1}/(\rho_{SWIR1}+\rho_{NIR})+[\rho_{NIR}/(\rho_{NIR}+\rho_{Red})+\rho_{Green}/(\rho_{Green}+\rho_{SWIR1})]\}$$

Where ρ_{Blue}, ρ_{green}, ρ_{Red}, ρ_{NIR}, ρ_{SWIR1} and ρ_{SWIR2} are the corresponding bands of Blue, Green, Red, Near Infrared and Short-Wave Infrared 1of TM and OLI, respectively.

Figure 5.2 shows the working Methodology that was followed for the identification and assessment of vulnerability of Eco-Environment in study area.

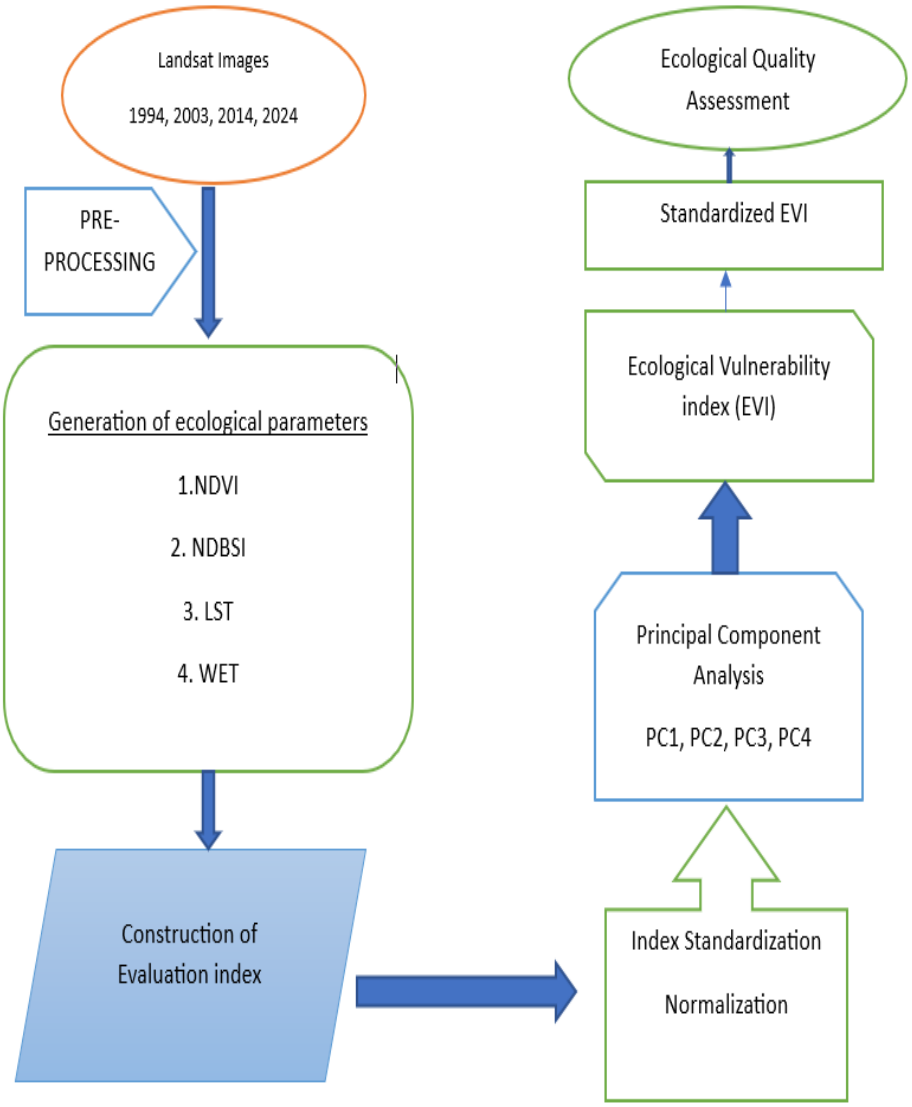

Fig. 5.2. Working methodology flow-chart

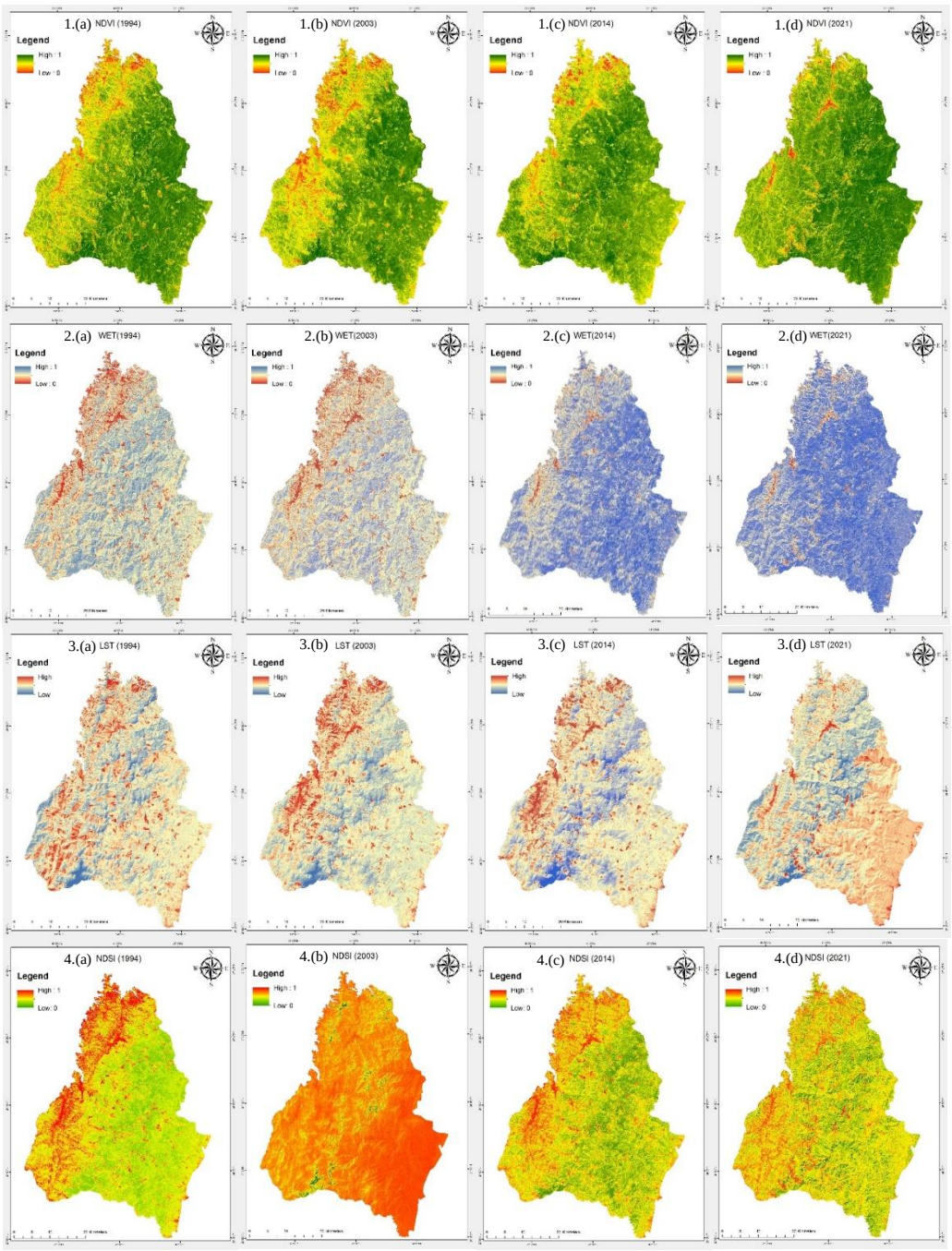

Figure 5.2. Remote Sensing-based Ecological Index (RSEI) Indicators

1. **NDVI (a) 1994. (b) 2003. (c) 2014. (d) 2021.**
2. **WET (a) 1994. (b) 2003. (c) 2014. (d) 2021.**
3. **LST (a) 1994. (b) 2003. (c) 2014. (d) 2021.**
4. **NDSI (a) 1994. (b) 2003. (c) 2014. (d) 2021.**

5.2.5 Land Surface Temperature (LST)

The common method of obtaining LST from Landsat datasets includes the conversion of digital numbers (DNs) of the thermal band, which is band 6 in Landsat TM and band 10 and band 11 in Landsat OLI, into at-satellite spectral radiance values (L_λ) as follows:

$$L = gian \times DN + bias$$

$$T = K_2 / \ln(K_1 / L + 1)$$

$$LST = T / [1 + (\lambda T / \rho) \ln \varepsilon]$$

Where L is the radiance value of Landsat5TM infrared band and Landsat 8OLI thermal band 10, and DN is the pixel value of the band, gain is the gain value, bias is the offset value of the thermal infrared band. T is the temperature, and K1 and K2 are the calibration parameter. K_1=607.76 W/(m^2.sr.µm) and k_2=1,260.56 K in Landsat 5TM and K_1=774.89 W/(m^2.sr.µm) and K_2=1,31.108 K in Landsat 8OLI, λ is the wavelength of the thermal band, ρ= 1.438 × 10^{-2} m K, and ε is the surface specific emissivity.

5.3 Index standardization

The unbalanced weight of each indicators as a result of varying dimensions, needs to be standardized into a uniform dimension between [0,1] prior to the calculation of PCA (Xu, 2013).

The following equation is used to normalize each indicator

$$SI_n = \frac{I_n - I_{min}}{I_{max} - I_{min}}$$

Where SI_n is the standard value of the nth index. I_n represent the value, $I_{max,}$ the maximum and I_{min} the minimum values of the nth index in pixel n, respectively.

5.4 Principal Component Analysis

Principal Component Analysis (PCA) is a robust statistical method predominantly employed for dimensionality reduction in extensive, intricate datasets. It is among the oldest and most extensively utilized multivariate analysis techniques. The primary objective of PCA is to diminish the number of variables in a dataset while retaining the most variability of the original data. It does this by transforming the original, often correlated variables into a new set of uncorrelated variables called Principal Components (PCs).

5.4.1 Principal Component Interpretation

The results of PCA given in Table 5.4, demonstrate that the first two components, PC1 and PC2, are overwhelmingly responsible for explaining the variance in the environmental indicators (NDVI, WET, LST, and NDSI) across all years. PC1 and PC2 consistently explain over 95% of the total variance in the data across all four years (ranging from 95.84% in 2014 to 98.25% in 1994).

Principal Component 1 (PC1) is the primary factor, explaining between 82.89% (1994) and 90.18% (2021) of the total variance. Principal Component 2 (PC2) is the secondary factor, contributing between 6.81% (2021) and 15.37% (1994). PC3 and PC4 are negligible, with their combined contribution never exceeding 4.6% in any year.

PC1 dominates variance, driven primarily by LST and NDVI, indicating a persistent inverse relationship between temperature and vegetation. Hydrological (WET) and soil (NDSI) indicators become more relevant in later years. The increasing eigenvalues of PC1 over time reflect growing environmental homogeneity and greater human or climatic influence on the landscape.

2021 stands out for its very high PC1 variance (90.18%) and strong NDSI loading, suggesting significant surface exposure or reflectance change, likely due to land use intensification.

5.4.2 Temporal Trend Interpretation

PC1's contribution increases from 82.9% in 1994 to 90.2% in 2021, suggesting growing dominance of a single environmental driver, mostly temperature and vegetation interactions. We see a trend where NDVI consistently loads negatively on PC1, showing declining vegetation influence associated with rising land surface temperatures (LST). Results also show NDSI's rising loading (especially in 2021) implies increasing surface exposure or soil reflectivity, possibly due to deforestation, land degradation, or urban expansion. The PCA results indicate that eco-environmental changes from 1994 to 2021 are increasingly dominated by thermal and vegetation dynamics. The progressive strengthening of PC1 suggests reduced environmental complexity, possibly due to anthropogenic land use changes, deforestation, and climate-induced surface warming.

Table 5.4. Results of principal component analysis

YEAR	INDICATORS	PC1	PC2	PC3	PC4
1994	NDVI	-0.65429	-0.73728	-0.16828	0.00255516
	WET	-0.28961	0.439175	-0.79346	0.306058289
	LST	0.694315	-0.49751	-0.51944	0.024229674
	NDSI	0.077214	-0.12659	0.268847	0.95170096
	Eigen Value	**0.02678**	**0.00496**	**0.00037**	**0.000193311**
	Contribution rate %	**82.8867**	**15.3665**	**1.14852**	**0.5982**
2003	NDVI	-0.64837	-0.73788	-0.10617	-0.154537388
	WET	-0.21551	0.349151	0.188317	-0.892291322
	LST	0.643423	-0.40635	-0.49534	-0.418951655
	NDSI	0.345221	-0.4105	0.841369	-0.066437216
	Eigen Value	**0.04113**	**0.00447**	**0.00165**	**0.000242209**
	Contribution rate %	**86.5961**	**9.41204**	**3.48192**	**0.509893392**
2014	NDVI	-0.6879	-0.72228	0.019781	-0.068626243
	WET	-0.17198	0.256687	0.117391	-0.943797053
	LST	0.639692	-0.58878	-0.37375	-0.323186234
	NDSI	0.296654	-0.25645	0.919859	-0.009392474
	Eigen Value	**0.02631**	**0.0036**	**0.00123**	**0.000067871**
	Contribution rate %	**84.306**	**11.534**	**3.94254**	**0.217492171**
2021	NDVI	-0.26358	-0.89784	0.352088	-0.02129294
	WET	-0.10299	0.04646	-0.0187	-0.993421012
	LST	0.153692	-0.39911	-0.90376	-0.017586001
	NDSI	-0.94673	0.180118	-0.24271	0.111139711
	Eigen Value	**0.09983**	**0.00754**	**0.00324**	**0.000090504**
	Contribution rate %	**90.1814**	**6.80889**	**2.92792**	**2.927915431**

5.5 Ecological vulnerability index Evaluation method

The ecological vulnerability index determines the characteristics and status of ecological vulnerability. When building ecological index besides the appearance of a single indicator, the combination of information from the above four indicators should also be included. A common method is to simply add up the individual indicators (Kearney *et al*., 1995), to simply multiply them by their respective weights and then add them up (Williams *et al*., 2009)

The multidimensional statistical method of principal component analysis is a multidimensional data compression technique that uses a sequential vertical rotation of the coordinate axes to concentrate the multidimensional information into a few characteristic components, which frequently represent specific characteristic information. It does this by linearly transforming multiple variables to select a few key variables (Xu, 2013). The fact that the weights of each indicator are automatically and impartially generated based on each indicator's contribution to each main component quantity rather than being artificially determined, thus, the possibility of biasness is evaded, is another benefit of employing principal component analysis. Another advantage of Principal component analysis, is that it represents the information conveyed by more variables using fewer comprehensive indicators by converting many indicators into a small number of uncorrelated comprehensive indicators.

The principal component may capture the information expressed by most variables when principal component analysis is performed on the indicator indexes, namely NDVI, WET, NDSI, and LST on QGIS, and the cumulative contribution rate of the primary component exceeds 85%, then we can calculate EVI (Yao et al., 2016; Wang and Su, 2018) as follows

$$\mathbf{EVI=r_1\gamma_1+ r_2\gamma_{2+}\ldots\ldots+ r_n\gamma_n}$$

Where EVI is the ecological vulnerability index. r_n and γ_n are the contribution rate of the nth principal component respectively.

Further the result of Ecological Vulnerability index is then standardized between the value of 0-10, so that the outcome can be interpreted more comprehensively. The following equation is used to standardize the values

$$SI_{EVI} = \frac{EVI_n - EVI_{min}}{EVI_{max} - EVI_{min}} \times 10$$

Where SI_{EVI} represents the standardized value, and it is between 0 and 10.

EVI_n, EVI_{min} and EVI_{max} are the value, minimum and maximum value of ecological vulnerability index, respectively. Then the standardized EVI was classified base on the ecological vulnerability classification, namely, negligible vulnerability, light vulnerability, medium vulnerability, strong vulnerability and extreme vulnerability.

5.6 Combination of the indicators

The quantification index is essential to the evaluation of ecological quality. As a consequence, the normalized indices (dryness, heat, wetness, and greenness) integrate the bands and provide the PCA result, which was displayed in Table 5.4.

Table 5.4 shows that for the four periods (1994, 2003, 2014 and 2021), the contribution rates of each index in the first principal component were 82.88 %, 86.59%, 84.30 % and 90.18 %, respectively. The relative stability of each index suggests that the majority of the four indexes' features were cantered in the first main component. The fact that both the NDVI and the WET are positive in the first principal component suggests that they work in concert to improve the ecological environment's quality. The natural environment is negatively impacted, as indicated by the negative LST and NDSI. Other primary components (PC2, PC3, and PC4) have unpredictable symbols and sizes, which makes ecological phenomena hard to describe. In conclusion PC1 represents the most variability among all the indices when compared to other PCs. As a result, RSEI is created by combining the four indications using PC1.

5.7 Ecological Status

The mean values of RSEI of 1994, 2003, 2014 and 2021 are taken into account so that the ecological environmental quality of Chandel district can be analysed. Table 5.7. shows that the mean value of RSEI in 1994, 2003, 2014 and 2021 was 2.8, 2.9, 3.22 and 3.6 respectively. There is a gradual increasing trend in the mean values with time. The overall RSEI improvement is the result of mixed trends in its constituent indices, with positive trends in Vegetation and Heat largely compensating for negative trends in Moisture and Dryness.\

The greenness which is denoted by NDVI, decrease from 0.84 in 1994 to 0.81 in 2003, a 3.57% reduction, and further decreases to 0.79 in 2014, which accounts about 2.46% decrease from 0.81 in 2003. But we see an increase of 13 % in 2021 at 0.9 from 0.79 in 2014.

Table 5.7. Mean values of RSEI and four indices

	1994	changes between 1994 and 2003 (%)	2003	changes between 2003 and 2014 (%)	2014	changes between 2014 and 2021 (%)	2021
NDVI	0.84	-3.57	0.81	-2.46	0.79	13.92	0.9
WET	0.74	-4.05	0.71	-2.81	0.69	-4.34	0.66
NDSI	0.38	160.52	0.99	-56.56	0.43	83.72	0.79
LST	0.36	-30.55	0.25	44	0.36	-2.77	0.35
RSEI	2.8	3.571	2.9	11.03	3.22	11.80	3.6

In the context of Wetness which is indicated by the index WET, there is a constant reduction trend throughout the period from 1994 to 2021. The mean value in the 1994 was 0.74, which was reduced by 4.05% to 0.71 in 2003, then reduced by 2.81% to 0.69 in 2014. Furthermore, the mean value in 2021 was 0.66 which accounts for 4.34% reduction from 0.69 in 2014.

The dryness indicated by NDSI increased by 160% in 2003 from 0.38 in 1994. Then decreased by about 56.56% to 0.43 in 2014. We can see an increase of 83.72% from 0.43 in 2014 to 0.79 in 2021. LST gives us the heat, which indicates a fluctuating

trend. First there is a decrease of 30% from 0.36 I 1994 to 2.9 in 2003. There is an increase of 44% from 2.9 in 2003 to 0.36 in 2014. Then, we see a small decrease of 2.77% from 0.36 in 2014 to 3.6 in 2021. This finding suggesting that soil exposure or dryness is a recurring and worsening issue in the later period.

LST (Land Surface Temperature): The temperature profile has been mostly stable, with a strong decrease of 30.55% in the first period (1994-2003), followed by a compensatory increase of 44% from 2003 t0 2014, and then stabilizing for a small net decrease of -0.01 by 2021.

The ecological health, as measured by the RSEI, has improved in Chandel District from 1994 to 2021, primarily driven by strong growth in vegetation (NDVI) and stable surface temperatures (LST). However, this improvement is masking significant underlying issues: A consistent decline in moisture (WET). A major and recurring increase in dryness/soil exposure (NDSI), which rebounded sharply in the most recent period (2014-2021). The district appears to be getting greener and hotter (or at least remaining warm) while getting drier and having more exposed/bare soil. The benefits from vegetation increase are outweighing the negative effects of dryness and moisture loss in the composite RSEI calculation.

5.8 Eco-environmental vulnerability dynamic

In order to assess the ecological environmental quality better, the RSEI index were standardized between the values of 0-10, and further classified into 5 classes, namely, Negligible vulnerability, Light vulnerability, Medium vulnerability, Strong vulnerability and Extreme vulnerability.

Table 5.8. shows the area distribution of ecological vulnerability in Chandel district. Fig. 5.8 (a), (b), (c) and (d) depicts the yearly area distribution of ecological vulnerability. There is a declining trend in the Negligible vulnerability class throughout the period from 1994-2003, 2003-2014 and 2014-202, accounting about 32.27%, 29.74%, 16.3% and 2.14% in 1994, 2003,2014 and 2021 respectively. In the

year 2021 only 2.14% of the total area was under the least vulnerable class i.e., negligible vulnerability, which accounts about 288 km^2 reduction in area. In the context of light vulnerability results shows increasing trends throughout the study period. There was a growth of about 26 km^2 in 2003 when compared to 1994. We see a massive growth of 207 km^2 from 2003 to 2014. 2021 recorded the largest growth of about 222 km^2 from 2014's 1200 km^2 to 1423 km^2 in 2021. Majority of the total area falls under Light vulnerability with 47.44%, 48.73%, 58.88% and 69.77% of the total area in 1994, 2003, 2014 and 2021, respectively.

We see a similar increasing trend throughout the study period for both Medium and strong vulnerability classes. A recorded area of 15.91%, 18%,19.88% and 22.37% of the total area was classified into Medium vulnerability in 1994, 2003, 2014 and 2021, respectively. Similarly, we see 4.37%, 3.54%,4.92% and 5.16% of the total area falling under Strong vulnerability class in 1994, 2003, 2014 and 2021, respectively.

As for the case of extreme vulnerability class, results in table 6, shows that, in 1994, 2003 and 2014, there was a negligible area of under 1 km^2 were categorized under extreme vulnerability. However, in the year 2021, for the first time a total of 11.39 km^2 in area was under the extreme vulnerability class. Fig. 6. Shows depicts the area in red classified as Extreme vulnerable and the an approximate of more than 16,600 population (census 2011) are residing under this classified area.

Table 5.8 Area Distribution of Ecological vulnerability in Chandel District

	1994			2003			2014			2021	
Vulnerability	**Area Km^2**	**%**	**1994-2003**	**Area Km^2**	**%**	**2003-2014**	**Area Km^2**	**%**	**2014-2021**	**Area Km^2**	**%**
Negligible vulnerability	658.2528	32.27	-51.6123	606.6405	29.74	-274.1229	332.5176	16.3	-288.864	43.6536	2.14
Light vulnerability	967.7124	47.44	26.1783	993.8907	48.73	207.045	1200.9357	58.88	222.1668	1423.1025	69.77
Medium Vulnerability	324.6165	15.91	42.4998	367.1163	18	38.4102	405.5265	19.88	50.8617	456.3882	22.37
Strong Vulnerability	89.1684	4.37	-17.0307	72.1377	3.54	28.3167	100.4544	4.92	4.8402	105.2946	5.16
Extreme vulnerability	0.0378	0	-0.0351	0.0027	0	0.351	0.3537	0.02	11.0394	11.3931	0.56

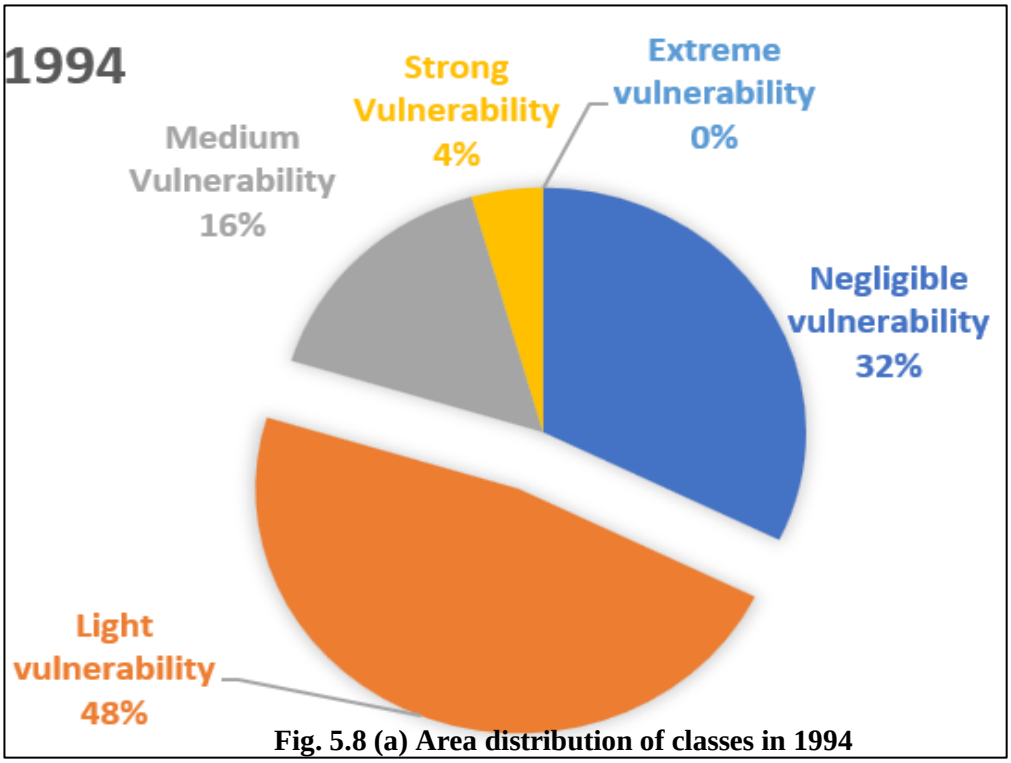

Fig. 5.8 (a) Area distribution of classes in 1994

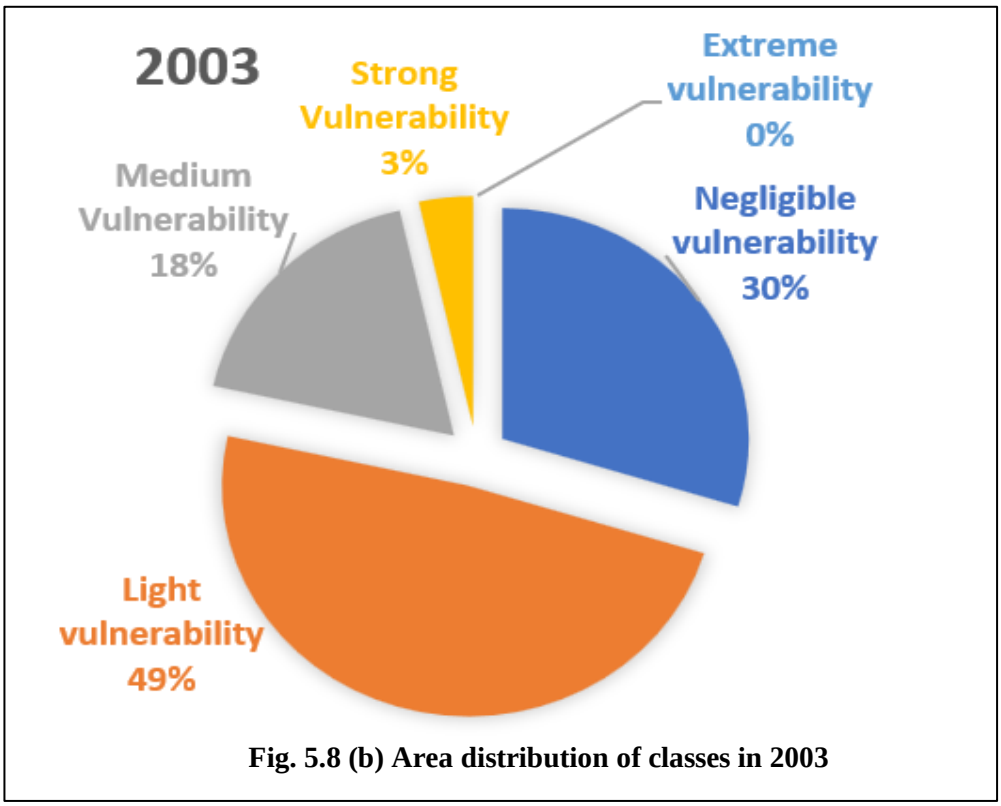

Fig. 5.8 (b) Area distribution of classes in 2003

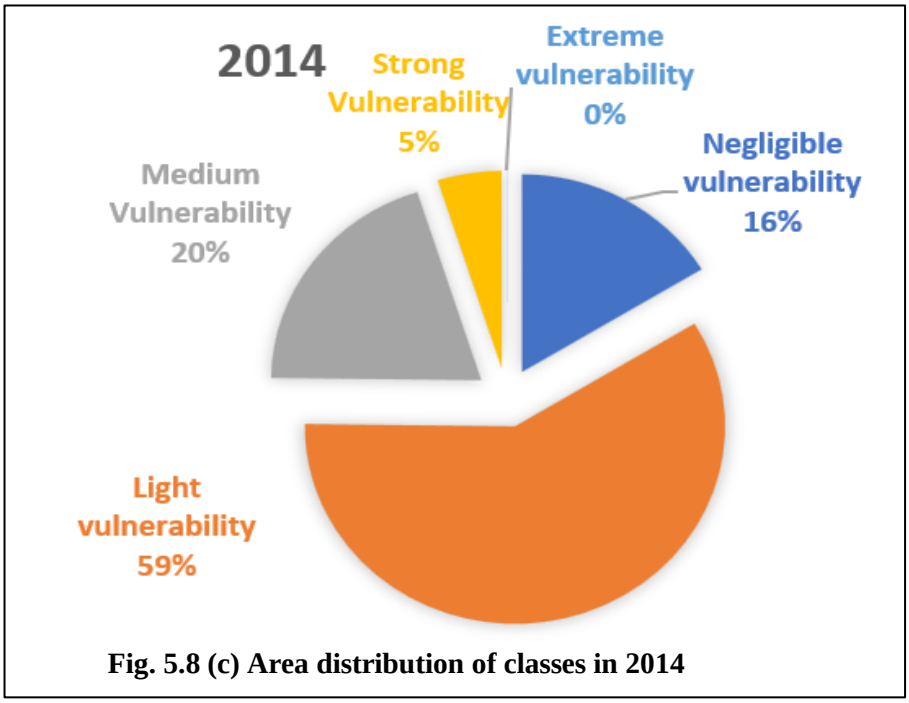

Fig. 5.8 (c) Area distribution of classes in 2014

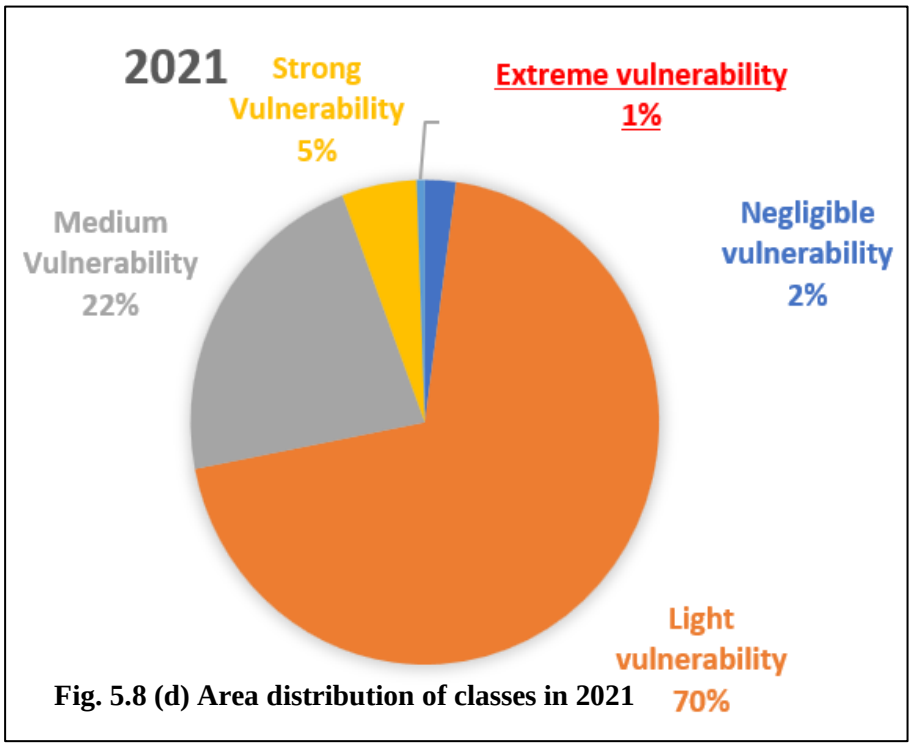

Fig. 5.8 (d) Area distribution of classes in 2021

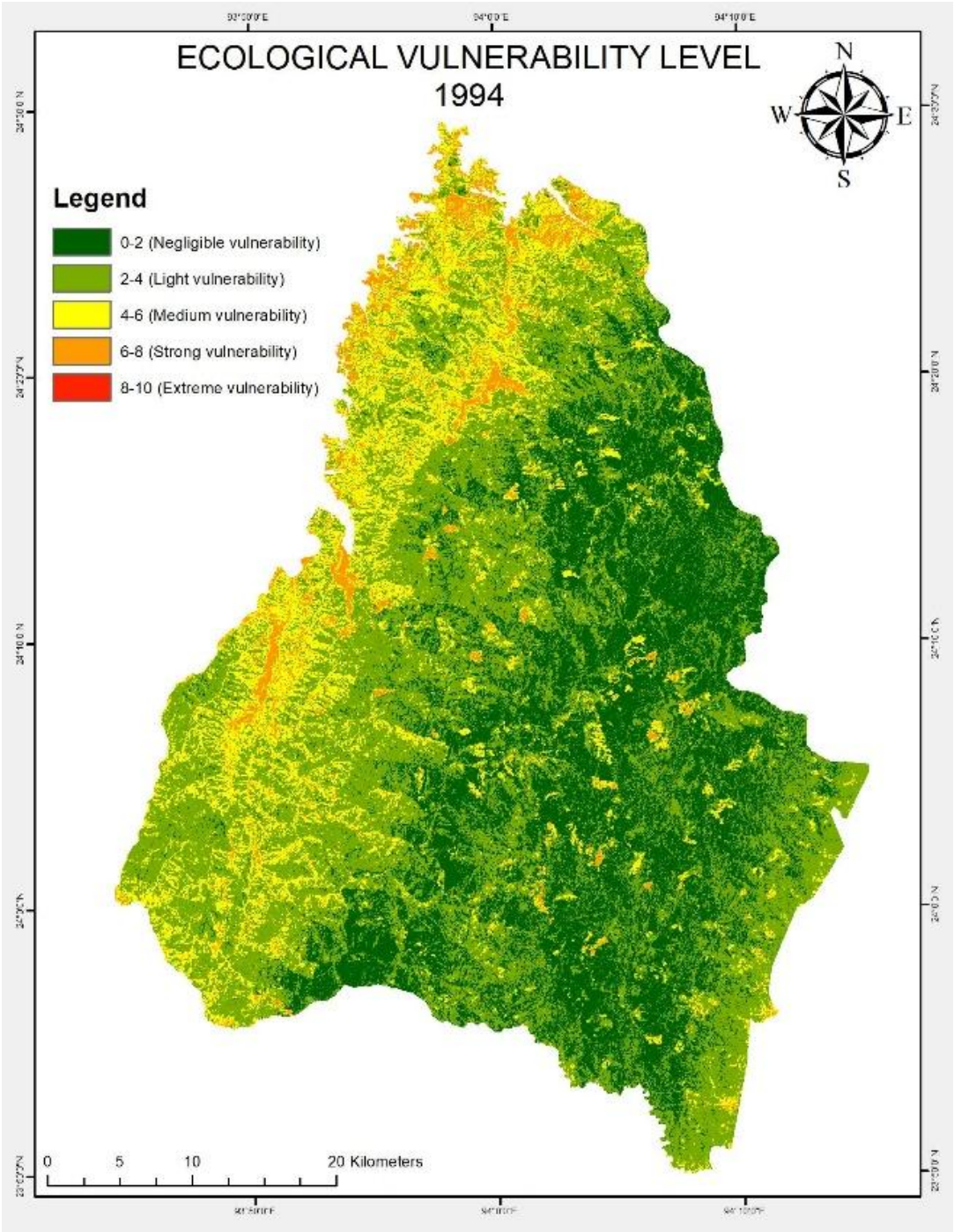

Figure 5.8 (e) Ecological vulnerability 1994

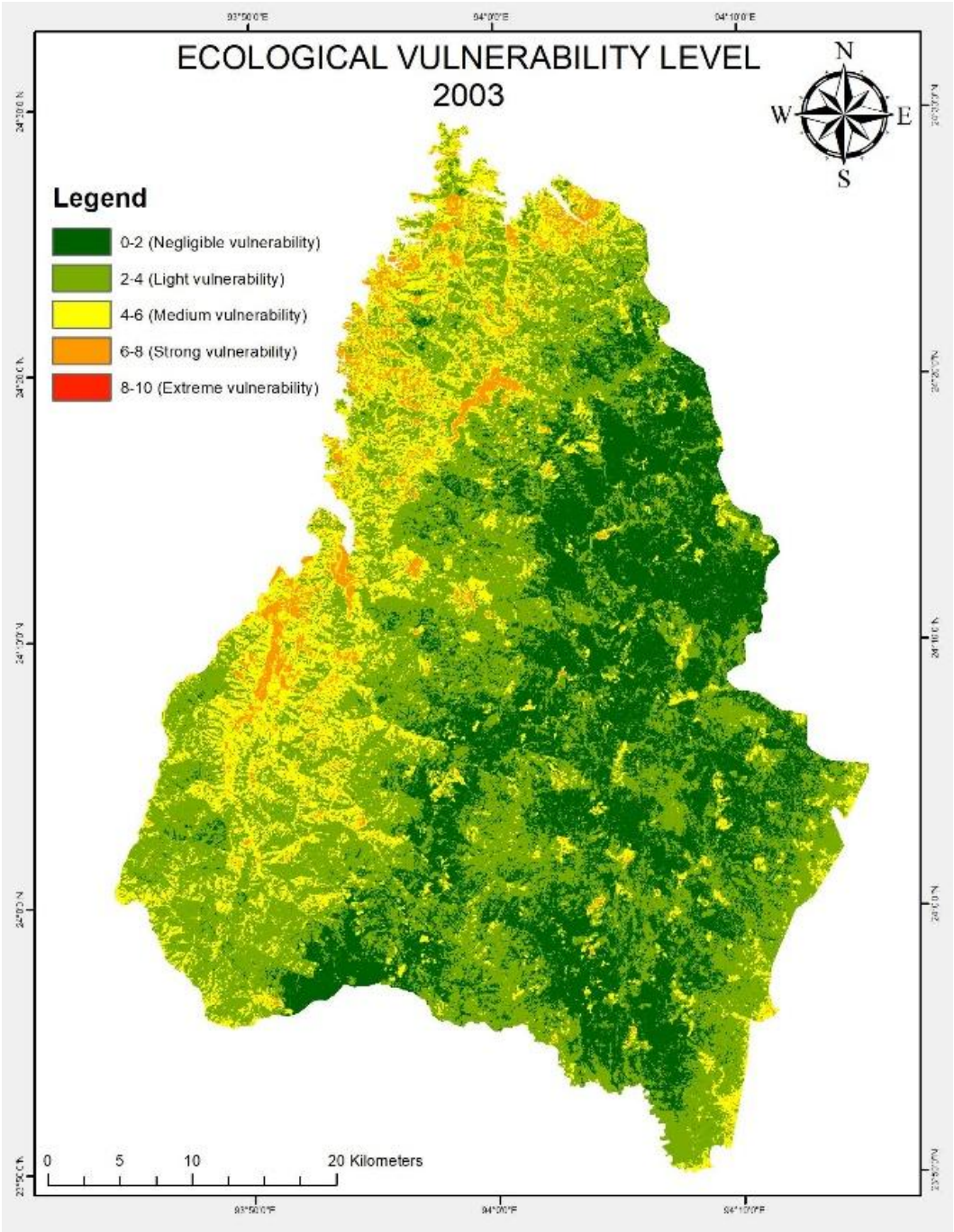

Figure 5.8 (f) Ecological vulnerability 2003

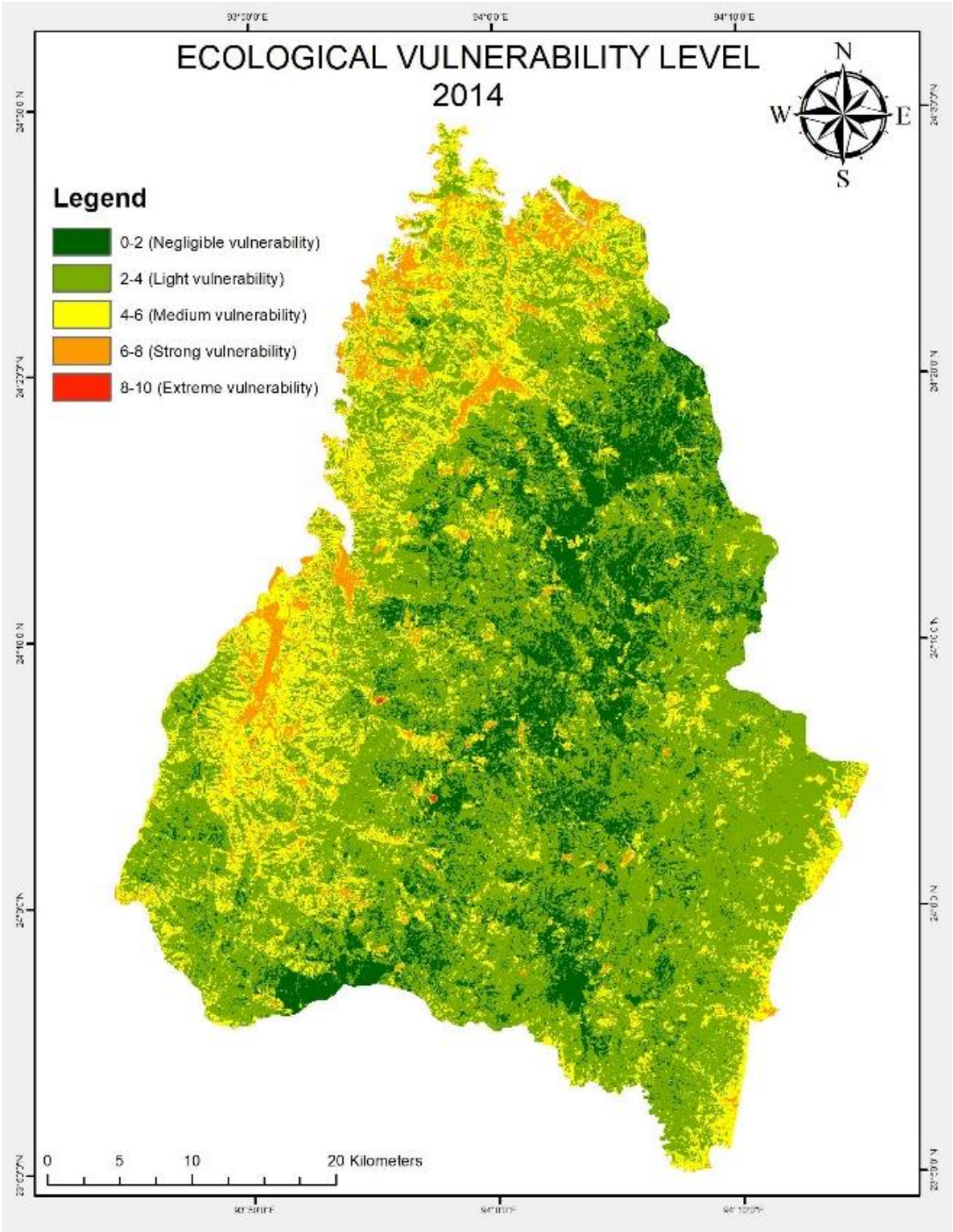

Figure 5.8 (g) Ecological vulnerability 2014

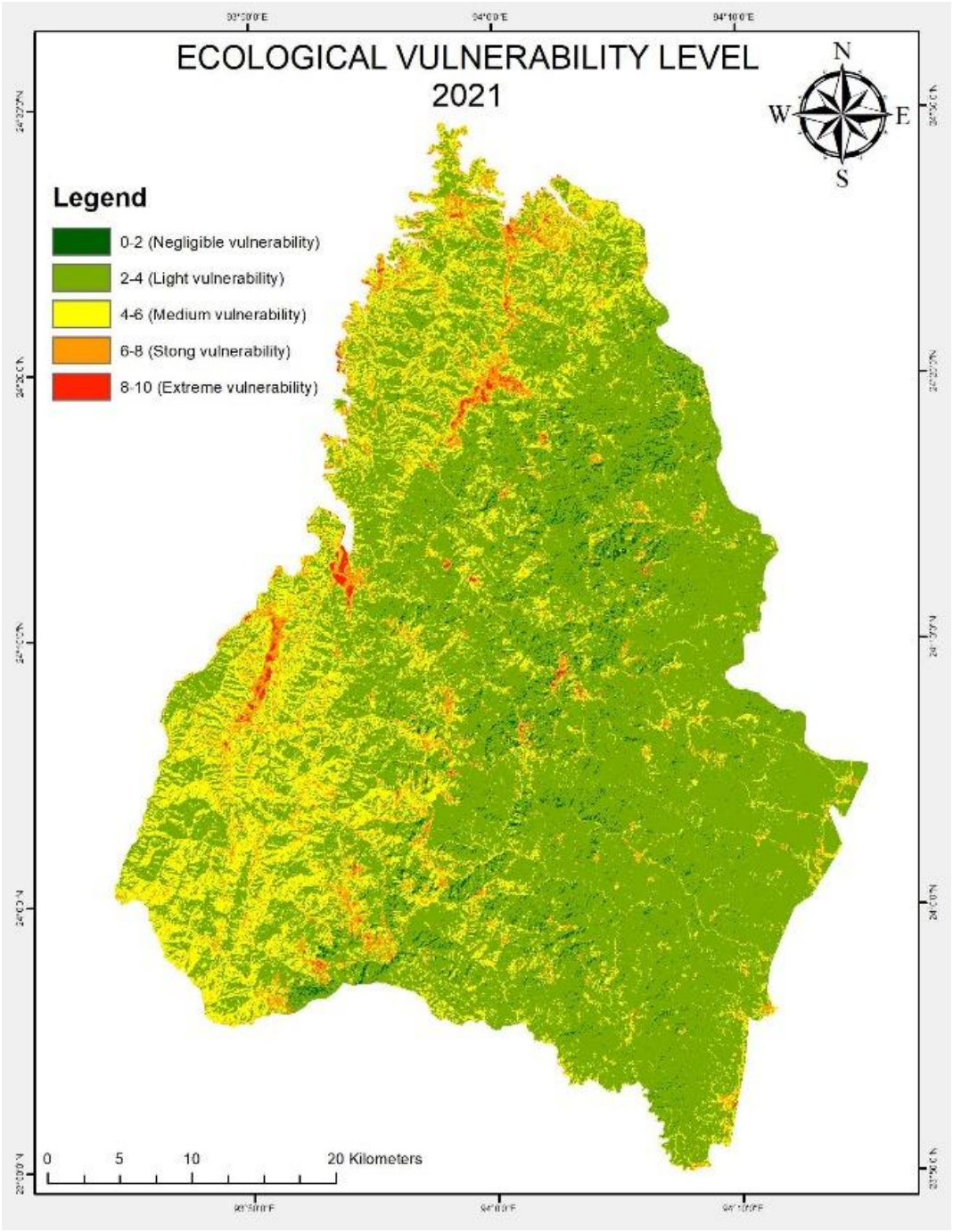

Figure 5.8 (h) Ecological vulnerability 2021

5.9 Eco-environmental vulnerability Class Transition

5.9.1 Vulnerability Class Transition (1994-2003)

Table 5.9.1 shows the Eco-environmental Vulnerability (EEV) Class Change from 1994 to 2003.

A majority (about 82%) of the area remained in the same vulnerability class, indicating eco-environmental vulnerability was stable during 1994–2003.

However, nearly about 18% of the area experienced vulnerability shift, showing local-scale environmental or land-use changes. The Light vulnerability about 984.62 km2 which was almost 76% of the unchanged area, indicating that lightly vulnerable ecosystems remained largely undisturbed between 1994 and 2003.

There was area that transition from lower to higher vulnerability levels;

- Light to Strong: 20.72 km^2
- Medium to Strong: 38.04 km^2
- Strong to Extreme 7.58 km^2
- Negligible to Strong 5.35 km^2
- Negligible to Extreme 0.42 km^2

There was a total area of 72.1 km^2 that increased in Vulnerability indicating that these areas became more environmentally stressed, likely due to deforestation, urban expansion, or agricultural intensification.

There was area that transition from higher to lower vulnerability levels as well:

- Strong to Light: 15.86 km^2
- Medium to Light: 147.16 km^2
- Negligible to Light: 288.92 km^2
- Extreme to Light: 0.14 km^2
- Extreme to Medium: 0.13 km^2

A total area of about 452 km² transition to a lower vulnerability class indicating that these areas experienced improvement, suggesting environmental recovery or management interventions, particularly in zones that transitioned to Light vulnerability.

Negligible to Light vulnerability (288.9 km²) is the largest single change, implying that formerly stable or resilient areas became slightly more vulnerable, as a result from anthropogenic pressure. Whereas Medium to Light vulnerability transition accounted for about 147.2 km², which shows partial improvement in ecological condition, potentially due to natural regeneration or reduced disturbance. Light vulnerability dominates both stable and changed zones, suggesting this class acts as a buffer between stability and stress. Overall trend was a mixed dynamic, with both degradation and improvement processes evident.

Table 5.9.1 Eco-environmental vulnerability Class Change 1994-2003

Class Change	Area in km^2
Extreme vulnerability-Light vulnerability	0.0020
Extreme vulnerability-Medium vulnerability	0.0074
Extreme vulnerability-Strong vulnerability	0.0178
Light vulnerability-Light vulnerability	699.8970
Light vulnerability-Medium vulnerability	111.5890
Light vulnerability-Negligible vulnerability	149.4750
Light vulnerability-Strong vulnerability	8.5448
Medium vulnerability-Extreme vulnerability	0.0027
Medium vulnerability-Light vulnerability	90.4943
Medium vulnerability-Medium vulnerability	188.9660
Medium vulnerability-Negligible vulnerability	18.0169
Medium vulnerability-Strong vulnerability	25.1206
Negligible vulnerability-Light vulnerability	196.2140
Negligible vulnerability-Medium vulnerability	27.0759
Negligible vulnerability-Negligible vulnerability	434.7470
Negligible vulnerability-Strong vulnerability	1.5715
Strong vulnerability-Light vulnerability	10.1019
Strong vulnerability-Medium vulnerability	37.9065
Strong vulnerability-Negligible vulnerability	3.7229
Strong vulnerability-Strong vulnerability	35.2261

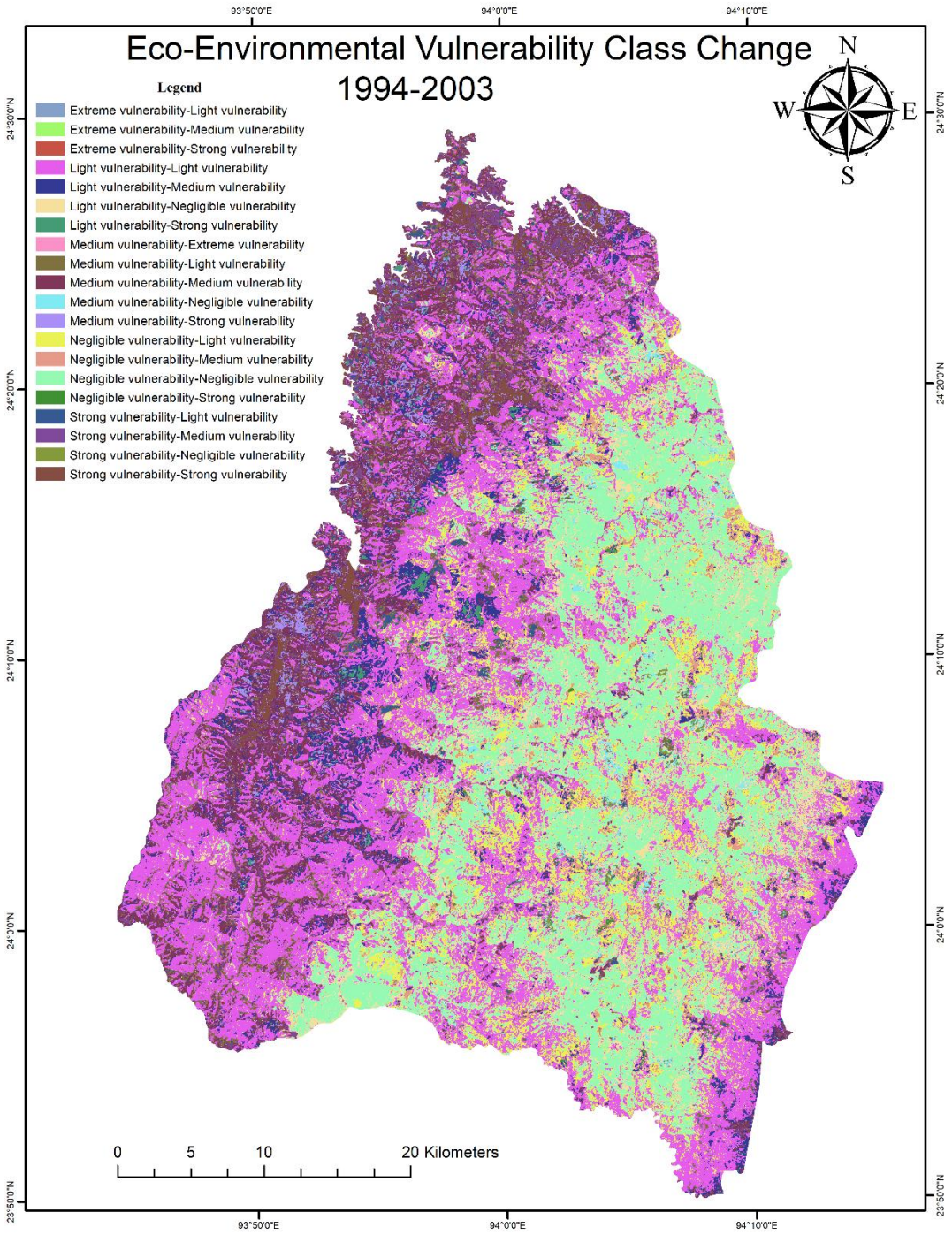

Figure 5.9.1 Eco-environmental vulnerability Class Change 1994-2003

5.9.2 Vulnerability Class Transition (2003-2014)

Table 5.9.2 presents the spatial transitions between eco-environmental vulnerability (EEV) classes from 2003 to 2014, showing how different vulnerability zones evolved in terms of area (km²). Roughly three-fourths of the total area (75%) remained in the same vulnerability class, showing overall eco-environmental stability, while about one-fourth (25%) experienced notable shifts, indicating localized environmental changes. The Light vulnerability class again dominated, covering about 61% of unchanged areas. Negligible and Medium vulnerability zones also showed significant persistence, reflecting continued environmental resilience.

From the table we can see transition from lower to higher vulnerability levels:

- Negligible to Medium: 25.28 km^2
- Negligible to Strong 3.61 km^2
- Light to Medium 146.40 km^2
- Light to Strong 12.90 km^2
- Medium to Strong 44.93 km^2

There was a total area of 233.3 km^2 that transitioned to a higher vulnerability class. Light to Medium accounted for 146.4 km² indicating that these was moderate land degradation. Medium to Strong accounted for about 44.9 km² which points to intensifying stress, from urban growth, deforestation, or agricultural expansion.

On the other hand, a total area of about 201.1 km2 transitioned from higher to lower vulnerability, which indicates that roughly 12% of the landscape during the period 2003-2014, improved in ecological condition, shifting to lower vulnerability categories. The largest transitions were from Medium to Light at about 101 km² and Light to Negligible about 62 km², suggesting partial recovery in several moderately stressed regions.

The Light vulnerability class remains the most dynamic, acting as both the main stable class and the most frequently changing one. Conversely, Negligible to Light accounted about 327 km² indicated newly disturbed areas

Overall, the degradation (233 km²) slightly exceeds improvement (210 km²), implying a net increase in vulnerability during 2003–2014. However, most transitions occur within lower classes (between Negligible and Light, light and Medium. Light and Medium zones are the most transitional, often near settlements, farmlands, or deforested belts.

Between 2003 and 2014, the eco-environmental condition of the study area remained largely stable, with moderate localized shifts. The dominance of Light vulnerability suggests that most areas was under mild environmental stress but still retained recovery potential. However, the growth of Medium and Strong zones signalled increasing pressure from anthropogenic activities, warranting continued environmental monitoring and land management strategies.

Table 5.9.2 Eco-environmental vulnerability Class Change 2003-2014

Class Change	Area in km^2
Extreme vulnerability-Medium vulnerability	0.0027
Light vulnerability-Extreme vulnerability	0.0689
Light vulnerability-Light vulnerability	775.0330
Light vulnerability-Medium vulnerability	146.4000
Light vulnerability-Negligible vulnerability	62.2965
Light vulnerability-Strong vulnerability	12.8969
Medium vulnerability-Extreme vulnerability	0.0818
Medium vulnerability-Light vulnerability	101.0400
Medium vulnerability-Medium vulnerability	205.7140
Medium vulnerability-Negligible vulnerability	13.7922
Medium vulnerability-Strong vulnerability	44.9320
Negligible vulnerability-Extreme vulnerability	0.1284
Negligible vulnerability-Light vulnerability	327.1860
Negligible vulnerability-Medium vulnerability	25.2836
Negligible vulnerability-Negligible vulnerability	249.7470
Negligible vulnerability-Strong vulnerability	3.6063
Strong vulnerability-Extreme vulnerability	0.0507
Strong vulnerability-Light vulnerability	8.1383
Strong vulnerability-Medium vulnerability	24.3208
Strong vulnerability-Negligible vulnerability	0.7669
Strong vulnerability-Strong vulnerability	37.2090

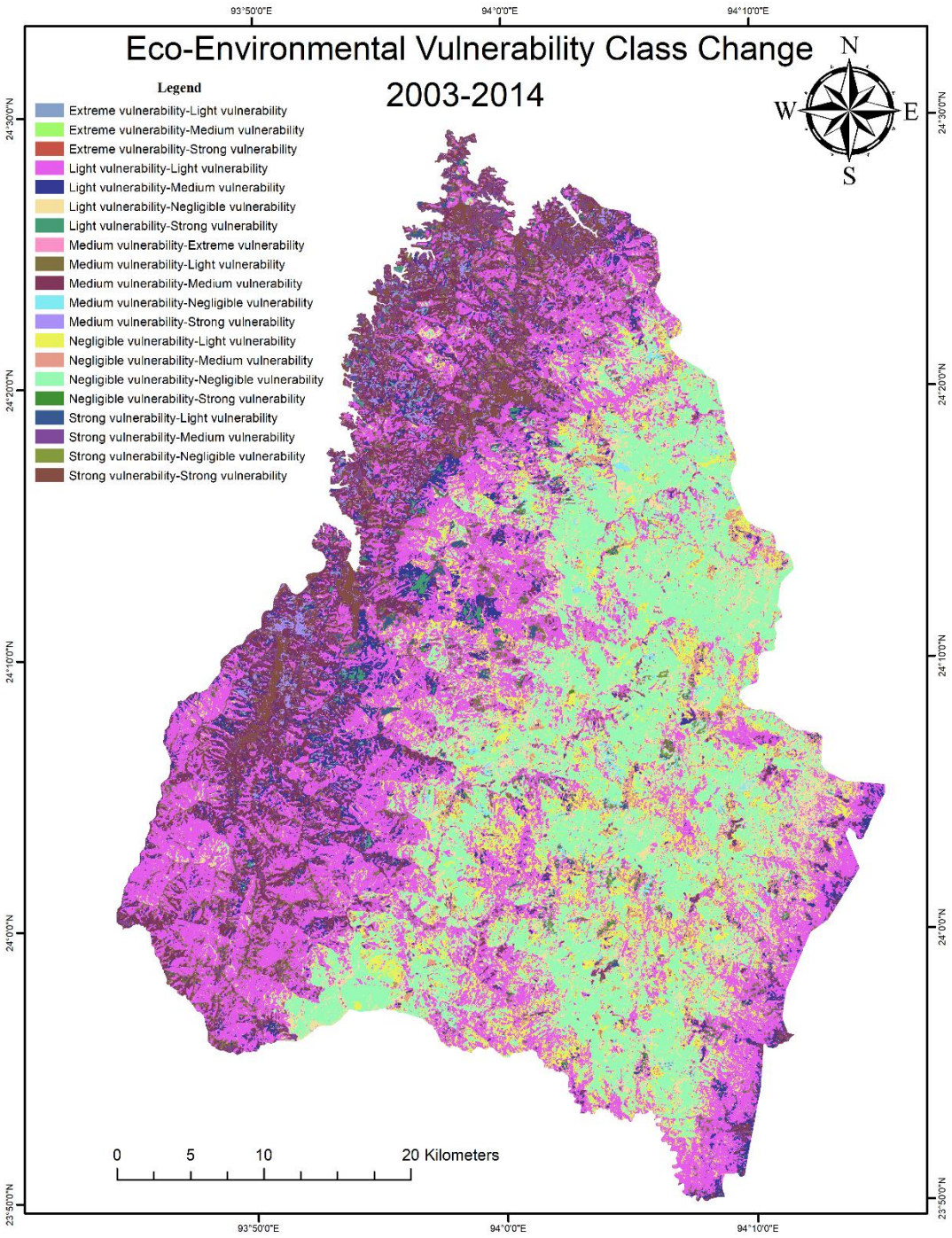

Figure 5.9.2 Eco-environmental vulnerability Class Change 2003-2014

5.9.3 Vulnerability Class Transition (2014-2021)

Table 5.9.3 shows the Eco-environmental Vulnerability (EEV) Class Change from 2014 to 2021. The table outlines the spatial transitions between eco-environmental vulnerability classes from 2014 to 2021, identifying which areas remained stable and which changed in vulnerability. Approximately 82% of the study area remained stable in its vulnerability class between 2014 and 2021, indicating continued eco-environmental resilience. About 18% underwent noticeable transitions, showing localized environmental or land-use changes during this period.
A total area of 74.8 km^2 transitioned from a lower to a higher vulnerability class in this period.

- Negligible to Strong: 5.35 km^2
- Light to Strong: 20.72 km^2
- Medium to Strong: 38.04 km^2
- Strong to Extreme: 7.58 km^2

An area of 38.0 km^2 Medium transitioned to Strong vulnerability and about 20.7 km^2 Light vulnerability transitioned to Strong vulnerability class indicating areas of environmental degradation or human disturbance.

Whereas a total area of 509 km^2 transitioned from a higher to a lower class. The changed area showed improvement in environmental conditions, shifting toward lower vulnerability levels. The most significant recovery trends were the transition of Negligible to Light accounting about 288.9 km^2 and from Medium to Light at about 47.2 km^2.

Light vulnerability continues to dominate the landscape, representing areas under mild but persistent environmental pressure. Improvement exceeds degradation, implying that natural recovery, vegetation growth, or conservation measures may have countered localized stress. Areas shifting toward Strong and Extreme vulnerability correspond to deforested, urbanized, or exposed land zones.

Between 2014 and 2021, the study area maintained a high degree of eco-environmental stability. While certain localized regions showed increased vulnerability, notably Medium to Strong and Light to Strong transitions, the overall landscape displayed resilience and recovery.

Table 5.9.3 Eco-environmental vulnerability Class Change 2014-2021

Class Change	Area in km^2
Extreme vulnerability-Extreme vulnerability	0.0222
Extreme vulnerability-Light vulnerability	0.1359
Extreme vulnerability-Medium vulnerability	0.1257
Extreme vulnerability-Strong vulnerability	0.0456
Light vulnerability-Extreme vulnerability	**1.4475**
Light vulnerability-Light vulnerability	**984.6190**
Light vulnerability-Medium vulnerability	184.4810
Light vulnerability-Negligible vulnerability	20.0418
Light vulnerability-Strong vulnerability	20.7241
Medium vulnerability-Extreme vulnerability	**1.2356**
Medium vulnerability-Light vulnerability	147.1570
Medium vulnerability-Medium vulnerability	**214.3690**
Medium vulnerability-Negligible vulnerability	0.6522
Medium vulnerability-Strong vulnerability	38.0384
Negligible vulnerability-Extreme vulnerability	0.4235
Negligible vulnerability-Light vulnerability	288.9160
Negligible vulnerability-Medium vulnerability	15.1383
Negligible vulnerability-Negligible vulnerability	16.7488
Negligible vulnerability-Strong vulnerability	5.3541
Strong vulnerability-Extreme vulnerability	**7.5756**
Strong vulnerability-Light vulnerability	15.8589
Strong vulnerability-Medium vulnerability	36.8695
Strong vulnerability-Negligible vulnerability	0.0467
Strong vulnerability-Strong vulnerability	38.0983

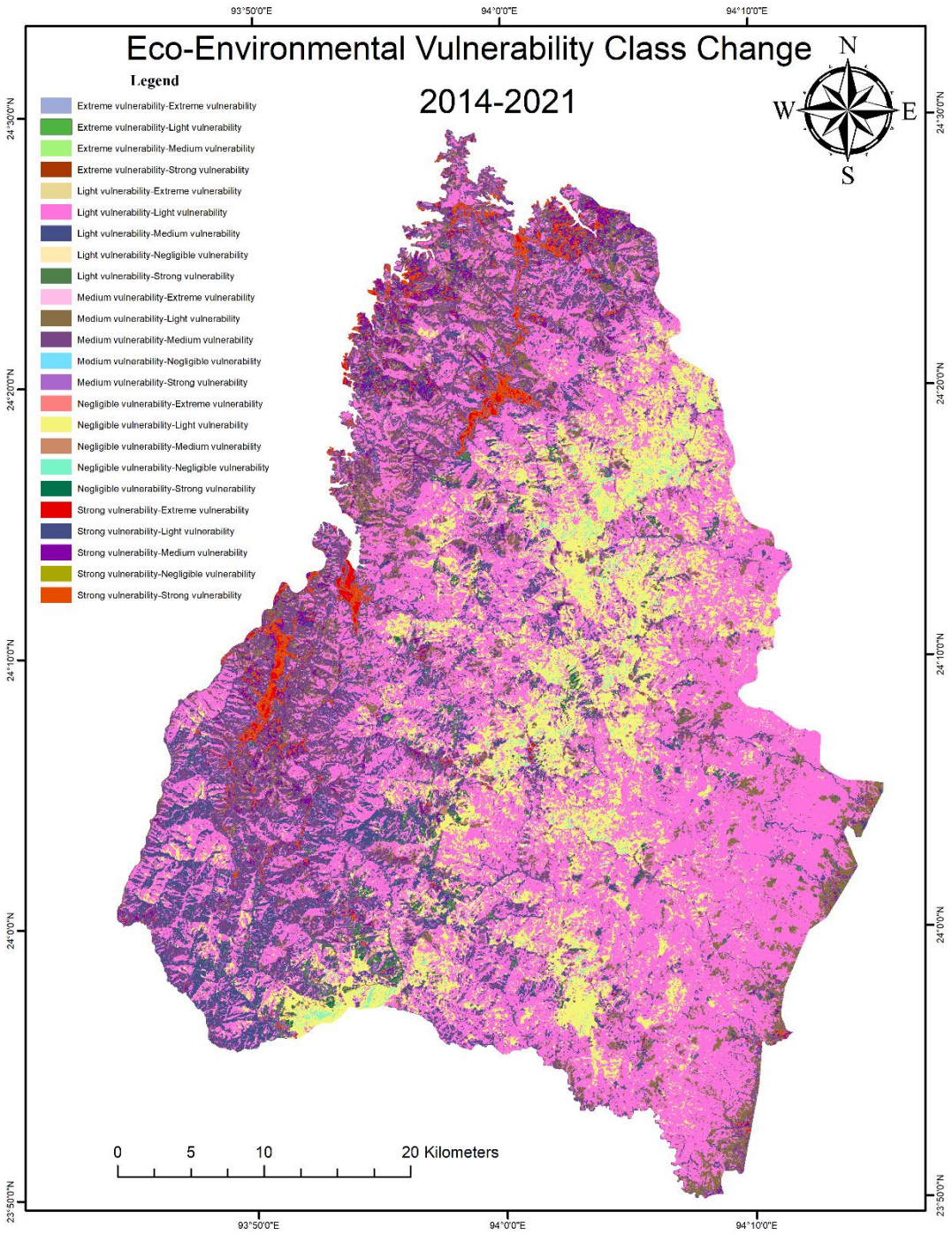

Figure 5.9.3 Eco-environmental vulnerability Class Change 2003-2014

Chapter 6. Summary and conclusion.

Chandel District, located in Manipur, India, is known for its rich biodiversity and pristine environment. However, increasing agricultural, urbanization and economic activities degrades the ecology and environment, while also causing Land coverage to evolve continually. The utilization of land space has altered as a result of human activity. Analysing and comprehending land use and land cover dynamics is essential for the sustainable management of natural resources and ecosystems. This study elucidates the dynamics of Land Use Land Cover in Chandel district from 1994 to 2021. This study utilized satellite images from Landsat 5 Thematic Mapper (1994), Landsat 7 ETM+ (2003), Landsat 8 OLI (2014), and Landsat 8 OLI (2021) to produce the Land Use Land Cover of the study area by Maximum Likelihood classification. Results showed both positive and negative growth in the courses has been noticed. An increase in built-up area and vegetation cover in 2021 compared to 1994. The Built-Up class has experienced significant growth throughout the years, expanding from 158 hectares in 1994 to 936 hectares in 2021. The agricultural land has decreased from 13,143 hectares to 9,254 hectares in 2021. The results of this study may facilitate improved management of the natural resources in the studied area. The growing population is the driving factor for the growth of built-up areas. On the other hand, we see a declining trend in the context of areas under Agriculture. It was observed that most of the conversion of agricultural land is towards built-up and conversion of agricultural land into built-up areas. These findings on the Land Use Land Cover dynamics of the study areas could be used for a Sustainable and better management of our Natural Resources and so, should be closely monitored with a scientific and sustainable approach.

Anthropogenic activities also generate various air pollutants which degrades the air quality and thus raises concern about adverse effects on the health of the atmosphere. Satellite data acquired through the Tropospheric Monitoring Instrument (TROPOMI) onboard the Sentinel-5P satellite are readily available and are proven to be efficient to analyse key atmospheric pollutants. This study analyses major pollutants namely carbon monoxide (CO), Formaldehyde (HCHO), nitrogen dioxide (NO_2) and ozone (O_3). Monthly mean of pollutants concentration was taken into account to analyse monthly variation for the year 2019, 2021 and 2024. Results show highest level of CO,

HCHO and NO_2 concentration during the month of March-April which is attributed to burning of cleared vegetation for Jhum Cultivation.

The findings provide insights into seasonal and yearly pollution trends and their potential impact on air quality and public health. While the pollution levels remain relatively moderate, proactive measures are necessary to mitigate future risks. Further research should focus on ground-based validation and policy recommendations. The finding and results of this study can be used by planners and policy-makers to mitigate air-pollution and formulate policies to enhance air quality.

The Eco-Environmental vulnerability of the study area was assessed using Landsat 5 TM, Landsat 7 +TM and Landsat 8 OLI images. Indices namely NDVI, WET, NDSI and LST, for the year 1994, 2003, 2014 and 2021 were generated and used for quantitative assessment of ecological vulnerability. Using these indices, a Remote Rensing based Ecological Index was constructed. Principal component analysis method was used for evaluation of the indicator indices. Ecological vulnerability index was calculated and classified into five vulnerability classes namely, Negligible vulnerability, Light vulnerability, Medium vulnerability, Strong vulnerability and Extreme vulnerability. The ecological vulnerability of Chandel is largely categorised under Light vulnerability throughout the study period, with the highest of 69.77% in 2021, followed by Medium vulnerability with 22.37% in 2021. 1994, 2003 and 2014 had negligible area under Extreme vulnerability, however, in the year 2021, an area of about 11.39 km^2 was classified as extreme vulnerability area. The area with Extreme vulnerability is associated with urban centres, economic activities and settlements are prominent. Whereas the areas with negligible or light vulnerability are associated with vegetation coverage or greeneries. Thus, we can conclude that Vegetation coverages are crucial for lowering the ecological vulnerability.

The eco-environmental vulnerability assessment across the three timelines (1994–2003, 2003–2014, and 2014–2021) also reveals an evolving pattern of environmental stress and recovery within the study area. Overall, the landscape demonstrates dominant stability with intermittent phases of both degradation and improvement,

reflecting the combined influence of natural processes and anthropogenic interventions.

During the first assessment period (1994–2003), the region experienced moderate eco-environmental disturbance. The Light vulnerability class dominated the landscape, with a large stable area of approximately 984.6 km², indicating overall ecological steadiness. Noticeable transitions occurred from Medium to Strong and Light to Strong vulnerabilities, signifying increasing human-induced stress, possibly from agricultural expansion, deforestation, or land clearing. However, transitions such as Medium to Light and Negligible to Light also reflected areas undergoing mild degradation rather than severe ecological collapse. Overall, this period marked a phase of environmental adjustment, where vulnerability increased slightly but remained largely within manageable limits.

In the second timeline (2003–2014), the eco-environmental system showed notable improvement and stabilization. A substantial portion of land remained in Light and Medium vulnerability classes, reflecting balanced ecological conditions. The area under Negligible and Medium vulnerabilities expanded slightly, suggesting localized recovery due to vegetation regrowth and reduced stress in certain zones. This phase can be characterized as a recovery period, where environmental management, forest regeneration, or reduced land pressure contributed to a general reduction in vulnerability levels.

In the most recent period (2014–2021), the eco-environmental conditions remained largely stable, with evidence of sustained resilience and minor localized degradation. Around 82% of the area maintained the same vulnerability class, dominated by Light and Medium vulnerability zones. The most significant positive shift was from Medium to Light vulnerability, while degradation primarily occurred in Medium to Strong and Light to Strong transitions. The persistence of Light vulnerability suggests moderate but enduring environmental pressure linked to land use and human activity. This period signifies relative ecological balance, though continued monitoring is necessary to prevent isolated areas of degradation from expanding.

This comprehensive study on the ecological vulnerability of Chandel district reveals that the overall ecological vulnerability of the study area is found to be mainly categorised under Light and medium vulnerability throughout the study period. However, in 2021, an area of 11.39 km^2 being graded as extreme vulnerability calls for formulation of measures to restore and regenerate the ecosystem quality.

This study was based on the ecological environmental indicators namely greenness, wetness, dryness and heat, and these selected indicators were used to generate the Remote sensing based ecological index by principal component analysis. Further studies can be made by selection of other indicators so that a more comprehensive assessment and evaluation can be achieved for better understanding and hence, implementation of proper ecological vulnerability evaluation, formulation, restoration and management.

In conclusion, the eco-environmental condition from 1994 to 2021 demonstrates that while anthropogenic pressure and natural processes have influenced vulnerability levels, the overall environmental stability of the region has been maintained or gradually enhanced. Conservation measures should target zones shifting toward higher vulnerability namely strong And Extreme Vulnerability areas. Continued sustainable land management, reforestation, and controlled development are essential to further strengthen resilience and prevent localized degradation from escalating into broader environmental vulnerability.

Bibliography

Achmad,A., S. Hasyim,B.Dahlan, andD.N.Aulia. 2015. "Modeling of UrbanGrowthinTsunami-prone City UsingLogistic Regression: Analysis of Banda Aceh, Indonesia." Applied Geography 62: 237–246. doi:10.1016/j.apgeog.2015.05.001

Adhikary, P. P., Barman, D., Madhu, M., Dash, C. J., Jakhar, P., Hombegowda, H. C., Naik, B. S., Sahoo, D. C., & Beer, K. (2019). Land use and land cover dynamics with special emphasis on shifting cultivation in Eastern Ghats Highlands of India using remote sensing data and GIS. *Environmental Monitoring and Assessment*, *191*(5). https://doi.org/10.1007/s10661-019-7447-7

Bai, Y., Ma, H., Zhang, B., Liang, j., Li, Z., Li, H., et al. (2009). Eco-environmental vulnerability analysis around Qinghai lake based on RS and GIS technology[J]. RemoteSens. Technol. Appl. 24 (05), 635–641. doi:10.11873/j.issn.1004-0323.2009.5.635https:// doi. org/ 10. 3390/ rs111 11332

Baig, M.H.A., Zhang, L., Tong, S., Tong, Q., 2014. Derivation of a tasselled cap transformation based on Landsat 8 at-satellite reflectance. Remote Sens. Lett. 5, 423–431.

Behera, M. D., Tripathi, P., Das, P., Srivastava, S. K., Roy, P. S., Joshi, C., Behera, P. R., Deka, J., Kumar, P., Khan, M. L., Tripathi, O. P., Dash, T., & Krishnamurthy, Y. V. N. (2018). Remote sensing-based deforestation analysis in Mahanadi and Brahmaputra river basin in India since 1985. *Journal of Environmental Management*, *206* (November), 1192–1203. https://doi.org/10.1016/j.jenvman.2017.10.015

Boori, M. S., & Amaro, V. E. (2011). Natural and eco-environmental vulnerability assessment through multi-temporal satellite data sets in Apodi valley region, Northeast Brazil. Journal of Geography and Regional Planning Vol. 4, pp. 216-230, April 20114(April), 216–230.

Cammerer, H., A. H. Thieken, and P. H. Verburg. 2013. “Spatio- temporal Dynamics in the Flood Exposure Due to Land Use Changes in the Alpine Lech Valley in Tyrol (Austria).” Natural Hazards 68: 1243–1270. doi:10.1007/s11069-012-0280-8.

Carlson TN, Ripley DA (1997) On the relation between NDVI, fractional vegetation cover, and leaf area index. Remote Sens Environ 62:241–252

Census of India 2011. District Census Handbook: Chandel. census2011.co.in

Climatic Research Unit, University of East Anglia, “High-resolution gridded datasets (CRU HRG)” [CRU TS & related datasets], https://crudata.uea.ac.uk/cru/data/hrg/

Crist, E. P. (1985). A TM Tasseled Cap equivalent transformation for reflectance factor data. Remote Sens. Environ. 17 (3), 301–306. doi:10.1016/0034-4257(85)90102-6

Deep, S., and A. Saklani. 2014. “Urban Sprawl Modeling Using Cellular Automata.” Egyptian Journal of Remote Sensing and Space Sciences 17: 179–187.

Dubovyk, O., R. Sliuzas, and J. Flacke. 2011. “Spatio-temporal Modelling of Informal Settlement Development in Sancaktepe District, Istanbul, Turkey.” ISPRS Journal of Photogrammetry and Remote Sensing 66: 235–246. doi:10.1016/j.isprsjprs.2010.10.002.

Duraisamy, V., Bendapudi, R., & Jadhav, A. (2018). Identifying hotspots in land use land cover change and the drivers in a semi-arid region of India. Environmental Monitoring and Assessment, 190(9). https://doi.org/10.1007/s10661-018-6919-5.

Džeroski, S. (2001). Applications of symbolic machine learning to ecological modelling. Ecological Modelling, 146(1-3), 263–273. https://doi.org/10.1016/S0304-3800(01)00305-6

Earth Resources Observation and Science (EROS) Center. (2020). Landsat 8-9 Operational Land Imager / Thermal Infrared Sensor Level-2, Collection 2 [dataset]. U.S. Geological Survey. https://doi.org/10.5066/P9OGBGM6.

Enete, A. A., & Amusa, T. A. (2010). Challenges of agricultural adaptation to climate change in Nigeria: A synthesis from the literature. Field Actions Science Reports. The Journal of Field Actions, (4), 1–7.

Fan, J., Gu, X., Guise, K. G., Liu, X., Fossella, J., Wang, H., & Posner, M. I. (2009). Testing the behavioral interaction and integration of attentional networks. Brain and Cognition, 70(2), 209–220.

Foley JA, De Fries R, Asner GP, Barford C, Bonan G, Carpenter SR, Chapin FS, Coe MT, Daily GC, Gibbs HK, Helkowski JH, Holloway T, Howard EA, Kucharik CJ, Monfreda C, Patz JA, Prentice IC, Ramankutty N, Snyder PK (2005) Global consequences of land use. Science 309:570–574

Foody, G. M. 2002. "Status of Land Cover Classification Accuracy Assessment." Remote Sensing of Environment 80: 185–201. doi:10.1016/S0034-4257(01)00295-4.

Foody, G.M., 2007. Editorial: ecological applications of remote sensing and GIS. Ecol. Inform. 2, 71-72.

Forman, R. T. T., & Alexander, L. E. (1998). Roads and their major ecological effects. Annual Review of Ecology and Systematics, 29, 207–231.

Government of Manipur. (n.d.). "Chandel District." Manipur State Portal. Retrieved from https://ccmanipur.mn.gov.in/en/chandel/

Government of Manipur. (n.d.). "Chandel Flora & Fauna." Chandel District Official Website. Retrieved from https://chandel.nic.in/flora-fauna/

Government of Manipur. (2023). District Profile: Chandel. ccmanipur.mn.gov.in

Gupta, K., Kumar, P., Pathan, S.K., 2012. Urban Neighborhood Green Index – a measure of green spaces in urban areas. Landscape Urban Plan. 105, 325–335.

Harris, L. D., & Silva-López, G. (1992). Forest fragmentation and the conservation of biological diversity. In P. L. Fiedler & S. K. Jain (Eds.), Conservation Biology: The Theory and Practice of Nature Conservation, Preservation and Management (pp. 197–237). Chapman and Hall

He, L., Shen, J., & Zhang, Y. (2018). Ecological vulnerability assessment for ecological conservation and environmental management. *Journal of Environmental Management*, *206*, 1115–1125. https://doi.org/10.1016/j.jenvman.2017.11.059

Hou, K., Tao, W., He, D., & Li, X. (2022). A new perspective on ecological vulnerability and its transformation mechanisms. Journal of Geographical Sciences, 32(8), 1435-1449. https://doi.org/10.1007/s11442-022-2009-3

Hu X, Xu H, 2018. A new remote sensing index for assessing the spatial heterogeneity in urbanecological quality: A case from Fuzhou City, China. Ecological Indicators 89:11-21. https:// doi. org/ 10. 1016/j. ecolind. 2018. 02. 006

Hu, X., & Xu, H. (2019). A new remote sensing index based on the pressure-state-response framework to assess regional ecological change. Environmental Science and Pollution Research (2019) 26:5381–5393. https://doi.org/10.1007/s11356-018-3948-0

Huang, C., Wylie, B., Yang, L., Homer, C., Zylstra, G., 2002. Derivation of a Tasselled Cap transformation based on Landsat 7 at-satellite reflectance. Int. J. Remote Sens. 23 (8), 1741–1748.

Ifeanyi, C. E., Adoh, E. N., & Alabi, M. O. (2010). Evaluation of eco-environmental vulnerability in Efon- Alaye using remote sensing and GIS techniques. Journal of Geography and Regional Planning Vol. 3(1), pp. 008-016, January, 2010.

Jabbar, M. T., & Dawood, A. S. (2015). Environmental Vulnerability Evaluation in Basra Province based on Remote Sensing and GIS Techniques. International Journal of Innovative Research in Science, Engineering and Technology, 4(1), 18401–18409. https://doi.org/10.15680/IJIRSET.2015.0401001

Jha, C. S., C. B. S. Dutt, and K. S. Bawa. 2000. "Deforestation and Land Use Changes in Western Ghats, India." Current Science 79: 231–238

Jing, Y., Zhang, F., He, Y., Kung, H., Johnson, V. C., & Arikena, M. (2020). Assessment of spatial and tempo- ral variation of ecological environment quality in Ebi- nur Lake Wetland National Nature Reserve, Xinjiang. China. Ecological Indicators, 110, 105874. https:// doi. org/ 10. 1016/j. ecoli nd. 2019. 105874

John, J., Bindu, G., Srimuruganandam, B., Wadhwa, A., & Rajan, P. (2020). Land use/land cover and land surface temperature analysis in Wayanad district, India, using satellite imagery. Annals of GIS, 26(4), 343–360. https://doi.org/10.1080/19475683.2020.1733662

Ju, W.M., Ping, G., Wang, J., 2010. Combining an ecological model with remote sensing and GIS techniques to monitor soil water content of croplands with a monsoon climate. Agric. Water Manage. 97, 1221–1231.

Kaly, U., Briguglio, L., McLeod, H., Schmall, S., Pratt, C., & Pal, R. (1999). Environmental Vulnerability Index (EVI) to summarise national environmental vulnerability profiles (Technical Report 275). SOPAC.

Kamal, P., Kumar, M., & Rawat, J. S. (2012). Application of Remote Sensing and GIS in Land Use and Land Cover Change Detection: A Case study of Gagas Watershed, Kumaun Lesser Himalaya, India. 342–345.

Karbalaei, S., & Solmaz, S. (2021). Spatiotemporal ecological quality assessment of metropolitan cities: a case study of central Iran. Environmental Monitoring and Assessment, 1–20. https://doi.org/10.1007/s10661-021-09082-2

Kearney, M. S., Rogers, A. S., and Townshend, J. R. G. (1995). Developing a model for determining coastal marsh “health”//third thematic conference on remote sensing for marine and coastal environments [J]. Seattle, Washington, 527–537.

Kerr, J.T., Ostrovsky, M., 2003. From space to species: ecological applications for remote sensing. Trends Ecol. Evol. 18, 299–305-587.

Khumlo, Khinis & Chongloi, Khumlo & Ansari, Meraj & Singh, K. & Singh, Amitabh. (2023). Assessment of Carbon Stock in Response to Varied Land Use Systems and Soil Depths in Chandel District, Manipur, India. International Journal of Environment and Climate Change. 13. 997-1001. 10.9734/ijecc/2023/v13i123762.

Krishna, N.D.R.; Kmaji, A.; Murthy, K.Y.V.N. and Rao, B.S.P. (2001). Remote Sensing and Geographical Information System for Canopy Cover Mapping, J. Indian Soc. Remote Sens., 29(3): 108-113

Kumar, P., Debnath, R., & Bardhan, R. (2019). Measuring accessibility in urban transport planning: A GIS-based approach. Journal of Urban Management, 8(1), 1–15.

Lambin, E. F., H. J. Geist, and E. Lepers. 2003. “Dynamics of Land-Use and Land-Cover Change in Tropical Regions.” Annual Review of Environment and Resources 28: 205–241. doi:10.1146/annurev.energy.28.050302.105459.

Lan, G., Jiang, X., Xu, D., Guo, X., Wu, Y., Liu, Y., & Yang, Y. (2023). Ecological vulnerability assessment based on remote sensing ecological index (RSEI): A case of Zhongxian County , Chongqing. January, 1–14. https://doi.org/10.3389/fenvs.2022.1074376

Landsat Science. (n.d.). The Thematic Mapper (TM). NASA. Retrieved September 18, 2025, from https://landsat.gsfc.nasa.gov/thematic-mapper/

Laurance, W. F., Goosem, M., & Laurance, S. G. (2009). Impacts of roads and linear clearings on tropical forests. Trends in Ecology & Evolution, 24(12), 659–669.

Li, A., Wang, A., Liang, S., & Zhou, W. (2006). Eco-environmental vulnerability evaluation in mountainous region using remote sensing and GIS — A case study in the upper reaches of Minjiang River, China. Ecological Modelling 192 (2006), 175–187. https://doi.org/10.1016/j.ecolmodel.2005.07.005

Li, L., Z. H. Shi, W. Yin, D. Zhu, S. L. Ng, C. F. Cai, and A. L. Lei. 2009. "A Fuzzy Analytic Hierarchy Process (Fahp) Approach to Eco-Environmental Vulnerability Assessment for the Danjiangkou Reservoir Area, China." Ecological Modelling 220 (23): 3439–3447. doi: 10.1016/j.ecolmodel.2009.09.005.

Li, N., Wang, J., Qin, F., 2020. The improvement of ecological environment index model RSEI. Arabian Journal of Geosciences. 13:403.

Lin, W., Pan, W.B., 2014. Research on ecological environment assessment of urban areas in Putian City. Environ. Sci. Manage. 39, 179–183.

Lo, C. P., and J. Choi. 2004. "A Hybrid Approach to Urban Land Use/cover Mapping Using Landsat 7 Enhanced Thematic Mapper Plus (ETM +) Images." International Journal of Remote Sensing 25: 2687–2700. doi:10.1080/ 01431160310001618428.

Maity, S., Das, S., Maity, J., Bera, B., Kumar, P., 2021. Assessment of Ecological Environment Quality in Kolkata Urban Agglomeration, India. Urban Ecosystems. https://doi.org/10.1007/s11252-022-01220-z.

Mallick, J., Y. Kant, and B. Bharath. 2008. "Estimation of Land Surface Temperature over Delhi Using Landsat-7 ETM+." Journal of Indian Geophysical Union 12: 131–140.

Mathan, M., & M, K. (2019). Monitoring spatio-temporal dynamics of urban and peri-urban land transitions using ensemble of remote sensing spectral indices-a case study of Chennai Metropolitan Area, India. *Environmental Monitoring and Assessment*, *192*(1), 15. https://doi.org/10.1007/s10661-019-7986-y

McFeeters, S. K. 1996. "The Use of the Normalized Difference Water Index (NDWI) in the Delineation of Open Water Features." International Journal of Remote Sensing 17: 1425–1432. doi:10.1080/01431169608948714.

Merz, B., Hall, J., Disse, M., & Schumann, A. (2010). Fluvial flood risk management in a changing world. Natural Hazards and Earth System Sciences, 10(3), 509–527.

Ministry of Agriculture & Farmers' Welfare. (2023). Annual Report 2022–23. Scribd link

Mustafa,A.,A.Heppenstall, H.Omrani,I.Saadi,M.Cools,andJ. Teller. 2018. "Modelling Built-up Expansion and Densification with Multinomial Logistic Regression, Cellular Automata and Genetic Algorithm." Computers, EnvironmentandUrban Systems 67: 147–156. doi:10.1016/j.compenvurbsys.2017.09.009.

N. P. S. Chauhan and R. K. Jagdish Singh "Status and distribution of sun bears in Manipur, India," Ursus 17(2), 182-185, (1 November 2006). https://doi.org/10.2192/1537-6176(2006)17[182:SADOSB]2.0.CO;2

North Eastern Development Finance Corporation. (2023). Climate of Manipur. databank.nedfi.com

Noss, R. F., & Cooperrider, A. Y. (1994). Saving nature's legacy: Protecting and restoring biodiversity. Island Press.

Noss, R. F., & Harris, L. D. (1986). Nodes, networks, and MUMs: Preserving diversity at all scales. Environmental Management, 10(3), 299–309.

Pal, S., and O. Akoma. 2009. “Water Scarcity in Wetland Area within Kandi Block of West Bengal: A Hydro-Ecological Assessment.” Ethiopian Journal of Environmental Studies and Management 2. doi:10.4314/ejesm.v2i3.48260.

Prenzel, B. 2004. “Remote Sensing-based Quantification of Land-cover and Land-use Change for Planning.” Progress in Planning 61: 281–299. doi:10.1016/S0305-9006(03)00065-5.

Rai, G., & Kumar, R. (2015). Structure and petrology of the Nagaland-Manipur Hill Ophiolitic Mélange zone, NE India: A Fossil Tethyan Subduction Channel at the India – Burma Plate Boundary. Episodes, 38(4), 301-314.

Rawat et al. (2024), Statistical Comparison of Simple and Machine Learning Based Land Use and Land Cover Classification Algorithms: A Case Study

Rawat, J. S., & Kumar, M. (2015). Monitoring land use/cover change using remote sensing and GIS techniques: A case study of Hawalbagh block, district Almora, Uttarakhand, India. *Egyptian Journal of Remote Sensing and Space Science*, *18*(1), 77–84. https://doi.org/10.1016/j.ejrs.2015.02.002

Reis, S. 2008. “Analyzing Land Use/land Cover Changes Using Remote Sensing and GIS in Rize, North-East Turkey.” Sensors 8: 6188–6202. doi:10.3390/s8106188.

Rimal, B., R. Sharma, R. Kunwar, H. Keshtkar, N. E. Stork, S. Rijal, S. A. Rahman, and H. Baral. 2019. “Effects of Land Use and Land Cover Change on Ecosystem Services in the Koshi River Basin, Eastern Nepal.” Ecosystem Services 38: 100963. doi:10.1016/j.ecoser.2019.100963.

Roy, A., & Srivastava, V. K. (2011). Geospatial approach to identification of potential hotspots of land-cover change for biodiversity conservation in Western Ghats of Goa. Current Science, 102(8), 1174–1180.

Sagan, C., O. B. Toon, and J. B. Pollack. 1979. “Anthropogenic Albedo Changes and the Earth’s Climate.” Science (80-) 206: 1363–1368. doi:10.1126/science.206.4425.1363.

SB, M., C, K., & K, A. (2017). Land Use/Cover and Vulnerability Mapping Through Remote Sensing and GIS In Astrakhan, Russia. *Journal of Earth Science & Climatic Change*, *08*(01), 1–6. https://doi.org/10.4172/2157-7617.1000380

Singh, A., 1989, Digital change detection techniques using remotely sensed data. International Journal ofRemote Sensing, 10, pp. 989–1003.

Singh, K. P., et al. (2020). Understanding the role of slope aspect in shaping the vegetation attributes and soil properties in Montane ecosystems. ResearchGate.

Singh, Leelambar & Singh, Ankita & Tripathi, Ravindra. (2025). Assessment of eco-environmental vulnerability, sustainability, and alignment with sustainable development goals in the Chambal River Basin, India. Theoretical and Applied Climatology. 156. 10.1007/s00704-025-05417-y.

Skondras, N. A., C. A. Karavitis, I. I. Gkotsis, P. J. B. Scott, U. L. Kaly, and S. G. Alexandris. 2011. “Application and Assessment of the Environmental Vulnerability Index in Greece.” Ecological Indicators 11 (6): 1699–1706. doi:10. 1016/j.ecolind.2011.04.010.

Song,J., S. Du, X.Feng, andL. Guo. 2014. “The Relationships between Landscape Compositions and Land Surface Temperature: Quantifying Their Resolution Sensitivity with Spatial Regression Models.” Landscape and Urban Planning 123: 145–157. doi:10.1016/j.landurbplan.2013.11.014.

Talukdar, S., Singha, P., Mahato, S., Praveen, B., Liou, Y. A., & Rahman, A. (2020). Land-Use Land-Cover Classification by Machine Learning Classifiers for Satellite Observations—A Review. Remote Sensing, 12(7), 1135. https://doi.org/10.3390/rs12071135

Turner, B. L., R. E. Kasperson, P. A. Matson, J. J. McCarthy, R. W. Corell, L. Christensen . . ., and C. Polsky. 2003. “A Framework for Vulnerability Analysis in Sustainability Science.” Proceedings of the National Academy of Sciences 100 (14): 8074–8079. doi:10.1073/pnas.1231335100.

U.S. Geological Survey. (n.d.). Landsat 7. USGS. Retrieved September 18, 2025, from https://www.usgs.gov/landsat-missions/landsat-7

U.S. Geological Survey. (2024). Landsat 8. Retrieved from https://www.usgs.gov/landsat-missions/landsat-8

USGS. (n.d.). Shuttle Radar Topography Mission (SRTM) 1 Arc-Second Global. Retrieved from https://www.usgs.gov/centers/eros/science/usgs-eros-archive-digital-elevation-shuttle-radar-topography-mission-srtm-1

Veefkind, J. P., de Haan, J. F., & Boersma, K. F. (2020). The TROPOMI/Sentinel-5P mission: Introduction and first results. Atmospheric Measurement Techniques, 13(1), 1-28. https://doi.org/10.5194/amt-13-1-2020

Venkatesh, R., Abdul Rahaman, S., Jegankumar, R., & Masilamani, P. (2020). Eco-Enviromental Vulnerability Zonation in essence of environmental monitoring and management. *International Archives of the Photogrammetry, Remote Sensing and Spatial Information Sciences - ISPRS Archives*, *43*(B5), 149–155. https://doi.org/10.5194/isprs-archives-XLIII-B5-2020-149-2020.

Wanyama, D., Kar, B., & Moore, N. J. (2021). Quantitative multi-factor characterization of eco-environmental vulnerability in the Mount Elgon ecosystem. *GIScience and Remote Sensing*, *58*(8), 1571–1592. https://doi.org/10.1080/15481603.2021.2000351

Ward, J. V., Tockner, K., Arscott, D. B., & Claret, C. (2002). Riverine landscape diversity. Freshwater Biology, 47(4), 517–539.Prager, Case & Jing, Xin & Henning, Jeremiah & Read, Quentin & Meidl, Peter & Lavorel, Sandra & Sanders, Nathan & Sundqvist, Maja & Wardle, David & Classen, Aimee. (2021).

Climate and multiple dimensions of plant diversity regulate ecosystem carbon exchange along an elevational gradient. Ecosphere. 12. 10.1002/ecs2.3472.

Wilcove, D. S., Rothstein, D., Dubow, J., Phillips, A., & Losos, E. (1998). Quantifying threats to imperilled species in the United States. BioScience, 48(8), 607–615. https://doi.org/10.2307/1313420

Wilcox, B. A., & Murphy, D. D. (1985). Conservation strategy: The effects of fragmentation on extinction. The American Naturalist, 125(6), 879–887. DOI: 10.1086/284386

Williams, Llewellyn & Kapustka, Lawrence. (2000). ECOSYSTEM VULNERABILITY: A COMPLEX INTERFACE WITH TECHNICAL COMPONENTS—Editorial. Environmental Toxicology and Chemistry - ENVIRON TOXICOL CHEM. 19. 10.1897/1551-5028(2000)019<1055: EVACIW>2.3.CO;2.

Wulder, M. A., Coops, N. C., Roy, D. P., White, J. C., & Hermosilla, T. (2018). Land cover 2.0. International Journal of Remote Sensing, 39(12), 4254–4284. https://doi.org/10.1080/01431161.2018.1452075

Xu, M., Cao, C., Zhong, S., Yang, X., Barjeece, B., Wang, K., Guo, H., Gao, X., Li, J., & Yang, Y. (2024). Ecological vulnerability assessment and spatial-temporal variations analysis in typical ecologically vulnerable areas of China. Frontiers in Ecology and Evolution, 12, 1406444. https://doi.org/10.3389/fevo.2024.1406444

Zhang, H., Wu, J., Gao, Y., & Chen, Z. (2017). Spatial assessment of ecological vulnerability in fuzhou district in China using remote sensing and GIS. *Nature Environment and Pollution Technology*, *16*(4), 1303–1312.

Zhang, Q.-P., Wang, J., Gu, H.-L., Zhang, Z.-G., & Wang, Q. (2018). Effects of Continuous Slope Gradient on the Dominance Characteristics of Plant Functional Groups and Plant Diversity in Alpine Meadows. Sustainability, 10(12), 4805. doi:10.3390/su10124805

Zou, T., and K. Yoshino. 2017. “Environmental Vulnerability Evaluation Using a Spatial Principal Components Approach in the Daxing’anling Region, China.” Ecological Indicators 78: 405–415.

Malekmohammadi, B., Blouchi, L.R., 2014. Ecological risk assessment of wetland ecosystems using Multi Criteria Decision Making and Geographic Information System. Ecol. Ind. 41, 133–144.

Niu, Y.Q., Wang, S.L., 2017. Research on coupling relationship between fragile ecological environment and poverty in Gansu province. Sheng Tai Xue Bao 37, 6431–6439.

Rouse, J.W., Haas, R.H., Schell, J.A., Deering, D.W., 1973. Monitoring vegetation systems in the Great Plains with ERTS. In: Conference Proceedings of the Third ERTS Symposium, NASA SP-351, Washington D.C, pp. 309–317.

Tomlinson, C. J., Chapman, L., Thornes, J. E., & Baker, C. (2011). Remote sensing land surface temperature for meteorology and climatology: A review: Remote sensing land surface temperature. Meteorological Applications, 18(3), 296–306. https:// doi. org/ 10. 1002/ met. 287

USGS (2019). Real-time Data. https://www.usgs.gov/products/data-and-tools/real-time-data

Wang, Y., and Dong, Z. (2013). Extraction of Remote Sensing Image Vegetation Information Based on the Tasseled Cap Transformation Image Fusion[J]. Geospatial Inf. (04), 85–86+9. doi:10.11709/j.issn.1672-4623.2013.04.031

Wang, Z., and Su, Y. (2018). Analysis of Eco-environment vulnerability characteristics of Hanzhong City, near the water source midway along the route of the south-to-north water transfer project, China[J]. Acta Ecol. Sin. 38 (02), 432–442. doi:10.5846/stxb201609261944

Williams, M., Longstaff, B., Buchanan, C., Llanso, R., and Dennison, W. (2009). Development and evaluation of a spatially-explicit index of Chesapeake Bay health. Mar. Pollut. Bull. 59 (1/3), 14–25. doi:10.1016/j.marpolbul.2008.11.018

Xiong, Y., Xu, W., Lu, N., Huang, S., Wu, C., Wang, L., Dai, F., & Kou, W. (2021). Assessment of spatial–temporal changes of ecological environment quality based on

RSEI and GEE: A case study in Erhai Lake Basin, Yunnan province. China. Ecological Indicators, 125, 107518. https:// doi. org/ 10. 1016/j. ecoli nd. 2021. 107518

Xu, H., Wang, Y., Guan, H., Shi, T., & Hu, X. (2019). Detect- ing ecological changes with a Remote Sensing Based Ecological Index (RSEI) produced time series and change vector analysis. Remote Sensing, 11(20), 2345. https:// doi. org/ 10. 3390/ rs112 02345

Xu, H.Q., Tang, F., 2013. A new generation of Landsat series satellites: new features of Landsat8 remote sensing imagery and its ecological and environmental significance. Acta Ecol. Sinica 33, 3249–3257.

Xu, H.Q., 2013b. Remote sensing evaluation index of regional ecological environment change. China Environ. Sci. 33, 889–897.

Yan, M., and Zhao, G. (2009). Ecological environment condition evaluation of estuarine area based on quantitative remote sensing——a case study in Kenli County[J]. China Environ. Sci. 29 (02), 163167. doi:10.3321/j.issn:1000-6923.2009.02.010

Yao,Yang, J., Wu, T., Pan, X., Du, H., Li, J., Zhang, L., Men, M., & Chen, Y. (2019). Ecological quality assessment of Xion- gan New Area based on remote sensing ecological index. Chinese Journal of Applied Ecology, 30(1), 277–284. https:// doi. org/ 10. 13287/j. 1001- 9332. 201901. 017

Yao, X., Yu, K., Liu, J., Yang, S. P., He, P., Deng, Y. B., et al. (2016). Spatial and temporal changes of the ecological vulnerability in a serious soil erosion area, Southern China. Chin. J. Appl. Ecol. 27 (03), 735–745. doi:10.13287/j.1001-9332.201603.022

Zawadzki, J., Przeździecki, K., & Miatkowski, Z. (2016). Determining the area of influence of depression cone in the vicinity of lignite mine by means of triangle method and LANDSAT TM/ETM+ satellite images. Journal of Environmental Management, 166, 605–614. https:// doi.org/ 10. 1016/j. jenvm an. 2015. 11. 010

Zhai, H., Xie, W., Li, S., & Zhang, Q. (2019). Urban ecological environment construction based on remote sensing eco- logical index. Ekoloji, 28(108), 1583–1588

Zhang, J.Q., Zhu, Y.Q., Fan, F.L., 2016. Mapping and evaluation of landscape ecological status using 657 658 geographic indices extracted from remote sensing imagery of the Pearl River Delta, China, between 1998 and 2008. Environ. Earth Sci. 75, 327–342.

Zhang, T.Y., Wang, L., Wang, H., Peng, L., Luo, C., 2017. Remote sensing monitoring of ecological environment in salinized irrigation areas of Manas river basin. Acta Ecol. Sinica 37, 3009–3018.

Zhu, W., A. Lu, and S. Jia. 2013. "Estimation of Daily Maximum and Minimum Air Temperature Using MODIS Land Surface Temperature Products." Remote Sensing of Environment 130: 62–73. doi:10.1016/j.rse.2012.10.034.

Photo plates

Field photos for LULC validation

Photo Plate 1: An overview of Chandel Town

Photo Plate 2: Chandel Forest Division

Photo Plate 3: An overview of Chakpikarong Sub-division.

Photo Plate 4: Chakpikarong main-town marketplace

Photo Plate 5: Dense vegetation cover of Chandel District

Photo Plate 6: An overview of vegetation cover/forest.

Photo Plate 7: paddy field

Photo Plate 8: Clearing of vegetation cover for cultivation

Photo Plate 9: Farmland in Chandel

Photo Plate 10: Terrace Farming

Photo Plate 11: Current Jhum Cultivation amidst forest cover.

Photo Plate 12: cleared vegetation for cultivation

Photo Plate 13: forest cover alongside agricultural land with settlement

Photo Plate 14: Current Jhum Land

Photo Plate 15: patches of cultivation in vegetation cover

Photo Plate 16: Plantation at Chakpikarong

Photo Plate 17: Agricultural land converted into Built-up

Photo Plate 18: Settlements amidst Paddy field

Photo Plate 19: Chakpi River

Photo Plate 20: Chakpikarong town along the Chakpi river

Photo Plate 21: Dry-season river at Modi Village.

Photo Plate 22: Summer view of river

Photo Plate 23: Charcoal Production

Photo Plate 24: Timber harvesting, a primary economic activity

Photo Plate 25: Timber for furniture.

Photo Plate26: Stone quarrying, another economic activity

Photo Plate 27: firewood produce of the study area

v 

Photo Plate 28: Air Quality Monitoring device used for taking air quality sample

Photo Plate 29: Air Quality sampling at Chandel

Photo Plate 30: District hospital

Photo Plate 31: Fire Sub-Station at Nahtham village.